UNIVERSITÀ DEGLI STUDI DI NAPOLI FEDERICO II

Civil, Architectural and Environmental Engineering Department (DICEA)

EXPERIMENTAL STUDY OF AIR ENTRAINMENT IN A HYDRAULIC JUMP ON PEBBLED ROUGH BED

By:

Farhad Bahmanpouri

Coordinator:

Prof. Ing. Andrea Papola

Supervisors:

Prof. Ing. Carlo Gualtieri

Prof. Ing. Hubert Chanson

In partial fulfillment of the requirements for the degree of Doctor of Philosophy at

The University of Napoli Federico II in 2019

Department of Civil, Architectural and Environmental Engineering

Abstract

Hydraulic jumps occur when upstream supercritical flow suddenly transitions into downstream subcritical flows. Extremely turbulent flow of the hydraulic jump associated with the development of large-scale turbulence, surface waves and spray, air entrainment and energy dissipation. Hydraulic jumps are commonly taking place in natural waterways and hydraulic structures. Enhancement of energy dissipation, fluid mixing or flow re-aeration are the usage of hydraulic jumps. Research of hydraulic jumps yet is a challenge and to date study of turbulence and two-phase air-flow properties are mostly limited to hydraulic jumps in smooth rectangular channels. Past studies on uniformly distributed roughness focused on the identification of the conjugate depth relationship and mean velocities flow and few of them measured even the turbulence and air-water parameters. No past study was conducted to investigate the effect of non-uniform bed roughness on the air-water flows in hydraulic jumps.

The present study systematically investigated the effects pebbled rough bed upon the basic flow patterns and air-water flow properties. The free-surface and air-water flow measurements were respectively recorded with the pointer gauge and intrusive phase-detection probes. Basic parameters of hydraulic jump including flow patterns and free-surface dynamics were carried out on smooth and rough bed configurations with two and one gate opening at upstream, respectively. The study of basic flow patterns covered a wide range of Froude numbers from 1.31 to 4.94 and Reynolds numbers from 4.2×10^4 to 2.3×10^5. The hydraulic jumps on the rough bed showed some characteristic flow patterns including a preaeration of the flow upstream of the hydraulic jump, an upwards shift of the jump roller resulting in a reduction of jump length, generation of larger eddies advecting downstream. An investigation of the fluctuations in impingement perimeter showed consistent statistical properties of longitudinally oscillating impingement positions across the central flow region on both bed types. Fluctuation of longitudinal water surface profile, exhibited the same trend on both bed types but a slightly higher standard deviation for smooth bed which was due to higher oscillation of water surface.

Basic properties of air –water flow including void fraction, bubble count rate, interfacial velocity and turbulent properties including turbulence intensity, correlation time scales, advection and length scale were investigated on both rough and smooth bed configurations with the same gate opening. Experiments of two-phase flow were conducted for a range of discharges $0.06 \leq Q_w \leq 0.1$ m^3/s, corresponding to upstream Froude numbers of $1.7 \leq Fr_1 \leq 2.84$ and to Reynolds numbers of $1.4 \times 10^5 \leq Re_1 \leq 2.2 \times 10^5$. The overall distributions of air-water flow properties were similar on both rough and smooth bed configurations. Comparative

analysis highlighted some distinctive effects of the bed roughness including an upwards shift of the hydraulic jump and an increase in bubble count rate, maximum and mean void fractions, and turbulent intensity in the region close to the jump toe.

The bubble-turbulence interplay induced the occurrence of bubble clustering, which was analysed on both rough and smooth bed configurations. The characteristic air-water time scale including particle chord time and length as well as properties including inter-particle arrival time, cluster count rate, cluster size and cluster proportion were investigated. Interparticle arrival time (IAT) analysis was also studied on both rough and smooth bed configurations. The result showed that near the jump toe, number of clustered bubbles was higher on rough bed which linked to big air entities and higher rate of bubble concentration.

The present thesis provides a description of the turbulent two-phase flow in hydraulic jump on pebbled rough bed. It is expected that this study would improve our knowledge of such a complex hydraulic process and address solid justification for future theoretical and numerical studies that have a long way ahead.

Acknowledgements

First of all, I want to thank my supervisors Prof. Carlo Gualtieri (UNINA) and Prof. Hubert Chanson (UQ) for the possibility to conduct my Ph.D. under their supervision. They allowed me to research independently and encouraged open-mindedness. I thank them for their continuous support of my Ph.D study and related research, for their patience, motivation, and immense knowledge throughout my Ph.D. project. I could not have imagined having a better supervisors for my Ph.D study.

Thanks to Dr. Stefan Felder for sharing the original code of his data acquisition and data analysis tools. And Thanks to Prof. Papola, the coordinator of Ph.D students, for his all assistance.

I would like to thank Jason Van Der Gevel and Stewart Matthews, technical staff of UQ‘s Civil Engineering lab for their assistance in the design, construction and improvements of the fume setup and especially rough bed setup.

I would like to thank my colleagues at UNINA for making my time at UNINA a colourful one. Among them are my office-mates Mohammad Daliri and Bikash Maharaj. Thanks to Majid, Yasaman, Shadi, Sahar, Jamal, Alireza, Mahan, Arash, Vida, Ensieh, Nicolo, Ivo, Gerardo, Fiore, Maria Rosa, Marilisa, Sofia, Akiko, Vincenzo, Gilbert, Greca and Dr. Hossein Ebrahimian. Thanks to my colleagues during the visiting period at UQ, Dr. Matthias Kramer and Dr. Hang Wang for their scientific assistance, and also thanks to Dr. Gangfu Zhang, Hamed, Armin & Bahar, and Davood.

I would like to thank my family, my parents and my brothers, for supporting me spiritually throughout my life and especially during my stay aboard.

Last but not least, I want to thank Faezeh (Faiy) for her patience during the Ph.D. project and her continuous love. Thanks sweetie.

Thanks for all your encouragement!

Table of Contents

List of Figures

List of Tables

List of Symbols

A_1 upstream flow cross-sectional area (m^2);
A_2 downstream flow cross-sectional area (m^2);
B characteristic width (m) in irregular channel defined as $B = (A_2\text{-}A_1)/(d_2\text{-}d_1)$;
B_1 upstream free-surface width (m);
B' integral characteristic width (m) in irregular channel;
C time-averaged void fraction defined as volume of air per unit volume of air and water;
C^* minimum void fraction at the boundary between shear layer and recirculation region;
C_{Fsec} void fraction corresponding to the secondary maximum bubble count rate in the recirculation region;
C_{max} maximum time-averaged void fraction in the turbulent shear region;
C_{mean} depth-averaged void fraction of a vertical cross-section;
c instantaneous void fraction;
dH total head loss (m);
$D^{\#}$ dimensionless air bubble diffusivity in the turbulent shear region: $D^{\#} = D_t/(V_1 \times d_1)$;
D^* dimensionless air bubble diffusivity in the upper free-surface region: $D^{\#} = D_t/(V_1 \times d_1)$;
D_t air bubble diffusivity (m/s^2);
d clear-water depth (m);
d_c critical depth of water (m) and $d_c = (q^2/g)^{1/3}$;
d_1 inflow water depth (m) immediately upstream of the jump toe;
d_2 downstream water depth (m);
d_{50} the value of grain sizes for which 50% of the material weight is finer (m);
d_{90} the value of grain sizes for which 90% of the material weight is finer (m);
F bubble count rate defined as the number of bubbles or water droplets per second (Hz);
F_{clu} cluster count rate (Hz) defined as the number of clusters per second;
$(F_{clu})_{max}$ maximum cluster count rate (Hz) in turbulent shear region;
F_{eddy} characteristic frequency of formation and downstream ejection of the large vortices in the shear layer (Hz);
F_{fric} flow resistance force ($kg \cdot m/s^2$);
F_{fs} characteristic frequency (Hz) of free surface fluctuations;
F_{max} maximum bubble count rate (Hz) in the turbulent shear region;
F_{toe} characteristic frequency (Hz) of longitudinal oscillations of jump toe position;
F_{sec} secondary maximum bubble count rate (Hz) in the recirculation region;
Fr_1 inflow Froude number: $Fr_1 = V_1/(g \times d_1)^{1/2}$;
f Darcy-Weisbach friction coefficient;
g gravity acceleration (m/s^2): g = 9.80 m/s^2 in Brisbane, Australia;
h upstream sluice gate opening (m);
K_s the roughness height (m) and equal to d_{50} (the median grain size of sediment particles);
K' integration constant;
K^* coefficient and $k^* = tanh^{-1}(0.1)^{0.5} = 0.3274$;
L_x longitudinal integral turbulent length scale (m);
L_{xx} advection length scale (m);
l_{ch} air bubble/water droplet chord length (m);
$(l_{ch})_a$ bubble chord length (m);
$(l_{ch})_w$ water droplet chord length (m);
Mo Morton number: $Mo = (g \times \mu^4)/(\rho \times \sigma^3)$;
N_{clu} average cluster size defined as the average number of particles per cluster;
$(N_{clu})_{max}$ local maximum average cluster size in turbulent shear region;

N	number of sample points in signal;
n	number of air-water interfaces detected by the phase-detection probe;
Q_w	flow rate (m^3/s);
q	water dischareg per unit width (m^2/s);
q_{ent}	air entrainment flux per unit width (m^2/s);
R_1	roughness type 1 by Felder and Chanson (2016);
R_2	roughness type 2 by Felder and Chanson (2016);
R_{xx}	normalised auto-correlation function;
$R_{xx'}$	normalised cross-correlation function between the signals of double-tip phase-detection probe sensors with a longitudinal separation;
R_{xy}	normalised cross-correlation function between the horizontal jump front oscillation signal and vertical free-surface fluctuation signal;
$(R_{xy})_{max}$	maximum/minimum cross-correlation coefficient between the horizontal jump front oscillation signal and vertical free-surface fluctuation signal;
Re_1	Reynolds number: $Re_1 = \rho \times V_1 \times d_1/\mu$;
St	Strouhal number: $St = F \times d_1/V_1$, F is a frequency;
SE	standard error;
T	statistical air-water interfacial travel time (s) between two phase-detection probe tips;
T_{scan}	sampling duration (s);
T_x	longitudinal integral turbulent time scale (s);
T_{xx}	auto-correlation time scale (s);
$T_{xx'}$	cross-correlation time scale (s) based on two probe signals with longitudinal separation
$T_{0.5}$	characteristic time lag (s) in the auto-correlation function for which $R_{xx} = 0.5$;
Tu	turbulence level as an approximation of the turbulence intensity;
t	instantaneous air-water interfacial travel time (s);
$(t_{ch})_a$	bubble chord time (s);
$(t_{ch})_a$	water chord time (s);
$(t_{ch})_{a,mean}$	mean bubble chord time (s) given: $(t_{ch})_{a,mean} = C/F$;
U	free-stream velocity (m/s) in the supercritical flow measured with Prandtl-Pitot tube;
U_{eddy}	vortex advection velocity (m/s)
U_w	depth-averaged flow velocity (m/s)
V	air-water interfacial velocity (m/s);
V_c	critical velocity (m/s) and $V_c = (gd_c)^{0.5}$;
V_{ej}	advection velocity (m/s) of large-scale vortices in the jump roller;
V_{max}	maximum air-water interfacial velocity (m/s) in the turbulent shear region;
V_{median}	median velocity (m/s) deduced from identification of sequent interfacial detection;
V_{rec}	average recirculation velocity (m/s) in the recirculation region;
V_1	average inflow velocity (m/s): $V_1 = Q/(W \times d_1)$;
W	channel width (m);
W_f	the weight force ($kg \cdot m/s^2$);
We	Weber number: $We = \rho \times V_1^2 \times d_1/\sigma$;
x	longitudinal distance (m) from the upstream sluice gate;
x_{toe}	instantaneous jump toe position (m);
$x_{toe'}$	standard deviation of instantaneous jump toe position (m);
x_1	longitudinal position (m) of jump toe;
Y_{Cmax}	vertical position (m) of the maximum void fraction in the turbulent shear region;
Y_{Fmax}	vertical position (m) of the maximum bubble count rate in the turbulent shear region;

Y_{Vmax} vertical position (m) of the maximum velocity in the turbulent shear region;

$Y_{0.5}$ vertical position (m) where the average velocity is half maximum: $Y_{0.5} = y(V = V_{max}/2)$;

Y_{50} vertical position (m) where the void fraction is 0.5;

Y_{90} vertical position (m) where the void fraction is 0.9;

y vertical distance (m) above the channel bed;

y^* vertical position (m) of the trough void fraction between the turbulent shear region and recirculation region;

z transversal distance (m) from the channel centreline;

Δx longitudinal separation distance (m) between the double-tip phase-detection probe tips;

Δz transversal separation (m) between two phase-detection probe tips;

$\Delta\tau$ time lag (s) for maximum correlation between free-surface fluctuation signals;

$Ø$ diameter (m);

δ boundary layer thickness (m);

η water elevation above the channel bed (m);

η' standard deviation of the water elevation above the channel bed (m);

κ the Kármán constant: $\kappa = 0.41$ for flow over a plane;

λ dimensionless coefficient of near-wake length scale;

μ dynamic viscosity (Pa·s);

ρ density (kg/m^3);

σ surface tension (kg·m/s^2);

θ the angle between the bed slope and horizontal;

τ time lag (s);

$\tau_{0.5}$ characteristic time lag (s) in the cross-correlation function for which $R_{xx'}(T+\tau_{0.5}) = (R_{xx'})_{max}/2$;

ω dimensionless coefficient for side-by-side particle clustering characterization.

List of Superscripts

(H) higher/upper;

(L) lower;

(l) leading;

(t) trailing;

$*$ at the boundary between turbulent shear region and recirculation region.

List of Subscripts

a,air air;

c instantaneous void fraction;

ch chord;

clu cluster;

ej ejection of large-size vortices;

i,j number of phase-detection probe sensor in four-point air-water flow measurement;

int integral;

max maximum/minimum value;

mean	mean value;
median	median value;
rec	recirculation flow property;
sec	secondary;
toe	jump toe;
w	water;
X	integral property in longitudinal direction;
x	property in longitudinal direction, particularly the horizontal free-surface position when specified;
y	property in vertical direction, particularly the vertical free-surface position when specified;
0.5	half of the maximum;
0.9	for void fraction equals 0.9;
1	upstream flow conditions;
2	downstream flow conditions;
50	void fraction equals 0.5;
90	void fraction equals 0.9.

List of Abbreviations

CHJ	classical hydraulic jump;
DEM	digital elevation model;
DES	detached eddy simulation;
DNS	direct numerical simulation;
FH	flume height;
FL	flume length;
FS	flume slope;
FW	flume width;
HDPE	high-density polyethylene;
LES	large eddy simulation;
LED	light emitting diode;
PDF	probability density function;
PIV	particle image velocimetry;
RANS	Reynolds-averaged Naiver-Stokes;
RH	roughness height;
VOF	volume of fluid.

1 INTRODUCTION

1.1 Presentation

An open channel flow can change from subcritical to supercritical in a relatively "low-loss" manner at gates or weirs. In these cases the flow regime evolves from subcritical to supercritical with the occurrence of critical flow conditions associated with relatively small energy loss (e.g. broad-crested weir). The transition from supercritical to subcritical flow is, on the other hand, characterized by a strong dissipative mechanism. It is called a hydraulic jump. A hydraulic jump is extremely turbulent. It is characterized by the development of large-scale turbulence, surface waves and spray, energy dissipation and air entrainment (Figure 1.1). The large-scale turbulence region is usually called the" roller". A hydraulic jump is a region of rapidly varied flow (Chanson 2004a). Figure 1.1 shows the hydraulic jump in the stilling basin of Paradise dam in Queensland, Australia. White waters as a sign of turbulent two-phase flow region with substantial air entrainment, intense turbulence development as well as splashes and droplet projections above the breaking surface are visible in Figure1.1.

Figure 1.1 Hydraulic jump in the stilling basin of the Paradise dam in Burnett River, Bundaberg QLD, Australia. Flow from left to right. Discharge estimated to be in excess of 6300 m^3/s with the Reynolds number of 1.9×10^7 (Courtesy of Hubert Chanson)

Energy dissipaters are designed to dissipate the excess in kinetic energy at the end of the chute before it re-enters the natural stream. Three types of energy dissipaters (Hager, 1992) have been commonly used: stilling basins, flip buckets, and roller buckets. Each dissipater has certain advantages and disadvantages and may be selected for a particular project depending upon the site characteristic. Energy dissipation on dam spillways is achieved usually by (1) a standard stilling basin downstream of a steep spillway in which a hydraulic jump is created to dissipate a large amount of flow energy and to convert the flow from supercritical to subcritical conditions, (2) a high velocity water jet taking off from a flip bucket and impinging into a downstream plunge pool or (3) a plunging jet pool in which the spillway flow impinges and the kinetic energy is dissipated in turbulent recirculation. Figure 1.2 shows a hydraulic jump downstream of a dam spillway during a flood (Chanson 2004a).

Figure 1.2 Hydraulic jump stilling basin in operation at the Hinze dam (Australia) on 29 January 2013; q_w=16.6 m^2/s, *Re*=1.6E7 (Felder and Chanson 2016)

The high energy loss that occurs in a hydraulic jump lead to its adoption as a part of high energy dissipater system below a hydraulic structure. The stilling basin is equipped with large blocks to assist with the energy dissipation (Figure 1.3). Accessories such as baffle blocks and sills are usually installed in the basins. The main function of such accessories is to shorten the length of the jump, to dissipate additional energy by increasing turbulence and to stabilize the jump in position.

Free surface flow is also can be used in dam spillways and industrial plants in order to enhance mixing and aeration for ecological purposes and/or chemical treatments (Figure 1.4).

Dissolved oxygen (*DO*) is very essential to healthy rivers, streams and lakes. Many naturally occurring biological and chemical processes use oxygen, thereby decreasing the *DO* concentration in water and causing greater stress. The aeration process replenishes the oxygen (Gualtieri and Pulci Doria 2012). However, aeration can be enhanced by modifying the flow pattern through phenomena like hydraulic jump and hydraulic drop. Hydraulic structures have an impact in enhancing the amount of dissolved oxygen in a river system, even though the water is in contact with the structure for only a short time (Raikar and Kamatagi 2015).

Figure 1.3 Baffle block in the stilling basin of the Hinze dam spillway (Australia) on 24 October 2014 - Each block, 3.2 m high, was designed based upon a physical model study (Felder and Chanson 2016)

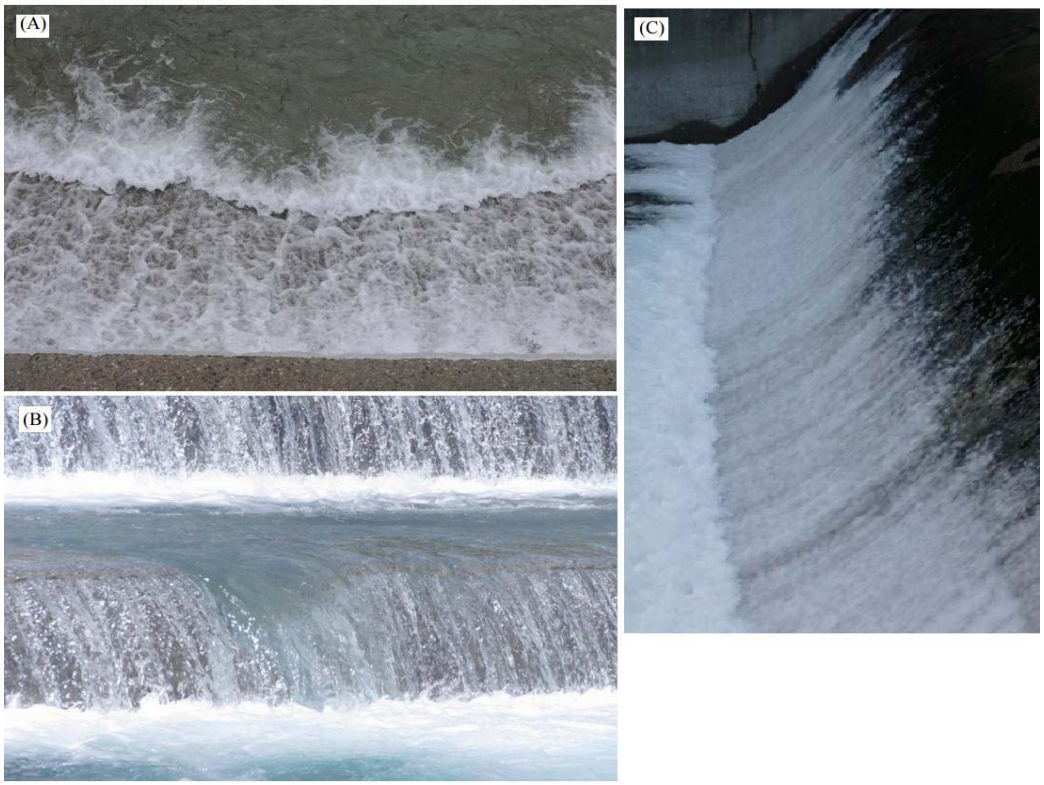

Figure 1.4 The process of mixing and aeration

The same quantity of oxygen transfer that normally would occur over several kilometers in a river can occur at a single hydraulic structure. The primary reason for this accelerated oxygen transfer is entrainment of air into the flow due to large number of bubbles.

The flow turbulence in hydraulic jumps is extremely complicated and three-dimensional, and it remains a challenge to engineers, scientists and researchers (Rajaratnam 1967; Chanson 2009a). Basic features of jumps with a breaking roller are the development of large-scale vortices, the air bubble entrapment at the jump toe, the interfacial aeration/de-aeration at the roller upper free-surface and the interactions between entrained bubbles and coherent turbulent structures in the jump roller, as seen in Figure 1.5.

Figure 1.5 Hydraulic jump in laboratory flume (Fr_1=6.5) (A) Hydraulic jump in the small flume (inflow conditions: Fr_1=6.5, Re_1=2.7E+4, V_1=2.2m/s, d_1=0.012m, W=0.25m) flow from left to right. (B) Hydraulic jump in the large flume (inflow conditions: Fr_1=6.5, Re_1=7.1E+4, V_1=3.1m/s, d_1=0.023m, W=0.5m) flow from left to right (Gualtieri and Chanson 2007)

Practical applications of artificial hydraulic jumps also include raising water levels in canals for irrigation improvement and reduction of pumping heads, and reducing uplift pressure under the foundations of hydraulic structures for damage prevention. A jump may also take place in a partially filled pipe flow before a valve or elbow, resulting in unfavorable noise, vibrations and unnecessary aerification (Wang 2014).

The hydraulic jump flow is characterized by the Froude number defined as the ratio of flow velocity to wave celerity, or equivalently the ratio of inertia to gravitational forces (Liggett 1994, Chanson 2004a, Castro-Orgaz and Hager 2009). The inflow Froude number Fr_1 of a hydraulic jump is defined as:

$$Fr_1 = \frac{V_1}{\sqrt{gd_1}} \tag{1.1}$$

Where V_1 is the mean velocity of the upstream supercritical flow, g is the gravity acceleration and d_1 is the inflow depth, with the subscript 1 denoting the upstream flow conditions.

Although there are different methods for classifying the hydraulic jumps, it can be broadly categorized according to the Froude number into (Montes 1998, Chanson 2009c):

a) Undular jumps, for 1.2 < Fr_1 < 1.5 to 4, with a relatively smooth increase in water elevation, continuous free-surface profiles transiting from supercritical to subcritical flow and downstream free-surface undulations;

b) Breaking jumps, for Fr_1> 1.5 to 4, with a marked roller at the transition region, turbulent fluctuating free-surfaces with spray, splashing and interfacial aeration and de-aeration, flow

recirculation next to the free-surface, substantial air entrapment at the locus where the upstream flow impinges into the downstream region, and formation of large-size vortical structures inside the flow.

The breaking hydraulic jumps might be further divided into oscillating jumps ($2.5 < Fr_1 < 4.5$), steady jumps ($4.5 < Fr_1 < 9$) and strong jumps ($Fr_1 > 9$). In practice, the so-called steady jump tends to provide optimum capacity of energy dissipation and scour protection (Hager 1992, Chanson 2004a). All hydraulic jumps investigated in the present thesis are breaking jumps.

The length of the jump roller is defined as the distance over which the water elevation increases monotonically from d_1 to d_2, where d_2 is the tailwater depth far downstream of the jump. The upstream and downstream depths $d_1$and d_2 are also called the conjugate depths or sequent depths. The ratio d_2/d_1 is deduced from the continuity and momentum principles for a horizontal flow with rectangular cross-section and negligible boundary friction (Belanger 1841, Chanson 2004a):

$$\frac{d_2}{d_1} = \frac{1}{2} \times (\sqrt{1+8Fr_1^2} - 1) \quad (1-2)$$

Equation (1-2) is also named the Bélanger equation.

In an integral form, the continuity and momentum principles give a system of equations linking the flow properties upstream and downstream of the jump (Lighthill 1978; Chanson 2012):

$$Q_w = V_1 \times A_1 = V_2 \times A_2 \quad (1-3)$$

$$\rho \times Q_w \times (\beta_2 \times V_2 - \beta_1 \times V_1) = \iint_{A_1} P \times dA - \iint_{A_2} P \times dA - F_{fric} + W_f \times \sin\theta \quad (1-4)$$

where:

Q_w is the water discharge

d and V are the flow depth and velocity respectively

ρ is the fluid density

g is the gravity acceleration

A is the flow cross-sectional area

β is a momentum correction coefficient

P is the pressure

Subscripts 1 and 2 refer to the upstream and down-stream flow conditions respectively

F_{fric} is the flow resistance force

W_f is the weight force and

θ is the angle between the bed slope and horizontal.

A complete solution for an irregular channel was developed (Chanson 2012; Leng and Chanson 2015).

For a horizontal channel, the solution of Equations (1.3) and (1.4) yields:

$$Fr_1^2 = \frac{1}{2} \times \frac{A_2}{A_1} \times \frac{B_1}{B_2} \times \left(\left(2 - \frac{B'}{B} \right) + \frac{B'}{B} \times \frac{A_2}{A_1} \right) + \frac{A_2}{A_2 - A_1} \times \frac{F_{fric}}{\rho \times g \times \frac{A_1^2}{B}} \quad (1-5)$$

where F_{fric} is the flow resistance force. For a hydraulic jump in a flat irregular channel, Equation (1-5) implies a smaller ratio of conjugate depths d_2/d_1 with increasing flow resistance. The effects of flow resistance on the conjugate depth ratio become negligible for $Fr_1 > 2$ to 3 (Chanson 2012). B_1 and B_2 are the upstream and downstream free-surface widths respectively. B and B' are characteristic transverse dimensions linked to the cross-sectional shape such as:

$$B = \frac{A_2 - A_1}{d_2 - d_1} \quad (1-6)$$

$$B' = \frac{\int_{A_1}^{A^2} \int \rho \times g \times (d_2 - y) \times dA}{\frac{1}{2} \times \rho \times g \times (d_2 - d_1)^2} \quad (1-7)$$

Equation (1-5) expresses the upstream Froude number as a function of the ratio of conjugate cross-sectional areas A_2/A_1, the flow resistance force and the irregular cross-sectional shape properties. For a fixed upstream Froude number, the effects of bed friction implies a smaller ratio of conjugate depths d_2/d_1 with increasing flow resistance, where d_2 and d_1 are the conjugate flow depths.

For a rectangular horizontal channel, the solution of the momentum and continuity equations yields (Chanson 2012):

$$Fr_1^2 = \frac{1}{2} \times \frac{d_2}{d_1} \times \left(\left(1 + \frac{d_2}{d_1} \right) + \frac{1}{\frac{d_2}{d_1} - 1} \times \frac{F_{fric}}{\rho \times g \times B \times d_1^2} \right) \quad (1-8)$$

The energy principle yields the total head loss in a hydraulic jump in a rectangular channel:

$$\frac{dH}{d_1} = \frac{1}{16} \times \frac{(\sqrt{1+8\times Fr_1^2}-3)^2}{(\sqrt{1+8\times Fr_1^2}-1)} \quad (1-9)$$

Based upon Equation (1-9), the energy dissipation rate exceeds 70% for a hydraulic jump with Froude number larger than 9.

To date, the length of the hydraulic jump roller L_r is only estimated with some empirical correlations. One of such correlations was proposed by Hager et al. (1990) for wide channel (i.e. $d_1/W < 0.1$):

$$\frac{L_r}{d_1} = 160 \times \tanh(\frac{Fr_1}{20}) - 12 \quad (1-10)$$

Where: the roller length L_r is defined as the distance from the jump toe to the surface stagnation point indicating the limit between the backward and forward flow (Hager et al. 1990).

For a classical hydraulic jump generated in a horizontal long-channel gradually varied flow, the jump location might be determined with both Bélanger equation and backwater equation:

$$\frac{\partial \eta}{\partial x} = \frac{-C_f \times Fr_1^2}{1-Fr_1^2} \quad (1-11)$$

where: η is the water elevation above the invert, x is the streamwise position and C_f is a friction coefficient related to the Darcy-Weisbach coefficient f by C_f= f/8. The hydraulic jump occurs where the upstream and downstream backwater Equations (Eq. (1-11)) yield the conjugate depths satisfying the Bélanger Equation (Eq. (1-2)).

The mathematical description of the free-surface profile is more challenging. Most analytical solutions of the roller surface elevation ignore the air entrainment thus the associated flow bulking. Valiani (1997) proposed an expression of the free-surface profile based upon the linear and angular momentum conservation:

$$\frac{\eta}{d_1} = \sqrt[3]{\frac{1}{8} \times (\sqrt{1+8\times Fr_1^2}-1)^3 - 1) \times \frac{x-x_1}{L_r} + 1} \quad (1-12)$$

1.2 Background and objectives

Flow mechanics of a hydraulic jump on rough bed is associated with the large number of parameters controlling and describing the flow regimes. Although the study of hydraulic jump spanned over more than two hundred years, our knowledge is far from a full understanding. The concept of mass and momentum conservation enabled theoretical descriptions of basic flow characteristics such as jump location, conjugate depth ratio, energy dissipation rate and possibly free-surface profile. Each single phenomenon, at macroscopic or microscopic level, is governed by a range of physical processes (e.g. air diffusion, buoyancy, shear stress, surface tension, etc.). The interactions between all processes make the flow regimes extremely complicated and difficult to study (Wang 2014).

The interpretation of the collected information is challenging, more intense for rough bed, because of the inherent complexity of the flow characteristics varying in length, width and time scales. Moreover, most practical applications of hydraulic jumps such as aeration, chemical mixing, energy dissipation downstream of spillways and reservoirs, flows mixing, etc. occur on rough beds.

To date, the only studies of air entrainment in hydraulic jump on rough bed are first Pagliara and Palermo (2015) which investigated just air concentration profile in hydraulic jump on inverse bed using a USBR single-tip conductivity and second Felder and Chanson (2016) which was conducted on two special bed roughness. In this study, new bed roughness was used in terms of hydro-environmental process to simulate the process of hydraulic jump on natural rivers and channels.

Based on previous studies, This PhD project is aimed to acquire information on turbulence and air-water flow characteristics of hydraulic jumps on the pebbled rough bed configuration. The following are the reasons for this research:

1- Comparing the rough bed and smooth bed, the hydraulic jumps on the rough bed exhibited some characteristic flow patterns including decreasing the conjugate depth ratio, increasing the bed shear stress, a preaeration of the flow upstream of the hydraulic jump, an upwards shift of the jump roller resulting in a reduction of jump length. The comparative analysis highlighted some distinctive effects of the bed roughness including an upwards shift of the hydraulic jump and an increase in bubble count rate and void fractions in the region close to the jump toe.

2- Bed and water surface features of the natural jump regions differ significantly from classical hydraulic jump conditions and engineering analogues with respect to boundary conditions.

All above-mentioned reasons are very important in order to design energy dissipating structures such as stilling basins downstream of weirs in order to optimize energy dissipation.

Systematic investigations were conducted in the University of Queensland (Australia) for laboratory experiments and in the University of Federico II Napoli (Italy) for analyzing the data based upon physical modelling and relevant data analysis. The work consisted of the design of experiments (~ 5%), the implement of experiments (~ 40%), the analysis of experimental data (~ 40%) and the presentation/publication of the outcome (~ 15%). The experiments and data analysis were primarily focused on the interpretation of turbulence development, air entrainment process and their interactions in classical hydraulic jumps. The experimental program encompassed visual observations, clear-water velocity measurements, free-surface measurements and air-water flow measurements. Relatively wide ranges of Froude and Reynolds numbers ($1.5 < Fr_1 < 5$, $4.2E4 < Re_1 < 2.3E5$) were tested with different similitude criteria to present a full-scale investigation. The flow patterns, turbulence and air-water flow properties, bubble clustering and the physical regimes were presented with consideration of the effects of Froude and Reynolds numbers. The current knowledge of the physics in hydraulic jumps was developed. Contributions were also made to an improved understanding of their application as flow re-aerators, fluid mixers or energy dissipaters.

1.3 Thesis outline

This thesis presents the experimental study and outcomes during the PhD project in the following order:

Chapter 1: Introduction. The hydraulic jump is introductory discussed in this section following with description of the background and objectives of the present.

Chapter 2: A literature review is presented in details in this chapter for hydraulic jump on the smooth bed, turbulent flow characteristics on macro roughness, hydraulic jump on the rough bed and finally the numerical simulation of hydraulic.

Chapter 3: Physical modelling and experimental methodology. The experimental facility, the instrumentation and the signal processing techniques are introduced and bed roughness configuration is described.

Chapter 4: Flow patterns and free-surface dynamics. The basic observation and free-surface measurement results for hydraulic jumps on both smooth and rough channel beds are shown. The free-surface profile and fluctuations are discussed together with the oscillations of jump toe.

Chapter 5: Basic air-water flow properties. The characteristics of air bubble advection and diffusion in the jump roller are presented in terms of the time-averaged void fraction, bubble count rate, and air-water interfacial velocity.

Chapter 6: The turbulence intensity and a series of characteristic turbulent time and length scales are calculated.

Chapter 7: Bubble clustering in a hydraulic jump on rough bed. Two criteria for cluster identification are applied: one criterion is based upon a comparison of the local instantaneous water chord time with the median water chord time, whereas the second identifies a cluster if the water chord time is smaller than the air chord time of the preceding bubble, i.e. a bubble is in the near-wake of the leading bubble. The effect of the inflow flow Froude number on the clustering process is also discussed. Furthermore, the clustering process is studied using a different approach, the analysis of the interparticle arrival time (IAT) of the bubbles.

Chapter 8: Conclusion. The key findings of the present thesis are summarized.

Appendix A: Photographs of Hydraulic Jumps to discuss on Flow patterns and free-surface dynamics.

Appendix B: Experimental flow conditions and characteristic air-water flow properties. Tabular presentation of flow conditions for all series of experiments is given. The characteristic air water flow properties and relevant empirical correlation functions are summarized for retrieval.

2 LITERATURE REVIEW

2.1 Presentation

The first description of hydraulic jump by Leonardo da Vinci may be traced back to the 16 century (Montes 1998). The early studies were mostly focused on the dimensions of hydraulic jumps, such as the jump length and conjugate depths. In this chapter previous studies divided to three parts first, hydraulic jump properties on smooth bed second, turbulent flow characteristics on a bed with macro-roughness and third, hydraulic jump properties on the rough bed. The second part shows that how different forms of the rough bed could affect the turbulent characteristics of the flow. And the third part reveals the previous investigations on the hydraulic jump in a channel with the rough bed up to now.

2.2 Air entrainment in hydraulic jumps

For a hydraulic jump with limited self-aeration in the upstream impinging flow, the air entrainment is a combination of two mechanisms. First, an air layer intruding into the roller is formed next to the inflow free-surface because of the surface air-water shear friction. Second, an analogy to plunging jet may suggests that an air trumpet is induced as a ventilated cavity at the water depth discontinuity (Cummings and Chanson 1997, Chanson and Brattberg 1998). The reversed flow above the jump toe pinched the air trumps and releases an air pocket into the downstream shear flow (Chanson 2009a). The air pocket is quickly broken into small air bubbles in the turbulent shear stress. The majority of bubbles are advected in the streamwise direction within large vortical flow structures. The advective diffusion of air bubbles is affected by a number of factors such as buoyancy, turbulence and its dissipation.

Both aeration and de-aeration take place at the roller free-surface. Air is entrapped as large-scale turbulence develops next to the roller surface as described in Chapter 4, while the air bubbles entrained at the jump toe are gradually released to the atmosphere after advection in the shear flow region (Wang 2014). Substantial surface fluctuations and air-water projections characterize a two-phase flow zone above the mean water elevations, with the time-averaged air content typically higher than 50%. The upper boundary of this area is considered at an elevation Y_{90}

where the air concentration reaches 90% (Cain and Wood 1981). This characteristic elevation is sometimes treated as the upper surface of jump roller. Both aeration and de-aeration flux are intense for strong hydraulic jumps considering the large amount of splashing at the free-surface as depicted in Chapter 4.

The air-water flow properties of a hydraulic jump include the time-averaged void fraction *C* defined as the proportion of time that the probe tip is in the air, and the bubble count rate *F* defined as the number of bubbles impacting the probe tip per second (Gualtieri and Chanson 2007). At a given location in the jump roller, the void fraction is linked to the entrained air and its advection and turbulent diffusion, while the bubble count rate is further linked with the turbulent shear field which influences the generation, breaking-up, coalescence and collapsing of bubbles (Wang, 2014). The void fraction and bubble count rate distributions in a vertical cross section of jump roller were measured in the literature with intrusive phase-detection techniques (Chanson and Brattberg 2000, Murzyn et al. 2005, Chanson 2007a, 2011, Gualtieri and Chanson 2007, Kucukali and Chanson 2008, Murzyn and Chanson 2009, Chachereau and Chanson 2011a, Wang 2014, Felder and Chanson 2018). Typical profiles are sketched in Figure 2.1 for hydraulic jumps with partially-developed inflow conditions together with the relevant characteristic parameters.

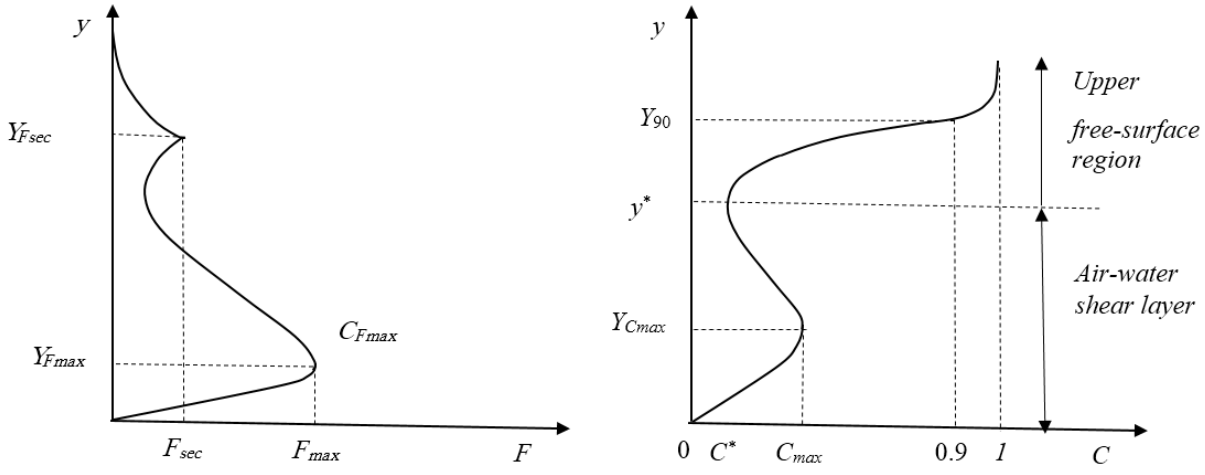

(A) Void fraction (B) Bubble count rate

Figure 2.1 Sketches of typical void fraction and bubble count rate distributions in hydraulic jump roller (based on Chanson 2010)

Based upon void fraction and bubble count rate profiles two main flow regions can be observed in the roller area, namely the turbulent shear region and the recirculation region above (Figure 2.1). In the turbulent shear region, a bell-shape profile of time-averaged void fraction started from the channel bed with zero void fraction to a characteristic elevation y^* with a local minimum value C^*. A maximum void fraction C_{max} is typically detected at an elevation Y_{Cmax} ($0 < Y_{Cmax} < y^*$). The bubble count rate increased rapidly from zero to a maximum F_{max} with the increasing distance from the invert to an elevation Y_{Fmax}. Further increase in elevation led to a reduction in bubble count rate, with some local minimum at the upper boundary of the turbulent shear region. The recirculation region included two regions; a bubbly flow region below and a splashing free-surface area above the mean water elevation. The void fraction increased monotonically from C^* to unity across the recirculation region, whereas the bubble count rate exhibited a secondary peak F_{sec} at an elevation Y_{Fsec} and decreased to zero above the roller surface. Note that F_{sec} could be greater than F_{max} when the air concentration in the turbulent shear region was low. In a jump with fully-developed or pre-aerated inflow conditions, different void fraction and bubble count rate profiles were observed (Resch and Leutheusser 1972a, Chanson 1997a).

Flow properties and regimes suggested that two different flow regimes are significant. In the turbulent shear region, a mixing shear layer developed, and the flow was characterized by a advection of air bubbles entrapped at the jump toe and transported downstream in large vortical structures (Hoyt and Sellin 1989, Chanson 2010). The flow properties were largely controlled by the turbulence field, though the buoyancy effects were not negligible and related 1to the flow de-aeration. On the other hand, the recirculating motions of free-surface flow and the air-water projections characterized the recirculation region, where the gravity force played a major role. In the present study, the boundary between the two flow regions was defined at the characteristic elevation y^* (Figure 2.1A).

Assuming a uniform advective velocity distribution equal to the inflow velocity V_1, a theoretically description of the void fraction distribution in the turbulent shear region may be deduced from the continuity equation of air bubbles in a control volume:

$$V_1 \times \frac{\partial C}{\partial x} + u_r \times \frac{\partial C}{\partial y} = D_t \times \frac{\partial^2 C}{\partial^2 y} \quad (2.1)$$

Where x and y are the longitudinal and vertical coordinates, respectively, and the bubble rise velocity u_r and diffusivity D_t are assumed constant. Note that the compressibility effects are neglected and steady flow conditions are applied (Chanson 2010). Given a variable $X = x-x_1+u_r/V_1 \times y$ with the longitudinal jump toe position, a classical two-dimensional advection-diffusion equation can be derived (Crank 1956):

$$V_1 \times \frac{\partial C}{\partial x} = D_t \times \frac{\partial^2 C}{\partial^2 y} \tag{2.2}$$

An analytical solution is achieved with the boundary condition of jump toe acting as a point source of air, i.e. $C = Q_{air}/Q$ at (x-$x_1 = 0$, $y = d_1$) where Q_{air} is the entrained air volume, Q is the air-water volume and d_1 the inflow depth (Chanson 2010). The application of the method of images yields:

$$C = \frac{\frac{Q_{air}}{Q}}{\sqrt{4 \times \pi \times D^{\#} \times X'}} \times \left(\exp\left(-\frac{(y'-1)^2}{X' \over 4 \times D^{\#}} \right) + \exp\left(-\frac{(y'+1)^2}{X' \over 4 \times D^{\#}} \right) \right) \tag{2.3}$$

where $X' = X/d_1$, $y' = y/d_1$, and $D^{\#}$ is a dimensionless turbulent diffusivity: $D^{\#} = D_t/(V_1 \times d_1)$. In first approximation, Equation 2.3 may be simplified as (Chanson 1995, 1997a):

$$C = C_{\max} \times \exp\left(-\frac{1}{4 \times D^{\#}} \times \frac{\left(\frac{y - Y_{C_{\max}}}{d_1} \right)^2}{\left(\frac{x - x_1}{d_1} \right)} \right) \qquad \text{for } 0 < y < y^* \tag{2.4}$$

The buoyancy effects is takes implicitly into account by using the Y_{Cmax} which is determined based upon experimental data (Chanson 2009a).

In the recirculation region, based upon analogy to water jets discharging into air with a uniform velocity distribution suggests that the void fraction follows an analytical solution of Equation 2.1 in the form of the Gaussian error function (Chanson 1989, Brattberg et al. 1998, Murzyn et al. 2005, Wang and Chanson 2018):

$$C = \frac{1}{2} \times \left(1 + erf \left(\frac{y - Y_{50}}{2 \times \sqrt{\frac{D^* \times (x - x_1)}{V_1}}} \right) \right) \quad \text{for } y > y^* \qquad (2.5)$$

where D^* is a dimensionless diffusivity in the upper free-surface region, and the Gaussian error function is defined as:

$$erf\ (u) = \frac{2}{\sqrt{\pi}} \int_0^u \exp(-t^2) \times dt \qquad (2.6)$$

Although Equation 2.5 fits the experimental data, the different flow patterns between a water jet and hydraulic jump roller free-surface may limit the analogy between the two types of flow. Therefore, the application of Equation 2.5 to the upper hydraulic jump roller may be debatable, especially for strong hydraulic jumps with marked surface recirculation and deformation (Wang 2014).

2.3 Hydraulic jump properties on smooth bed

Ehrenberger (1926) was the first to study the phenomenon of air entrainment in open channels. He conducted investigations in a rectangular channel with slopes varying from 15.5 to 76.2 per cent and discharges ranging from 3.00 to 44.46 L/sec. He classified the flow into four layers, a top layer composing of drops of water flying through the air parallel to the water surface, below which a layer consisting of a closely packed layer of air bubbles in water, followed by a layer of water containing individual air bubbles and finally a bottom layer of clear water near the bed. Following that, the air entrainment in hydraulic jump was studied in terms of the air entrapment rate which was a key design consideration in close conduit flows (Kalinske and Robertson 1943). Early laboratory studies were reviewed by Rao and Kobus (1971) and Wood (1991).

Chanson (1997a) developed an analysis of the air entrainment processes in free-surface flows. Those flows were investigated as homogeneous mixtures with variable density. Several types of air-water free-surface flows were studied: plunging jet flows, open channel flows, and turbulent water jets discharging into air. Experimental observations reported by the author confirmed the concept that the air-water mixture behaves as a homogeneous compressible fluid in each case.

The free-surface dynamics were measured by Mouaze et al. (2005) and Murzyn et al. (2007) with intrusive wire gauges, whereas non-intrusive acoustic displacement meters were applied by Murzyn and Chanson (2009) and Chachereau and Chanson (2011b) yielding similar results in terms of free-surface profile, fluctuation magnitude and frequencies. An empirical law of self-similar free-surface profile was proposed by Chanson (2011) within the roller length.

Gualtieri and Chanson (2007) investigated the effect of Froude number on the basic air-water flow properties, especially for the maximum void fraction and bubble count rate in the shear layer. The comparison of results with previous studies demonstrated that, at a fixed distance from the jump toe, the maximum void fraction C_{max} increased with increasing Fr_1. The vertical locations of the maximum void fraction and bubble count rate were consistent with previous studies. They also derived an empirical correlation between the upper boundary of the air diffusion layer and the distance from the impingement point. The scale effects were discussed by Wood (1991) and Chanson (1997a), followed by Chanson (2007b), Murzyn and Chanson (2008), Chanson and Gualtieri (2008) and Chanson and Chachereau (2013).

Some recent investigations which involved in signal processing technique have done in term of turbulence characteristics, e.g. turbulent time and length scales. (Chanson 2007a) studied the turbulence characteristics of hydraulic jump with identical Froude numbers, but a range of Reynolds numbers and relative channel widths. The results showed drastic scale effects at small Reynolds numbers in terms of void fraction and bubble count rate distributions. The void fraction distributions implied comparatively greater detrainment at low Reynolds numbers leading to a lesser overall aeration of the jump roller, while dimensionless bubble count rates were drastically lower especially in the mixing layer. The experimental results suggested also that the relative channel width had little effect on the air-water flow properties for identical inflow Froude and Reynolds numbers. The investigation on turbulent time and length scales had done by Chanson and Carosi (2007a, 2007b).

The analysis of inter-particle arrival time also pointed out that the bubble/droplet clustering existed widely in the bubbly flow and spray region rather than random particle distributions (Gualtieri and Chanson 2004, Heinlein and Fritsching 2006).

The particle clustering was investigated particularly in hydraulic jump by some researchers. Gualtieri and Chanson (2010) addressed the bubble clustering process in hydraulic jumps using experimental data collected in a rectangular horizontal flume with partially developed inflow

conditions. Two criteria for cluster identification were applied: one criterion was based upon a comparison of the local instantaneous water chord time with the median water chord time, whereas the second identified a cluster if the water chord time was smaller than the air chord time of the preceding bubble, i.e. a bubble was in the near-wake of the leading bubble. The results highlighted significant patterns in clusters production both over the flow depth and the distance from the jump toe. The investigation continued by Chanson (2010), Gualtieri and Chanson (2013) and Chachereau and Chanson (2011a) in longitudinal dimension.

Wang (2014) conducted a series of laboratory tests in a channel with smooth bed in order to evaluate the flow patterns, total pressure, turbulence and air-water flow properties and the physical regimes with relatively wide ranges of Froude and Reynolds numbers with different similitude criteria. The results highlighted the linkage of the advection and diffusion of air bubbles to both buoyancy effects and dissipation of turbulence and kinetic energy. The correlation analysis between the simultaneously sampled water elevation, void fraction and total pressure signals revealed that a downstream shift of jump toe position corresponded to a decreasing water level in the first half roller and an increasing water level in the second half roller. The results also highlighted that the turbulence level was linked to the Reynolds number and the longitudinal dissipation process was further affected by the Froude number. The large turbulence intensity and turbulent length and time scales were contributed by both fast velocity fluctuations and relatively slow free-surface deformations and large vortical structures. The total pressure in the main shear layer varied corresponding to the water level fluctuations, while the pressure in the lower shear region varied with the longitudinal velocity decelerations.

Some other studies have done in different hydraulic structures such as in circular plunging jets, stepped chute flows and drop-shaft flows in order to investigate the turbulence characteristics, the procedure of air entrainment and energy dissipation and the scale effects (Boes 2000, Chanson and Toombes 2002a, 2002b, Chanson 2004b, Chanson et al. 2004, Felder and Chanson 2009, 2011, 2012b, Bung 2013, Felder 2013). These works also provided good references in instrumentation and signal processing technology.

Table 2.1 summaries some of researches on hydraulic jump on a smooth bed.

Table 2.1 Summary of literature review of air entrainment in hydraulic jump on smooth bed

Reference	Experimental condition Flume dimension (cm)	Range of Froude/ Reynolds numbers	Discharge /Velocity	Instrumentation	Measured parameters	Results
Ehrenberger (1926)	Rectangular channel *FS*: 15.5 to 76.2 %	_	*Q*:3.00-44.46 L / s	_	-Discharge -Upstream depth -Tailwater depth -Jump length -Roller length -Velocity -Air concentrations -Bubbles frequency -Turbulence intensity	-The flow was into four layers, a top layer composing of drops of water flying through the air parallel to the water surface, below which a layer consisting of a closely packed layer of air bubbles in water, followed by a layer of water containing individual air bubbles and finally a bottom layer of clear water near the bed.
Chanson (1995)	-A vertical supported jet -A horizontal hydraulic jump	_	V_1: 1.97–9 m/s	Conductivity probe (single tip, 0.35 mm inner electrode), PD inflow conditions	-Discharge -Velocity -Air concentrations -Bubbles frequency -Turbulence intensity	-The "advection" of air bubbles within the turbulent shear layer is a complex function of the upstream flow conditions. -The turbulent shear layer is characterized by a highly aerated core in which the air concentration follows a Gaussian distribution. The results indicate that the main properties of the Gaussian distributions are nearly "free" from buoyancy effects. With the vertical supported jet, a change of air entrainment mechanism is observed for impact velocities larger than 4-8 m/s. At larger inflow velocities, the air entrainment occurs via an air sheet set into motion by the impinging jet. The air layer behaves as a ventilated cavity, releasing intermittently large pockets of air that are later broken up into bubbles of smaller sizes.
Chanson (1997a)	-Plunging jet flows -Open channel flows Turbulent water jets discharging into air	_	_	_	-Discharge -Velocity -Air concentrations -Bubbles frequency -Turbulence intensity	-Air-water mixture behaves as a homogeneous compressible fluid in each case.

Gualtieri and Chanson (2007)	A horizontal channel *FL*: 320 *FW*: 25	Fr_1: 5.2-14.3 *Re*: 24000-48000	–	A single-tip conductivity probe (needle probe design). The probe consisted of a sharpened rod (platinum wire ϕ =0.35 mm)	-Discharge -Upstream depth -Velocity -Air concentrations -Bubbles frequency -Turbulence intensity	-The comparison of results with previous studies demonstrated that, at a fixed distance from the jump toe, the maximum void fraction Cmax increases with the increasing Fr_1. -The vertical locations of the maximum void fraction and bubble count rate were consistent with previous studies.
Gualtieri and Chanson (2010)	A horizontal channel *FL*: 320 *FW*: 25	Fr_1: 6.5-14.3 *Re*: 24000-48000	V_1: 2.23-4.48 m/s	A single-tip conductivity probe (needle probe design). The probe consisted of a sharpened rod (platinum wire ϕ =0.35 mm)	-Air concentrations -Bubbles frequency -Turbulence intensity -Bubble clustering	-The maximum number of clusters per second decreases with increasing distance from the jump toe and decreases with decreasing inflow Froude Fr_1. -The maximum clustering rate was observed within the turbulent shear layer, suggesting that the clustering process is most intense in the regions of large turbulent shear stresses.
Wang (2014)	A horizontal channel *FL*: 320 *FW*: 50	Fr_1: 2.8-10 *Re*: 21000-160000	*Q*: 0.0173-0.0815 m^3/s	-Video camera (Sony Handycam HDR-CW100E) -Prandtl-Pitot tube -Acoustic displacement meter -A double-tip phase-detection conductivity probe -Total pressure probe	-Discharge -Upstream depth -Tailwater depth -Jump length -Roller length -Velocity -Air concentrations -Bubbles frequency -Turbulence intensity -Bubble clustering	-The turbulence level was linked to the Reynolds number and the longitudinal dissipation process was further affected by the Froude number. -The large turbulence intensity and turbulent length and time scales were contributed by both fast velocity fluctuations and relatively slow free-surface deformations and large vortical structures. -The total pressure in the main shear layer varied corresponding to the water level fluctuations, while the pressure in the lower shear region varied with the longitudinal velocity decelerations.

FL: Flume Length, *FW*: Flume Width, *FH*: Flume Height, *FS*: Flume Slope

2.4 Turbulent flow characteristics on a bed with macro roughness

Tachie and Adane (2007), Wang et al. (2007), Tachie and Shah (2008), Agelinchaab and Tachie (2008) and Tsikata (2012) investigated the pressure gradient and turbulent flow properties in a channel with micro roughness as divided into two types, *d*-type and *k*-type ribs. Different angles with flow direction: zero angle or straight and inclined with different angels; 30, 45, and 60 were analyzed.

Tachie and Shah (2008) revealed that, for a given rib inclination, profiles of the mean velocity, turbulent intensities, and Reynolds shear stress did not vary significantly with rib geometry. They also showed that the inclined ribs reduced the level of the Reynolds stresses, triple velocity correlations, and transport of both the turbulent kinetic energy and Reynolds shear stress compared to the straight ribs.

Fang et al. (2015) investigated highly-disturbed turbulent flows in a square channel with *V*-shaped ribs mounted on one wall. A planar particle image velocimetry (*PIV*) system was used to measure the fully developed turbulent flow at the channel midspan and two off-center planes. *V*-shaped rib configurations with three different inclinations (60, 45 and 30 degree) were studied and compared to the perpendicular (90 degree) rib case. The statistics of the first and second order moments were studied in terms of velocity, vorticity, shear rate and Reynolds stresses. Their result showed that secondary flows were induced by the V-shaped ribs, which appeared as a pair of large-scale streamwise counter-rotating vortices in the cross-stream direction. The ratio between different components of the Reynolds normal stresses showed that it was more isotropic above the *V*-shaped ribs compared to the perpendicular rib case.

Table 2.2 summaries the previous researches on turbulence flow features in a channel with d-type and *k*-type roughness.

Table 2.2 Summary of literature review on turbulent flow properties in channel with d-type and k-type roughness

Reference	Experimental condition Flume dimension (cm)	Range of Froude/ Reynolds numbers	Discharge /Velocity	Instrumentation	Measured parameters	Results
Ehrenberger (1926)	Rectangular channel *FS*: 15.5 to 76.2 %	_	*Q*:3.00-44.46 L / s	_	-Discharge -Upstream depth -Tailwater depth -Jump length -Roller length -Velocity -Air concentrations -Bubbles frequency -Turbulence intensity	-The flow was into four layers, a top layer composing of drops of water flying through the air parallel to the water surface, below which a layer consisting of a closely packed layer of air bubbles in water, followed by a layer of water containing individual air bubbles and finally a bottom layer of clear water near the bed.
Chanson (1995)	-A vertical supported jet -A horizontal hydraulic jump	_	V_1: 1.97–9 m/s	Conductivity probe (single tip, 0.35 mm inner electrode), PD inflow conditions	-Discharge -Velocity -Air concentrations -Bubbles frequency -Turbulence intensity	-The "advection" of air bubbles within the turbulent shear layer is a complex function of the upstream flow conditions. -The turbulent shear layer is characterized by a highly aerated core in which the air concentration follows a Gaussian distribution. The results indicate that the main properties of the Gaussian distributions are nearly "free" from buoyancy effects. With the vertical supported jet, a change of air entrainment mechanism is observed for impact velocities larger than 4-8 m/s. At larger inflow velocities, the air entrainment occurs via an air sheet set into motion by the impinging jet. The air layer behaves as a ventilated cavity, releasing intermittently large pockets of air that are later broken up into bubbles of smaller sizes.

Chanson (1997a)	-Plunging jet flows -Open channel flows Turbulent water jets discharging into air	_	_	_	-Discharge -Velocity -Air concentrations -Bubbles frequency -Turbulence intensity	-Air-water mixture behaves as a homogeneous compressible fluid in each case.
Gualtieri and Chanson (2007)	A horizontal channel *FL*: 320 *FW*: 25	Fr_1: 5.2-14.3 *Re*: 24000-48000	_	A single-tip conductivity probe (needle probe design). The probe consisted of a sharpened rod (platinum wire ϕ =0.35 mm)	-Discharge -Upstream depth -Velocity -Air concentrations -Bubbles frequency -Turbulence intensity	-The comparison of results with previous studies demonstrated that, at a fixed distance from the jump toe, the maximum void fraction Cmax increases with the increasing Fr_1. -The vertical locations of the maximum void fraction and bubble count rate were consistent with previous studies.
Gualtieri and Chanson (2010)	A horizontal channel *FL*: 320 *FW*: 25	Fr_1: 6.5-14.3 *Re*: 24000-48000	V_1: 2.23-4.48 m/s	A single-tip conductivity probe (needle probe design). The probe consisted of a sharpened rod (platinum wire ϕ =0.35 mm)	-Air concentrations -Bubbles frequency -Turbulence intensity -Bubble clustering	-The maximum number of clusters per second decreases with increasing distance from the jump toe and decreases with decreasing inflow Froude Fr_1. -The maximum clustering rate was observed within the turbulent shear layer, suggesting that the clustering process is most intense in the regions of large turbulent shear stresses.
Wang (2014)	A horizontal channel *FL*: 320 *FW*: 50	Fr_1: 2.8-10 *Re*: 21000-160000	*Q*: 0.0173-0.0815 m^3/s	-Video camera (Sony Handycam HDR-CW100E) -Prandtl-Pitot tube -Acoustic displacement meter -A double-tip phase-detection conductivity probe -Total pressure probe	-Discharge -Upstream depth -Tailwater depth -Jump length -Roller length -Velocity -Air concentrations -Bubbles frequency -Turbulence intensity -Bubble clustering	-The turbulence level was linked to the Reynolds number and the longitudinal dissipation process was further affected by the Froude number. -The large turbulence intensity and turbulent length and time scales were contributed by both fast velocity fluctuations and relatively slow free-surface deformations and large vortical structures. -The total pressure in the main shear layer varied corresponding to the water level fluctuations, while the pressure in the lower shear region varied with the longitudinal velocity decelerations.

FL: Flume Length, *FW*: Flume Width, *FH*: Flume Height, *FS*: Flume Slope

2.5 Hydraulic jump properties on rough bed

Hughes and Flack (1984) measured hydraulic jump characteristics over several artificially roughened test beds in a horizontal rectangular flume with smooth side walls. Experiments included a smooth test bed, two strip roughness test beds and three densely packed gravel test beds provided a relative roughness range from 0.0-0.9. The testing program involved some 200 hydraulic jump observations which included flow rate, upstream depth, tailwater depth and jump length. Observations showed that boundary roughness reduces both the sequent depth and the length of a hydraulic jump, and that the observed reductions were related to both Froude number and the degree of roughness.

Ead and Rajaratnam (2002) evaluated the hydraulic jumps on corrugated beds. Experiments were performed for a range of Froude number from 4 to 10. They found that the tailwater depth required to form a jump was appreciably smaller than that for the corresponding jumps on smooth beds. Also, length of the jumps was about half of those on smooth beds. The integrated bed shear stress on the corrugated bed was about 10 times that on smooth bed.

Carollo et al. (2007) surveyed the depth ratio and roller length for hydraulic jump on rough gravel bed with 5 different bed material size in a long flume with 14.4 m length, 0.6m width and 0.6m height. 408 runs for Froude number between 1.9 and 9.9 were performed.

Defina et al. (2008) investigated the bed friction effect on the stability of a stationary hydraulic jump in a rectangular upward sloping channel through a combined theoretical and experimental approach. Two different approaches, one approach examined the speed adopted by the weakly perturbed jump, the other used the difference of momentum function across the slightly displaced jump, were compared these for the case of a wide rectangular channel.

Pagliara et al. (2008) analyzed the hydraulic jump that occurs in homogeneous and non-homogeneous rough bed channels. The parameters that influenced the sequent flow depth and the length of the jump were systematically investigated. The experimental study involved about 200 tests, which included measurements of flow rate, sequent depths, roller depth and length and jump length. They stated that viscous effects are not significant on jump properties.

Abbaspour et al. (2009) studied the effect of sinusoidal corrugated bed on hydraulic jump characteristics. The analysis of velocity profiles at different sections in the jump showed that the velocity profiles were similar to those of a simple plane wall jet. The normalized boundary layer

thickness δ/b was equal to 0.57 for jumps on a corrugated bed, compared to 0.16 for the simple wall jet. The analysis and comparison of the bed shear force and shear stress coefficient showed that shear stress on a corrugated bed is about 10 times that of a smooth bed.

Elsebaie and Shabayek (2010) evaluated the effect of different shapes of corrugated beds on the characteristics of hydraulic jumps. Five shapes of corrugations (sinusoidal, triangular, trapezoidal with two side slopes and rectangular) of the same amplitude and wavelength were tested. It was found that, for all shapes of corrugated beds, the tailwater depth required to form a jump was appreciably smaller than that for the corresponding jumps on smooth beds. Further, the length of the jump on the different corrugated beds was less than half of that on smooth beds. The integrated bed shear stress on the corrugated beds was more than 15 times that on smooth beds. For the same amplitude and wavelength, it was found that the effect of the shape of corrugations is relatively small.

Pagliara et al (2010) measured two-phase flow properties over rough bed materials. They used coarser protruding materials over the rough bed to intensify the aeration in the mixed air-water flow. Flow discharges ranging between 0.02 and 0.09 m^3/s and slopes between 0.18 and 0.44 were tested. Air concentration measurements and flow patterns were compared with the basic configuration. A detailed study of the flow properties in the inner layers of air-water mixed flow exhibited that the coarseness of the bed materials enhances air entrainment, with its influence indicated in the concentration profile.

Pagliara et al. (2011) continued their research on hydraulic jump on rough bed. Crushed angular rocks and hemispherical boulders were used to intensify the roughness of the bed. The facility consisted of a rough bed chute of 8 m long and 0.3 m wide, a recirculation ensured the water supply, and a magnetic flow meter (OPTIFLUX 2000) for the discharge measurement. The result showed that the void fraction and frequency analysis reveals that there is a strong interaction between the water surface and rough bed elements, resulting in stable drag vortices and stable shear vortices between the rough bed elements.

Neluwala et al. (2013) assessed the characteristics of hydraulic jumps formed on rough, horizontal channel beds under different flow. 140 experimental runs were carried out for various roughness beds for a range of flow rate 10-25 L/s while changing the roughness density (8% to 37.5%) and the element sizes (0.8 cm to 1.5 cm).The hydraulic parameters such as, initial water depth, sequent water depth, and flow rate were measured for different bed roughness. The

analysis of experimental data showed that the rough bed reduces the distance to the jump from the gate and the sequent depth ratio than those on smooth beds while creating a high energy loss.

Carollo et al. (2013) stated that the hydraulic *B*-jump has the toe section located on a positively sloping upstream channel and the roller end on a downstream horizontal channel. They analyzed the *B*-jump on a rough bed, such as at the transition from a block ramp to the stilling basin. Laboratory measurements of the sequent depth were carried out using three different channel slopes for the rough bed and a single slope for the smooth bed. The result showed that depth ratio is a power function of the group (F_1 −1), whereas the scale coefficient m depends on the others dimensionless groups.

Ahmed et al. (2014) identified the characteristics of submerged hydraulic jump on corrugated beds. Thirty experimental runs were carried out considering wide range of Froude numbers ranging from 1.68 to 9.29. Experiments were conducted for both smooth and rough bed. The results confirm that sequent depth and jump length were reduced by average values 15.14% and 21.03%, respectively, whereas, jump efficiency was increased by 50.31% at optimum spaced roughness compared to a classical jump, respectively. The result showed that spaced corrugated bed sheets increased the eddies that were created between bed sheets and consequently increased the bed shear stress, The amount of shear stress was found to be a function of Froude number.

This work could be biased because such a configuration shows the inflow invert at the same elevation as the top of the roughness. This implies that the top of the roughness is equivalent to a pseudo-bottom. In real condition roughness level is higher than bed level so it has effect on flow properties.

Pagliara and Palermo (2015) reported the results of an experimental investigation of hydraulic jump properties in flows over adverse-sloped rough beds, including the effect of air entrainment. Furthermore, a semi-theoretical predictive relationship was proposed to estimate jump characteristics for a wide range of hydraulic and geometric conditions covering both rough and smooth beds. The result showed that the increase of Reynolds shear stresses induced by the bed roughness resulted in a reduction of the sequent depth ratio. The reduction was more prominent for increasing relative roughness and bed slope. Results also showed that air entrainment profiles were significantly influenced by the relative equivalent depth d_e / d_{84} (the ratio between effective depth and a characteristic diameter of base material). They showed that air concentration increased when d_e / d_{84} decreased. This was mainly due to both the presence of drag and shear

vortices between the stones and an increasing interaction between the free surface and the stones. Furthermore, streamwise oriented vortexes were also visible and were more stable for low relative flow depth.

Felder and Chanson (2016) studied the air-water flows in hydraulic jumps with channel bed roughness. Two different rubber mat configurations of macro-roughness were investigated as shown in Figure 2.2. Experiments were conducted at the University of Queensland for a range of discharges $0.012 \leq Q \leq 0.106$ m^3/s, corresponding to upstream Froude numbers of $1.7 \leq Fr_1 \leq 6.5$ and to Reynolds numbers of $6.3 \times 10^4 \leq Re_1 \leq 2.1 \times 10^5$. They used two double-tip conductivity probe systems for measuring air entrainment properties.

Figure 2.2 Two kind of bed configurations by Felder and Chanson (2016)

Furthermore the experiments were documented using digital cameras Canon max^{TM} DOS 450D and PentaxTMK-3 as well as video camera Sony^{TM} Handycam HDR-CW100E and a digital camera Casio^{TM} Exilim EX-10 with high speed video capabilities. Their measurements included

distributions of void fraction, bubble count rate, interfacial velocity, turbulence intensity, and further advanced air-water flow properties. The result showed these features: some characteristic flow patterns including a pre-aeration of the flow upstream of the hydraulic jump, an upwards shift of the jump roller resulting in a reduction of jump length, a clear water flow region underneath the jump and a stabilization of the jump toe fluctuations. Upwards shift of the hydraulic jump and an increase in bubble count rate and void fractions in the region close to the jump toe were the result of their experiments. Also, they concluded that in the second half of the hydraulic jumps the rough bed lead to elevated levels of void fraction in the recirculation region suggesting a lesser aeration of the free-surface region.

Considering hydraulic jump in natural rivers two studies were done; first Comiti et al. (2006), they evaluated experimental tests and field data on the dimensions of standing waves created by artificial drops in steep gravel bed rivers. Fluvial gravels with d_{50}=8.7 mm were used as bed material on a flume with 0.03% bed slope. The result showed that the dimensionless wavelength and wave amplitude were correlated to the Froude number at the sill. The transition between roller and undular jumps at drops was argued to likely represent a critical stage for the stability of morphological structures such as step pools. Second study was Vallè and Pasternack (2006) which they tested high-resolution digital elevation models (*DEMs*) for natural submerged and unsubmerged jump regions, in a bedrock step-pool mountain channel against the classical hydraulic jump (*CHJ*). The slope of field study channel was 0.043 % and the average particle diameter of the pebbles and cobbles was 0.085 m (variance=0.0013 m^2). The results showed that abrupt topographic elements such as mid-channel boulders, bed steps, or channel knickpoints were hypothesized to represent potential cases for submerged jump conditions, as was often observed for plunge pools below abrupt bed steps. Conversely, bed topographic elements such as low angle transverse bedrock outcrops and moderately dipping knickpoints or glides represented potential cases for unsubmerged jump conditions due to low jet inclination angles and tailwater conditions favoring the presence of the hydraulic jump roller on the free surface and unsubmerged jump conditions.

Despite relevant studies in the past two centuries, the hydraulic jump is not fully understood. Detailed knowledge on the interactions between turbulence and two-phase flow is still limited. Tables 2.3 and 2.4 present the summary of literature review and effect of bed roughness on flow properties, respectively.

Table 2.3 Summary of literature review of hydraulic jump on rough bed

Reference	Flume dimension (cm)	Roughness (*RH* mm)	Range of Froude numbers	Range of Reynolds numbers	Discharge rate $(\frac{m^3}{s})$	Instrumentation	Investigated flow properties
Hughes and Flack (1984)	*FL*=213 *FW*=30.5 *FH*= - *FS*=0.0	-Two strip roughness beds (*RH*: 3.2 and 6.4) three densely packed gravel beds (*RH*: 4.3-11.3)	3.44-8.04 2.34-10.5	-	0.010-0.015	-Calibrated orifice for measuring discharge -Piezometers for measuring tailwater depth -Pitot-static tube for measuring velocity -Point gauge	-Discharge -Upstream depth -Tailwater depth -Jump length -Roller length -Velocity
Ead and Rajaratnam (2002)	*FL*=760 *FW*=44.6 *FH*= 60 *FS*=0.0	-Corrugated aluminum Sheets (*RH*=13 and 22)	4-10	50,800–206,756	0.023-0.092	-Magnetic flowmeter for measuring discharge -Prandtl tube for measuring velocity (*Ø*=3 mm) -Point gauge	-Discharge -Upstream depth -Tailwater depth -Jump length -Roller length -Velocity -Water surface profile
Carollo et el. (2007)	*FL*=1400 *FW*=60 *FH*= 60 *FS*=0.0	-Crashed gravel particles (d_{50}: 4.6, 8.2, 14.6, 23.9, 32)	1.1-9.9		-	-Point gauge for measuring flow depth -Graduated rule for measuring roller length	-Upstream depth -Tailwater depth -Jump length -Roller length -Velocity
Defina et al. (2008)	FL=200 FW=38 FH= 50 FS=0.04	-Spherical pebbles of ball-clay (*RH*: 9.6-10.5)	1.9-10.57	$0.5*10^5$-$1*10^5$	-	-Magnetic flowmeter for measuring discharge	-Discharge -Upstream depth -Tailwater depth -Jump length -Roller length -Velocity
Pagliara et al. (2008)	*FL*=600 *FW*=35 *FH*= 50 *FS*=0.0	-Homogeneous and non-homogeneous sediments, gravel (d_{50} : 6.26-45.6) -Rough bed with Boulders, metallic	2.2-12.2	21000-110000	0.006-0.031	-Magnetic flowmeter for measuring discharge -Digital video recording for measuring depths	-Discharge -Upstream depth -Tailwater depth -Jump length -Roller length -Velocity -Water surface profile

		hemispheres (38 and 65)					
Abbaspour et al. (2009)	*FL*=1000 *FW*=29.5 FH= 50 *FS*=0.0	-Corrugated polyethylene sheet (*RH*: 15,20,25,35)	0.286-0.625 3.8-8.6	61,200-175,600	0.03-0.08	- Ultra Sonic sensors and VisiDAQ software for measuring depths - Micro Propeller velocity meter	-Upstream depth -Tailwater depth -Jump length -Roller length -Velocity
Elsebaie and Shabayek (2010)	*FL*=900 *FW*=25 *FH*= 32 *FS*=0.0	-Corrugated plastic sinusoidal and corrugated wooden triangular, trapezoidal with two side slopes and rectangular	3-7.5	49,523-142,157	-	- V-notch for measuring discharge - Point gauge for measuring flow depth	-Discharge -Upstream depth -Tailwater depth -Jump length -Roller length -Velocity -Water surface profile
Pagliara et al (2010)	*FL*=700 *FW*=30 *FH*= - *FS*=0.18-0.44	-Crushed angular elements (d_{50} =43.41) -Hemispherical coarser elements of diameter d_b=55 mm (cobbles or boulders) on the rough bed	0.67-2.42	-	0.006-0.009	- Krohne OPTIFLUX 2000 KC magnetic flow meter for measuring discharge - Point gauge for measuring flow depth -Air water flow properties were measured using a USBR single tip conductivity probe air concentration meter (6mm diameter tip) -High speed camera for flow visualizations	-Discharge -Upstream depth -Tailwater depth -Jump length -Roller length -Velocity -Water surface profile -Air concentrations -Bubbles frequency
Pagliara et al (2011)	Chute Length: 800 Wide: 30 Slope: 0.26-0.46	-Crushed angular rocks (d_{50} =43.41) - -Hemispherical boulders (d_b=55 mm)	1.02-2.35	-	0.09-0.027	- Magnetic flow meter (OPTIFLUX 2000) for the discharge measurement - intrusive single tip conductivity probe (tip $\varnothing$=6 mm) - Point gauge	-Discharge -Upstream depth -Tailwater depth -Jump length -Roller length -Velocity -Water surface profile -Air concentrations -Bubbles frequency

Neluwala et al. (2013)	*FL*=1200 *FW*=30 *FH*= 30 *FS*=0	-Rectangular wooden strips Height: 8,12,15 element spaces: 4,5,6,8,10 cm	2.5-6	-	0.007-0.026	- Depth gauges - *V*-notch for measuring discharge	-Discharge -Upstream depth -Tailwater depth -Jump length -Roller length -Velocity
Carollo et al. (2013)	*FL*=490 *FW*=30.4 *FH*= 24 Angle =8.5,12,17.5	-Crushed angular elements (d_{50} =54)	1.76-6.11	-	-	-Electro-magnetic flow meter for measuring discharge - Point gauge	-Discharge -Upstream depth -Tailwater depth -Velocity
Ahmed et al (2014)	*FL*=2500 *FW*=30.4 *FH*= 24 Angle =0	-Triangular corrugated sheet (height: 40, width:40)	1.68-9.29	-	0.03-0.04	- Ultrasonic-Flow meter for measuring discharge - Point gauge	-Discharge -Upstream depth -Tailwater depth -Jump length -Roller length -Velocity
Pagliara and Palermo (2015)	Channel 1: *FL*=600 *FW*=34.5 *FH*= 50 *FS*=-0.05 Channel 2: *FL*=600 *FW*=35 *FH*= 70 *FS*=-0.1	-Gravel (d_{50}: 6.26,19.33,30.62)	2-9.5	-	-	- Point gauge for measuring flow depth -Air water flow properties were measured using a USBR single tip conductivity probe air concentration meter (6mm diameter tip)	-Discharge -Upstream depth -Tailwater depth -Jump length -Roller length -Velocity -Air concentrations -Bubbles frequency
Felder and Chanson (2016)	*FL*=320 *FW*=50 *FH*= 41 *FS*=0.0	-Two different rubber mat A: *RH*: 12 B: *RH*: 39	1.5-6.5 1.7-4.6	2.3×10^4-2.1×10^5 6.3×10^4-2.1×10^5	0.012-0.103 0.032-0.106	- Two double-tip conductivity probe systems for measuring air entrainment properties (tip $\varnothing$= 0.0125 and 0.25mm) - Pointer gauge -Digital cameras high speed video capabilities	-Discharge -Upstream depth -Tailwater depth -Jump length -Roller length -Velocity -Air concentrations -Bubbles frequency -interfacial velocity -turbulence intensity

FL: Flume Length, *FW*: Flume Width, *FH*: Flume Height, *FS*: Flume Slope, *RH*: Roughness Height

Table 2.4 Effect of bed roughness on flow properties

Reference	Conjugate depth ratio d_2/d_1	Jump and roller length	Bed shear stress	Rate of energy dissipation (jump efficiency) E_2/E_1	Rate of air entrainment	Void fraction profile	Velocity profile
Hughes and Flack (1984)	Decrease (reduction was significant for $Fr_1>3.5$	Decrease	-	-	-	-	-
Ead and Rajaratnam (2002)	Decrease	Decrease (Jump length decreases to half)	Increase (10 times)	-	-	-	The axial velocity profiles at different sections in the jump were found so be similar. The maximum velocity u at any section in terms of the velocity U of the supercritical stream was well correlated with the longitudinal distance x in terms of L, and relation was the same as that for jumps on smooth beds.
Carollo et el. (2007)	Decrease (with increase in roughness height -or for given roughness height- with increase in $Fr_{1)}$	Decrease (with increase in roughness height)	-	-	-	-	-
Defina et al. (2008)	Stability of the jump on a upward sloping channel was driven by the amount of friction	-	-	-	-	-	-

	rather than wall flow regime						
Pagliara et al. (2008)	Increase with increase in Fr_1	Increase with increase in Fr_1	-	-	-	-	-
Abbaspour et al. (2009)	Decrease	Decrease (Jump length decreases to half)	Increase (10 times)	Increase (also was increased with increase in Fr_1)	-	-	The velocity profile variations were similar to that of a wall jet, so the boundary layer growth and the maximum velocity, u, decreased with increasing longitudinal distance (x) from the beginning of the jump
Elsebaie and Shabayek (2010)	Decrease	Decrease (Jump length decreases to less than half)	Increase (15 times)	-	-	-	-
Pagliara et al (2010)	-	-	-	-	-Coarseness of the bed materials enhances air entrainment.	- Both the element shape and the surface roughness affected these profiles, with a peak in the wake region for the higher slope.	-
Pagliara et al (2011)	-	-	-	-	-The maximum turbulence intensity decreased with the relative submergence, while the bubble frequency distribution was affected by the rough bed elements. -*C* increases with increase in slope	- *F* distribution presented a rising limb, an intermediate region and a recession limb in the direction normal to the flow - F max occurred generally in the range of $0.3<C<0.6$ -More than 70% of the clusters had two bubbles with an	-

						average number of bubbles per cluster Nbc = 2.2 in the bubbly flow region	
Neluwala et al. (2013)	The maximum effect of roughness elements occurred at a roughness density of 0.23. At this stage the sequent depth ratio reduced up to 34%	-	-	-	-	-	-
Carollo et al. (2013)	Decrease	Decrease	-	-	-	-	-
Ahmed et al (2014)	Decrease (15.4 %)	Decrease (21.03 %)	Increase	Increase (50.31 %)	-	-	-
Pagliara and Palermo (2015)	Decrease (The reduction was more prominent when increasing relative roughness and bed slope)	Decrease	-	-	Increase when d_e/d_{84} decrease. Mainly due to both the presence of drag and shear vortices between the stones and an increasing interaction between the free surface and the stones	Air entrainment profiles were significantly influenced by the relative equivalent depth d_e/d_{84} (the ratio between effective depth and a characteristic diameter of base material)	-

Felder and Chanson (2016)	Decrease (Increase with increase in $Fr_{1)}$	Decrease With upwards shift of the jump roller resulting in a reduction of jump length.	Increase and the more violent motion of the free surface led to entrapment of air from above	Increase	Increase in bubble count rate and void fractions in the region close to the jump toe. The air entrainment length in hydraulic jumps over large roughness appeared to be smaller than that in a comparable hydraulic jump on smooth bed.	Overall similar void fraction distributions in particular in the first half of the hydraulic Jump. Similar maximum void fraction distributions within the shear layer region *C* Max. In the second half of the hydraulic jump the rough bed led to elevated levels of void fraction in the recirculation region.	The overall velocity distribution was similar for all bed roughness configurations showing a boundary layer close to the channel bed. In the recirculation region, negative velocities were observed for both rough bed configurations at the start of the jump. At positions further downstream, the velocity profiles differed substantially between the two rough bed configurations.

2.6 Numerical simulation

Despite the relatively large number of experimental investigations of breaking waves, numerical investigations on this subject are limited. Researchers conducted first numerical investigations on hydraulic jump on smooth and rough bed from 1970 (Rouse 1970, Narayanan 1975) and has continued until now (Javan and Eghbalzadeh, 2013, Witt et al. 2015, Bayon et al. 2016). Gharangik & Chaudhry (1991) considered one-dimensional Boussineq's equations to describe the height and velocity change of a hydraulic jump on a slightly sloped bottom wall.

Long et al. (1991b) solved the two-dimensional Reynolds-averaged Navier–Stokes (*RANS*) equations with the k–ε turbulence model to describe the surface profile and mean velocities in hydraulic jumps. They employed 'body fitted coordinates' to describe only the water phase and fit their mesh to the water body.

Chippada et al. (1994) employed a similar methodology, but with a moving body-fitted mesh to track the interface. Zhou and Stansby (1999) extended such calculations to the transverse direction, but solved only two-dimensional shallow water equations.

The *VOF* method was introduced for free-surface modelling (Sarker and Rhodes 2002, Zhao et al. 2004, Farsadizadeh et al. 2009, Ebrahimi et al. 2013, Mortazavi et al. 2014, Xiang et al. 2014). Ma et al. (2001) considered a two-dimensional k–ε model and an additional volume of fluid (*VOF*) equation to track the evolution of the free surface, and thus eliminated the need for use of complex body-fitted mesh algorithms. They used an earlier version of the *VOF* method which did not utilize the recent sharp surface reconstruction algorithms.

Carvalho et al. (2008) performed a similar *RANS* calculation, but with a *VOF* method that utilized geometric surface reconstruction. More recently, Lubin et al. (2009) attempted to use *VOF* to perform *LES* of a two-dimensional (2-D) hydraulic jump without a *RANS* model. However, despite integrating the equations for a long physical time, they were not able to make the jump stable and stationary.

Ma et al. (2011) simulated a 2-D *RANS* and a 3-D detached-eddy simulation (*DES*) hydraulic jump with a two-fluid model. They proposed an air entrainment model which was tuned based on the kinetic energy of the fluid and the mean velocity gradient near the interface. Their model involved multiple parameters that were tuned against experimental results such as the probability density function (*PDF*) of the bubble size distribution. Gonzalez and Bombardelli (2005) applied

the *LES* (large eddy simulation) model. The air-water properties were treated with a local void fraction. Current *DNS* and *LES* approaches are restricted to some turbulence investigations with simple geometries and low Reynolds numbers (~ 10^5 for *DNS*) (Prosperetti and Tryggvason 2009, Chanson 2013).

Mortazavi et al. (2016) for the first time presented a comprehensive quantitative data for a wide range of phenomena in a turbulent breaking wave using *DNS*. They used direct numerical simulation *(DNS*) for a stationary turbulent hydraulic jump with inflow Froude number of 2, Weber number of 1820 and the density ratio of 831. A non-dissipative geometric volume of fluid (*VOF*) method was used to track the detailed interactions between turbulent flow structures and the nonlinear interface dynamics. The result included mean velocity fields, Reynolds stresses, turbulence production and dissipation, velocity spectra and air entrainment data. They showed that the bubble formation had a periodic nature. Meaning that the bubbles were generated in patches with a specific frequency associated with the roll-up frequency of the roller at the toe of the jump, with its footprint apparent in the velocity energy spectrum.

Table 2.5 describes the summary of some important researches on the numerical simulation of hydraulic jump.

Table 2.5 Summary of literature review on numerical study of hydraulic jump

Reference	Developed numerical method	Software	Range of Froude/ Reynolds numbers	Investigated parameters	Comment
Long et al. 1991	-A standard two-dimensional *k-ε* turbulence model -An offset control volume method	-	Fr_1:3.2-8.2	-Mean flow -Surface profile -Turbulence characteristics of submerged hydraulic jumps	-The *k-ε* turbulence model has limitations when it is applied to strongly recirculating flows.
Ma et al. 2011	-*RANS* (Reynolds-averaged Navier–Stokes) -*DES* (Detached Eddy Simulation)	-	Fr_1=1.8 *Re*=88500	-Surface profile -Void fraction	- The void fraction profiles predicted by both methods are in agreement with the experimental data in the lower shear layer region - In the upper roller region behind the toe, the averaged results of the *DES* turbulence model gives accurate predictions while a *RANS* turbulence model does not.
Bayon et al. 2016	-	-OpenFOAM -FLOW-3D	Fr_1:4.5-13	-Sequent depth ratio, -Roller length -Mean velocity profiles -Velocity decay or free surface profile	- *CFD* model parameters can exert significant effects on flow aeration. In this case, air entrapment and bubble size is obviously conditioned by mesh element size.
Mortazavi et el. 2016	-direct numerical simulation (*DNS*) -A non-dissipative geometric volume of fluid (*VOF*) method	-	Fr_1=2 Web Number=1820 *Re*=88000	-Mean velocity fields -Reynolds stresses -Turbulence production -Dissipation -Velocity spectra -Air entrainment	-The bubble formation is found to have a periodic nature. -The bubbles are generated in patches with a specific frequency associated with the roll-up frequency of the roller at the toe of the jump, with its footprint apparent in the velocity energy spectrum.

3 PHYSICAL MODELLING AND EXPERIMENTAL PROCESSING

3.1 Dimensional analysis

In order to theoretically and numerically analyze the hydraulic jumps at small scales, a large number of relevant equations to describe the turbulent flow structures between gas and liquid i.e. two-phase flow should be considered as well as the interactions between entrained bubbles and coherent structures (Chanson 2013). Considering a hydraulic jump, the outputs of analyzed data must be verified in terms of a broad range of two-phase flow parameters: "no experimental data means no validation" (Roache 2009). To identify the parameters of preferential relevance through dimensional analysis, several simplifications may be considered. In open channel flows the compressibility of the two-phase flow is not taken into account since has little effect on air bubble diffusion process as well as mixing layer characteristics (Chanson 1997b). For a hydraulic jump in a horizontal rectangular channel, dimensional considerations result in a series of dimensionless relationships in terms of the turbulent air-water flow properties at a position (x,y,z) within the hydraulic jump as functions of the fluid properties and boundary conditions. Assuming the upstream flow depth d_1 as the characteristic length scale, a simplified dimensional analysis yields:

$$\frac{\eta}{d_1}, \frac{\eta'}{d_1}, \frac{\eta_{toe}'}{d_1}, \frac{F_{fs} \times d_1}{V_1}, \frac{F_{toe} \times d_1}{V_1}, \frac{F_{ej} \times d_1}{V_1}, C, \frac{F \times d_1}{V_1}, \frac{V}{V_1}, \frac{v'}{V_1}, \frac{l_{ch}}{V_1}, N_{clu}, \frac{F_{clu} \times d_1}{V_1}, \frac{L_x}{d_1}, ...$$
$$= \mathrm{F}_1\left(\frac{x - x_1}{d_1}, \frac{y}{d_1}, \frac{z}{d_1}, \frac{x_1}{d_1}, \frac{W}{d_1}, \frac{\delta}{d_1}, \frac{V_1}{\sqrt{g \times d_1}}, \frac{\rho_w \times V_1 \times d_1}{\mu_w}, \frac{\rho_w \times V_1^2 \times d_1}{\sigma}, ... \right) \quad (3.1)$$

where:

η water elevation above the channel bed (m);
η' standard deviation of the instantaneous water elevation (m) above the channel bed;
η_{toe}' standard deviation of the instantaneous jump front position (m);
F_{fs} characteristic frequency (H_z) of free surface fluctuations;
F_{ej} characteristic frequency of formation and downstream ejection of the large vortices in the shear layer (Hz);
F_{toe} characteristic frequency (H_z) of longitudinal oscillations of jump toe position;
d_1 inflow water depth (m) immediately upstream of the jump toe;
C time-averaged void fraction defined as volume of air per unit volume of air and water;
F bubble count rate defined as the number of bubbles or water droplets per second (Hz);
V air-water interfacial velocity (m/s);
V_1 average inflow velocity (m/s): $V_1 = Q/(W \times d_1)$;
v' standard deviation of instantaneous velocity (m/s);
l_{ch} air bubble/water droplet chord length (m);

N_{clu} average cluster size defined as the average number of particles per cluster;
F_{clu} cluster count rate (Hz) defined as the number of clusters per second;
L_x longitudinal integral turbulent length scale (m);
x longitudinal distance (m) from the upstream sluice gate;
y vertical distance (m) above the channel bed;
z transversal distance (m) from the channel centreline;
x_1 longitudinal position (m) of jump toe;
W channel width (m);
δ boundary layer thickness (m);
g is the gravity acceleration
ρ_w water density (kg/m^3);
μ dynamic viscosity (Pa·s);
σ surface tension (kg·m/s^2);

The seventh, eighth and ninth terms on the right hand side of Equation (3.1) are respectively the Froude number Fr_1, Reynolds number Re_1 and Weber number We. In a hydraulic jump, the momentum considerations indicate the significance of the inflow Froude number so that Froude similitude is commonly applied (Bélanger 1841, Henderson 1966, Liggett 1994, Chanson 2004a). Since the hydraulic jump is a turbulent shear flow, the Reynolds number is also considered as a relevant parameter (Rouse et al. 1959, Chanson and Chachereau 2013). By introducing the Morton number Mo which can be written as a combination of the Froude, Reynolds and Weber number:

$$Mo = \frac{g \times \mu_w^4}{\rho_w \times \sigma^3} = \frac{We^3}{Fr_1^2 \, \mathrm{Re}^4} \tag{3.2}$$

Now, Equation (3.1) may be rewritten as:

$$\frac{\eta}{d_1}, \frac{\eta'}{d_1}, \frac{\eta_{toe}{}'}{d_1}, \frac{F_{fs} \times d_1}{V_1}, \frac{F_{toe} \times d_1}{V_1}, \frac{F_{ej} \times d_1}{V_1}, C, \frac{F \times d_1}{V_1}, \frac{V}{V_1}, \frac{v'}{V_1}, \frac{l_{ch}}{V_1}, N_{clu}, \frac{F_{clu} \times d_1}{V_1}, \frac{L_x}{d_1}, \ldots = \mathrm{F}_2\left(\frac{x - x_1}{d_1}, \frac{y}{d_1}, \frac{z}{d_1}, \frac{x_1}{d_1}, \frac{W}{d_1}, \frac{\delta}{d_1}, Fr_1, Re, Mo, \ldots\right) \tag{3.3}$$

Based on the Morton number definition in case of using the same fluids (e.g. air and water) in model and prototype, the Morton number is an invariant which can be omitted from Equation (3.3). When both air and water are used in laboratory and at full scale, it yields:

$$\frac{\eta}{d_1}, \frac{\eta'}{d_1}, \frac{\eta_{toe}{}'}{d_1}, \frac{F_{fs} \times d_1}{V_1}, \frac{F_{toe} \times d_1}{V_1}, \frac{F_{ej} \times d_1}{V_1}, \mathrm{C}, \frac{F \times d_1}{V_1}, \frac{V}{V_1}, \frac{v'}{V_1}, \frac{l_{ch}}{V_1}, N_{clu}, \frac{F_{clu} \times d_1}{V_1}, \frac{L_x}{d_1}, \ldots = \mathrm{F}_3\left(\frac{x - x_1}{d_1}, \frac{y}{d_1}, \frac{z}{d_1}, \frac{x_1}{d_1}, \frac{W}{d_1}, \frac{\delta}{d_1}, Fr_1, \mathrm{Re}, \ldots\right) \tag{3.4}$$

Equation (3-4) highlights the most essential variables for the physical modelling of a classic hydraulic jump based on the upstream flow depth d_1 as a characteristic length scale. Since the surface tension was considered of lesser significance compared to the viscous effects in the turbulent shear region of a hydraulic jump, the Reynolds number was chosen instead of the Weber number for the present analysis (Chanson 1997a).

For experimental works, as in present study, it is impossible to satisfy simultaneously both Froude and Reynolds similarities in case of applying the same fluids in model and prototype (Equation 3.4). Laboratory modelling is typically conducted based upon a Froude similitude, and the present study is no exception. It should be considered that the air bubble entrainment might be adversely affected by adverse scale effects in small size models (Rao and Kobus 1971; Chanson 1997a; Murzyn and Chanson 2008, Chanson and Gualtieri, 2008; Felder and Chanson 2016). Herein the experiments at relatively large Reynolds numbers was performed to minimize potential scale effects, although these might not be avoidable (Chanson and Chachereau 2013, Felder and Chanson 2016, 2018).

3.2 Experimental facilities

The experiments were conducted in the hydraulic laboratory at the University of Queensland, in a flume used previously in several experimental works (Wang 2014; Wang et al. 2014b; 2015, Felder and Chanson 2016, 2018). The rectangular test section was 3.2 m long, 0.5 m wide and 0.41 m high and consisted of a horizontal high-density polyethylene (*HDPE*) bed and glass sidewalls. A constant flow rate was supplied from an upstream head tank through a vertical sluice gate equipped with a semi-circular edge ($Ø$ = 0.3 m) to prevent flow contraction under upstream gate (Figure 3.1). To control the location of the hydraulic jump within the experimental test section, an adjustable vertical overshoot slice gate was set at the downstream end of the flume. In the present experiments, the jump toe position was located at x_1 = 1 m downstream of the sluice gate for all flow conditions. Water was fed into the head tank from a constant head reservoir. The flow rate was measured with a Venturi meter mounted in the supply pipe with an accuracy of ±2%. *LED* light projector and gray wall were used for recording videos with high speed cameras on smooth bed (Figure 3.2). Table 3.1 summarizes the experiments conditions of the present study and Felder and Chanson (2016, 2018).

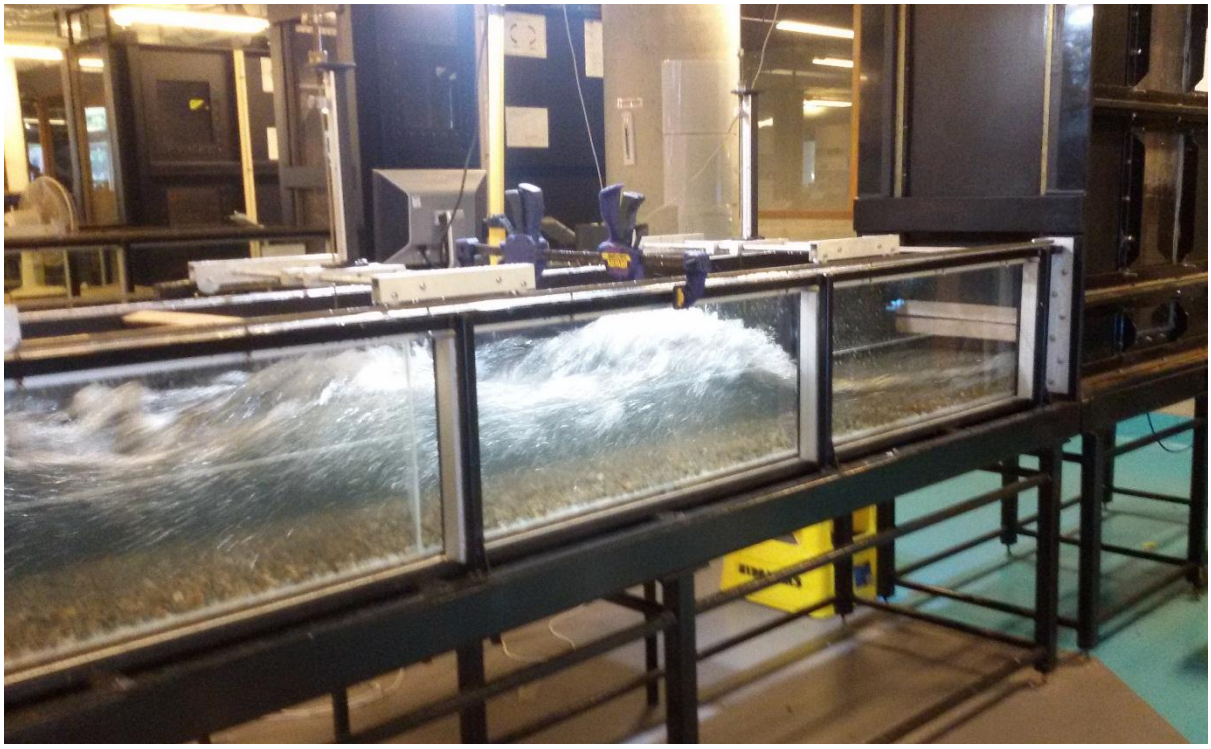

Figure 3.1 Side view of channel. Upstream head tank on the right. Flow from right to left – Flow conditions: Q = 0.07 m^3/s, Fr_1 = 1.93, d_1 = 0.084 m, x_1 = 1.0 m

Table 3-1 Experimental flow conditions (x = x_1 = 1 m)

Experiment	Bed type	h_1 (m)	Q (m^3/s)	d_1(m)	Fr_1	Re_1	Comment
Present study	smooth	0.03	0.02-0.044	0.031-0.0325	2.17-4.94	4.2E+4-9.5E+4	High video speed camera, 240fps Point gauge
		0.06	0.036-0.095	0.06-0.063	1.54-3.93	7.8E+4-2.0E+5	
	rough	0.06	0.042-0.1	0.078-0.085	1.31-2.87	9.6E+4-2.3E+5	
	smooth	0.06	0.078	0.0675	2.84	1.7E+5	Conductivity probe
	rough	0.06	0.06-0.1	0.0825-0.0835	1.7-2.84	1.4E+5-2.2E+5	
Felder and Chanson (2016, 2018)	smooth	0.036	0.054	0.036	5.1	1.1E+5	Air-water flow measurements. Testing of sensors
	rough 1	0.02-0.052	0.012-0.103	0.034-0.066	1.6-6.5	3.3E+4-2.1E+5	Flow observations. Air-water flow measurements
	rough 2	0.02-0.052	0.032-0.106	0.036-0.073	1.7-4.6	6.3E+5-2.1E+5	

Where: h_1 is the upstream gate opening and x is the position of cross section where air bubbles were measured

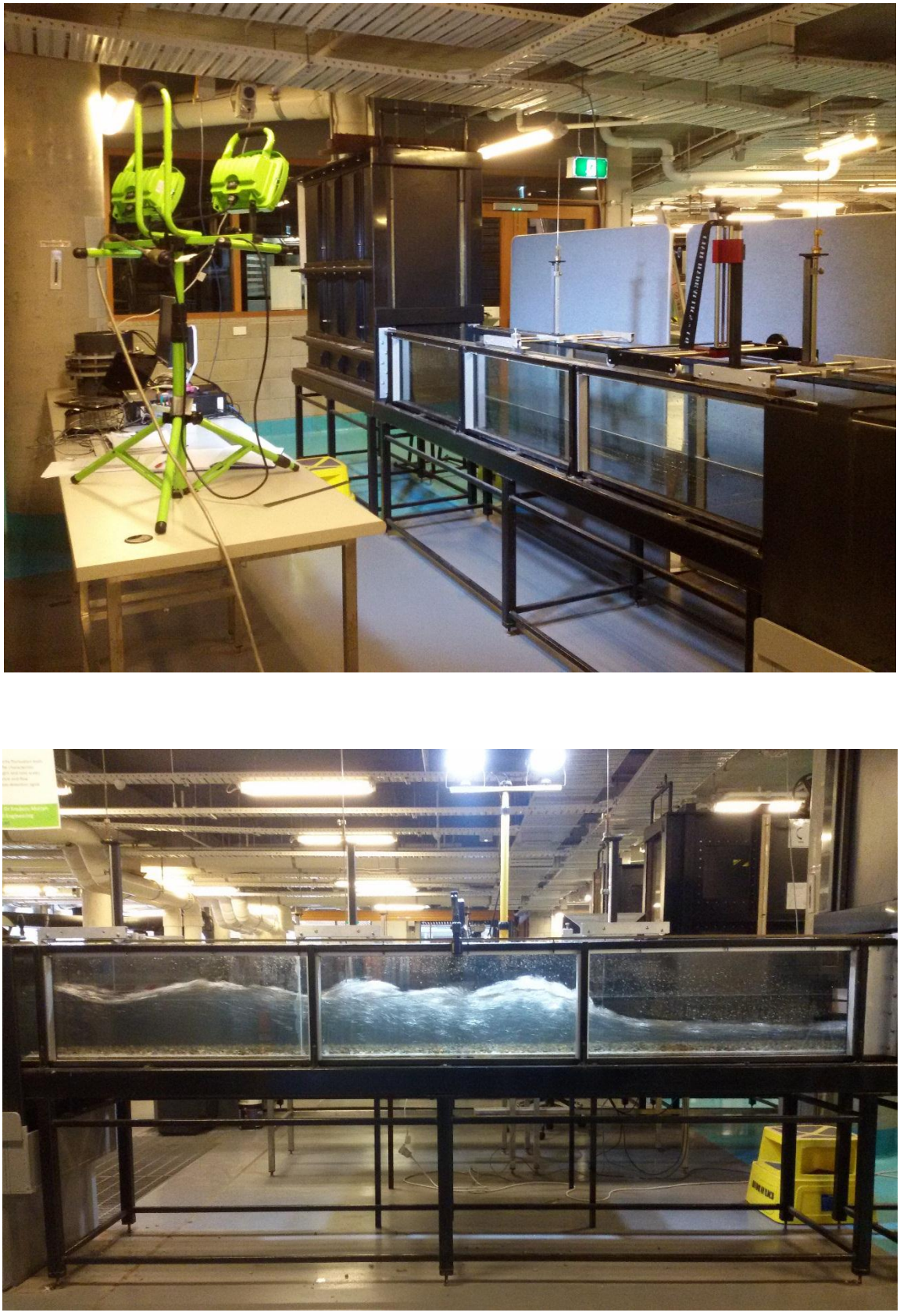

Figure 3.2 Initial setup of flume for recording videos with high speed cameras; up: *LED* light and wall for smooth bed condition and down: *LED* for rough bed, flow condition: Q = 62.18 L/s, d_1 = 0.082m Fr_1 = 1.78, x_1 = 1 m with flow from right to left

Experiments were conducted for different Froude numbers on both smooth and rough bed. Air flow properties were measured at 8 cross sections, 7 downstream of and one upstream of jump toe position, for both smooth and rough bed. For each cross section, data were collected for 30 to 50 points per vertical profile depending on flow depth. The effect of bed roughness on hydraulic jump were studied using a pebbled bed. Experiments also were conducted on smooth bed as the reference. To achieve an uniform channel bed roughness, gravels were installed on the whole length of the channel including upstream of and underneath the upstream sluice gate. The same gravel bed was previously used by Li and Chanson (2018).

The gravels were fixed on the wooden boards using tile adhesive, (DUNLOP, trade resaflex) (Figure 3.3a). Then these two plates were attached and stuck together using nuts and bolts and Silicone adhesive, respectively (Figure 3.3b). Then the boards were installed on the channel HDPE bed from upstream to downstream covering whole length of the channel, including beneath the upstream sluice gate and in the upstream reservoir (Figure 3.3c). To prevent the uplifting of the boards, two plexi-glass walls were fixed to the boards on both sides of flume (Figure 3.3d). This setup decreased the channel width to 0.475 m. Side walls were included into a woody black wall to have proper background for video recording and one white Plexiglas wall to record video and take photo from the hydraulic jump process.

Table 3.2 presents the properties of gravels. The gravel materials were mixed natural river pebbles sieved between 9.5 mm and 13.2 mm with d_{50} = 0.011 m and ρ_s = 2530 kg/m^3.

Table 3.2 Properties of gravels

Particle Size (mm)	Weight (g)	Volume (ml)	Density (g/cm^3)	Average density (g/cm^3)
(9.5, 13.2)	2031.4	800	2.54	2.53
	1920.4	760	2.53	
	1738.4	690	2.52	

3.3 Instrumentation and signal processing

Experiments were carried out in two series (Table 3.1). For the first group, observations were conducted using high speed video recording camera, Casio Ex-10 Exilim camera (240 frame per second). The clear-water flow depths, including the supercritical inflow depth at upstream and the subcritical tailwater depth at downstream, were measured using a rail mounted point gauges with an accuracy of 0.2 mm.

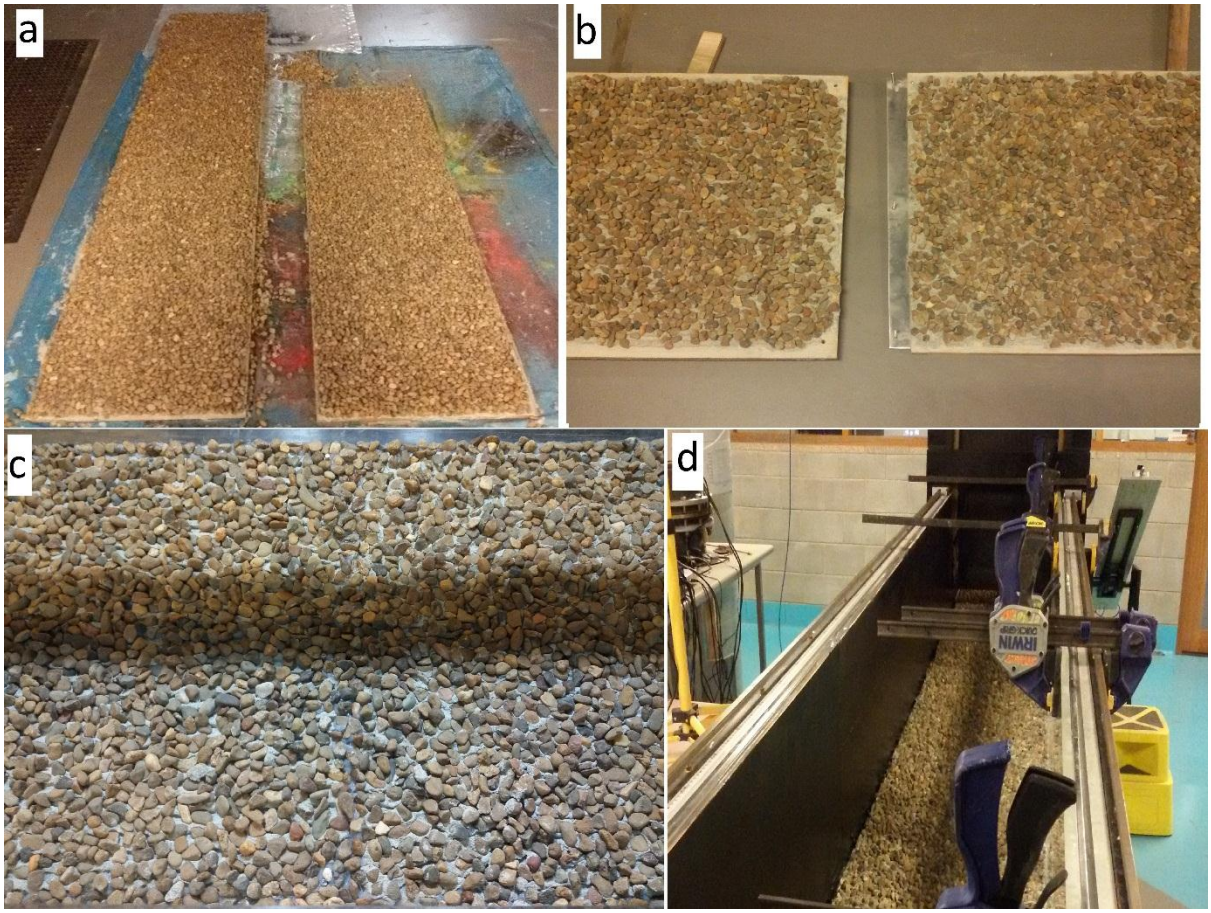

Figure 3.3 Preparing bed roughness, a: installing gravels, b: attaching plates, c: sticking plates and putting on channel d: black and white walls on two sides

Gate opening was adjusted using a ruler on top of the gravels to achieve the average height. Figure 3.4 shows gate opening setup. Water depth measurements using point gauge were based on the average height of gravels as done for the gate opening.

Figure 3.4 Measuring gate opening using ruler

For the second series of experiments, the air-water flow properties were measured on the center line of the channel with a dual-tip phase-detection conductivity probe. The conductivity probe, also known as the resistivity probe, is an intrusive phase-detection probe

used to discriminate between air and water phases (Crowe et al. 1998, Chanson 2002). The conductivity probe was previously used in several studies of hydraulic jumps at the University of Queensland (Gualtieri and Chanson, 2007; Murzyn and Chanson 2008; Chachereau and Chanson 2011; Wang 2014; Felder and Chanson 2016). The phase-detection conductivity probes were excited by an electronic system (Ref. UQ82.518) designed with a response time less than 10 µs. A LabVIEW^{TM} data acquisition software designed by Prof. Stefan Felder (University of Queensland, Australia) enabled a simultaneous recording of up to eight conductivity sensors (Felder 2013). Application of similar phase-detection probes was documented by Chanson (2007a, 2010), Kucukali and Chanson (2008), Murzyn and Chanson (2009), Chachereau and Chanson (2011a) and Zhang et al. (2013). The outputs of these probe sensors were acquired with a high-speed data acquisition system (NI USB-6251 BNC) connected to a desktop computer. A rail-mounted trolley provided support to all intrusive probes. The probe elevations in the vertical direction were supervised by a MitutoyoTM digimatic scale unit with an accuracy of 0.01 mm. Figure 3.5 shows in detail the dimension and position of conductivity probe.

Figure 3.5 Conductivity probe a: dimension (Δx = 6.5 mm, Δz = 2.1 mm), b: zero level for rough bed and c: with supporter against flow direction during measurement

As previously used by Toombes (2002), Chanson (2007b) and Felder and Chanson (2013, 2105, 2016) and Wang (2014) the double-tip phase-detection probe was scanned at 20 kHz frequency for 90 and 180 s at each measurement position. Note that previous experiments demonstrated that the sampling frequency higher than 20 kHz and sampling duration more than 30-40 s have no effect on void fraction and bubble count rate as well as air-flow properties (Chanson 2007b, Felder and Chanson 2015). The output voltage signals ranged from -1 to 4.5 V. Each voltage drop corresponded to a detection of air bubble. However, the

switch between the two voltage limits was not instantaneous because of the wetting and drying of the sensor tips. The single threshold technique was applied to the air-water voltage signal with a bimodal probability distribution (Cartellier and Achard 1991). Based on threshold value the voltage signal below the air- water threshold was identified as air and otherwise as water. Toombes (2002) demonstrated that the deviation of air concentration was less than 1% with a threshold between 40 to 60% of the voltage range. In the present study, the threshold value was set to 50% of the voltage difference, between the two distinctive peaks in voltage probability distribution of the signal. Based upon this single threshold technique, the raw signal was converted into a binary file in which 0 stood for water and 1 stood for air.

Instantaneous void fraction c, i.e., $c = 0$ for water and $c = 1$ for air was extracted from binary file. The time-averaged void fraction C was calculated as the signal sampling rate and sampling duration based on the time-averaged void fraction C:

$$C = \frac{1}{N} \times \sum_{1}^{N} c \tag{3.5}$$

where N is the number of samples given by the product of the sampling rate and sampling duration. The time-averaged void fraction was simply the volume of air per unit volume of air and water. The bubble count rate or bubble frequency F, defined as the number of air bubbles or water droplets per second, was calculated as half of the total number of air-water interfaces divided by the sampling duration. The bubble chord time $(t_{ch})_a$ was defined as the time between the detections of a water-to-air interface and the next air-to-water interface. The water chord time $(t_{ch})_w$ was defined as the time between the detections of an air-to-water interface and the following water-to-air interface. The chord times were counted in the signal between two instantaneous void fraction changes. The air chord length $(l_{ch})_a$ and water chord length $(l_{ch})_w$ derived from multiplication of chord times by the time-averaged interfacial velocity V.

3.4 Statistical analysis of raw signals and turbulent air-water flow properties

The two sensors of the double-tip phase-detection probe were scanned simultaneously, the corresponding signals being denoted x and x', respectively. To find out the relevance between the signals as a function of the time lag a cross-correlation analysis was applied. The cross-correlation coefficient was calculated as:

$$R_{xx'} = \frac{\sum (x - \bar{x}) \times (x' - \bar{x}')}{\sqrt{\sum (x - \bar{x})^2 \times (x' - \bar{x}')^2}} \quad (3.6)$$

where $\bar{x}$ and $\bar{x}'$ are the mean values of data array [x] and [x'], respectively. When $x' = x$, Equation (3.6) gives the auto-correlation coefficient R_{xx} for the data array [x]. Typical auto- and cross-correlation functions together with some key values are sketched in Figure 3.6. In the present study, the correlation functions were the average of ten and twenty correlation functions, for 90 s and 180 s sampling duration, respectively, deduced from non-overlapping raw signal segments of 9 s each to minimize any bias. Note that sampling frequency higher than 20 kHz and sampling duration more than 30-40 s have no effect on void fraction and bubble count rate as well as air-flow properties (Chanson 2007a, Felder and Chanson 2015).

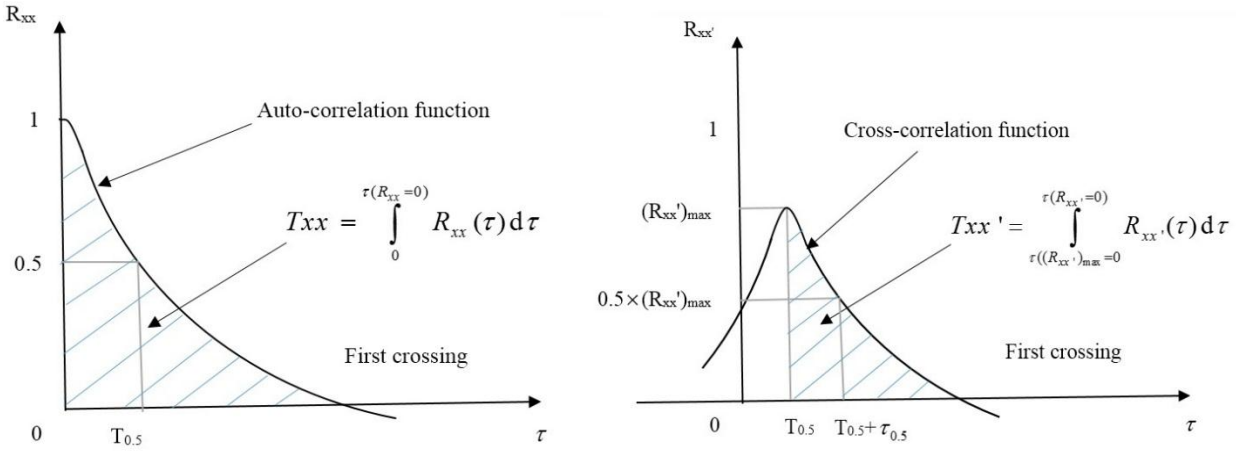

(A) Auto correlation function (B) Cross correlation function

Figure 3.6 Definition sketch of correlation functions of the phase-detection probe signals

Based upon the correlation analysis results, the time-averaged air-water interfacial velocity was calculated as:

$$V = \frac{\Delta x}{T} \quad (3.7)$$

where Δx is the longitudinal distance between the two phase-detection probe tips (present study Δx = 0.0065m) and T is time lag corresponding to the maximum cross-correlation coefficient: $R_{xx'}(T) = (R_{xx'})_{max}$ (Figure 3.6 B). The accuracy of measurements depended on both the air concentration and flow situations. For an ideal case, the measurement was valid in a high-speed flow with $0.05 < C < 0.95$ and constant flow direction against the phase-detection probe orientation. The velocity V was defined as the longitudinal component of the air-water interfacial velocity. The time-averaged travel time of interfaces between the two

sensor tips and the interfacial time-averaged velocity were derived from cross-correlation analyses between the two simultaneously sampled signals of the conductivity probe. As demonstrated by Rao and Kobus (1971), Cain and Wood (1981) and Chanson (1997a), the air-water interfacial velocity was considered equal to the fluid velocity (i.e. no slip) in the streamwise direction of high-speed bubbly flows. Note that interfacial velocity in a Hydraulic jump is often compared to the wall jet (Rajaratnam 1965, Chanson and Brattberg 2000).

In Figure 3.6 B, the time lag $T > 0$ demonstrates a positive velocity while the negative velocity in the recirculation region yielded $T < 0$.

The turbulence intensity $Tu = v'/V$ was estimated considering some key assumptions (Chanson and Toombes 2002a, Felder and Chanson 2013). The final Equation of Tu was extracted based upon Chanson and Toombes (2002a) as it follows:

$$Tu = 0.851 \times \frac{\sqrt{\tau_{0.5}^2 - T_{0.5}^2}}{T} \tag{3.8}$$

The auto-correlation time scale T_{xx} and cross-correlation time scale $T_{xx'}$ derived based on the integral of the correlation functions from the maximum to the first zero-crossing:

$$Txx = \int_0^{\tau(R_{xx}=0)} R_{xx}(\tau) d\tau \tag{3.9}$$

$$Txx' = \int_T^{\tau(R_{xx'}=0)} R_{xx'}(\tau) d\tau \tag{3.10}$$

The auto-correlation time scale T_{xx} defined as a measure of the characteristic advective time of bubbly flow structures (e.g. eddies advecting the air-water interfaces) in the streamwise direction (Chanson and Carosi 2007a). It further yielded the advective length scale L_{xx}:

$$L_{xx} = V \times T_{xx} \tag{3.11}$$

The advective length scale L_{xx} was introduced as a characteristic longitudinal size of advecting eddies (Chanson and Carosi 2007b). Note that the cross-correlation time scale T_{xx} is a function of the longitudinal distance between probe tips Δx.

3.5 Experimental flow conditions

Experiments were carried out in two steps for both smooth and rough bed. They were both aimed at two groups, Group A: basic observations and free-surface measurements, and Group B: two-phase flow measurements. Basic parameters were measured using point gauge and meter. They included the conjugate depths d_1 and d_2 the jump roller length L_r and the air flow

(bubby flow) length L_{air}. Overhead-view videos recorded the longitudinal oscillations of the impingement edge as well as the fluctuations in its transverse perimeter profile, F_{toe}. The formation and advection of large vortices in jump roller, F_{eddy} and U_{eddy}, were measured by means of side-view video records. The air-water properties were extracted using conductivity probe. Quantification of the transverse impingement perimeter and water surface were done using high speed video recording from upside and side view, respectively.

Tables 3.3 and 3.4 present the experiments for Group A and B, respectively, listing the main flow parameters of each experiment. Before beginning the main test in each step, trial runs were conducted to check the process and quality of data. Repeating experiments could increase the accuracy of instrumentation and measurement process and reduce the uncertainties in experiments. Since the flow properties varied rapidly in the jump roller length as well as with flow conditions, the accuracy of the experiment relied strongly upon the determination of Froude and Reynolds numbers and the relative measurement location in the roller. The first ones were linked to the flow rate and inflow depth measurements, and the second was linked to the mean jump toe position. Table 3.5 lists the date of each experiment.

Table 3.3 Experiments for the basic parameters and free surface measurements (Group A)

Experiment	Bed type	h_1 (m)	Run	d_1 (m)	W/d_1	Q (m^3/s)	Fr_1	Re_1
Basic parameters And free surface measurements	Smooth	0.03	AS1	0.0322	15.53	0.02	2.17	4.2E+4
			AS2	0.0325	15.38	0.026	2.9	5.7E+4
			AS3	0.031	16.13	0.031	3.62	6.6E+4
			AS4	0.0315	15.87	0.033	3.79	7.1E+4
			AS5	0.032	15.62	0.035	4.0	7.7E+4
			AS6	0.032	15.62	0.04	4.48	8.6E+4
			AS7	0.032	15.62	0.044	4.94	9.5E+4
		0.06	AS8	0.061	8.2	0.036	1.54	7.8E+4
			AS9	0.06	8.33	0.044	1.92	9.5E+4
			AS10	0.06	8.55	0.048	2.18	1.0E+5
			AS11	0.06	8.55	0.054	2.47	1.2E+5
			AS12	0.061	8.2	0.073	3.12	1.6E+5
			AS13	0.062	8.06	0.078	3.25	1.7E+5
			AS14	0.063	7.94	0.089	3.62	1.9E+5
			AS15	0.062	8.06	0.095	3.93	2.0E+5
	Rough	0.06	AR1	0.078	6.09	0.043	1.31	9.6E+4
			AR2	0.0785	6.05	0.051	1.57	1.1E+5
			AR3	0.082	5.8	0.062	1.78	1.4E+5
			AR4	0.084	5.65	0.07	1.93	1.6E+5
			AR5	0.085	5.59	0.076	2.07	1.7E+5
			AR6	0.083	5.72	0.085	2.4	1.9E+5
			AR7	0.084	5.65	0.092	2.56	2.1E+5
			AR8	0.082	5.79	0.1	2.87	2.3E+5

3.5.1 Limitations of the study

Experiments on rough bed faced a problem regarding initial flume setup. Twice the bed raised caused by the buoyancy of woody plates and uplift pressure beneath the hydraulic jump roller. The problem was solved by using two boards on both sides of the channel to overcome the buoyancy effect. Only three Reynolds number were implemented on rough bed. Finally, due to the short time of staying at the University of Queensland, two and a half months, the number of experiments was limited in terms of trial and main runs.

Table 3.4 Experiments for the air-flow parameters (Group B)

Experiment	Bed type	Run	h_1 (m)	d_1 (m)	W/d_1	Q (m^3/s)	Fr_1	Re_1	x-x_1	x_1/d_1	$(x$-$x_1)/d_1$
Air-flow parameters	Smooth	BS1	0.06	0.067	7.4	0.0781	2.84	1.7E+5	-0.3	10.37	-4.44
									0.1	12.3	1.48
									0.15	17.04	2.22
									0.3	19.26	4.44
									0.45	21.48	6.67
									0.6	23.7	8.89
									0.8	26.67	11.85
									1.1	31.11	16.3
	Rough	BR1	0.06	0.083	5.69	0.061	1.7	1.4E+5	-0.3	8.38	-3.59
									0.1	13.17	1.2
									0.15	13.77	1.8
									0.3	15.69	15.57
									0.45	17.36	17.36
									0.65	19.76	19.76
									1.0	23.95	11.98
									1.15	25.75	13.77
		BR2		0.083	5.69	0.07	1.96	1.6E+5	-0.3	8.38	-3.59
									0.1	13.17	1.2
									0.15	13.77	1.8
									0.3	15.57	3.6
									0.45	17.36	5.39
									0.6	19.16	7.18
									0.8	21.56	9.58
									1.1	25.15	13.17
		BR3		0.082	5.76	0.1	2.84	2.2E+5	-0.3	8.48	-3.64
									0.1	13.33	1.21
									0.15	13.94	1.82
									0.3	15.76	3.64
									0.45	17.57	5.45
									0.6	19.39	7.27
									0.8	21.82	9.7
									1.1	25.45	13.33

Table 3.5 List of the experiments based on type and date

Date	Bed type	Parameter	Instrumentation	Comment
01.06.2.17-02.06.2.17	Smooth	Basic parameters	Point gauge	Trial tests
05.06.2017-06.06.2017	Smooth	Basic parameters	Point gauge	Main tests
0706..2017-09.06.2017	Smooth	Flow patterns	High-speed camera	Main tests
26.06.2017 and 28.06.2017	Smooth	Air water properties	Conductivity probe	Trial tests
30.06.2017 and 07.07.2017-13.07.2017	Smooth	Air water properties	Conductivity probe	Main tests
21.07.2017	Rough	Basic parameters	Point gauge	Trial
22.07.2017-26.07.2017	Rough	Basic parameters	Point gauge	Main tests
31.07.2017	Rough	Flow patterns	High-speed camera	Main tests
01.08.2017-10.08.2017	Rough	Air flow properties	Conductivity probe	Main tests

4. FLOW PATTERNS AND FREE-SURFACE DYNAMICS

4.1 Presentation

Hydraulic jumps are characterised by the inflow Froude number Fr_1, the inflow Reynolds number Re_1, the inflow length x_1/d_1 and boundary roughness characteristics (Henderson 1966, Chanson 2004a). In this study, these parameters were set using different water discharges Q and upstream gate openings h. The longitudinal jump toe position was controlled by adjusting the height of the downstream overshoot gate. The glass sidewalls of flume enabled the observation of basic flow patterns, although the visualised plane was located in a region affected by sidewall friction.

The effects of bed roughness upon the flow patterns are presented in this Chapter, based upon visual observations. The flow pattern observations were focused on the configurations with the rough bed. First, basic flow patterns are presented using the photographs taken during the experiments. Second, the results in terms of basic parameters including the conjugate depth relationship, the jump roller length, the air-flow length, the boundary friction force and the shear stress, are presented and discussed. Third, the oscillations of jump toe position and vortex advection speed, recorded with a high speed camera, are developed. Finally, the results in terms of impingement perimeter and water surface profile are presented. The Chapter ends with a summary of key findings. Additional photographs for a wide range of discharges are presented in Appendix A to complement this Chapter.

4.2 Basic flow patterns by visual observation

The flow patterns were tested for two different gate openings relative to the defined zero position for smooth bed and one gate opening for rough bed (adjusted using a ruler on top of the gravels for rough bed). The jump toe was positioned at a distance x_1 =1 m downstream of the sluice gate for all tests.

Common characteristics of hydraulic jump on smooth bed have been discussed extensively in the literature (Ehrenberger 1926, Hughes and Flack 1984, Chanson 1995, Pagliara et al. 2008, Chanson 2010, Wang and Chanson 2015). Recently Felder and Chanson (2016, 2018) investigated the basic flow patterns and parameters of hydraulic jump, as well as air-flow properties, on uniformly-distributed bed macro-roughness, in a same experimental flume at

the University of Queensland. This data set was used as reference for comparison with the present study. The focus herein is to present the features of hydraulic jump on a pebbled rough bed. Based on the inflow Froude number, the jumps were classified as undular jumps without air bubbles, undular jumps with small air entrainment, hydraulic jumps with small roller and wavy surface downstream and hydraulic jumps with distinct jump toe roller. For $Fr_1 < 1.5$ undular hydraulic jumps without air bubbles were observed on rough bed (Figure 4.1). The flow patterns highlighted a three dimensional free-surface profile with instable undulations, oscillating in both longitudinal and transverse directions. In addition small free-surface ripples were observed. Both the wavy free-surface and the ripples are visible in Figure 4.1. Within the central section of the undular jump, clearly distinct standing waves were observed with several troughs and peaks. The flow depths of troughs and peaks were recorded when the flow conditions allowed accurate recording. This flow condition was the same as the undular hydraulic jump on uniform bed roughness observed by Felder and Chanson (2016, 2018) for $Fr_1 < 2.2$.

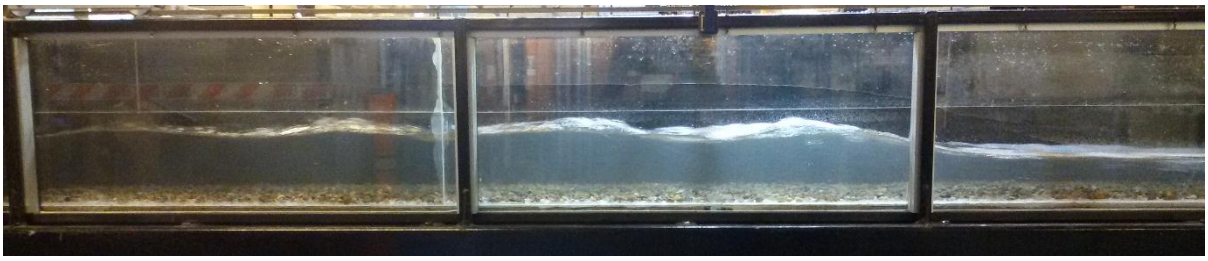

Figure 4.1 Hydraulic jump on rough bed, flow condition: Run AR1, $Q = 0.043$ m^3/s, $Fr_1 = 1.31$, flow from right to left

A: Smooth bed, flow condition: Run AS8, $Q = 0.036$ m^3/s, $Fr_1 = 1.54$, flow from right to left

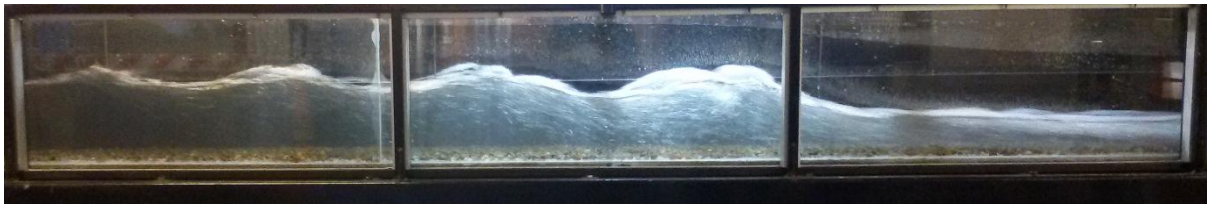

B: Rough bed, flow condition: Run AR2, Q = 0.051 m^3/s, Fr_1 = 1.57, flow from right to left
Figure 4.2 Comparison between hydraulic jump type and free surface pattern between rough and smooth bed (same gate opening h = 0.06 m)

For 1.5 < Fr_1 < 2.1 undular hydraulic jumps with air entrainment were observed for rough bed while, for smooth bed, no undulation was seen and the jump roller appeared (Figures 4.2 and 4.3). These jumps were similar in appearance to the non-aerated undular hydraulic jumps, but with stronger free-surface fluctuations and standing waves. A key feature was the entrainment of air at the first undular wave crest downstream of the jump toe position which gradually vanished in following wave crests. The entrained air consisted of groups of bubbles were released progressively towards the free-surface during the advection. In addition, small white capping was observed at the surface of the first wave crest which decreasing at following wave crests (Figures 4.2B and 4.3B).

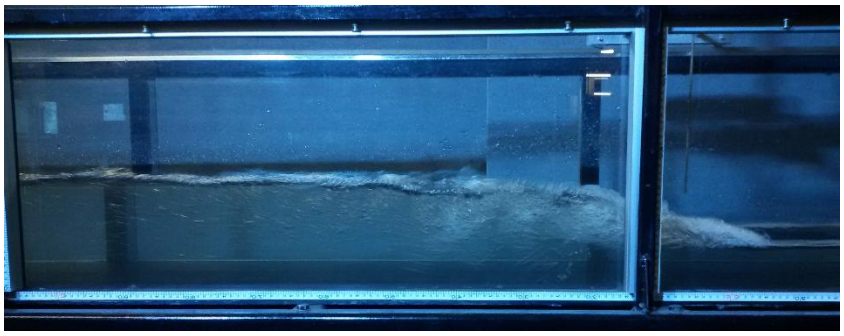

A: Smooth bed, flow condition: Run AS9, Q = 0.044 m^3/s, Fr_1 = 1.92, flow from right to left

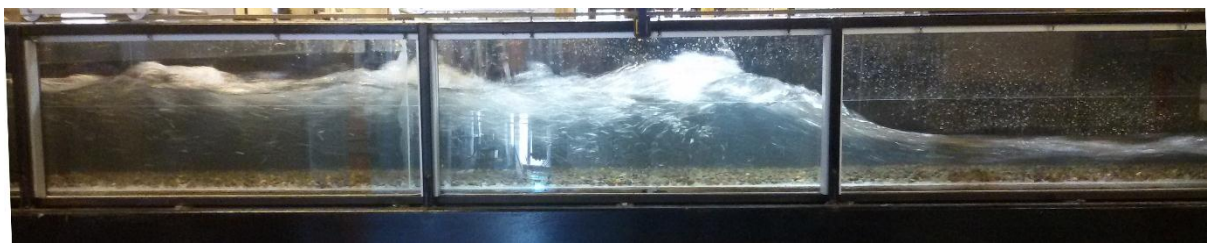

B: Rough bed, flow condition: Run AR4, Q = 0.07 m^3/s, Fr_1 = 1.93, flow from right to left
Figure 4.3 Comparison between hydraulic jump type and free surface pattern between rough and smooth bed (for the same gate opening h = 0.06 m)

The air entrainment process as well as the formation of surface air caps were not stationary and were linked to the fluctuating motion of the undular hydraulic jump and the three dimensional flow features.

With an increasing inflow Froude number, for $2.1 < Fr_1 < 2.5$, the rate of air entrainment increased on rough bed, and large eddies were observed. The jump roller was unstable, resulting in secondary undulations of the free surface further downstream (Figure 4.4). In addition, from the first wave crest, a mass of flow moved backward producing negative velocity in the recirculation region (Figure 4.4B). The presence of a clear water flow region next to the bed resulted in a very distinctive formation of vortex-street downstream of the jump toe, with periodic air bubble vortex shedding into the clear water core region under the jump. The interactions between the clear water boundary layer and the vortex shedding led to the formation of large scale eddies within the flow consisting of tube-like vortical structures that were advected downstream. These structures were visible in the aerated roller region.

A: Flow condition: Run AR5, $Q = 0.076$ m^3/s, $Fr_1 = 2.07$ flow from right to left

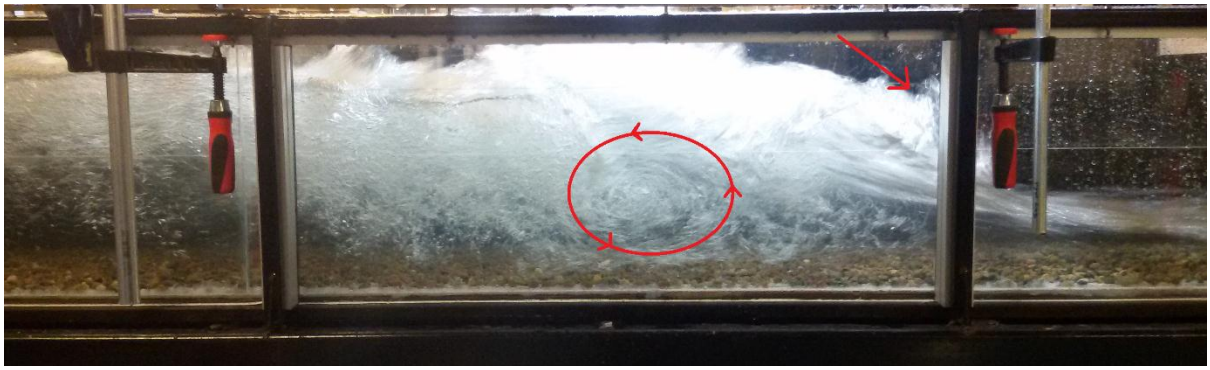

B: Flow condition: Run AR6, $Q = 0.085$ m^3/s, $Fr_1 = 2.4$, flow from right to left

Figure 4.4 Hydraulic jump on rough bed, undular jump with unstable roller ($h = 0.06$ m). Red circles show the formation of vortex, red line show the negative flow

For 2.5 < Fr_1 < 3.1, the hydraulic jump had a marked roller with strong turbulence downstream of the jump toe for both rough and smooth beds (Figure 4.5). For all flow conditions, the jump toe fluctuated in the longitudinal direction, in a manner similar to the known features of hydraulic jumps on smooth bed (e.g. Chachereau and Chanson 2011; Wang et al. 2014). Some irregular surface fluctuation caused by larger vortical structures downstream of the jump toe and stronger backward flow in the recirculation zone, was observed on the rough bed (Figure 4.5B and C). The key differences were the longer aerated flow length, and a severe splashing of the jump toe on rough bed. The shorter aerated flow length on the rough bed, compared to that on the smooth bed, could be associated with the higher rate of energy dissipation and higher flow depth (higher Reynolds number) on rough bed. The bed roughness increased the shear stress and the more violent fluctuation of the free surface resulted in the entrapment of air from above. The jump roller appeared shorter and showed some upward motion as seen on bed type 2 by Felder and Chanson (2016) but for 3 < Fr_1 < 4.3.

4.3 Conjugate depth relationship

For all the flow configurations on both smooth and rough beds, free-surface profile recordings were conducted using pointer gauge measurements. The upstream conjugate depth was measured slightly upstream of the jump toe at x_1 = 0.9 m and the subcritical conjugate depth was measured at the downstream end of jump roller which was variable for each flow condition.

A: Rough bed, flow condition: Run AR7, Q = 0.085 m^3/s, Fr_1 = 2.4, flow from right to left

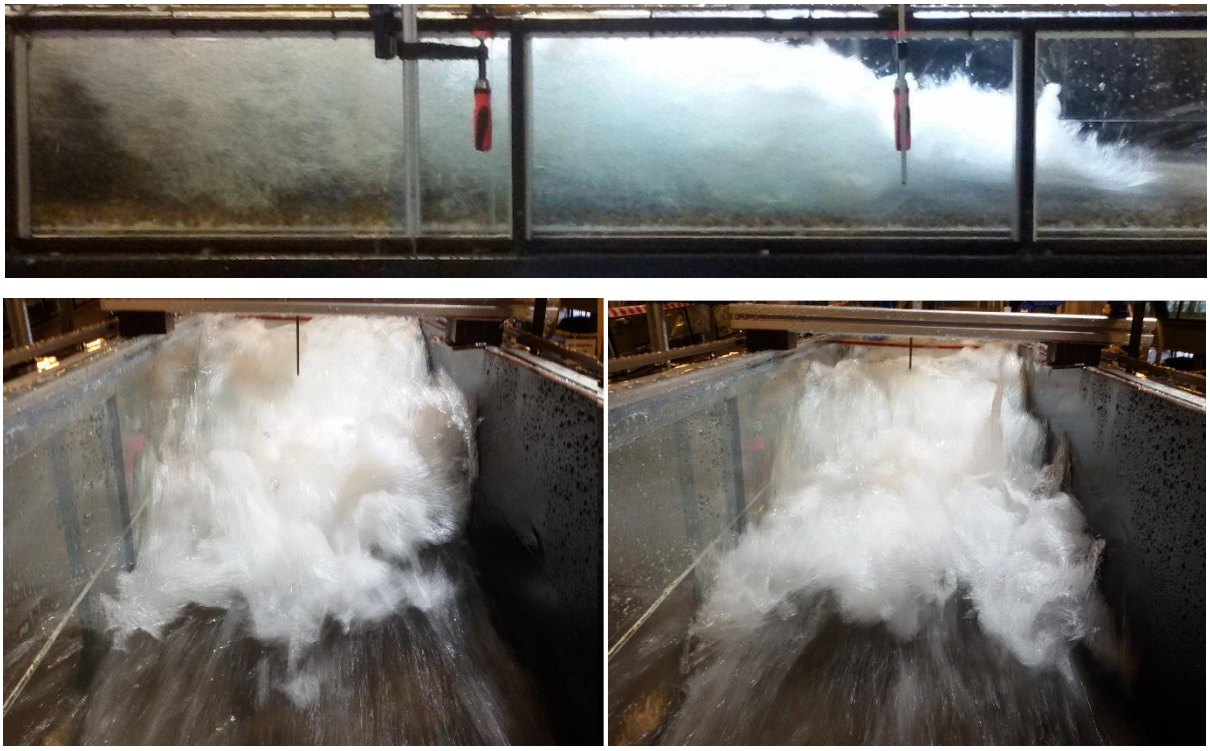

B: Rough bed, flow condition: Run AR8 Q = 0.1 m^3/s, Fr_1 = 2.87, up: from right to left, down: flow from bottom to top

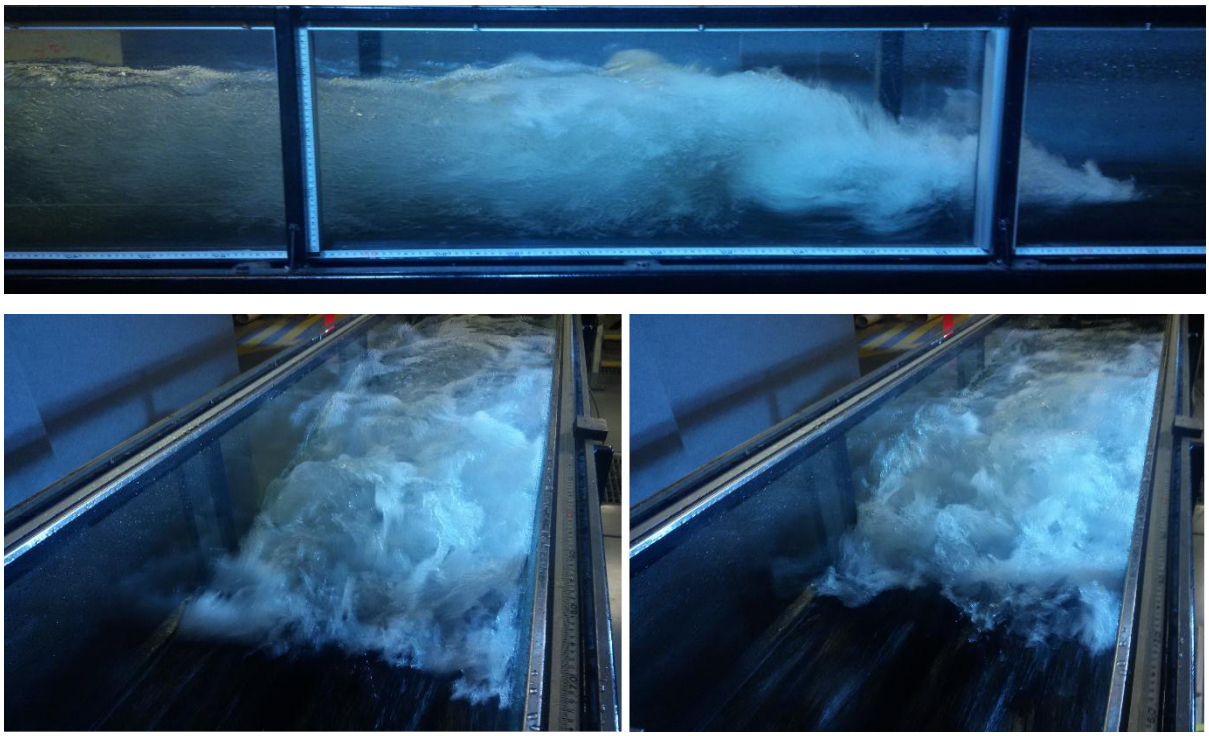

C: Smooth bed, flow condition: Run AS12 Q = 0.073 m^3/s, Fr_1 = 3.1, up: from right to left, down: flow from bottom to top

Figure 4.5 Comparison between hydraulic jump type and free surface pattern between rough and smooth bed (same gate opening h = 0.06 m and 2.5 < Fr_1 < 3.1)

For a rectangular horizontal channel, the solution of the momentum and continuity equations yields (Chanson 2012):

$$Fr_1^2 = \frac{1}{2} \times \frac{d_2}{d_1} \times \left(\left(1 + \frac{d_2}{d_1} \right) + \frac{1}{\frac{d_2}{d_1} - 1} \times \frac{F_{fric}}{\rho \times g \times B \times d_1^2} \right) \quad (4.1)$$

where F_{fric} is the flow resistance force, ρ is the fluid density, g is the gravity acceleration, and B_1 and B_2 are the upstream and downstream free-surface widths, respectively. The upstream Froude number is a function of the ratio of conjugate depths d_2/d_1 and the flow resistance force F_{fric}. For a fixed upstream Froude number, the effects of bed friction yield a smaller ratio of conjugate depths d_2/d_1 with the increasing flow resistance. This finding is consistent with physical data in laboratory flumes (Leutheusser and Schiller 1975; Pagliara et al. 2008, Felder and Chanson 2018). In the case of a smooth horizontal rectangular prismatic channel ($F_{fric} \approx 0$), Equation 4.1 may be simplified into the classical Bélanger equation, as described in Chapter 1, Equation 1.2 (Bélanger 1841).

Carollo et al. (2009) suggested an empirical relationship between conjugate depths:

$$\frac{d_2}{d_1} = 1 + \sqrt{2} \exp\left(\frac{-K_s}{d_c}\right) (Fr_1 - 1)^{0.963} \quad (4.2)$$

where K_s is the roughness height and equal to d_{50} (the median grain size of sediment particles), and d_c is critical depth of water as $d_c = (q^2/g)^{1/3}$.

Considering the present data and those from Felder and Chanson (2016, 2018), an empirical relationship was derived. It relates the conjugate depth ratio with the inflow Froude number Fr_1 and the characteristic roughness (K_s/d_{90}):

$$\frac{d_2}{d_1} = 1 + \sqrt{2} \left(0.7 \exp\left(0.7 \frac{K_s}{d_{90}} \right) (Fr_1 - 1)^{1.05} \right) \qquad 1 < Fr_1 < 4 \quad (4.3)$$

where $K_s = d_{50}$ and d_{90} is the value of grain sizes for which 90% of the material weight is finer. For rough bed data $R = 0.90$ and $SE = 0.35$ while for smooth bed data $R = 0.99$ and $SE = 0.13$. Figure 4.6B presents the results including the Equation 4.3. Although pointer gauge can pinpoint accurately the location of the free-surface in clear water flows, the exact location of the interface between the flowing fluid and the above atmosphere could become undetermined, when air is entrained within the flow. The conjugate depth d_2 and consequently the ratio d_2/d_1 were different from previous studies, slightly higher than those

from Murzyn et al. (2007), and Chachereau and Chanson (2011b). The relationship between conjugate depths ratio and inflow Froude number is presented in Figure 4.6 for both rough and smooth bed configurations. Experimental data of some previous studies on both smooth and rough beds hydraulic jumps were added to Figure 4.6. The comparison highlighted differences between smooth and rough bed configurations. All the present data on both smooth and rough beds were above the dimensionless relationship $d_2/d_1=Fr_1$, suggested by Ead and Rajaratnam (2002) for hydraulic jumps on corrugated channel beds. The observed conjugate depths data were consistent with theoretical predictions based on Equation 4.1 illustrating a loss of momentum through friction effects on the channel bed for a pebbled rough bed. The data were in agreement overall with previous studies on roughness effects (e.g. Hughes and Flack 1984; Carollo et al. 2007; Afzal et al. 2011; Pagliara and Palermo 2015; Felder and Chanson 2018). For $2 < Fr_1 < 2.5$, the conjugate depths ratio for present rough bed as well as roughness type 2 data of Felder and Chanson (2016, 2018) was higher than the empirical relationship for the rough bed (Equation 4.2). This could be due to the undular jump that creates strong oscillations in the water level.

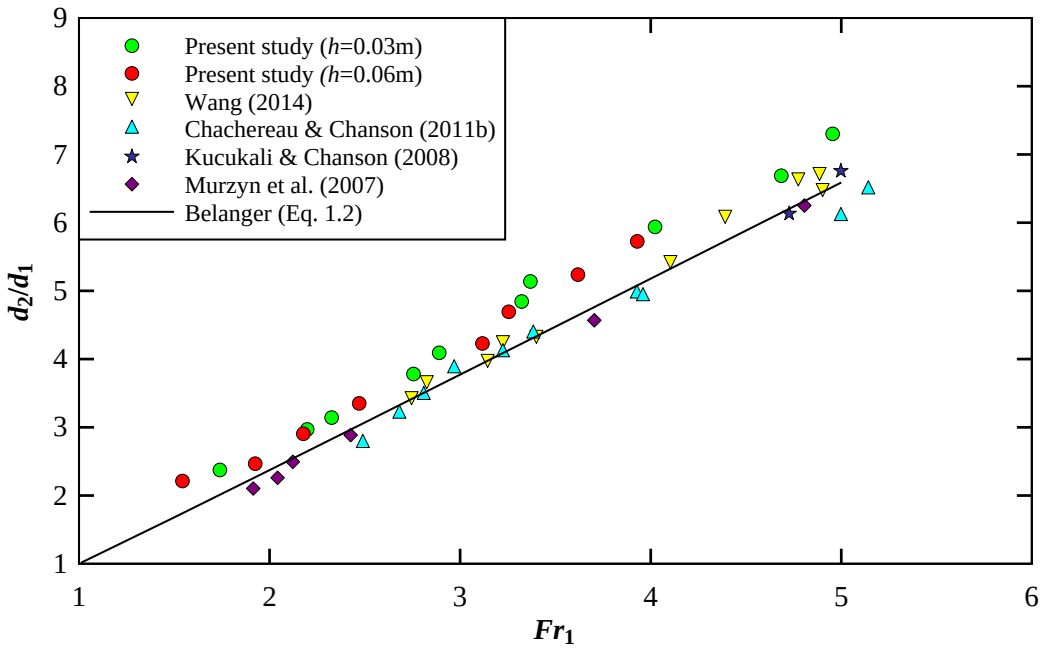

A: Comparison between the present study (smooth bed) and previous studies on smooth bed

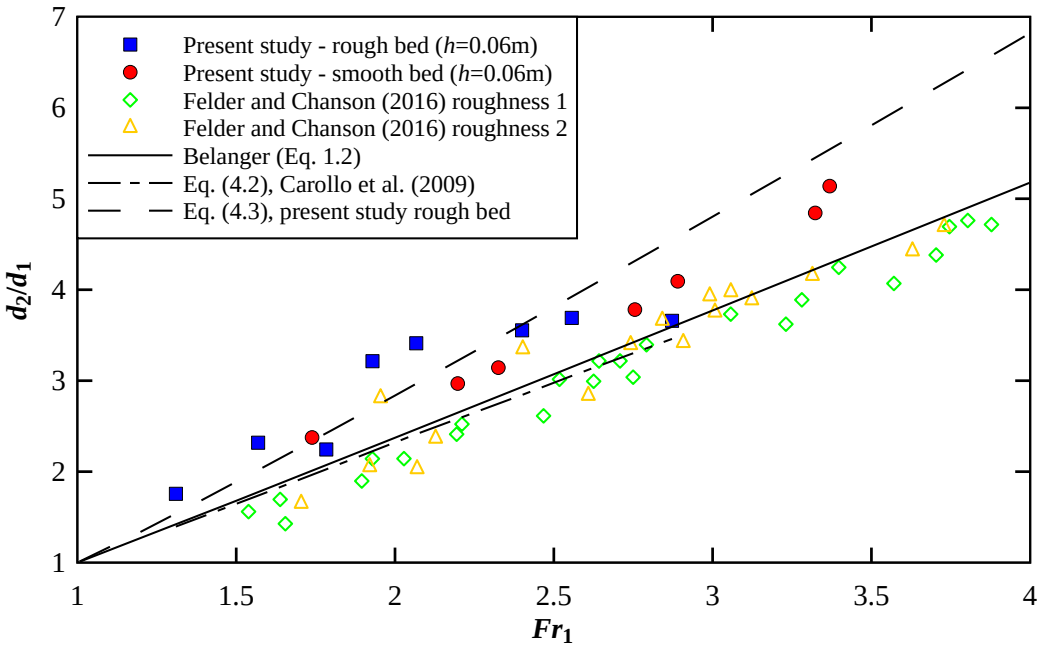

B: Comparison between the present study and previous studies on rough bed
Figure 4.6 Conjugate depth ratio

The pointer gauge measurements were performed for several seconds, and the mean free-surface recording was averaged. For all measured data, the uncertainties of the conjugate depth d_1 recordings were within a 0.2 cm accuracy. Based upon Chanson and Brattberg (2000), Chanson (2007) and Pagliara and Palermo (2015), the use of the equivalent clear water flow depth, i.e. upstream air-water data, should be considered as an accurate prediction of the flow depth. A comparison of the upstream pointer gauge data with available upstream conductivity probe data for both smooth and rough beds confirmed this point (Figure 4.7A).

The characteristic flow depth Y_{90}, i.e. the depth where C = 0.9, highlighted that the recording of the flow depth with a pointer gauge is prone to uncertainties, when the free-surface is uneven, aerated and broken-up (Felder and Chanson 2018).

The equivalent clear-water depth d was proposed as (Wood 1984):

$$d = \int_0^{Y_{90}} (1-C)dy \tag{4.4}$$

The depth to depth comparison of characteristic flow depth Y_{90} vs pointer gauge and equivalent clear water vs pointer gauge (Figure 4.7B) demonstrated the effect of highly bubbly flow on rough bed with higher inflow Froude number. The pointer gauge depth

overestimated the equivalent clear-water depth, yielding an underestimation of the Froude number.

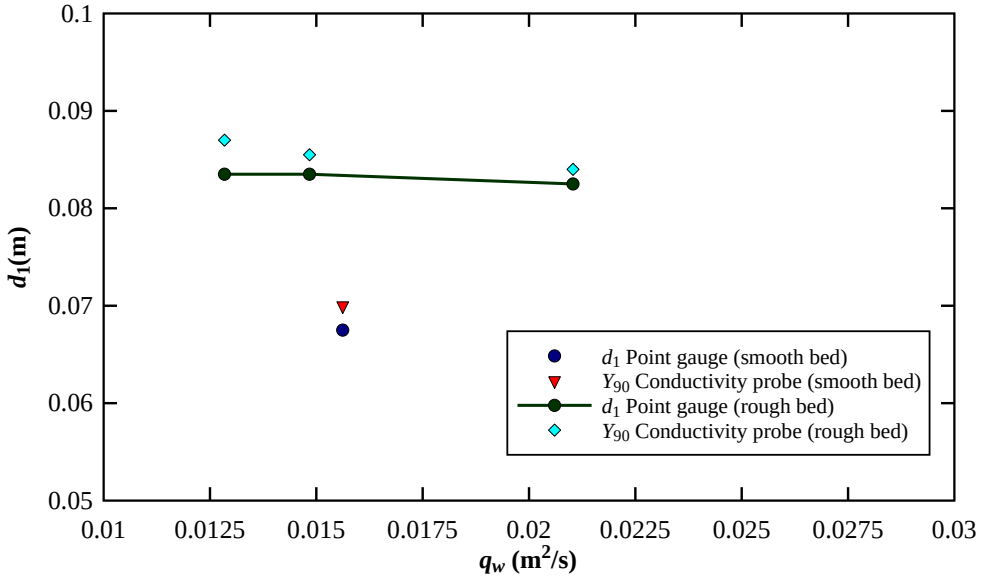

A: Comparison between pointer gauge measurements and the characteristic water flow depth (conductivity probe data)

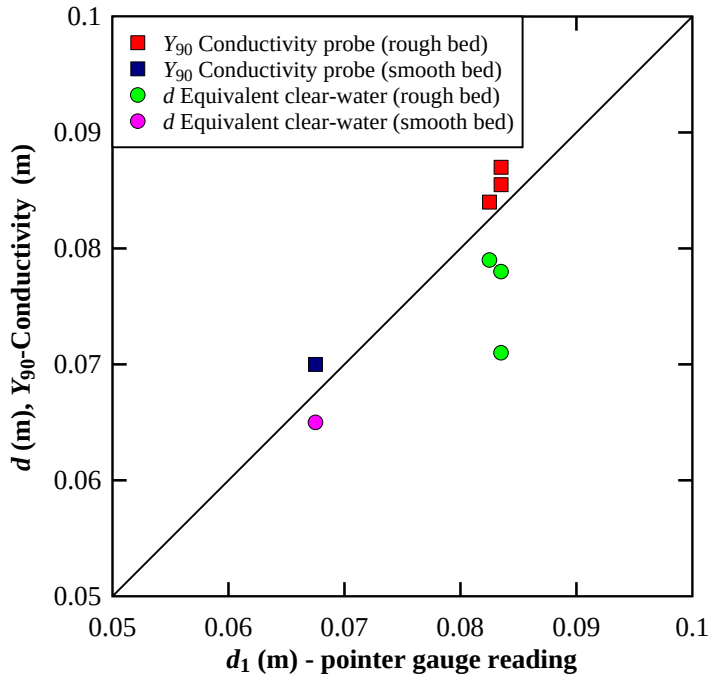

B: Comparison between pointer gauge measurements, conductivity probe data and equivalent clear water.

Figure 4.7 Comparison between different methods of water depth measurement upstream of jump toe

4.4 The jump roller and aerated flow lengths

The jump roller length L_r is defined as the longitudinal distance over which the water elevation increases monotonically (Murzyn et al. (2007), Murzyn and Chanson (2009)). Herein L_r was derived from the observed mean free-surface profiles. The dimensionless roller length L_r/d_1 is presented in Figure 4.8 as a function of the inflow Froude number Fr_1 and compared with those from previous studies including the observations on smooth bed (Murzyn et al. 2007, Kucukali and Chanson 2008, Murzyn and Chanson 2009, Wang 2014) and on rough bed (Carollo et al. 2007).

Given the visual observation, the maximum roller height was about 10–20% larger than the downstream flow depth, i.e. the conjugate depth depending upon both on the inflow Froude numbers Fr_1 and the experimental conditions (Gualtieri and Chanson 2007).

A linear relationship between the relative roller length and inflow Froude number was derived by Wang (2014), and Wang and Chanson (2015) as:

$$\frac{L_r}{d_1} = 6 \times (Fr_1 - 1) \quad (4.5)$$

Figure 4.8B shows that the jump roller length on a pebbled rough bed was shorter than that on smooth bed for the same inflow Froude number. On a pebbled bed, the increase in bed friction led to a shortening of the jump roller length.

An empirical relationship was derived based upon present data and those from Carollo et al. (2009) in terms of inflow Froude number and characteristic roughness (K_s/d_1):

$$\frac{L_r}{d_1} = 6 \times (Fr_1 - 1)^{(1-0.64 \times \frac{K_s}{d_1})} \qquad 1 < Fr_1 < 5 \quad (4.6)$$

Equation 4.6 yielded R = 0.95 and SE = 0.7 for rough bed condition. In case of $K_s=0$ equation 4.6 led to Eq. 4.5, i.e. to smooth bed condition, and resulted in R = 0.98, and SE = 1.47. Figure 4.8B presented the observed data together with Equations 4.6 and 4.5. Note that for the present study the range of inflow Froude number on rough bed configuration was 1.3 < Fr_1 < 2.9.

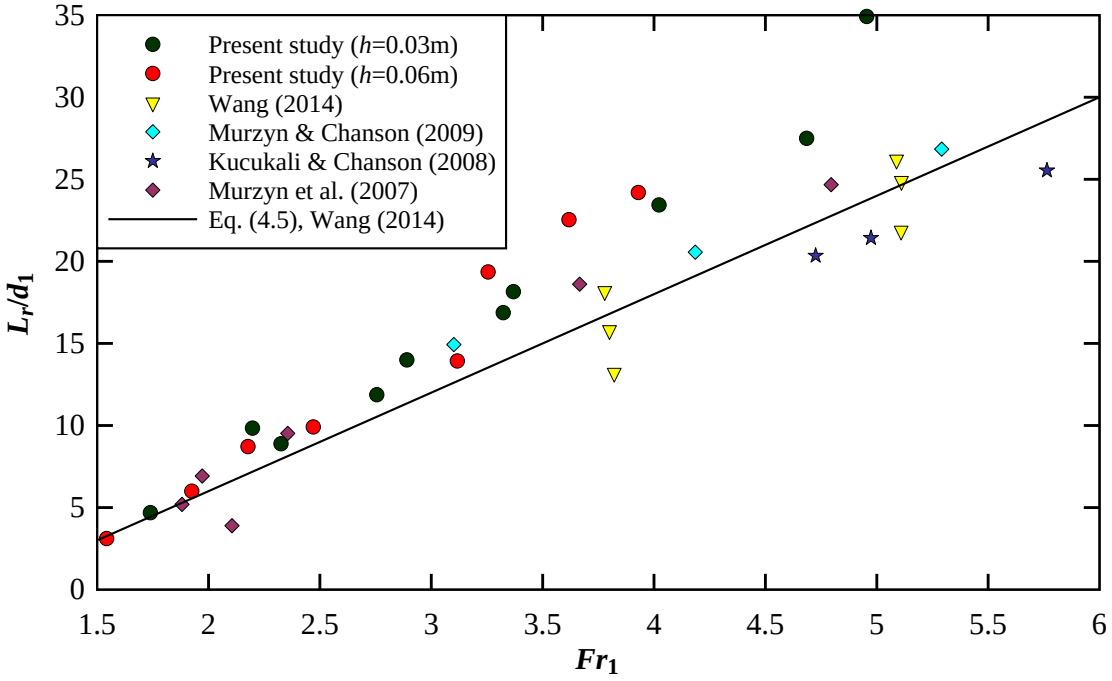

A: Comparison between the present study (smooth bed) and previous studies on smooth bed

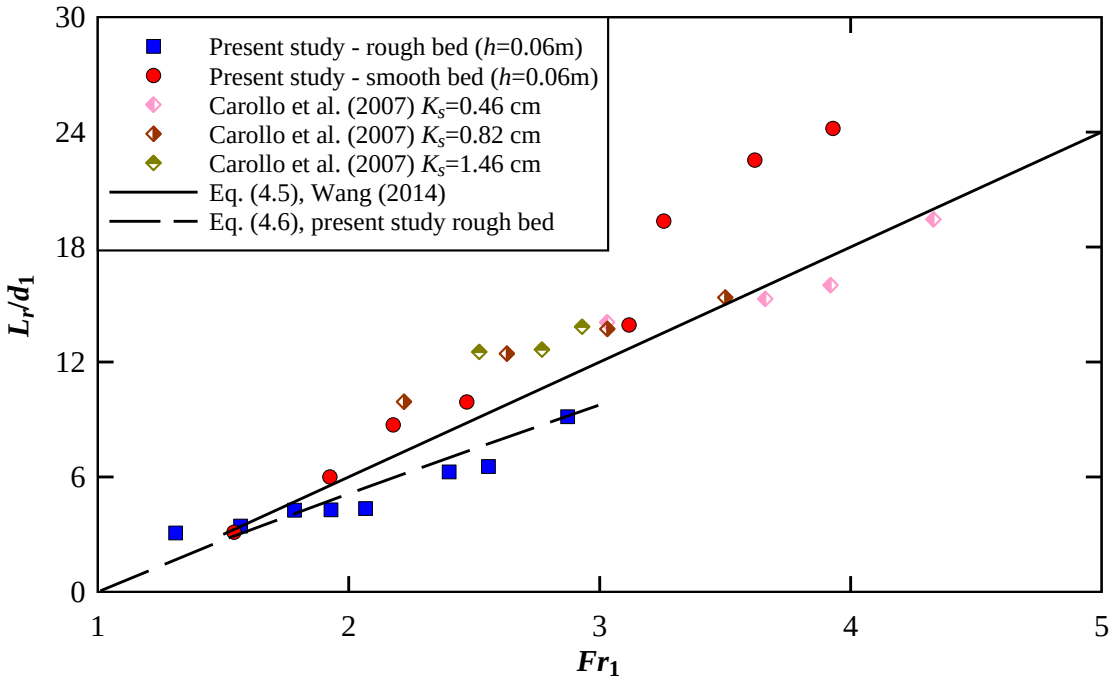

B: Comparison between the present and previous studies on rough bed

Figure 4.8 Jump roller length

The length of the bubbly flow region L_{air} was measured based upon sidewall observations of the entrained air bubbles. L_{air} is defined as the average length of the bubbly flow region. The result for both smooth and rough beds were compared in Figure 4.9 with the observations by Chanson (2011) on smooth bed. The difference between this study and the observations by Chanson (2011) could be due to a different definition of the bubble length in flow and of the end point where the bubbles disappear. Comparison between two gate openings on smooth bed showed that a higher Reynolds number led to higher dimensionless length of air-flow, possibly because of the smaller level of turbulence for lower Re_1 (lower gate opening).

For the same inflow Froude number Fr_1 and the same gate opening, the aerated flow length on rough bed was slightly shorter than on the smooth bed. It was in agreement with visual observations presented in section 4.2. A comparison between jump roller length and air flow length is shown in Figure 4.10, highlighting a shorter length of jump roller on rough bed with a shorter length of aerated flow.

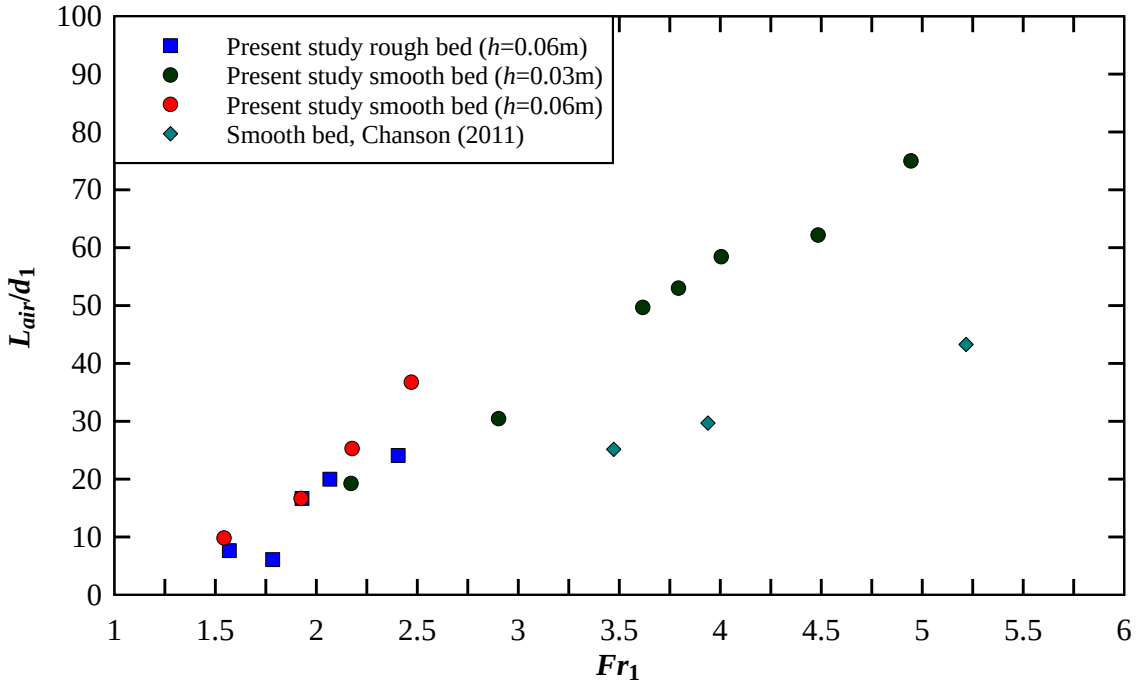

Figure 4.9 Air flow length L_{air} for both smooth and rough beds, comparison with Chanson (2011) on smooth bed

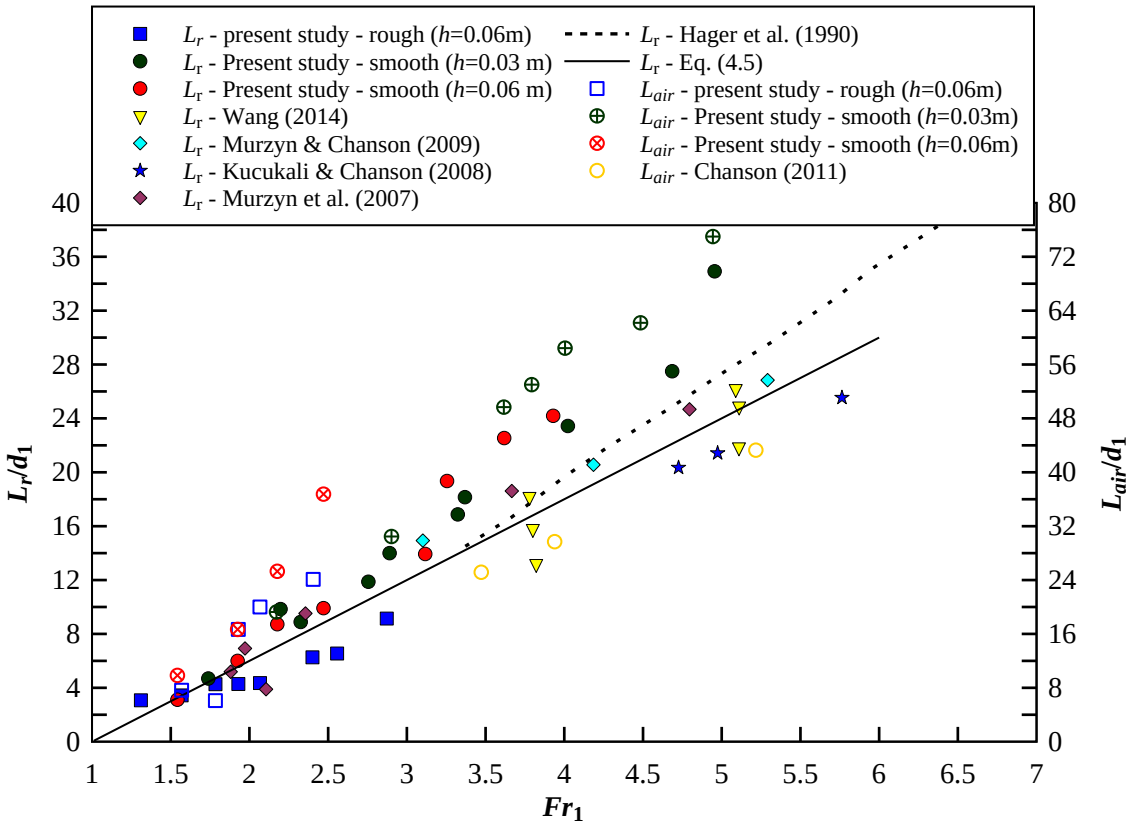

Figure 4.10 Relationship between dimensionless air flow length and jump roller length

4.5 Boundary friction force and shear stress

Based upon momentum considerations for a rectangular horizontal channel (Equation 4.1), the boundary friction force may be derived as a function of the ratio of conjugate depths and the inflow Froude number Fr_1 as:

$$\frac{F_{fric}}{\rho \times g \times B \times d_1^2} = \left(\frac{Fr_1^2}{\frac{1}{2} \times \frac{d_2}{d_1}} - \left(1 + \frac{d_2}{d_1}\right) \right) \times \left(\frac{d_2}{d_1} - 1\right) \tag{4.7}$$

Assuming the roller length to be about $L_r = 6 \times (Fr_1 - 1) \times d_1$, the average boundary shear stress beneath the roller equals:

$$\frac{\tau_0}{\frac{1}{2} \times \rho \times V_1^2} = \frac{\left(\frac{d_2}{d_1} - 1\right)}{3 \times Fr_1^2 \times (Fr_1 - 1)} \times \left(\frac{Fr_1^2}{\frac{1}{2} \times \frac{d_2}{d_1}} - \left(1 + \frac{d_2}{d_1}\right) \right) \tag{4.8}$$

The boundary friction force and average boundary shear stress were estimated based upon the jump roller length, observed ratios of conjugate depths and inflow Froude numbers using Equations 4.7 and 4.8, respectively. The results are shown in Figure 4.11. The boundary friction force for smooth bed highlighted an increasing trend with the increasing inflow Froude number regardless of the gate opening h_1. On the pebbled bed, an increasing trend for $Fr_1 < 2$ followed by decreasing trend for $Fr_1 > 2$ was observed. Overall, the boundary friction force for rough bed was higher than on smooth bed. For the same inflow Froude number, the value of dimensionless average boundary shear stress for rough bed was higher than smooth bed. For $Fr_1 > 2$ the trend of variation was the same for smooth bed with different gate opening and there was no significant difference.

4.6 Oscillations of the jump toe position

The hydraulic jump was observed to shift its longitudinal position about a mean position x_1, in both fast and slow manners, depending upon the inflow conditions. The fast change in jump toe position, or longitudinal oscillations, was studied by several researchers, including Long et al. (1991), Gualtieri and Chanson (2007), Chanson and Gualtieri (2008), Murzyn and Chanson (2009) and Wang (2014). The jump toe oscillations were related to the development of turbulent flow structures in the roller and air entrapment at the impingement point (Long et al. 1991). Long et al. (1991) and Gualtieri and Chanson (2007) investigated jump toe oscillation in terms of Strouhal number ($St = F_{toe}.d_1/V_1$) and found a range St = 0.005-0.05 for high inflow Froude numbers $5.2 < Fr_1 < 14.3$. In a numerical study, Richard and Gavrilyuk (2013) demonstrated that the oscillation frequency was not affected by the distance to the downstream end of the channel. The study of such very slow motion is limited up to date.

Herein the jump toe oscillation characteristics are presented for both rough and smooth beds in terms of the inflow Froude number. The fast change of instantaneous jump toe position was observed to take place in a pseudo-periodic manner. It is believed that the oscillation of jump toe and the generation and advection of large scale vortices in the roller were linked (Long et al. 1991, Mossa and Tolve 1998, Chanson 2010 Wang et al. 2015). Vortical structures formed continuously at the jump toe and were advected downstream in the shear layer. Visual observations suggested some interactions between the two-phase flow characteristics. That is, a formation of vortex was often seen with an instantaneous

downstream movement of jump toe, and the maximum shift of the toe position seemed to take place when the vortex detached from the impingement point (Wang 2014). Simultaneously the jump toe shifted upstream while the detached vortex was advected downstream in the shear layer. Both motions might be associated with the air entrainment at the jump toe.

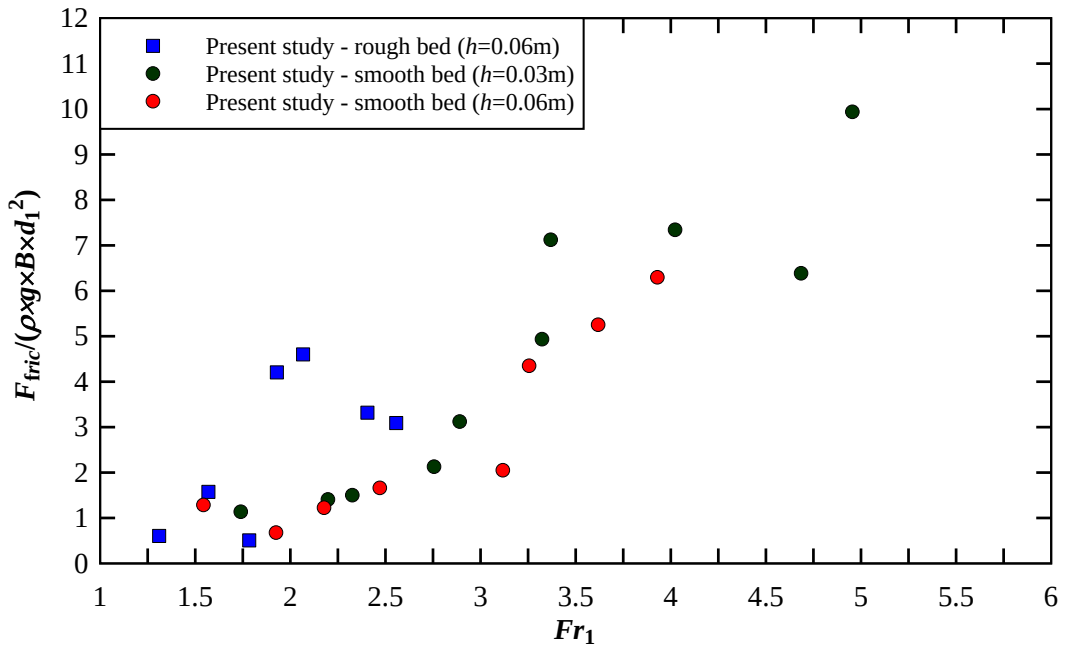

A: Dimensionless boundary friction force

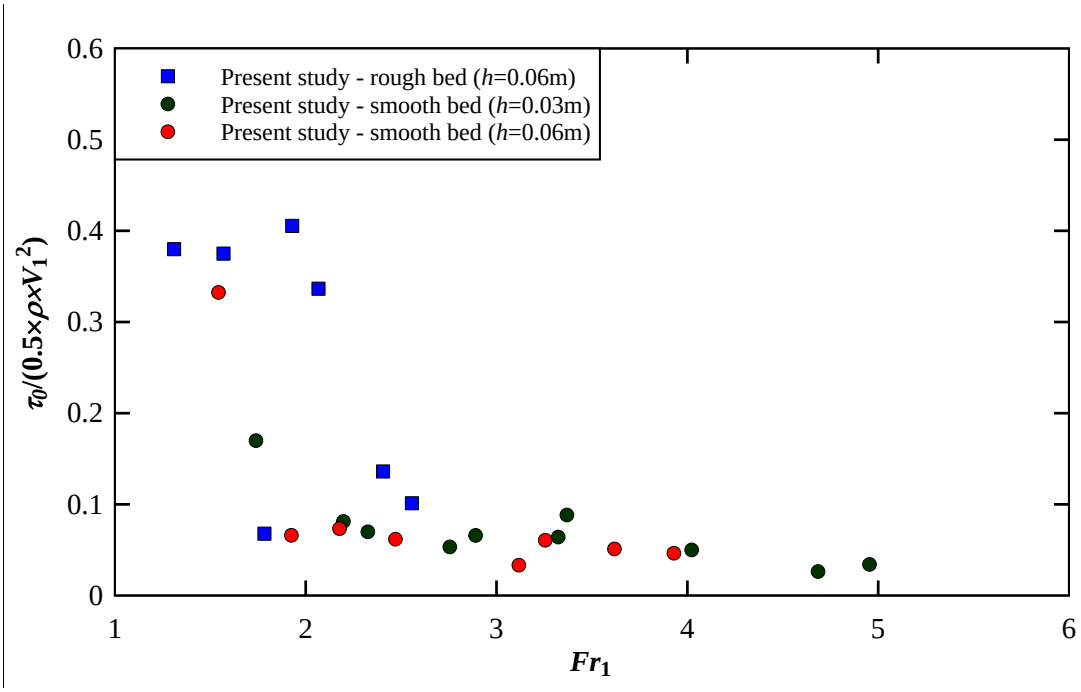

B: Dimensionless boundary shear stress

Figure 4.11 Dimensionless boundary friction force and dimensionless shear stress

The jump toe oscillation frequencies and the advections of large vortices were observed through the sidewalls. The observed average oscillation frequencies F_{toe} were found between 0.5 and 0.7 Hz for rough bed, and 0.4 and 0.9 Hz for smooth bed. Dimensionless oscillations $F_{toe}\times d_1/V_1$ for the present study were compared with those from previous studies[1] in Figure 4.12. For the rough bed, the experimental data were slightly higher than those on smooth bed. This could be related to the large vortices associated with the pebbled rough bed that enhanced the oscillations of the jump toe position. Overall, $F_{toe}\times d_1/V_1$ exhibited a decreasing trend with increasing inflow Froude number.

The formation of large-size vortices in the roller was observed with a typical ejection frequency, termed F_{eddy}, between 0.5 and 0.6 Hz for rough bed and between 0.6 and 1 Hz for smooth bed. This frequency decreased with increasing inflow Froude number on both rough and smooth bed configurations, although the observations were sometimes difficult due to the rapid pairing and merging of two successive eddies. The dimensionless characteristic frequency of large vortex ejections are shown in Figure 4.13. The trend of variation was decreasing with increasing inflow Froude number, albeit with almost no difference between rough and smooth bed.

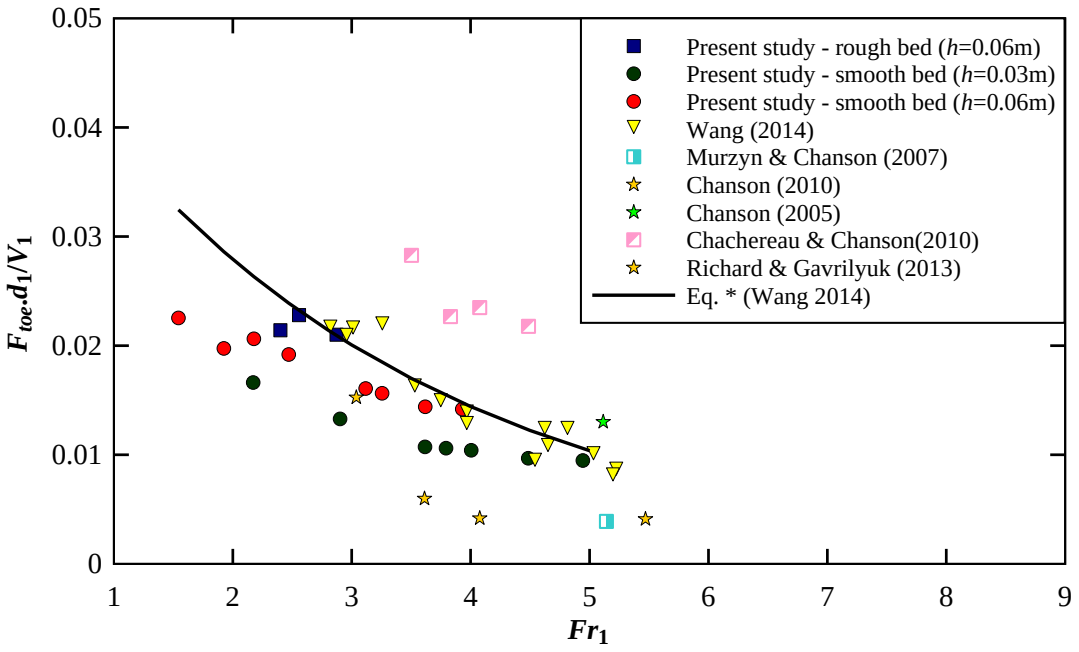

A: As functions of the inflow Froude number

[1] Wang (2014) based on experimental data correlation extracted dimensionless characteristic frequencies of longitudinal jump toe oscillations and large vortex ejections, respectively, as follow:

*) $\frac{F_{toe}\times d_1}{V_1} = 0.054 \times Exp(-0.33 \times Fr_1)$ $2.8 < Fr_1 < 7.1$

**) $\frac{F_{ej}\times d_1}{V_1} = 0.034 \times Exp(-0.26 \times Fr_1)$ $2.8 < Fr_1 < 7.1$

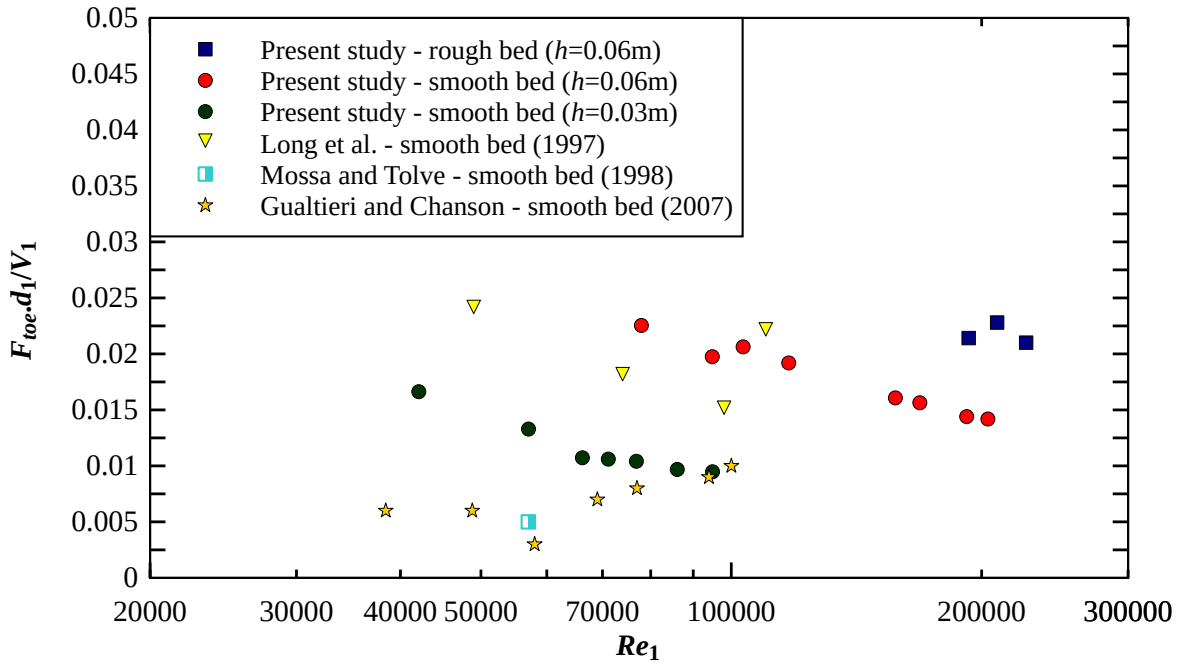

B: As functions of the inflow Reynolds number

Figure 4.12 Dimensionless characteristic frequency of longitudinal jump toe oscillations

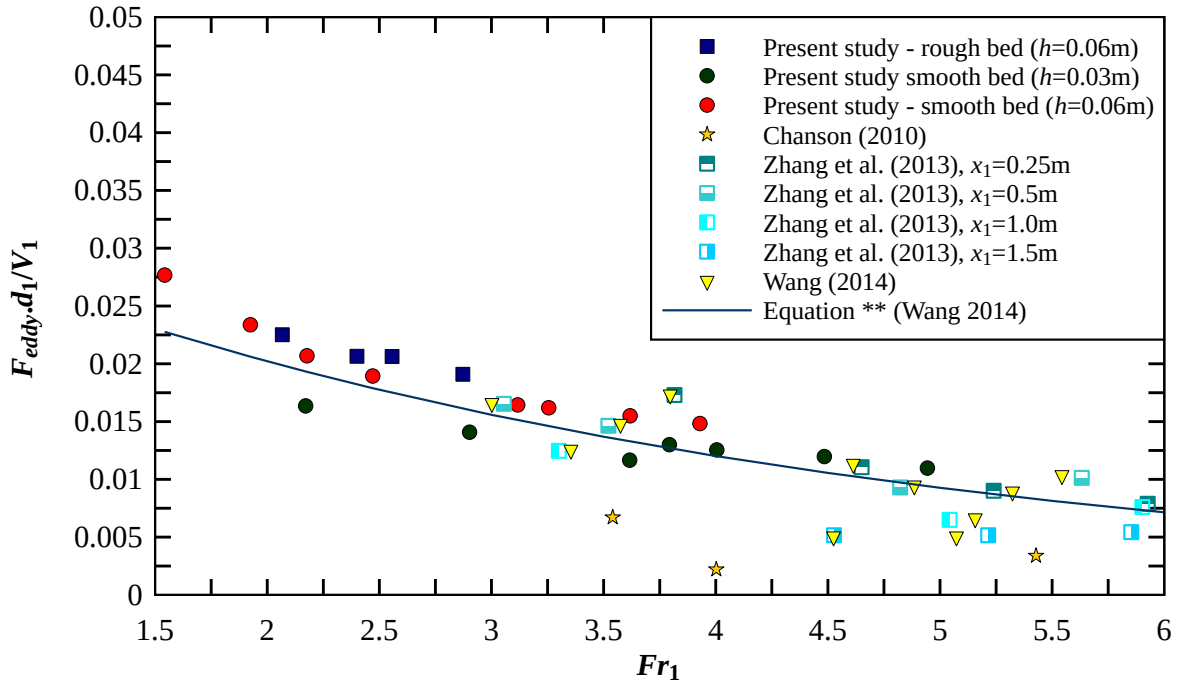

Figure 4.13 Dimensionless characteristic frequencies of large vortex ejections as a function of the inflow Froude number

The data presented in Figures 4.12 and 4.13 suggested that:

- The fluctuating features of the jump roller, .i.e. the dimensionless frequencies F_{toe} and F_{eddy}, were observed to decrease with the increasing Fr_1, on both bed types. This trend was in agreement with previous studies;
- The observed characteristic frequency of jump toe oscillation F_{toe} and vortex production F_{eddy} were comparable. On the smooth bed, the former was in the range 0.4 to 0.9, while the latter was in the range 0.6 to 1. On the rough bed, F_{toe} was in the range 0.5 to 0.7, while F_{eddy} was in the range 0.5 to 0.6;
- For $2.2 < Fr_1 < 3.0$, the dimensionless frequency of jump toe oscillation was $0.021 < F_{toe} \times d_1/V_1 < 0.023$ and $0.014 < F_{toe} \times d_1/V_1 < 0.022$ for rough and smooth bed configurations, respectively. While the dimensionless frequency of large vortex ejections was $0.019 < F_{eddy} \times d_1/V_1 < 0.02$ on both rough and smooth bed configurations;
- For $Fr_1 > 2.0$, large vortices appeared (Section 4.2) and fluctuating features of the jump roller, .i.e. the dimensionless F_{toe} and F_{eddy}, showed higher values for the rough bed for the inflow Froude number. Hence, for $Re_1 > 1.7E+5$, $F_{toe} \times d_1/V_1$ was above 0.022 and 0.014 on rough and smooth bed configurations, respectively. On the other hand, for $2.2 < Fr_1 < 3.0$, $F_{eddy} \times d_1/V_1$ was in average 0.02 for both rough and smooth bed configurations.

4.7 Vortex advection velocity

Surface fluctuations were observed to propagate downstream at the free-surface when vortical flow structures were formed and advected in the jump roller. Figure 4.14 sketches the advection of large vortices in a developing mixing layer on smooth bed. The vortex advection velocity is denoted U_{eddy} and was observed visually from side-view video records for different flow conditions. It was recorded as the average velocity of the vortices, formed at the jump toe position, until they vanished in the downstream region. Figure 4.15 shows the dimensionless vortex advection velocity U_{eddy}/V_1 as function of the inflow Froude number Fr_1 and the inflow Reynolds number Re_1.

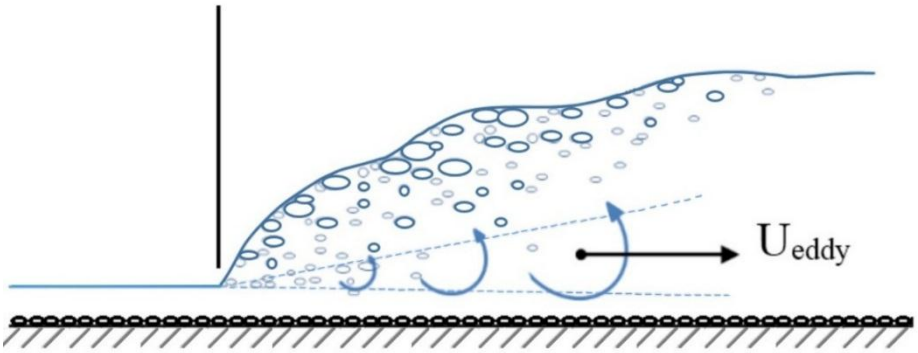

Figure 4.14 Sketch of advection of large vortices in the shear layer on rough bed (based on Wang et al. 2015)

The vortex advection velocity U_{eddy}/V_1 was nearly independent of both inflow Reynolds number and inflow Froude numbers, with an average U_{eddy}/V_1 = 0.43 for both gate opening of smooth bed and U_{eddy}/V_1 = 0.46 for rough bed. The results were comparable to the advection velocity data of Chanson (2010), which provided a mean value U_{eddy}/V_1 = 0.32 and Wang (2014), with an average value U_{eddy}/V_1 = 0.41. These earlier results were obtained for smooth bed. The production of large vortices was related to the fast longitudinal jump toe oscillations and they carried a large amount of entrapped air that resulted in flow bulking of the free-surface. The flow bulking was associated to free surface fluctuations and wave propagation, when the vortices were advected within the turbulent shear layer.

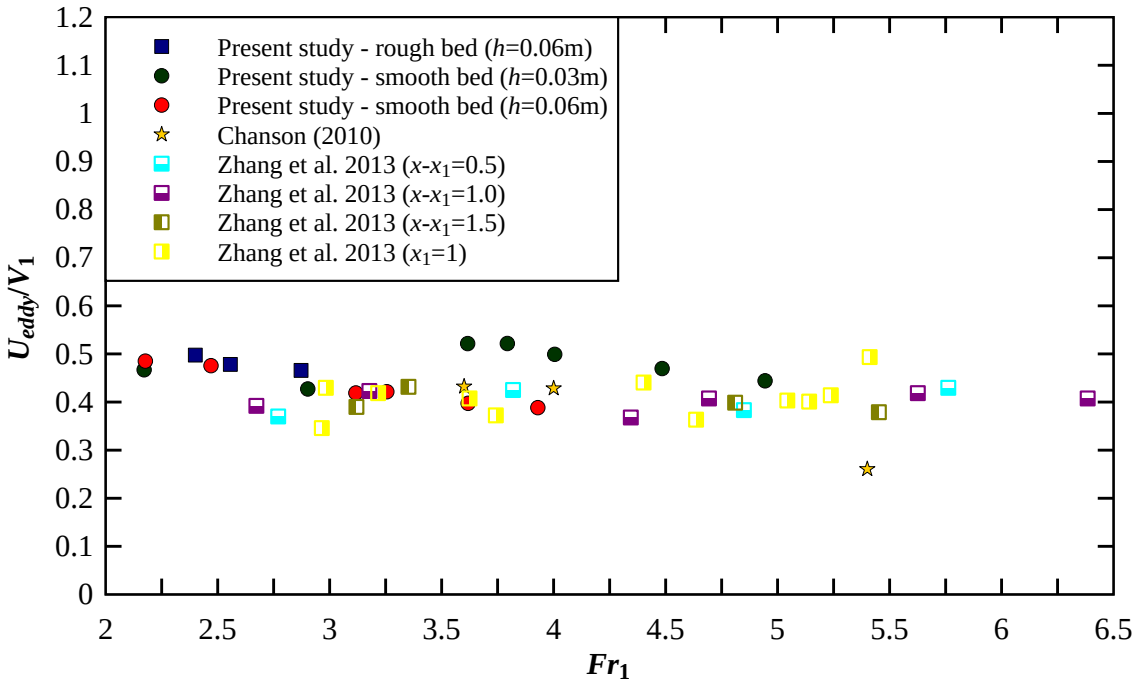

A: Dimensionless advection velocity of large vortices in the jump roller based on inflow Froude number, comparison with previous studies on smooth bed

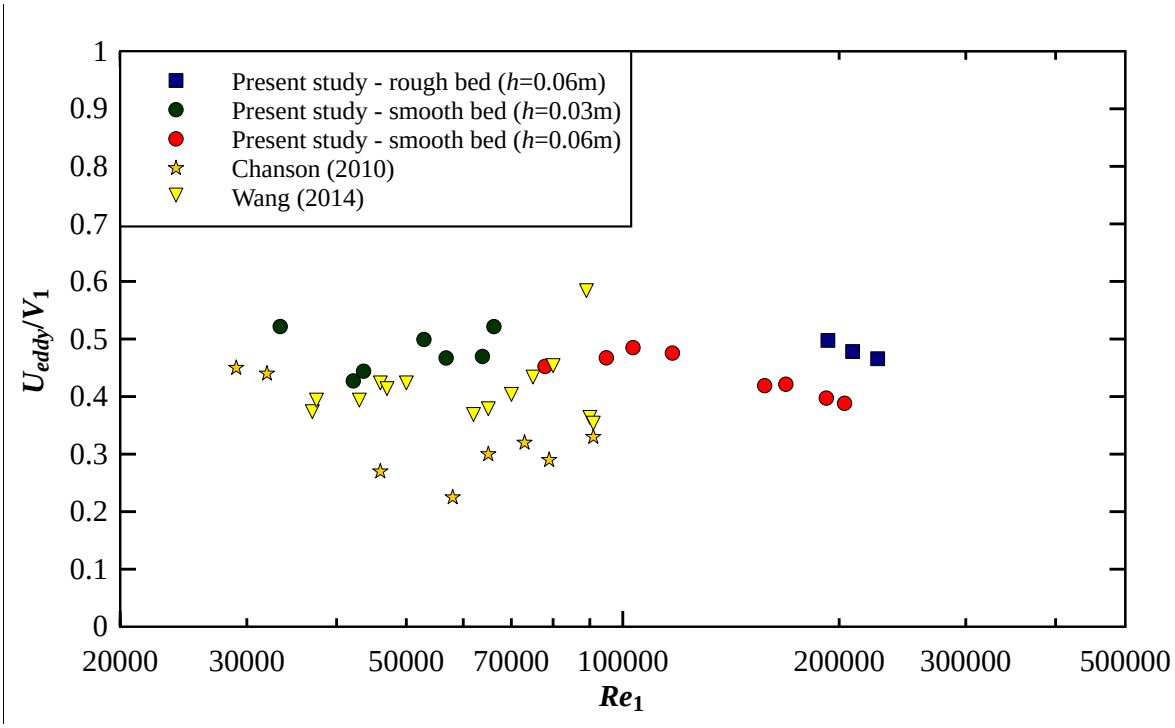

B: Dimensionless advection velocity of large vortices in the jump roller based on inflow Reynolds number, comparison with previous studies on smooth bed

Figure 4.15 Dimensionless advection velocity of large vortices in the jump roller

4.8 Investigation of impingement perimeter and water surface profile

The hydraulic jump has been most often studied in two dimensions considering a constant variation in transverse direction. Investigation of transverse flow structures received little attention until recently on smooth bed (Kucukali and Chanson 2008, Murzyn and Chanson 2009, Chachereau and Chanson 2011a, 2011b, Zhang et al. 2013, Wang 2014).

Herein an investigation was focused on the transverse perimeter of hydraulic jump toe and the variation of water surface profile. The instantaneous perimeter profiles as well as the water surface profiles, were recorded using video cameras and quantified with a minimum of 50 and 120 data points per full width for up and side views, respectively. A total of 2500 continuous frames one in 5 frames (500 out of 2500) were extracted to analyse both top and side views for each flow condition. Four flow conditions, one on smooth and three on rough bed, were considered, as listed in Table 4.1.

Table 4.1 Flow conditions for observations of transverse impingement perimeter and water surface variation, x_1 = 1 m

Bed type	Q (m^3/s)	h (m)	Run	d_1 (m)	Fr_1	Re_1
Smooth	0.08	0.06	AS13	0.062	3.25	1.7E+5
Rough	0.1	0.06	AR8	0.082	2.87	2.2E+5
	0.092		AR7	0.084	2.56	2.1E+5
	0.085		AR6	0.083	2.4	1.9E+5

4.8.1 Impingement perimeter

Figure 4.16 presents 6 frames for the jump toe perimeter, with a time step of 0.5s between frames, plus the median jump toe perimeter for all 500 frames. As seen in Figures 4.16A and B, different shapes of jump toe perimeter were observed on both bed types. The arc-shaped perimeter bending towards downstream was the most frequently observed flow pattern in the highly turbulent flow, as reported by Wang (2014) on smooth bed. Some effect of boundaries were noted next to the channel sidewalls. The development of lateral boundary layers induced smaller velocities at the sidewalls compared to in the central free-stream region. The local inflow Froude number on the channel centerline was thus slightly larger than that near the wall, and a further downstream jump toe position was predicted by the backwater curves.

The impingement perimeter data suggested that:

- For $Fr_1 > 2.8$, the range of local variation of the jump toe perimeter was $-3 < (x_{toe}-x_1)/d_1 < 2.4$ and $-3.2 < (x_{toe}-x_1)/d_1 < 4.5$ for smooth and rough bed with Fr_1 = 3.25 and 2.87, respectively. This highlighted the higher range of fluctuations on the rough bed that could be a sign of instability of hydraulic jump on rough bed (Figure 4.16A and B);
- For lower inflow Froude numbers on rough bed, i.e. Fr_1 = 2.56 and 2.4, the range of local variation of the jump to perimeter was $-1.65 < (x_{toe}-x_1)/d_1 < 3.05$ and $-1.75 < (x_{toe}-x_1)/d_1 < 1.75$ for Fr_1 = 2.56 and 2.4, respectively. It highlighted the higher range of variation of jump toe perimeter corresponding to the higher inflow Froude number (Figure 4.16 C and D);
- For Fr_1 = 2.56 and 2.4 on rough bed (Figure 4.16 C and D), unsymmetrical shape of jump toe perimeter was related to undular jump with an unstable roller condition as well as irregularity of jump toe oscillation (Section 4.2).

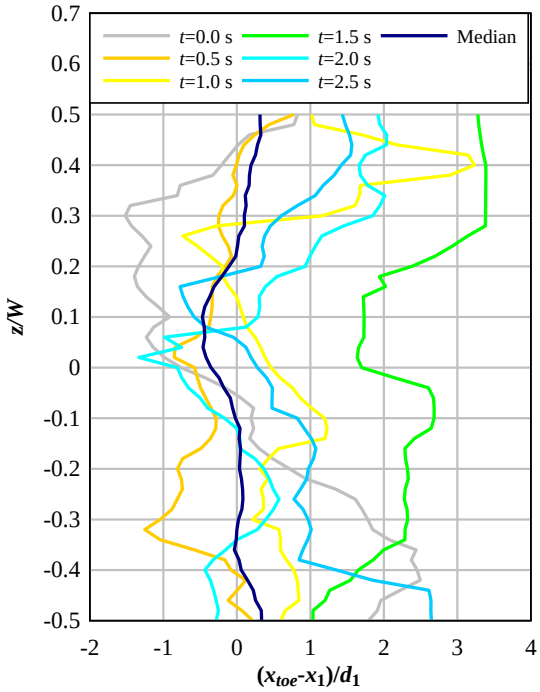

A: Jump toe perimeter, smooth bed, Run AS13

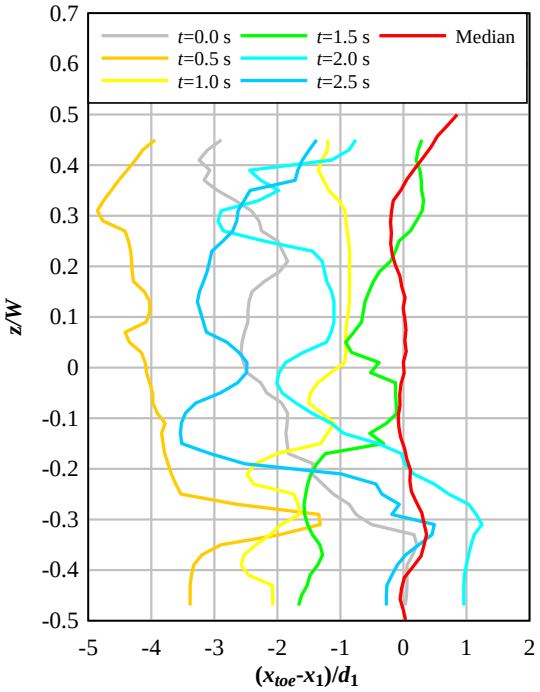

B: Jump toe perimeter, rough bed Run AR8

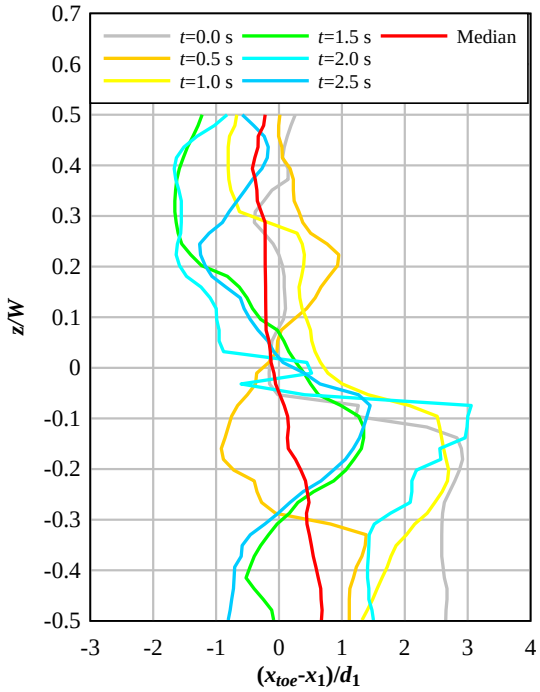

C: Jump toe perimeter, rough bed, Run AR7

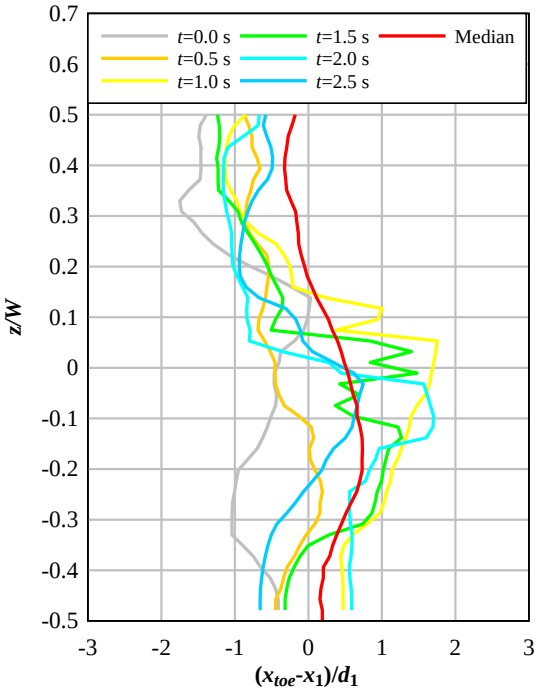

D: Jump toe perimeter, rough bed Run AR6

Figure 4.16 Continuous frames with time step of 0.5 s for jump toe perimeter. Run AR8*:* Q = 0.1 m^3/s, Fr_1 = 2.87, Run AR7*:* Q = 0.092 m^3/s, Fr_1 = 2.56 and Run AR6*:* Q = 0.085 m^3/s, Fr_1 = 2.4 for rough bed and Run AS13: Q = 0.078 m^3/s, Fr_1= 3.25 for smooth bed with the same gate opening h= 0.06 m

The local impingement point was recorded every 1 mm across the full channel width, as well as in the longitudinal direction for water surface. At each transverse location z ($-0.5 \leq z/W \leq 0.5$), the median impingement point position and the standard deviation x_{toe}' were calculated. The results are shown in Figures 4.17 for the full transverse cross-section. As seen in Figure 4.17, the general trend of median jump toe perimeter was the same for both bed types as well as the standard deviation of jump toe perimeter, except possibly for $Fr_1 = 2.4$ on rough bed because of undular effect of jump type. In Figure 4.17B, despite of different x_1 used by Wang (2014) on smooth bed, the standard deviation was in a same range for all the cases.

A comparison between the present study and the data of Wang (2014) on smooth bed suggested that:

- Regardless of the bed type, rough or smooth, the time-averaged jump toe perimeter profile was nearly straight across the transverse direction in the central flow region ($-0.3 < z/W < 0.3$) for $Fr_1 > 2.5$ (Figure 4.17B);
- For $Fr_1 = 2.4$ on rough bed, the shapes of variation for median and standard deviation of the jump toe oscillation were different from those in the other flow conditions (Figure 4.17A and B). This could be associated with undular type of hydraulic jump with unstable roller (Section 4.2);
- Regardless of the bed type, rough or smooth, the impingement point fluctuations were about constant across the channel for each flow condition, with some larger values next to the sidewalls. The data suggested an approximately 0.1 m wide boundary-affected region next to each sidewall.

The probability density function (*PDF*) of instantaneous impingement and water surface positions was obtained at each transverse location and longitudinal position, respectively. Data processing was done using *dfittool* function of Matlab software. Figure 4.18 plots all *PDFs* through the width of central flow region for inflow Froude numbers $Fr_1 = 2.4$, 2.56, 2.87 on rough and for $Fr_1 = 3.25$ on smooth bed for whole width of channel.

Different type of distributions were tested and the best data fit was based on Anderson Darling Statistic (Anderson and Darling 1952). The method is based on a comparison of the empirical distribution function of a given sample with the theoretical distribution to be tested and is defined as (Stephens 1974).

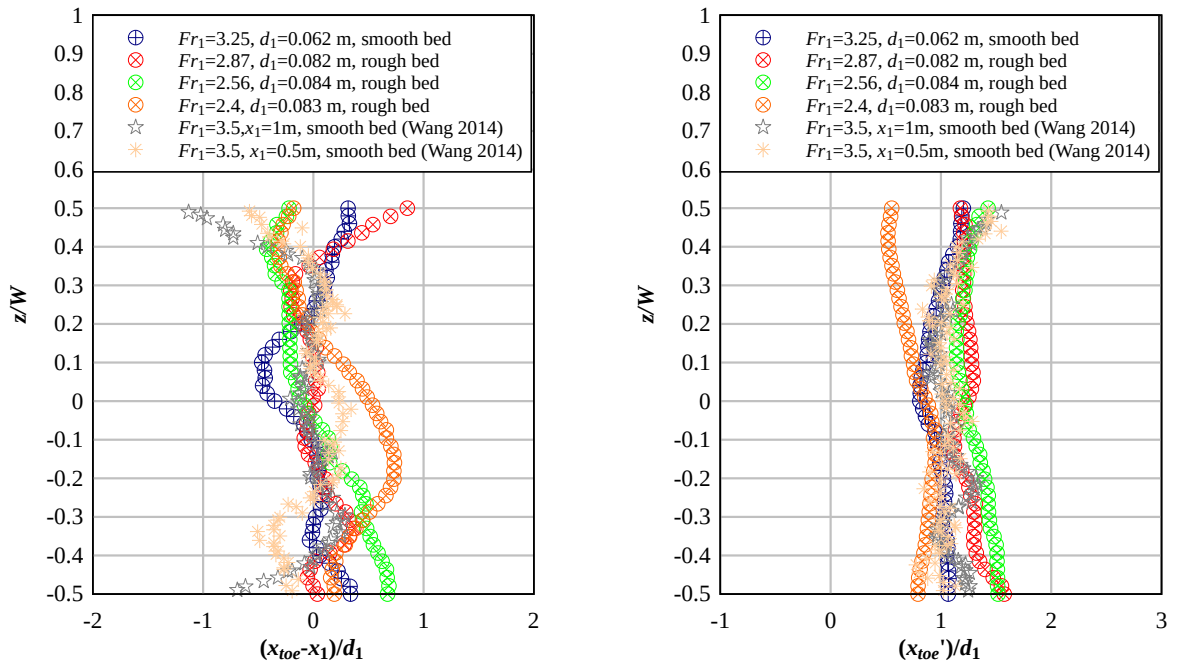

(A) Median jump toe perimeter profiles (B) Standard deviation of instantaneous jump toe position

Figure 4.17. Median and standard deviations of the instantaneous jump toe position for both bed types through the full channel width, comparison with Wang (2014). Run AR8*: Q* = 0.1 m^3/s, Fr_1 = 2.87, Run AR7*: Q* = 0.092 m^3/s, Fr_1 = 2.56 and Run AR6*: Q* = 0.085 m^3/s, Fr_1 = 2.4 for rough bed and Run AS13: *Q* = 0.078 m^3/s, Fr_1 = 3.25 for smooth bed with the same gate opening *h* = 0.06 m

For a specified data set and distribution, the best data fit gives the smallest Anderson Darling statistics (Stephens 1974, Marsaglia and Marsaglia 2004).

For the jump toe perimeter, the agreement between the *PDF* and the normal distribution, as reflected by the normalized correlation coefficient, indicated some randomness in the longitudinal impingement point fluctuation.

For hydraulic jump with stable roller i.e. $Fr_1 > 2.8$, a broader distribution of instantaneous jump toe position was observed on rough bed. $-3.4 < (x_{toe}-x_1)/d_1 < 4.2$ and $-3.4 < (x_{toe}-x_1)/d_1 < 2.9$ on rough and smooth bed, respectively. A higher PDF_{max} value was found on the smooth bed: PDF_{max} = 0.42 and 0.3 for smooth and rough bed, respectively (Figure 4.18). The findings were in agreement with the data presented in Figures 4.16 and 4.17.

For hydraulic jump with unstable roller, i.e. Fr_1 = 2.56 and 2.4 on rough bed, a broader distribution of the instantaneous jump toe position was observed for Fr_1 = 2.56. So that $-3.4 < (x_{toe}-x_1)/d_1 < 4.4$ and $-1.3 < (x_{toe}-x_1)/d_1 < 3.1$ while PDF_{max} = 0.23 and 0.53 for Fr_1 = 2.56 and 2.4, respectively. The broader distribution demonstrated the larger domain of variation of the jump toe perimeter for Fr_1 = 2.56, while the PDF_{max} showed the more tendency of the jump

toe perimeter to the average value. The asymmetric shape of data distribution for Fr_1 = 2.4 on rough bed was linked to the asymmetric shape of the median jump toe perimeter (4.17A). Overall, for rough bed, the domain of variation for jump toe perimeter increased with increasing inflow Froude number. For both bed types, regardless of inflow Froude number, the data followed a normal distribution.

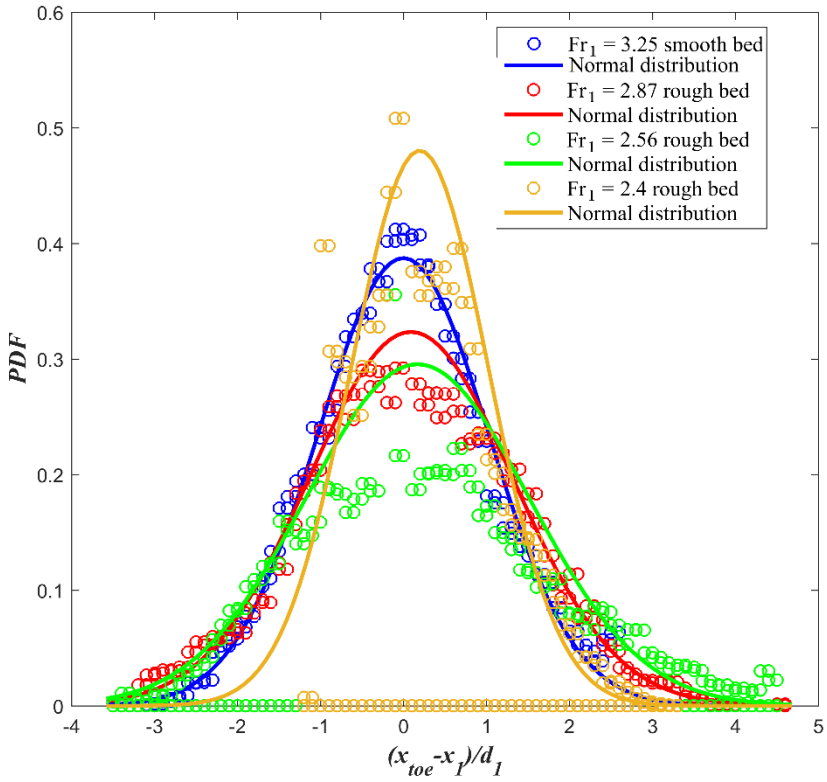

Figure 4.18 Probability density functions of instantaneous jump toe position; Fr_1 = 2.87, 2.56, 2.4 with d_1 = 0.082, 0.84, 0.083 m, respectively, on rough bed, Fr_1 = 3.25, d_1 = 0.062 m on smooth bed

4.8.2 Water surface profile

Figure 4.19 presents 6 instantaneous longitudinal water surface profile recorded with a time step of 0.5s for frames, plus the median water surface profile for all 500 frames. The range of local fluctuations in vertical water surface elevations was $\Delta(\eta/d_1)$ = 2.4 for smooth bed with Fr_1 = 3.25 and was $\Delta(\eta/d_1)$ = 1.1 for rough bed with Fr_1 = 2.87. η is the elevation of water surface. For lower inflow Froude numbers, i.e. Fr_1 = 2.4 and 2.56, the highest fluctuation of water surface was observed in the roller area close to the jump toe. The domain of variation for water surface close to the jump toe was $\Delta(\eta/d_1)$ = 2.04 and 1.31 for Fr_1 = 2.4 and 2.56 on rough bed, respectively. While further downstream $\Delta(\eta/d_1)$ = 0.83 and 0.57 for Fr_1 = 2.4 and

2.56 on rough bed, respectively.

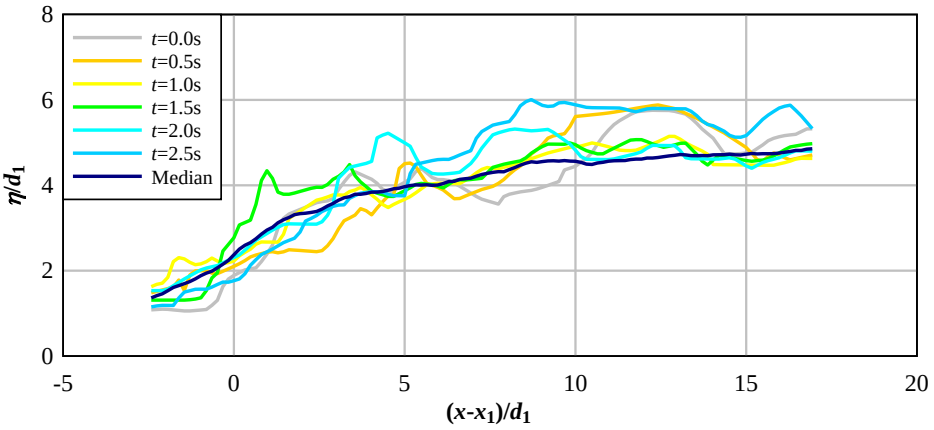

A: Longitudinal water profile, smooth bed, Run AS13

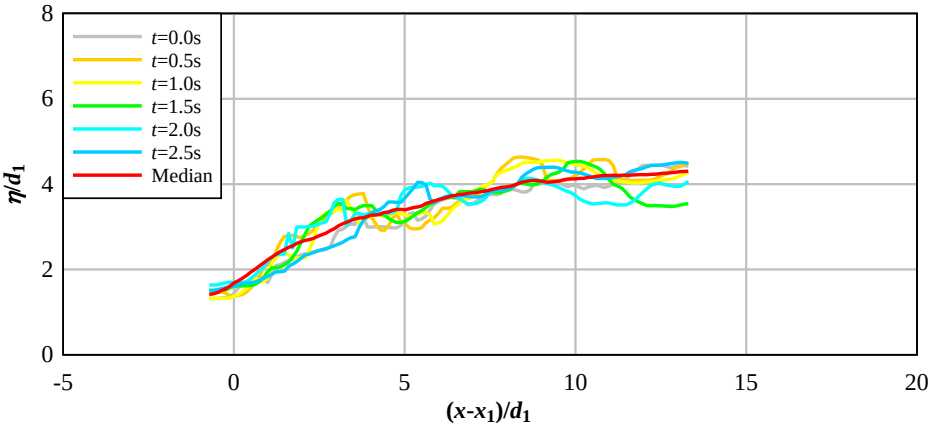

B: Longitudinal water profile, rough bed, Run AR8

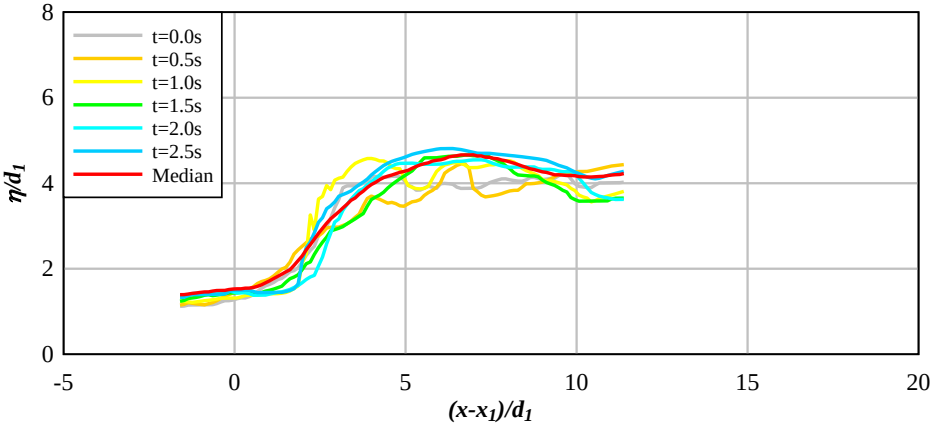

C: Longitudinal water profile, rough bed, Run AR7

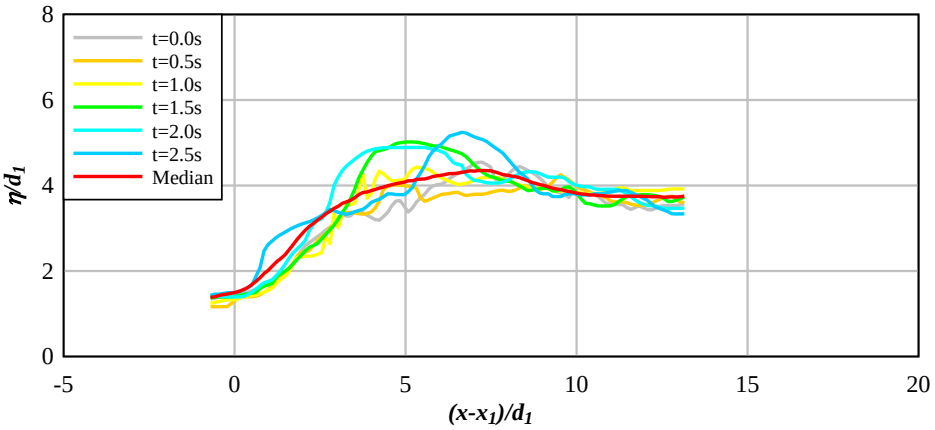

D: Longitudinal water profile, rough bed, Run AR6

Figure 4.19 Continuous frames with time step of 0.5s for jump toe perimeter and longitudinal water profile, Run AR8*: Q* = 0.1 m^3/s, Fr_1 = 2.87, Run AR7*: Q* = 0.092 m^3/s, Fr_1 = 2.56 and Run AR6*: Q* = 0.085 m^3/s, Fr_1 = 2.4 for rough bed and Run AS13 *Q* = 0.078 m^3/s, Fr_1 = 3.25 for smooth bed with the same gate opening *h* = 0.06 m

Overall, these findings were in agreement with undular jump with unstable roller and irregular water surface fluctuation on rough bed discussed in Section 4.2.

The local water surface profile was recorded every 1 mm along the longitudinal direction for all inflow conditions on both rough and smooth bed configurations. The results are shown in Figures 4.20 and they suggested that:

- On both bed types a comparable trend of variation for median water surface profile (increased with increasing longitudinal distance from the jump toe) as well as the standard deviation of water surface profile (fluctuated in roller length while it decreased further downstream) was observed;
- On both bed types, the median water surface profile monotonically increased regardless of the bed roughness type and the inflow Froude number (Figure 4.20A);
- For all inflow conditions on both rough and smooth bed configurations, the maximum fluctuation of the water surface level was observed close to the jump toe position (Figure 4.20B). However, the fluctuations in water surface on smooth bed were higher than on rough bed showing that the rough bed had a stronger control effect on the flow fluctuations;

- The standard deviation of the water surface profile had a higher range of fluctuations on smooth bed, with $0.14 < \eta'/d < 0.59$ and $0.16 < \eta'/d < 0.4$ for smooth ($Fr_1 = 3.25$) and rough ($Fr_1 = 2.87$) bed, respectively (Figure 4.20B);
- On rough bed, the lower inflow Froude number resulted in higher range of fluctuation of water surface level so that $0.09 < \eta'/d < .51$, $0.19 < \eta'/d < 0.45$ and $0.16 < \eta'/d < 0.4$ for $Fr_1 = 2.4$, 2.56 and 2.87, respectively (Figure 4.20B);
- For $Fr_1 < 2.8$ on rough bed, although the median value of water surface profile was derived from the average of 10 s, the undular behavior of hydraulic jump along the roller length affected the variation of water surface profile (Figure 4.20A).

To analyze the *PDFs* for the longitudinal water surface profile, the longitudinal distance was subdivided into three regions for all inflow Froude numbers. Based upon the median water surface profiles (Figure 4.19), three regions were selected along the jump roller length for both rough and smooth bed configurations (Figure 4.21):

- $0.0 < (x - x_1) / L_r < 0.27$;
- $0.27 < (x - x_1) / L_r < 0.57$;
- $0.57 < (x - x_1) / L_r < 1.0$.

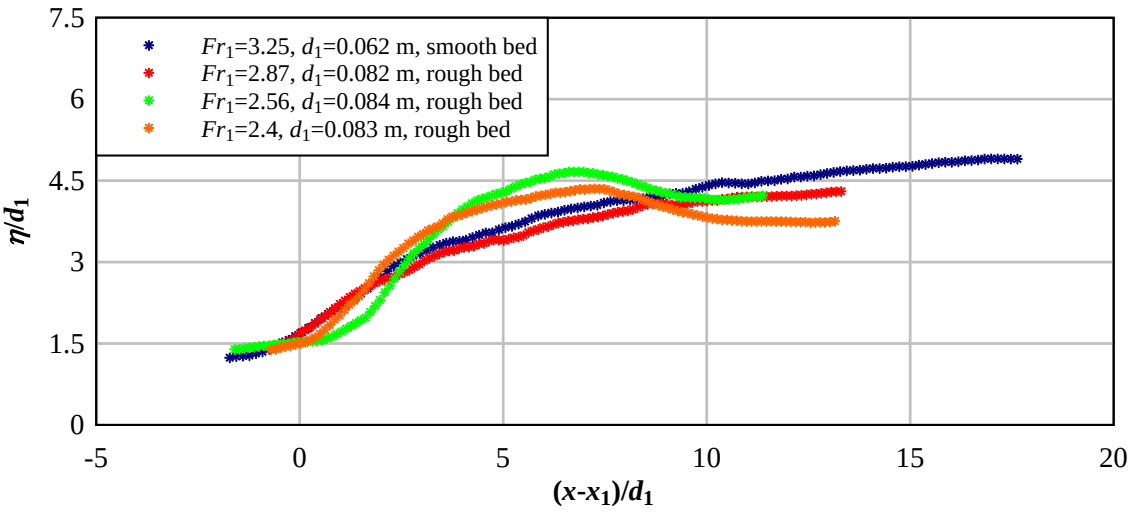

A: Median water surface profiles

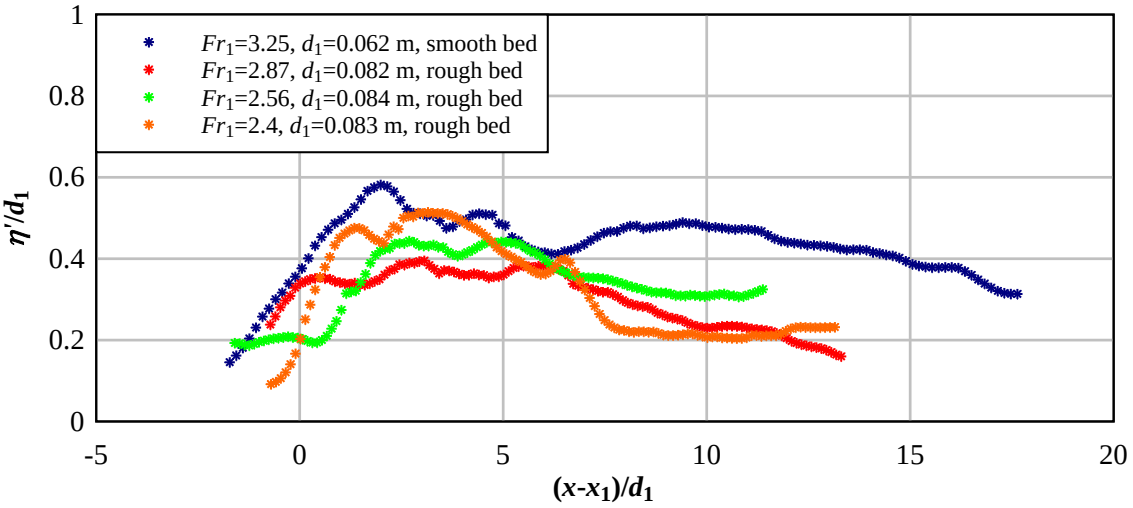

B: Standard deviation of water surface profile

Figure 4.20 Median and standard deviations of the instantaneous water surface profile on both bed types through the full channel width. Run AR8*:* Q = 0.1 m^3/s, Fr_1 = 2.87, Run AR7*:* Q = 0.092 m^3/s, Fr_1 = 2.56 and Run AR6*:* Q = 0.085 m^3/s, Fr_1 = 2.4 for rough bed and Run AS13 Q = 0.078 m^3/s, Fr_1 = 3.25 on smooth bed for the same gate opening h = 0.06 m

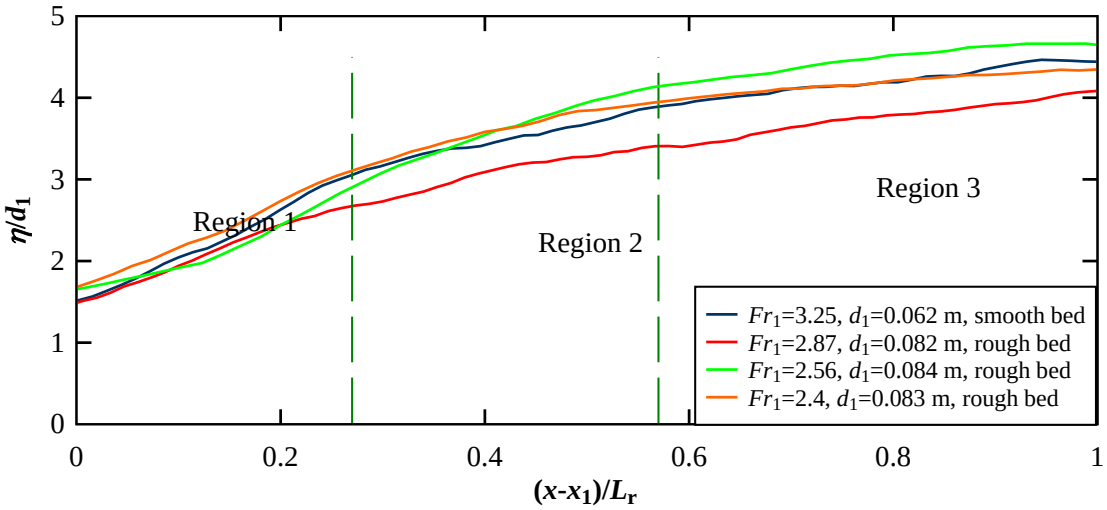

Figure 4.21 Three regions along the jump roller length

Figure 4.22 presents the *PDFs* for the three regions of the longitudinal water surface profile. Different types of distribution were tested and the best fit was selected based on the Anderson-Darling test statistic, mean, and variance.

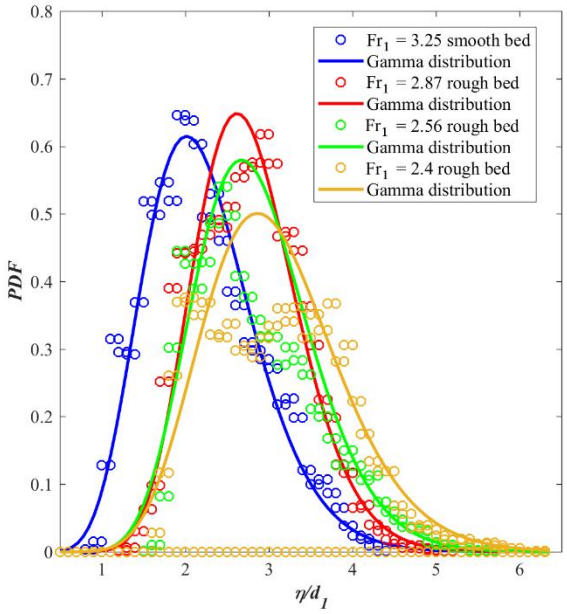

A: First region $0.0 < (x - x_1) / L_r < 0.27$

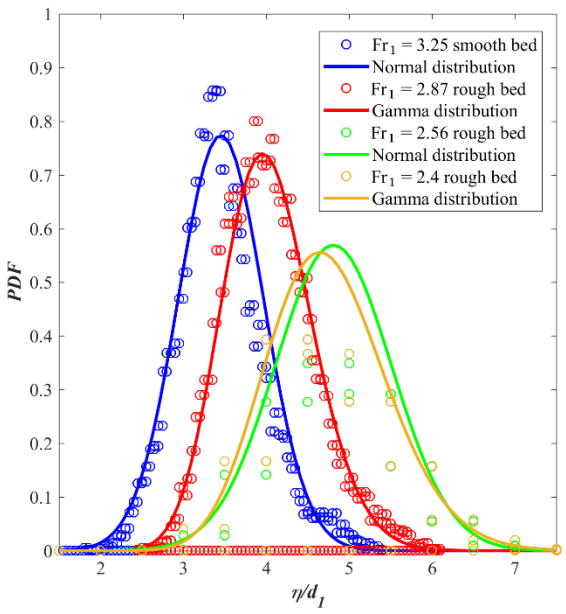

B: Second region $0.27 < (x - x_1) / L_r < 0.57$

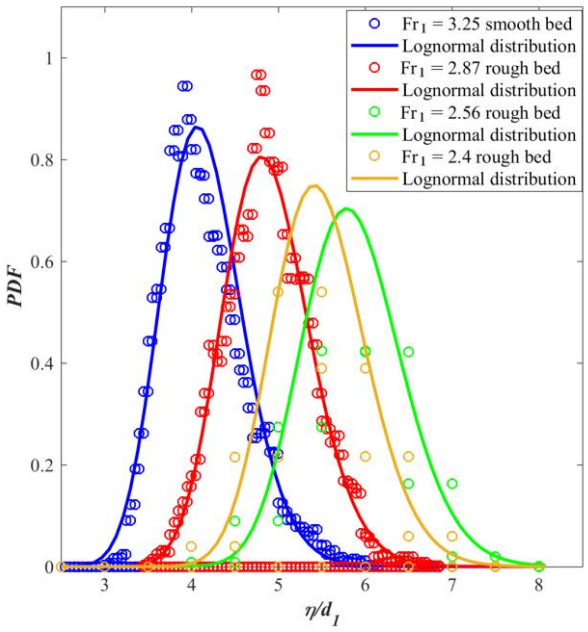

C: Third region $0.57 < (x - x_1) / L_r < 1.0$

Figure 4.22 Probability density functions of instantaneous water surface profile; Fr_1 = 2.87, 2.56, 2.4 with d_1 = 0.082, 0.84, 0.083 m, respectively, on rough bed, Fr_1 = 3.25, d_1 = 0.062 m on smooth bed

The broader shape of *PDFs* in Figure 4.22, especially in the first and third regions (Figure 4.22A and C) was associated with a higher standard deviation of water surface profile as shown in Figure 4.21B. In the first region, the probability density function of the

instantaneous water surface profile had a comparable range of variation on both bed types for the hydraulic jump with the stable roller, i.e. $Fr_1 > 2.8$. It had also a comparable range of variation for the undular jump with unstable roller, $Fr_1 = 2.56$ and 2.4 on rough bed.

In the second region, the domain of variation of water surface profile was $\Delta\eta/d_1 = 4$ for $Fr_1 > 2.8$ on both rough and smooth bed configurations, while it was $\Delta\eta/d_1 = 5$ for $Fr_1 = 2.56$ and 2.4 on rough bed showing the larger domain of fluctuation on rough bed at the middle of roller length.

In the third region, the domain of variation of water surface profile was $\Delta\eta/d_1 = 3.5$ for $Fr_1 > 2.8$ on both rough and smooth bed configurations, while it was $\Delta\eta/d_1 = 4$ for $Fr_1 = 2.56$ and 2.4 on rough bed suggesting the larger domain of fluctuation on rough bed at the end of roller length. The higher PDF_{max} value demonstrated the tendency of data toward the average value which had the highest magnitudes in the third region showing the lower fluctuation of water surface at the end of the roller length. In the third region, the larger PDF_{max} on rough bed might be associated with the higher magnitudes of d_2/d_1 on rough bed (Figure 4.6). The findings were in agreement with the parameters presented in Figure 4.20. In the first region of roller length, i.e. close to the jump toe, regardless of the inflow condition on both rough and smooth bed configurations, the Gamma distribution was the best fit for the instantaneous water surface profile. While in the third region of roller length as the end of roller, regardless of the inflow condition on both rough and smooth bed configurations, the lognormal distribution was the best fit.

In the second region of roller length, for $Fr_1 = 3.25$ on smooth bed as well as for $Fr_1 = 2.56$ on rough bed, the Gamma distribution was the best fit for the instantaneous water surface profile. For $Fr_1 = 2.87$ and 2.4 on rough bed, the best fit was the Normal distribution. Overall, for $Fr_1 > 2.5$, regardless of the bed type, all the statistical properties of the fluctuating impingement perimeter as well as the longitudinal profile of water surface were consistent along the transverse cross section. If compared with the results by Wang (2014) in Figure 4.17A and B, the trend of variation for both impingement perimeter and longitudinal profile of water surface was independent from the inflow conditions. This was confirmed from the data presented in Figures 4.19 and 4.20. The findings supported the assumption of quasi-two-dimensional flow in hydraulic jumps. It should be noted that the results herein presented were based upon a limited data set; duration of 10s and only three inflow Froude numbers were investigated on rough and one inflow Froude numbers was investigated on smooth bed configuration. More inflow condition as well as a longer duration of flow process should be considered to achieve more comprehensive results.

4.9 Summary

The flow patterns and free-surface dynamics in hydraulic jumps were studied based upon visual observations and non-intrusive free-surface measurements. Different types of hydraulic jumps corresponding to the inflow Froude number Fr_1 on both pebbled rough and smooth bed were presented. At the same inflow Froude number, pebbled rough bed resulted in larger undulations for $1.5 < Fr_1 < 2.1$ and higher air entrainment in the jump roller area for $2.1 < Fr_1 < 3.1$.

The basic flow properties including the free-surface profile, conjugate depths and jump roller length were found to be function of the inflow Froude number. A larger Froude number Fr_1 resulted in a larger conjugate depths ratio d_2/d_1 and in a longer roller L_r/d_1 and air flow L_{air}/d_1, with the same trends for both bed types. A smaller roller length was observed for rough bed due to the effect of the rough bed on the flow.

Boundary friction force and shear stresses were investigated based upon the free-surface data and momentum considerations.

The macroscopic fluctuating nature of hydraulic jumps was analysed based upon high-speed videos. Longitudinal jump toe oscillations were recorded between 0.5 and 0.7 Hz on rough bed and 0.4 and 0.9 Hz on smooth bed. The production rate of large vortices was found in a frequency range from 0.5 to 0.6 Hz on rough bed and from 0.6 to 1 Hz on smooth bed. The dimensionless frequencies were decreasing with increasing Froude number on both rough and smooth beds. The findings suggested some correlations between the jump toe oscillation and large vortex formation.

Comparable dimensionless velocities/celerities were observed for the vortex advection in the roller length. The velocities were constant independent of the Froude and Reynolds numbers on both bed types, with an average $U_{eddy}/V_1 = 0.43$ on smooth bed and $U_{eddy}/V_1 = 0.46$ on rough bed.

A survey of the fluctuations in impingement perimeter transverse profiles showed consistent statistical properties of longitudinally oscillating impingement positions across the central flow region on both bed types. Fluctuation of longitudinal water surface profile, extracted from side videos, showed the same trend on both bed types but a slightly higher standard deviation for smooth bed which was due to higher oscillation of water surface.

Probability density functions of instantaneous jump toe position as well as instantaneous water surface profile with the best distribution fit was presented on both rough and smooth bed configurations with different inflow Froude numbers.

5 BASIC PROPERTIES OF AIR-WATER FLOW

5.1 Presentation

The transition from supercritical flow to subcritical flow results as a hydraulic jump usually involves air entrainment. The process of flow aeration starts at the jump toe where the supercritical flow impinges into the jump roller as well as through the roller free-surface, associated with drastic splashing and surface deformation (Figure 5.1). The advection and diffusion of the entrapped air lead to a two-phase turbulent flow motion in the roller. This Chapter presents a physical study of the air-water flow properties in a classical hydraulic jump on pebbled rough bed. Void fraction, bubble count rate and interfacial velocity were measured in both supercritical and subcritical flow regions. At the end, comparative analysis of characteristic air-water flow depths were reported and discussed. The experimental results were compared with those on smooth bed as well as with those of previous literature studies.

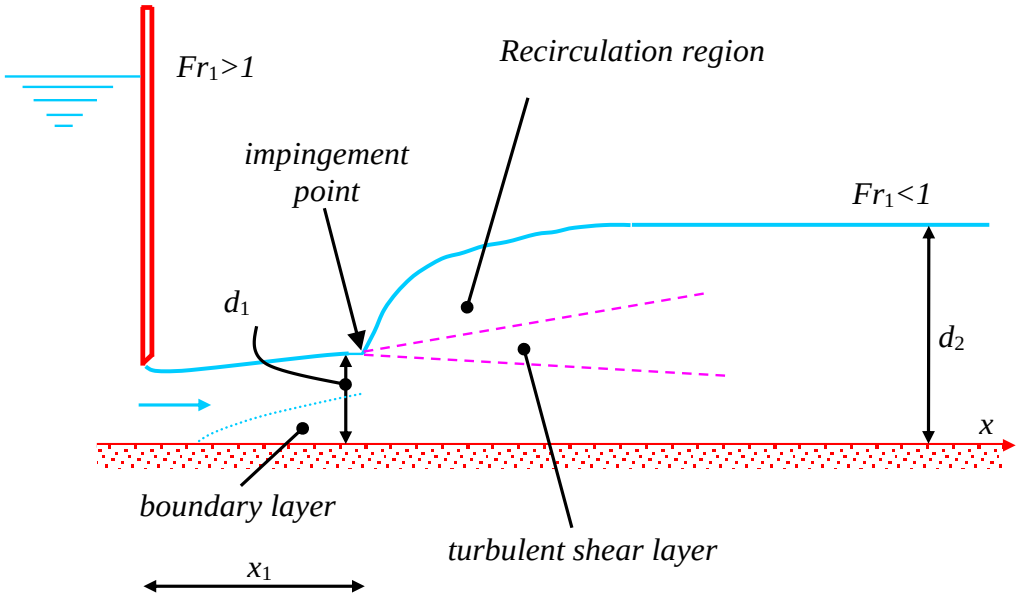

Figure 5.1 Air entrainment in classical hydraulic jumps with partially-developed inflow conditions (based on Gualtieri and Chanson 2007a)

5.1.1 Experimental flow conditions

The air-water flow properties were measured locally using a double-tip phase-detection

conductivity probe. The phase-detection probe was sampled at 20 kHz, for 90 or 180 seconds. Herein, the hydraulic jump was investigated on rough bed with various inflow Froude numbers in the range from 1.27 to 2.84 as well as on smooth bed with an inflow Froude number, Fr_1 = 2.84, as a reference (Table 5.1). An upstream gate opening h = 0.060 m was used on both bed types. The intake aspect ratio was h/W = 0.12 where W = 0.5 m was the channel width on smooth bed and h/W = 0.13 where W = 0.474 m was the channel width on rough bed. Measurements were collected at eight longitudinal cross sections on the channel centerline, one upstream of and seven sections downstream of jump toe position. The flow conditions and measurement properties are listed in Table 5.1, where x_1 is the longitudinal jump toe position, d_1 is the inflow depth, and V_1 is the average inflow velocity: $V_1 = Q/(W \times d_1)$.

Table 5.1 Summary of flow conditions for basic air-water flow measurements

Experiment	Bed type	h_1 (m)	Q (m^3/s)	Fr_1	Re_1	Sampling duration (s)	Instrumentation
Air entrainment properties	smooth	0.06	0.078	2.84	1.7E+5	90	Double tip phase detection probe
	rough	0.06	0.06	1.70	1.4E+5	90	
			0.07	1.96	1.6E+5	180	
			0.10	2.84	2.2E+5	180	

5.2 Air-flow properties in supercritical flow

5.2.1 Time-averaged void fraction

A key air-water flow property is the air concentration C, i.e. the time-averaged void fraction at a position (x, y) within the flow. The time-averaged void fraction C was deduced from the time series of instantaneous void fraction signals recorded by the phase-detection probe. As observed by Felder and Chanson (2016), the shape of the void fraction distributions was very similar to the profiles observed in self-aerated spillway flows, with an S-shape profile and low void fractions close to the channel bed (Straub and Anderson 1958, Cain and Wood 1981, Felder and Chanson 2013, Kramer and Chanson 2018). The present data compared well with a solution of the advection-diffusion equation (ADE) developed for air-water skimming flows on stepped spillways (Chanson and Toombes 2002):

$$C = 1 - \tanh^2\left(K' - \frac{\frac{y}{Y_{90}}}{2 \times D_o} + \frac{\left(\frac{y}{Y_{90}} - \frac{1}{3}\right)^3}{3 \times D_o}\right) \quad \text{for } 0 < y < Y_{90} \quad (5.1)$$

where K' is an integration constant and D_o is a function of the mean air concentration C_{mean} only:

$$K' = K^* + \frac{1}{2 \times D_o} - \frac{1}{81 \times D_o} \quad (5.2)$$

$$C_{mean} = 0.7622 \times (1.0434 - \exp(-3.614 \times D_o)) \quad (5.3)$$

$$C_{mean} = \frac{1}{Y_{90}} \int_{y=0}^{y=Y_{90}} C \times dy \quad (5.4)$$

where $k^* = tanh^{-1}(0.1)^{0.5} = 0.3274$. Typical void fraction distributions upstream of the hydraulic jump toe are shown in Figure 5.2 for the rough bed configuration and compared to the smooth bed data. The experimental data are presented as functions of the dimensionless vertical elevation y/d_1. The data showed the strong pre-aeration of the flow on rough bed with the increasing Fr_1, although surface waves might have some impact on the void fraction profiles (Toombes and Chanson 2007).

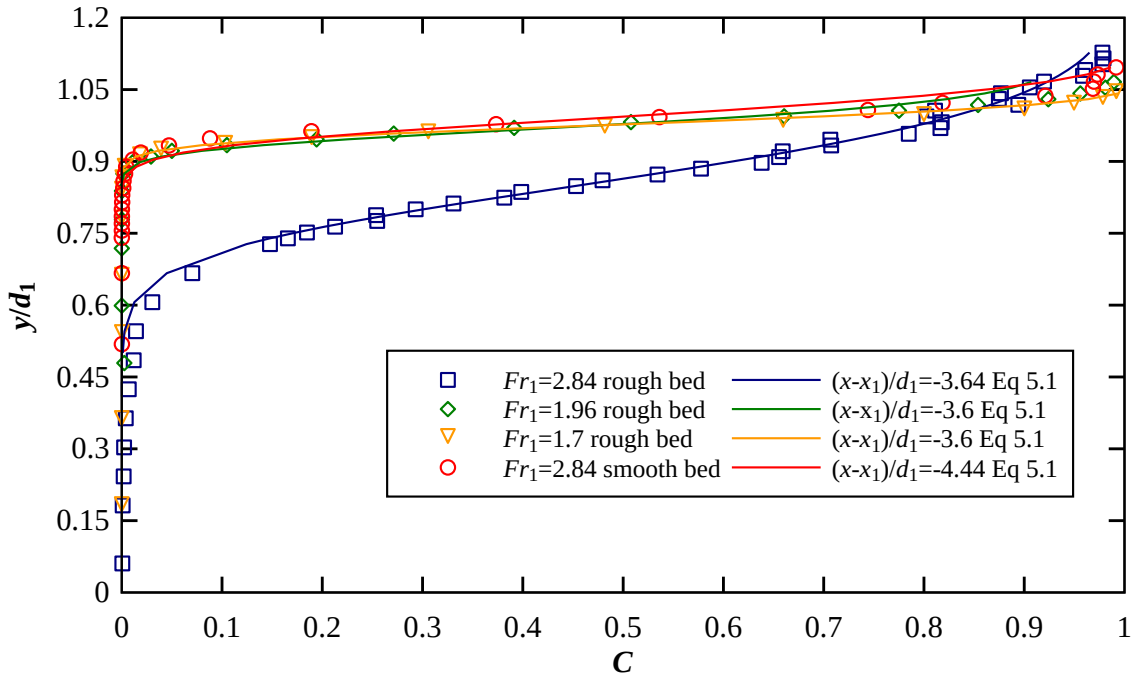

Figure 5.2 Void fraction distributions upstream of hydraulic jump on both rough and smooth beds gate opening h = 0.06 m, comparison with the advection-diffusion equation (Equation 5.1)

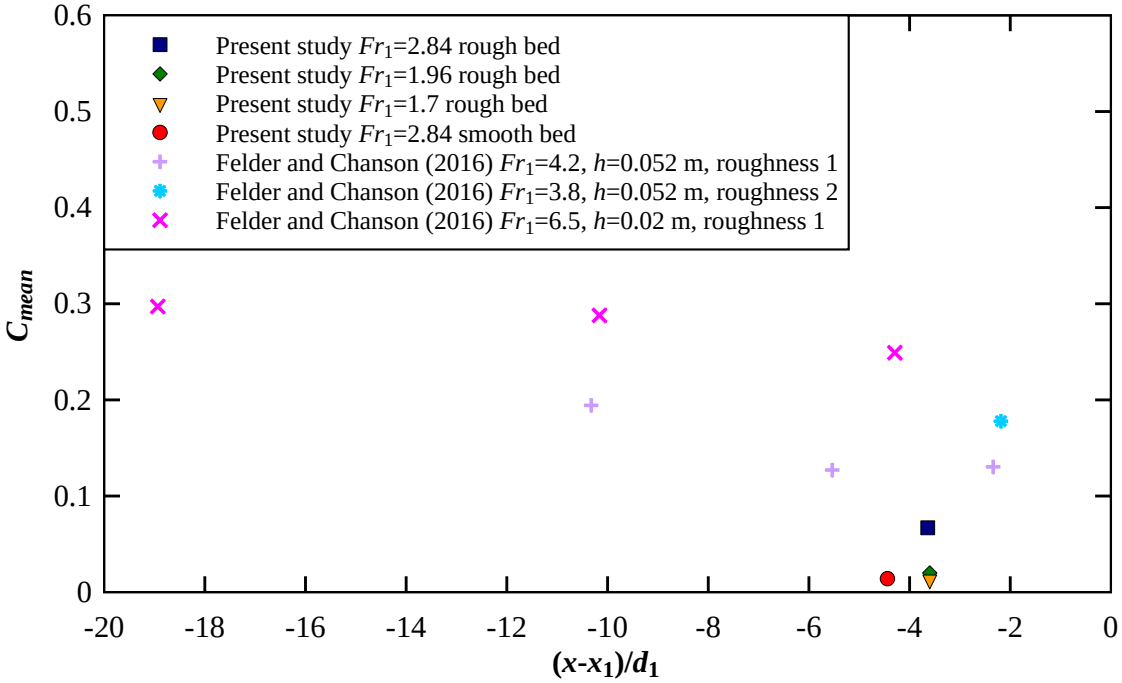

Figure 5.3 Mean void fractions upstream of hydraulic jump, gate opening h = 0.06 m for present study or both rough and smooth beds, compared with the data with Felder and Chanson (2016)

The longitudinal distribution of mean void fraction C_{mean} in the supercritical inflow is presented in Figure 5.3. In comparison to Felder and Chanson (2016) data, an increase in gate depth and depth, respectively, decreased the overall flow aeration, confirming visual observation (Chapter 4). A marked increase in pre-aeration was also observed with an increase in channel bed roughness. This is consistent with Felder and Chanson (2016). For the same bed roughness, the aeration increased with increasing inflow Froude number.

5.2.2 Bubble count rate

The dimensionless bubble count rate distributions in the supercritical flows were analysed for both rough and smooth beds with the same gate opening, h = 0.06 m (Figure 5.4). Overall, the bubble count rate distributions showed a sharp increase of bubble count rates from close to zero at the channel bed to a distinct maximum in a flow region where $C \approx 0.5$. Then, it decreased sharply in the upper flow region close to the free-surface. For Fr_1 = 2.84 on rough bed, the number of air bubbles was comparatively larger in the bubble flow region that at lower levels, highlighting the strong pre-aeration of the flow. The shape of the distributions was consistent with observations on hydraulic jump, spillways, and plunging jets (Chanson 1997a; Chanson and Toombes 2002, Felder and Chanson 2016). The flow on the rough bed

showed larger numbers of bubbles for all the inflow Froude numbers.

The local maximum bubble count rates on both rough and smooth bed are presented in Figure 5-5. The data showed a larger bubble count on the rough bed with higher inflow Froude number. This is consistent with the larger air entrainment observed with the increasing roughness.

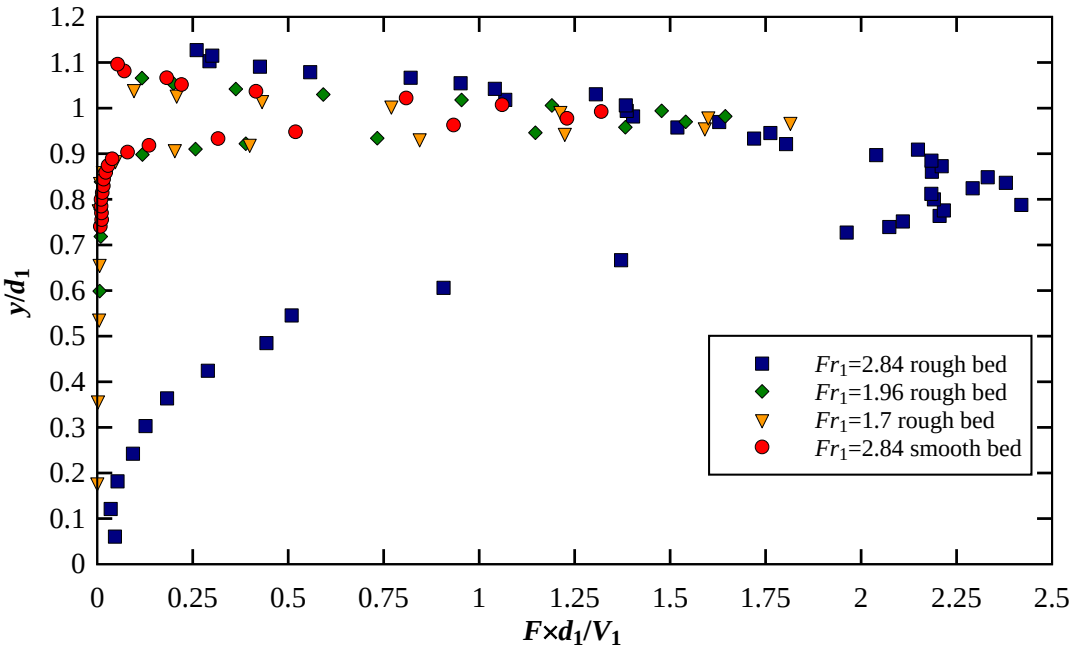

Figure 5.4 Bubble count rate distributions upstream of the hydraulic jump

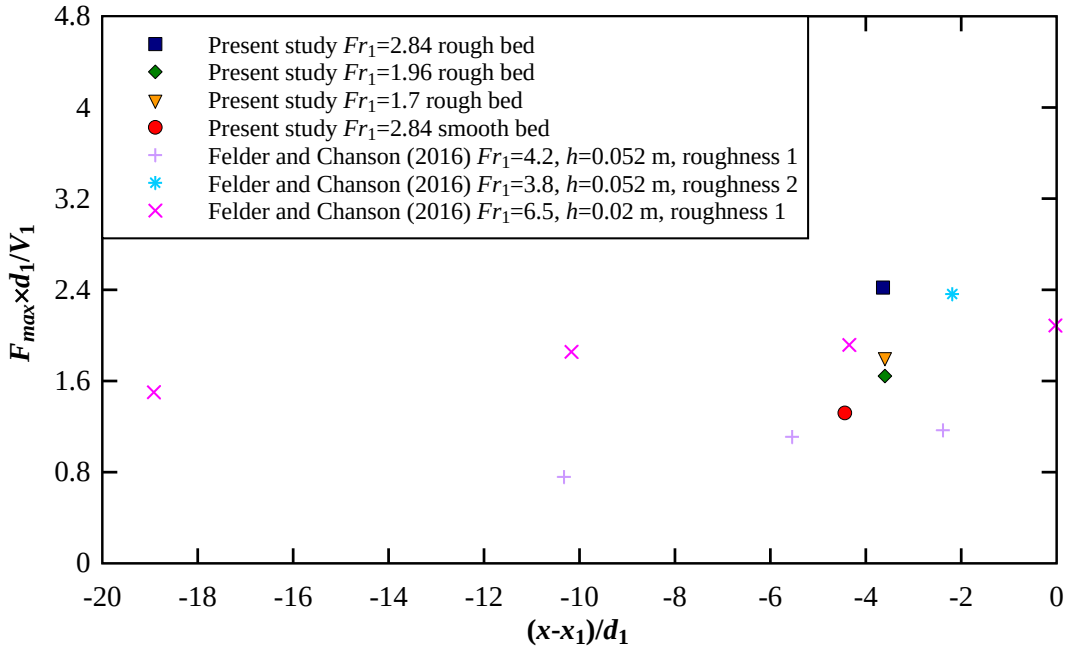

Figure 5.5 Maximum bubble count rate distributions upstream of the hydraulic jump

Furthermore, the local bubble count rate maximum for all rough beds was comparatively higher than that on smooth bed. A comparison between present results and the data of Felder and Chanson (2016, 2018) indicated a higher bubble count rate on pebbled rough bed.

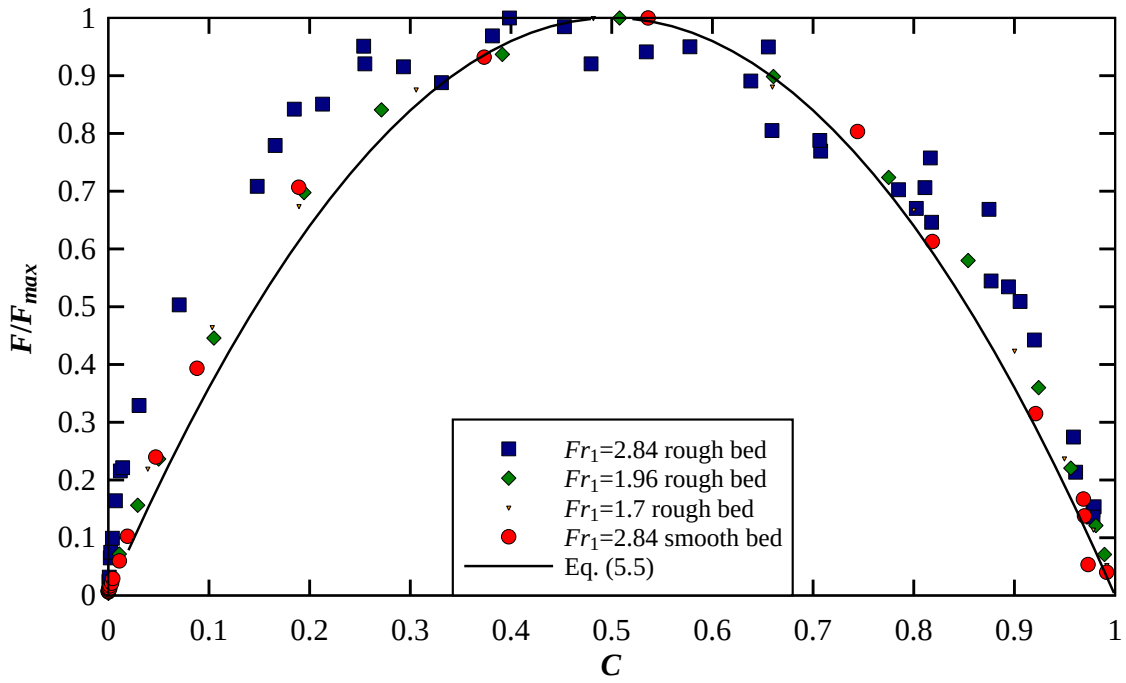

Figure 5.6 Dimensionless relationship between bubble count rate and void fraction upstream of the hydraulic jump

Typical dimensionless bubble count rate distributions F/F_{max} as functions of void fraction C are presented in Figure 5.6. The data were included three inflow Froude numbers on rough bed and one on smooth bed, at upstream of hydraulic jump, x-x_1 = -0.9 m. All the present data suggested that the bubble frequency distributions were correlated reasonably well by a parabolic law:

$$\frac{F}{F_{max}} = 4C(1-C) \tag{5.5}$$

where C is the time-average void fraction and F_{max} is the cross-sectional maximum bubble count rate. Such a parabolic relationship was previously observed in a number of other air–water flows, including supercritical open channel flows, two-dimensional free-falling jets and within the turbulent shear region of hydraulic jumps (Chanson 1997, Chanson and Toombes 2002, Toombes and Chanson 2007 and 2008, Wang 2014). The result showed the higher bubble count rate on rough bed for larger inflow Froude number. For $Fr_1 < 2$ on rough bed as well as for $Fr_1 = 2$ on smooth bed, the dimensionless bubble count rate distributions

completely corresponded to the parabolic curve since the remarkable bubble count rate observed only near the surface (Figure 5.4). While for Fr_1 = 2.84 on rough bed, some oscillations were observed around the parabolic curve which could be due to notable bubble count rates for the whole depth of flow (Figure 5.4).

5.2.3 Interfacial velocity

The interfacial velocity was measured with the double-tip conductivity probe based upon a cross-correlation technique. The interfacial velocity distributions in the supercritical flows are illustrated in Figure 5.7 in dimensionless terms as V/V_{90} where V_{90} is the interfacial velocity where C = 0.9. The data are shown separately on both rough and smooth bed configurations. Some scatter of experimental data was observed for all flow conditions. The distributions were different from the typical velocity profiles downstream of the hydraulic jump in terms of magnitudes close to the bed and absence of negative velocities (Section 5.3.6) as seen on rough bed in Felder and Chanson (2016). For all flow conditions, the flow velocities appeared fully developed furthest away from the sluice gate. The difference in interfacial velocity distributions between the rough and smooth bed types suggested that roughness enhanced momentum transfer in the boundary layer and hence the boundary layer growth.

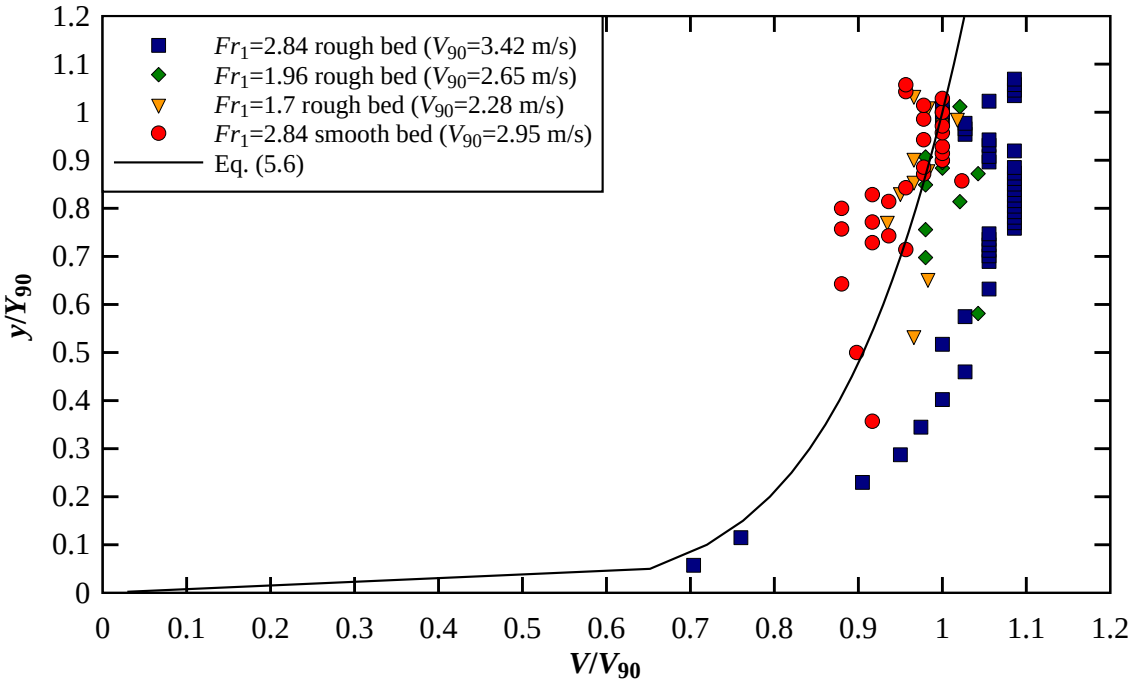

Figure 5.7 Interfacial velocity distributions upstream of hydraulic jump on both rough and smooth beds

These dimensionless velocity distributions are comparable well with a simple power law:

$$\frac{V}{V_{90}} = \left(\frac{y}{Y_{90}}\right)^{\frac{1}{n}} \qquad 0 < y < Y_{90} \qquad (5-6)$$

where n is equal to 7 on rough bed.

Felder and Chanson (2013) found that the power law exponent on stepped spillways was $n \approx 10$. It appeared that the roughness enhanced the momentum transfer into the boundary layer and hence resulted in the growth of the boundary layer.

Table 5.2 presents the data of the dimensionless characteristic interfacial velocity V_{90}/V_1 and the dimensionless depth-averaged flow velocity U_w/V_1. Note that U_w was calculated based on $U_w = q_w/d$ where q_w is the discharge per unit width (m^2/s) and d is the equivalent clear-water flow depth. The data showed that the interfacial velocities V_{90}/V_1 observed on rough bed were larger than those on smooth bed. This was in agreement with the strong velocity gradient between channel bed and free-stream. Furthermore, the comparison showed a strong effect of the roughness upon the velocity distribution. The higher magnitude of U_w/V_1 on rough bed demonstrated the larger rate of bubble count on rough bed since the U_w was derived based on equivalent clear-water flow depth.

Table 5.2 Characteristic velocities upstream of hydraulic jump

Study	Bed type	Fr_1	$(x-x_1)/d_1$	V_{90}/V_1	U_w/V_1
Present	pebbled	2.84	-3.64	1.35	1.16
		1.96		1.5	1.07
		1.7		1.48	1.06
	smooth	2.84	-4.44	1.23	1.04
Felder and Chanson 2016	roughness 1	4.2	-10.32	1.12	1.03
			-5.57	1.12	1.02
			-2.28	1.12	1.0
	roughness 1	6.5	-19.01	1.26	1.23
			-10.13	1.2	1.12
			-4.3	1.15	1.0
	roughness 2	3.8	-2.14	1.3	1.0

5.3 Air-flow properties in the hydraulic jump flow

5.3.1 Time-averaged void fraction

The time-averaged void fraction measurements were performed on the channel centerline, at several vertical cross sections downstream of the jump toe x_1. The present data sets with the

rough and smooth beds were compared to previous hydraulic jump data on smooth and rough beds with similar inflow Froude numbers. The present comparison is limited to the basic air-water flow properties.

Figures 5.8A to 5.8D present the void fraction profiles for different inflow Froude numbers with the same inflow length x_1/h = 16.67 on both rough and smooth beds. Each graph shows the void fraction profiles at several longitudinal positions downstream of jump toe position. Analytical solutions were given by Equations 2.4 and 2.5 for the turbulent shear layer and the recirculation region, respectively, are plotted for comparison. The full data set is available in the digital appendix.

The experimental data showed a similar void fraction for inflow Froude number larger than 2 on both rough and smooth bed. For inflow Froude number less than 2 (Figures 5.8B and 5.8C) the void fraction in the shear region was very low because of lower bubbly flow, as presented in Chapter 4. In the recirculation zone, close to the water surface, it started to increase suddenly.

A characteristic void fraction C^*, defined as the local minimum void fraction at the boundary between shear and recirculation regions (Figure 2.1), identified the virtual boundary that divided the void fraction profile into two parts; the turbulent shear region below and recirculation region above this elevation y^*. For an inflow Froude number larger than 2 on both rough and smooth beds (Figures 5.8A and 5.8D), all the void fraction distributions had comparable shapes independently of the bed roughness. The void fraction profile exhibited a maximum C_{max} in the turbulent shear region ($0 < y < y^*$) and a rapid increase from C^* to unity in the recirculation region ($y > y^*$).

For an inflow Froude number lower than 2 (Figures 5.8B and 5.8C) no local void fraction maximum C_{max} was observed in the turbulent shear region. For each experimental flow condition with $Fr_1 > 2$, the profile shape varied significantly with increasing longitudinal positions in the shear region, while relatively consistent trends were seen in the upper free-surface region. For $Fr_1 > 2$, the results showed similar void fraction profiles in the upper free-surface region.

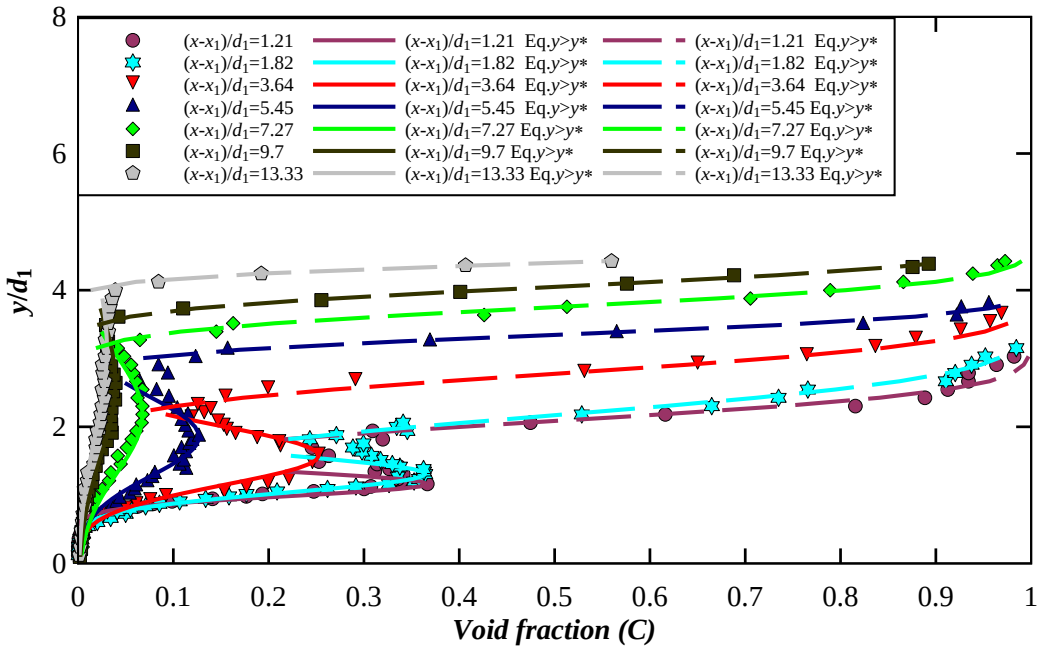

A: Rough bed, Run BR3, Q = 0.1 m^3/s, d_1 = 0.0825 m, Fr_1 = 2.84, Re_1 = 2.2E+5

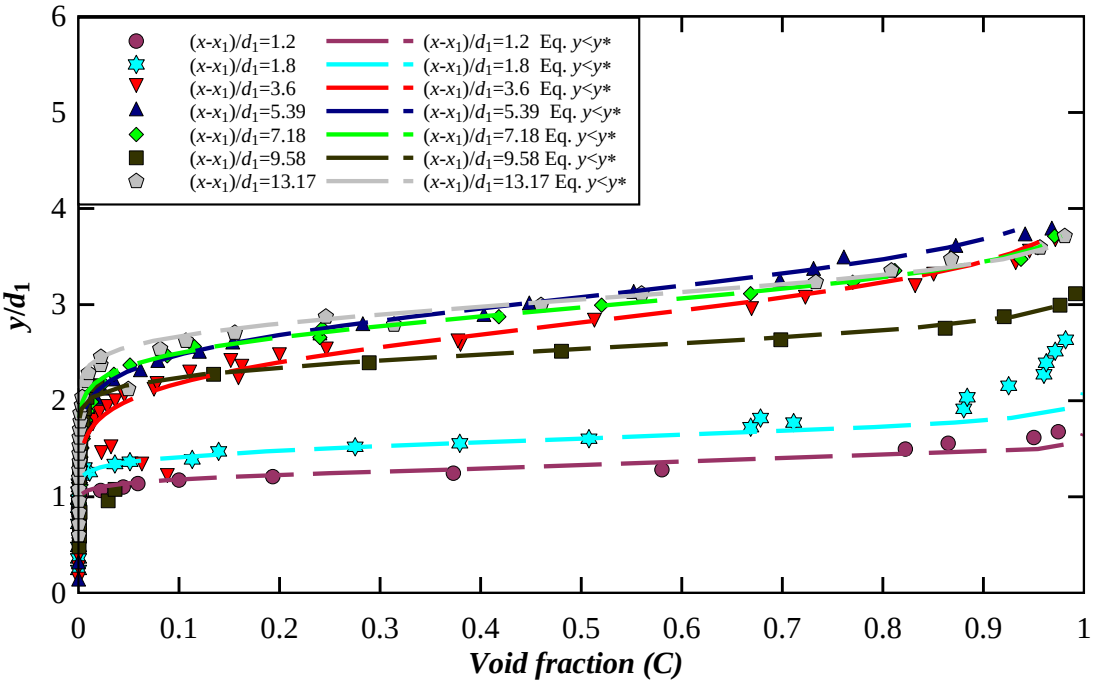

B: Rough bed, Run BR2, Q = 0.07 m^3/s, d_1 = 0.0835 m, Fr_1 = 1.96, Re_1 = 1.6E+5

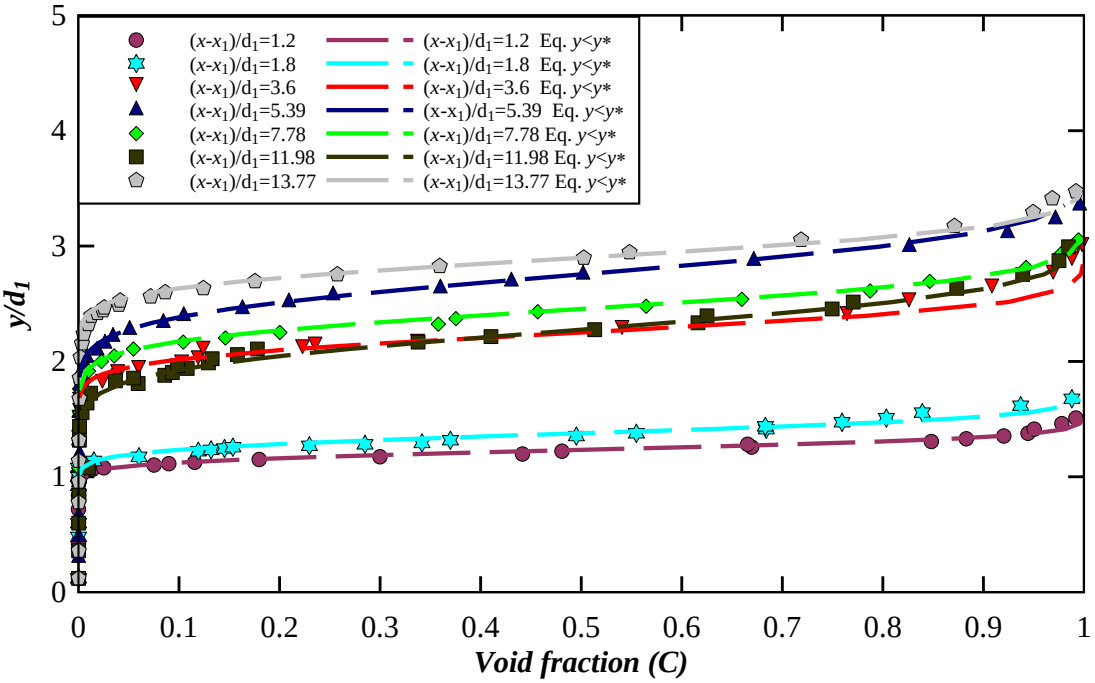

C: Rough bed, Run BR1, Q = 0.061 m^3/s, d_1 = 0.0835 m, Fr_1 = 1.7, Re_1 = 1.4E+5

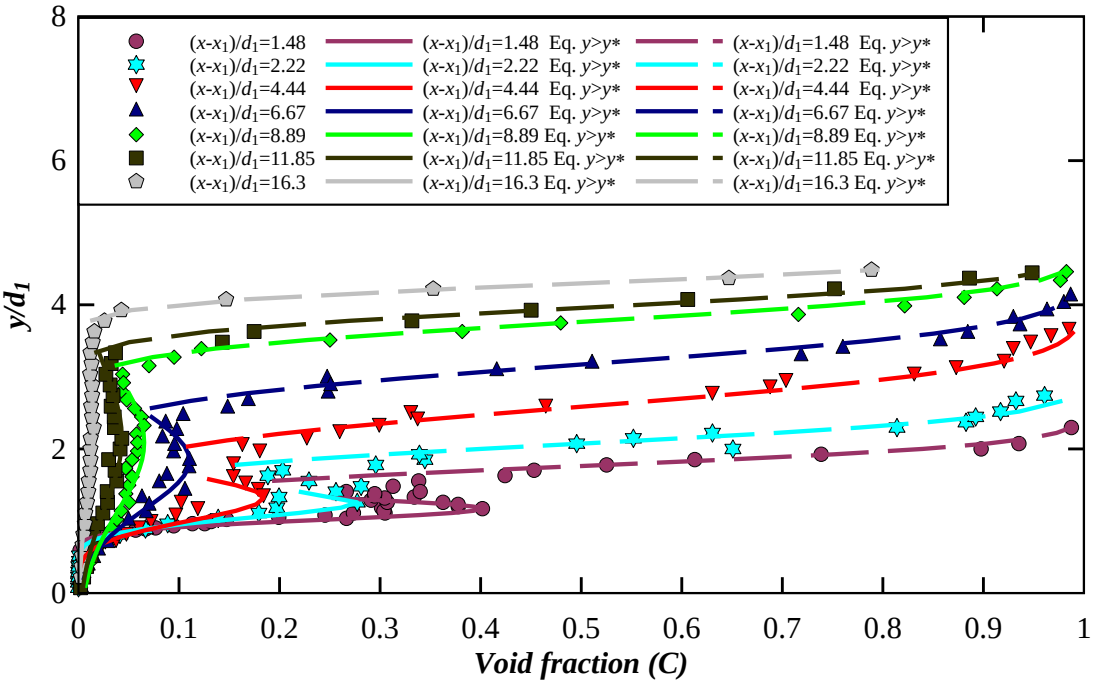

D: Smooth bed, Run BS1, Q = 0.078 m^3/s, d_1 = 0.0675 m, Fr_1 = 2.84, Re_1 = 1.7E+5

Figure 5.8 Time-averaged void fraction profiles on the channel centerline, comparison with analytical solution on both rough and smooth beds

The comparison of void fraction data between rough and smooth channel beds for the same

inflow Froude number Fr_1 = 2.84, suggested that the distributions of maximum void fraction C_{max} within the shear layer region were comparable, so that close to jump to C_{max} was 0.4 and 0.37 at x-x_1/d_1 = 1.21 and 1.48 on rough smooth and bed respectively (Figure 5.8A and D).
The dimensionless vertical elevation y/d_1 of local minimum void fraction values C* was higher on the rough bed so that close to the jump toe, at first three cross-sections, y/d_1 was 1.7, 1.81, 2.17 and 1.41, 1.63, 1.76 on rough and smooth beds, respectively. This demonstrated that the higher inflow Reynolds number on rough bed with the same inflow Froude number was associated with the upward shifting of the vertical elevation of C* (Figure 5.8A and D). In turn, this resulted in the upward shift of the turbulent shear region with the increasing bed roughness indicating that an increase in roughness resulted in shorter jump roller length.

The longitudinal distributions of the void fraction were comparable (Figure 5.8A and D) for Fr_1 = 2.84 on both rough and smooth bed configurations. While for Fr_1 < 2 on rough bed, the same trend of variation for C was observed. Due to the undular type of hydraulic jump and low aerated flow there was no maximum void fraction in the shear region (Figure 5.8B and C). On rough bed, differences in the recirculation region in the middle of the roller with elevated levels of void fraction demonstrated a lower aeration of the free-surface region (Figure 5.8A, B, and C). As discussed in Section 4.2, the increase in Fr_1 on rough bed resulted in a stronger bubbly flow. Furthermore, for Fr_1 < 2 the type of hydraulic jump was undular. There was no significant differences between the values of C_{max} and C* on rough and smooth beds with same inflow Froude number, C_{max} = 0.37, 0.36, 0.25 and C* = 0.25, 0.24, 0.12 on rough bed and C_{max} = 0.4, 0.28, 0.18 and C* = 0.27, 0.19, 0.15, for the first three cross-sections close to jump. However, the rate of bubbles should be considered. The bubble count rate will be presented in the next Section.
All the findings were in agreement with the results of Felder and Chanson (2016, 2018), who compared rough bed (rubber mat roughness) with smooth bed. In the presents study a comprehensive analysis was carried out to find out the differences between air-flow parameters on pebbled rough bed, smooth bed, and rubber mat bed.

The longitudinal distribution of the vertical profile of the void fraction on both rough and smooth beds with an inflow Froude numbers Fr_1 = 2.84 is presented in Figure 5.9. The data, as well as the visual observations (Section 4.2), showed a longer bubbly flow region on rough bed. For 5 < (x-x_1)/d_1 < 9 downstream of the jump toe, the value of C in the shear region was

slightly higher on rough bed. While for $(x\text{-}x_1)/d_1 > 9.0$ downstream of the jump toe, on both rough and smooth beds, the void fraction C was almost zero.

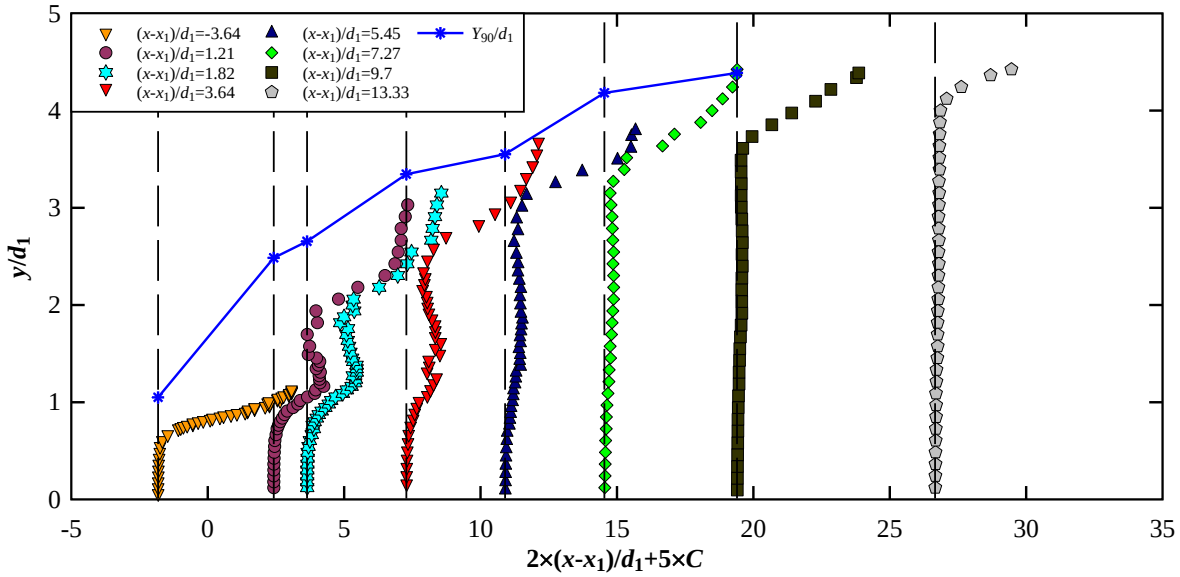

A: Rough bed, Run BR3, Q = 0.1 m^3/s, d_1 = 0.0825 m, Fr_1 = 2.84, Re_1 = 2.2E+5

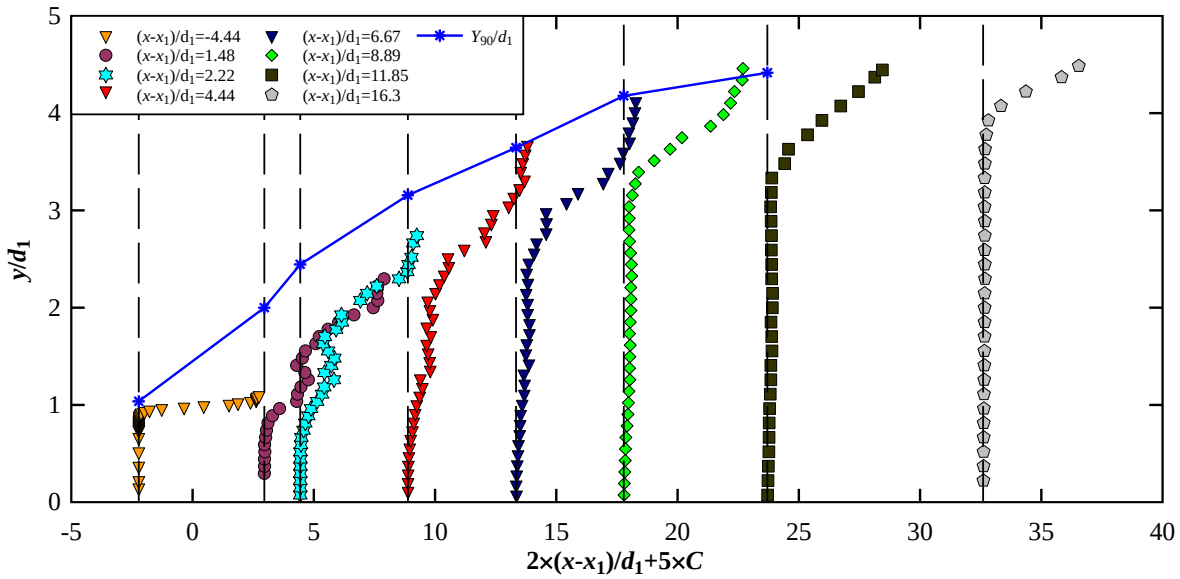

B: Smooth bed, Run BS1, Q = 0.078 m^3/s, d_1 = 0.0675 m, Fr_1 = 2.84, Re_1 = 1.7E+5

Figure 5.9 Void fraction distributions in hydraulic jump, comparison with the characteristic flow depth Y_{90}/d_1

5.3.2 Comparison of characteristic void fraction parameters

In hydraulic jumps with partially-developed inflow conditions, the void fraction distributions showed a characteristic shape in the developing shear layer with a local maximum in void fraction (Resch and Leutheusser 1972, Thandaveswara 1974, Chanson 1995). Several characteristic parameters of void fraction distributions were investigated in this section. The depth-averaged void fraction C_{mean} (Equation 5.4) is shown in Figure 5.10 as a function of the dimensionless distance from the jump toe position $(x\text{-}x_1)/d_1$ (Figure 5.10A) and as a function of relative longitudinal position to jump roller length $(x\text{-}x_1)/L_r$ (5.10B). The colored filled symbols are the present data. The present data were compared well with previous data with the same Froude number range and with the empirical correlation of Wang (2014). Wang (2014) proposed the following best fit for the depth-averaged void fraction, based upon experiments performed for $3.8 < Fr_1 < 10$:

$$C_{mean} = 0.45 \times \exp\left(-\frac{1}{3.33 \times (Fr_1 - 1)} \times \frac{x - x_1}{d_1}\right) \qquad 3.4\times10^4 < Re_1 < 1.6\times10^5 \qquad (5.6)$$

$$C_{mean} = 0.45 \times \exp\left(-1.8 \times \frac{x - x_1}{L_r}\right) \qquad 0.05 < (x\text{-}x_1)/L_r < 1 \qquad (5.7)$$

Though the empirical correlation was valid for $3.8 < Fr_1 < 10$, the comparison of present data with empirical correlation with the data of Wang (2014) showed a good agreement.

The longitudinal variation of C_{mean} was independent of bed roughness so that the mean void faction decreased with increasing distance from the jump toe. This trend was observed in all the experiments. An empirical equation was developed for rough bed including bed roughness for $0 < (x\text{-}x_1)/d_1 < 20$ and $2.8 < Fr_1 < 4.3$:

$$C_{mean} = k \exp\left(-\frac{1}{3.8 \times (Fr_1 - 1)} \times \frac{x - x_1}{d_1}\right) + \left(0.05 \exp\left(\frac{K_s}{d_1}\right)^{0.3}\right) - b \qquad (5.8)$$

where for smooth and pebbled rough bed: $k = 0.3$ and $b = 0.03$, while for uniform rough bed: $k = 0.1\ Fr_1$ and $b = 0.18(K_s/d_1)$. For the present rough bed with $Fr_1 = 2.84$, Equation (5.8) yielded: $R = 0.95$, $SE^1 = 0.03$.

[1] Standard Error

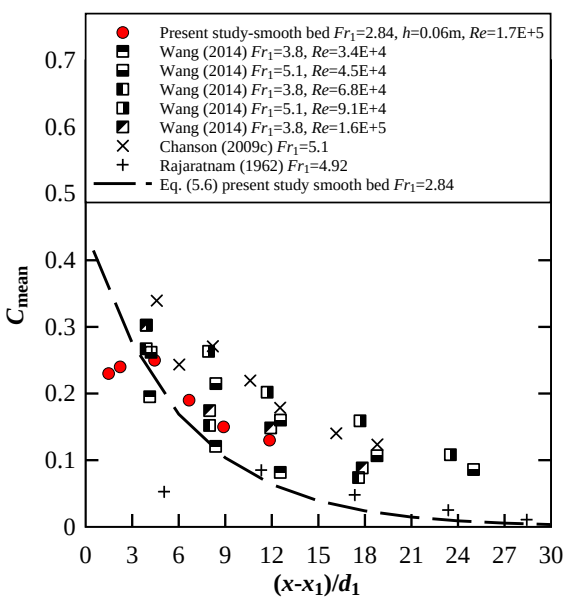

A: Dimensionless longitudinal distribution of the depth-averaged void fraction, smooth bed

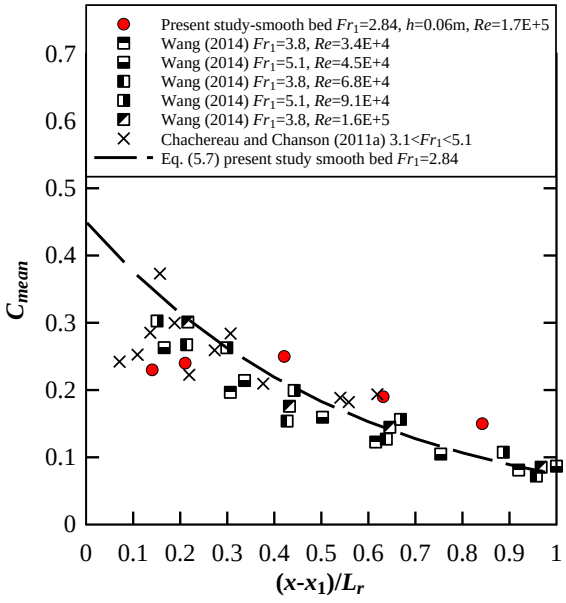

B: Dimensionless longitudinal distribution related to the dimensionless roller length of the depth-averaged void fraction, smooth bed

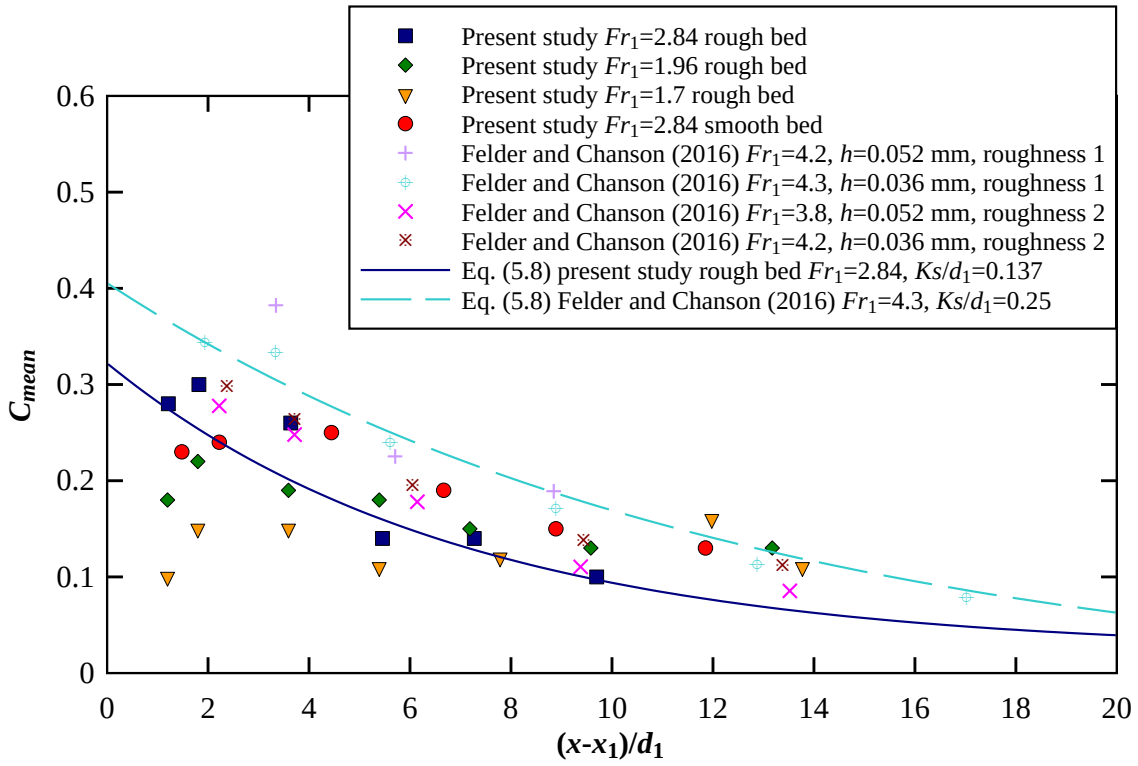

C: As functions of dimensionless longitudinal jump toe position, rough bed

Figure 5.10 Depth-averaged void fraction C_{mean}

Equation (5.8) is plotted in Figure 4.10C for present rough bed with Fr_1 = 2.84 and K_s/d_1 =

0.137 and for rough bed data of Felder and Chanson (2018) for Fr_1 = 4.3 and K_s/d_1 = 0.25. Equations (5.6) - (5.8) implied a relative high de-aeration rate close to the jump toe. The depth-averaged void fraction decreased exponentially along the roller with C_{mean} = 0.1 next to the end of roller ((x-x_1)/L_r = 1) on both rough and smooth bed configurations. Equation (5.8) suggested an approximate depth-averaged void fraction at the jump toe C_{mean} (x = x_1) = 0.45 on smooth bed and C_{mean}(x = x_1) = 0.32 for the present pebbled rough bed. These void fractions may be considered as the percent of entrained air at the jump toe and free-surface aeration of the supercritical impinging flow. The mean void fraction in the supercritical flow upstream of the jump toe was found to be around 0.07 and 0.02 for rough and smooth bed respectively, hence negligible (Figure 5.3). Considering this assumption, the other percent of air entrapped through the roller length was higher on rough bed.

A comparison between the depth-averaged void fraction on rough bed with smooth channel bed and the data of Wang (2014) suggested that for all the inflow Froude numbers on rough bed the trend of variation for C_{mean} was similar (Figure 5.10C). Equations (5.6) - (5.8) demonstrated that the rate of longitudinal decay in C_{mean} was associated with the length of jump roller which was only a function of the inflow Froude number for smooth bed while it was function of the inflow Froude number and roughness on rough bed. For the same inflow Froude number Fr_1 = 2.84, the same trend of variation for C_{mean} was observed on both rough and smooth beds and, as expected, the higher magnitudes were associated with the rough bed configurations. On rough bed, the longitudinal position of maximum C_{mean} was closer to the jump toe demonstrating that air entrainment on rough bed was faster to reach the maximum air entrainment level. C_{mean} reached the maximum value in second cross-section after jump toe, (x-x_1/d_1) = 1.81, 1.8, and 1.8 for Fr_1 = 2.84, 1.96, and 1.7 respectively, because of the larger air entrainment into the flow, then decreased until the end of roller. For Fr_1 < 2 on rough bed, further downstream a longitudinal oscillation in C_{mean} magnitude was observed which could be related to flow depth oscillation (Section 4.2). For 2 < (x-x_1)/d_1 < 14, C_{mean} on the present rough bed with Fr_1 = 2.8 and on the second roughness type of Felder and Chanson (2016) with Fr_1 = 3.8 had a similar trend of variation, but with different gate opening, h = 0.052 m. The advective diffusion of air bubbles within large-scale vortical structures was considered as the basis of two-phase shear flow. Wang (2014) observed that the core of the highly-aerated vortices resulted in a maximum void fraction C_{max} in the turbulent shear region (0 < y < y*). With increasing distance from the jump toe, the longitudinal distribution of void fraction profile suggested a decrease in C_{max}, as the air

bubbles were advected and dispersed in the flow. As observed by Chanson and Brattberg (2000) and Murzyn et al. (2007), the corresponding vertical position Y_{Cmax} increased due to the influence of buoyancy and the interactions between the enlarged vortices and the channel bottom (Figures 5.11 and 5.12). The higher magnitude of Y_{Cmax} observed on rough bed (Section 5.3.1) could be caused by the larger rate of interactions between the enlarged vortices and channel bottom. Figure 5.11 presents the distribution of maximum void fraction data C_{max} as a function of the dimensionless longitudinal position $(x\text{-}x_1)/d_1$ (Figures 5.11A, smooth bed, and 5.11C, rough bed) and of the relative position in the jump roller $(x\text{-}x_1)/L_r$ (Figures 5.11B, smooth bed, and 5.11D, rough bed). The present study was compared with previous literature studies and the data of Wang (2014). Wang (2014) proposed the following best fit for the depth-averaged local maximum void fraction:

$$C_{max} = 0.5 \times \exp\left(-\frac{1}{1.8 \times (Fr_1 - 1)} \times \frac{x - x_1}{d_1}\right) \quad (5.9)$$

$$C_{max} = 0.5 \times \exp\left(-3.4 \times \frac{x - x_1}{L_r}\right) \quad 0 < (x\text{-}x_1)/L_r < 1 \quad (5.10)$$

These equations are based upon experiments performed for $3.8 < Fr_1 < 10$ and $3.4 \times 10^4 < Re_1 < 1.6 \times 10^5$.

Considering Equation (5.9) for smooth bed, empirical equations were developed for C_{max} and C^* on rough bed including bed roughness for $0 < (x\text{-}x_1)/d_1 < 20$ and $2.8 < Fr_1 < 4.3$:

$$C_{max} = 0.5 \exp\left(-\frac{1}{1.8 \times (Fr_1 - 1)} \times \frac{x - x_1}{d_1}\right) + \left(0.03 \exp\left(\frac{K_s}{d_1}\right)^{0.4}\right) \quad (5.11)$$

$$C^* = k \exp\left(-\frac{1}{1.8 \times (Fr_1 - 1)} \times \frac{x - x_1}{d_1}\right) + \left(0.06 \exp\left(\frac{K_s}{d_1}\right)^{0.2}\right) - b \quad (5.12)$$

where in Equation (5.12) for smooth and pebbled rough bed: $k = 0.32$ and $b = 0.0$ while for uniform rough bed: $k = 0.11 Fr_1$ and $b = 0.045$. For the present rough bed with $Fr_1 = 2.84$, Equation (5.11) yielded: $R = 0.98$, $SE = 0.03$ and Equation (5.12) yielded: $R = 0.98$, $SE = 0.015$.

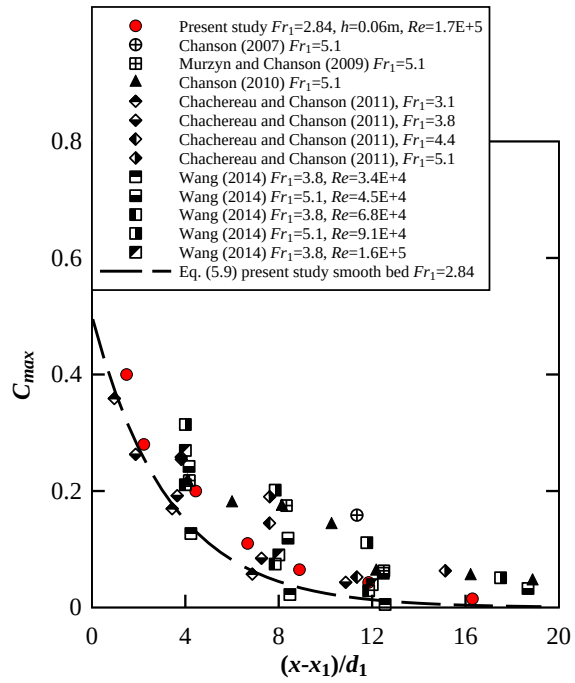

A: Dimensionless longitudinal distribution of the maximum void fraction, smooth bed

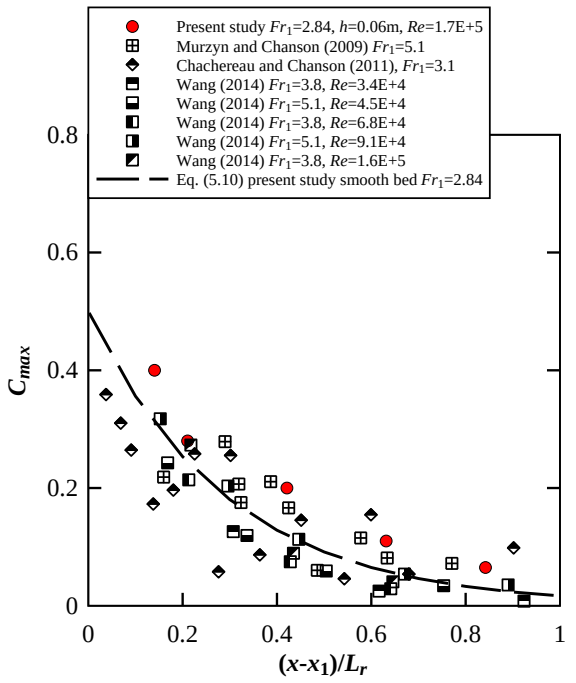

B: Dimensionless longitudinal distribution related to the dimensionless roller length of the maximum void fraction, smooth bed

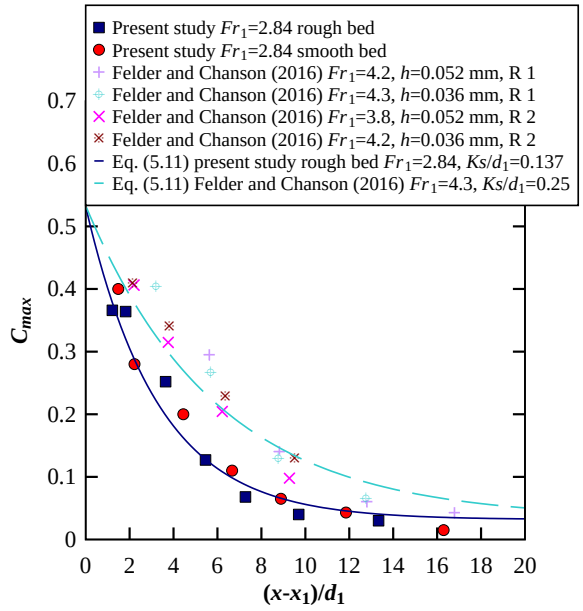

C: Dimensionless longitudinal distribution of the maximum void fraction, rough bed

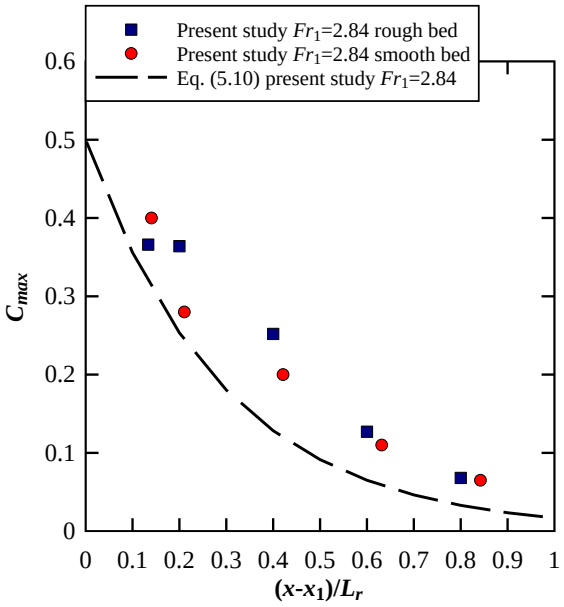

D: Dimensionless longitudinal distribution related to the dimensionless roller length of the maximum void fraction, rough bed

Figure 5.11 Longitudinal variation of the maximum void fraction $C_{max,}$ comparison with previous studies, *R*1 and *R*2 roughness types 1 and 2 of Felder and Chanson (2016)

As shown in Figure 5.11, a good agreement could be observed between all the datasets on both rough and smooth bed configurations. Different decay rates were observed between different Froude numbers, with a similar trend for all the cases, from the jump toe to the end of the roller. Considering the present results and the data from Felder and Chanson (2016), the maximum void fraction near jump toe was independent of inflow Froude and Reynolds number and its magnitude was restricted to 0.42. In both the present study and that of Felder and Chanson (2016), the magnitude of C_{max} on rough bed was higher than the data by Wang (2014) on smooth bed. This suggested that the maximum void fraction was higher on rough bed. Based on Figures 5.11B and 5.11D, all data exhibited slightly higher decrease in the first half roller. C_{max} approached zero at the end of roller as most air bubbles were released to the free-surface or dispersed in the water column. Air bubbles were transported within the vertical cross-section, up to the free-surface by buoyancy. There was no significant difference between rough and smooth bed configurations. Overall, the trend in terms of C_{mean} and C_{max} was similar on both smooth and rough bed configurations (Figures 5.10 and 5.11). The differences in terms of local void fraction minimum, C^*, between smooth and rough bed hydraulic jumps are presented in Figure 5.12. The pebbled rough bed had no significant effect on C^*, while uniform rubber mat bed type (Felder and Chanson 2016) resulted in higher magnitudes of C^*.

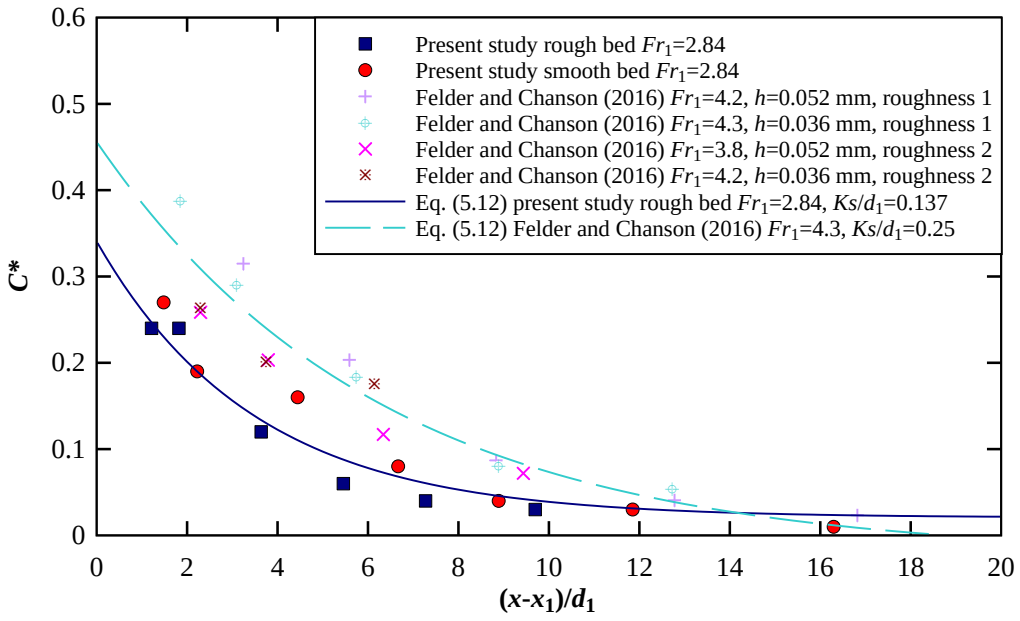

Figure 5.12 Local void fraction minimum at boundary of shear and recirculation regions in the hydraulic jumps on both smooth and rough beds, comparison with Felder and Chanson (2016, 2018) on rough bed

The time-averaged void fraction profile was well fitted by Equations 2.4 and 2.5 in the turbulent shear region ($0 < y < y^*$) and recirculation region ($y > y^*$), respectively (Figure 5.9). For each cross-section, depth-averaged diffusion coefficients were extracted from the data's best fit, namely $D^{\#}$ in Equation 2.4 for $0 < y < y^*$ and D^* in Equation 2.5 for $y > y^*$. $D^{\#}$ characterised the advective diffusion of the air in the shear layer, whereas D^* reflected the upper free-surface aeration process (Chanson 2010). The results are shown in Figures 5.13 and 5.14 in terms of $D^{\#}$ and D^* as functions of the relative roller length $(x\text{-}x_1)/L_r$ and jump toe position $(x\text{-}x_1)/d_1$, respectively. The experimental data for $D^{\#}$ and D^* from the present study were compared with those from previous studies on smooth and rough bed as well as with the data of Wang (2014). Wang (2014) proposed the following best fit for $D^{\#}$ and D^*:

$$D^{\#} = 0.1 \times \left(1 - \exp\left(-2.3 \times \frac{x - x_1}{L_r}\right)\right) \qquad 0 < y < y^* \tag{5.13}$$

$$D^* = 0.008 \times \exp\left(-3.3 \times \frac{x - x_1}{L_r}\right) \qquad y > y^* \tag{5.14}$$

These equations are based upon experiments performed for $0 < (x\text{-}x_1)/L_r < 1$. Empirical equations were developed for $D^{\#}$ and D^* on rough bed including bed roughness for $0 < (x\text{-}x_1)/d_1 < 20$ and $2.8 < Fr_1 < 4.3$:

$$D^{\#} = 0.055\left(1 - \exp\left(-\frac{1}{2.75 \times (Fr_1 - 1)} \times \frac{x - x_1}{d_1}\right)\right) + \left(0.1\exp\left(\frac{K_s}{d_1}\right)^{0.4}\right) - b \tag{5.15}$$

where $b = 0.11$ for rough bed and $b = 0.0$ for smooth bed.

$$D^* = 0.03\exp\left(-\frac{1}{0.072 \times (Fr_1 - 1)} \times \frac{x - x_1}{d_1}\right) + \left(0.001\exp\left(\frac{K_s}{d_1}\right)^{0.4}\right) - b \tag{5.16}$$

where $b = 0.00006(x\text{-}x_1)/d_1$ for rough bed and $b = 0.0$ for smooth bed. These empirical equations were included to Figures 5.13 and 5.14. For rough bed with $Fr_1 = 2.84$, Equation (5.15) yielded $R = 0.95$, $SE = 0.006$ and Equation (5.16) yielded $R = 0.92$, $SE = 0.002$.

The data presented in Figure 5.13 for the dimensionless diffusivity in the shear region $D^{\#}$ suggested that $D^{\#}$ increased with increasing distance from the jump toe. This variation was associated with the formation of vortices in the shear layer that started close to jump to and developed to downstream by enlargement in size in the form of large eddies. The trend of variation of $D^{\#}$ was comparatively similar to that observed in past studies on both rough and smooth bed (Chanson and Brattberg 2000, Chanson 2010, Chachereau and Chanson 2011,

Wang 2014, Felder and Chanson 2016). $D^{\#}$ increased along the jump roller length for both rough and smooth beds (5.13A and C) while further downstream, it decreased along the length of channel on smooth bed (5.13B) and it kept horizontal value on rough bed (Figure 5.13D) which could be because of different length of advected vortices resulted in energy dissipation. $D^{\#}$ had the same value of 0.05 in the jump roller region for both rough and smooth bed (Figure 5.13C). The location of the maximum $D^{\#}$ was $(x\text{-}x_1)/d_1$ = 8.9 and 13.33 on smooth and rough bed, respectively (5.13C) which was associated with dissipation of large eddies in the shear layer further downstream of jump toe. However, along the jump roller length the variation was pretty similar for both bed configurations including the maximum value at the end of jump roller (5.13D). The range of maximum value of $D^{\#}$ was 3 < $(x\text{-}x_1)/d_1$ < 12 (Figure 5.13B) and 5.5 < $(x\text{-}x_1)/d_1$ < 13.4 (Figure 5.13D) on smooth and rough bed, respectively.

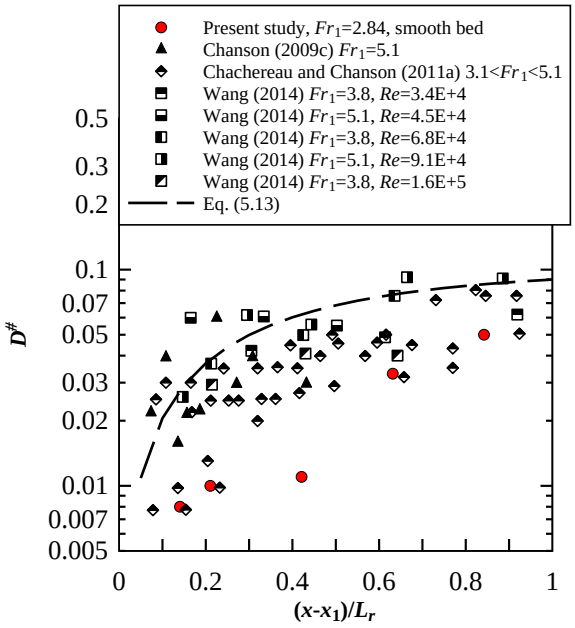

A: As functions of relative longitudinal position in jump roller, smooth bed

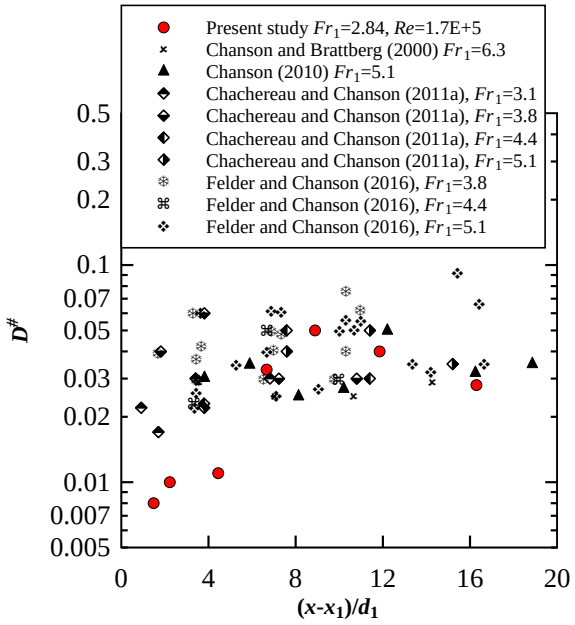

B: As functions of the dimensionless longitudinal position, smooth bed

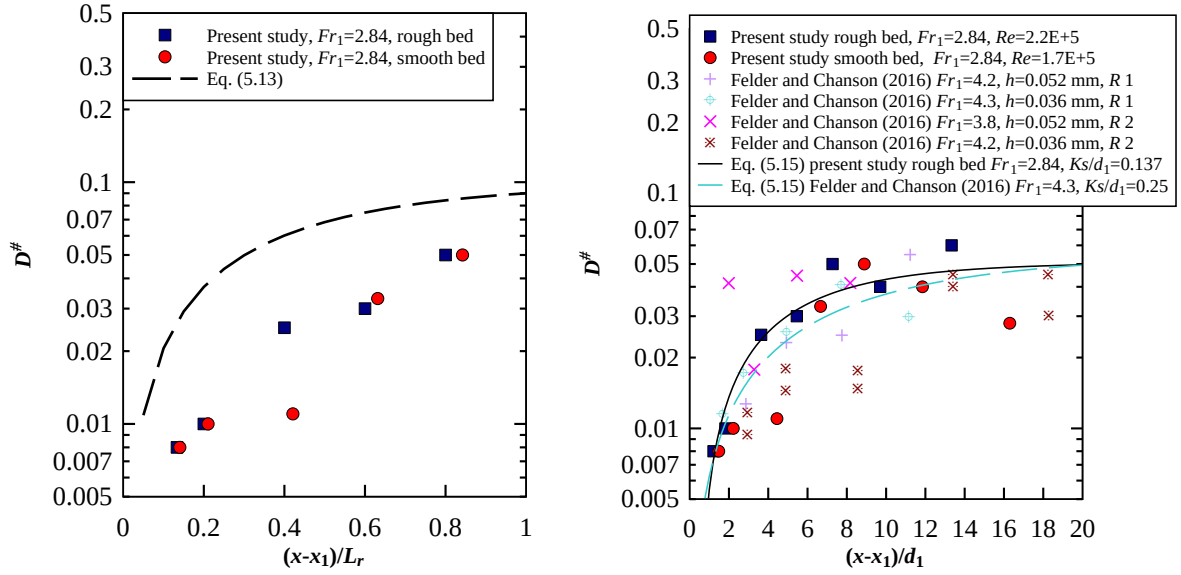

C: As functions of relative longitudinal position in jump roller, rough bed

D: As functions of dimensionless longitudinal position, rough bed

Figure 5.13 Dimensionless turbulent diffusivity in the turbulent shear region. *R*1 and *R*2 roughness types 1 and 2 of Felder and Chanson (2016)

The data presented in Figure 5.14 for the dimensionless diffusivity in the recirculation region highlighted that D^* decreased with increasing distance from the jump toe. This variation was associated with larger backward flow motions with the negative velocity near jump toe which vanished along the roller length by increasing the distance from jump toe. In the jump roller, D^* variation was on smooth bed comparable to that of Wang (2014) as well as to the empirical correlation of Wang 2014. However, the maximum values were 0.0035 and 0.005 for the present and the Wang (2014) studies, respectively (Figures 5.14A). The trend of variation along the channel of D^* was comparable to that of Felder and Chanson with the same maximum value of about 0.012. Regarding D^*, the comparison between rough and smooth bed showed a higher value of D^* in the jump roller area on rough bed at the first half of jump roller length, with a maximum of 0.012 and 0.0035 on rough and smooth bed, respectively. This is probably due to the higher level of turbulence on rough bed. The same values were observed in the second half of the jump roller length (Figure 5.14C).

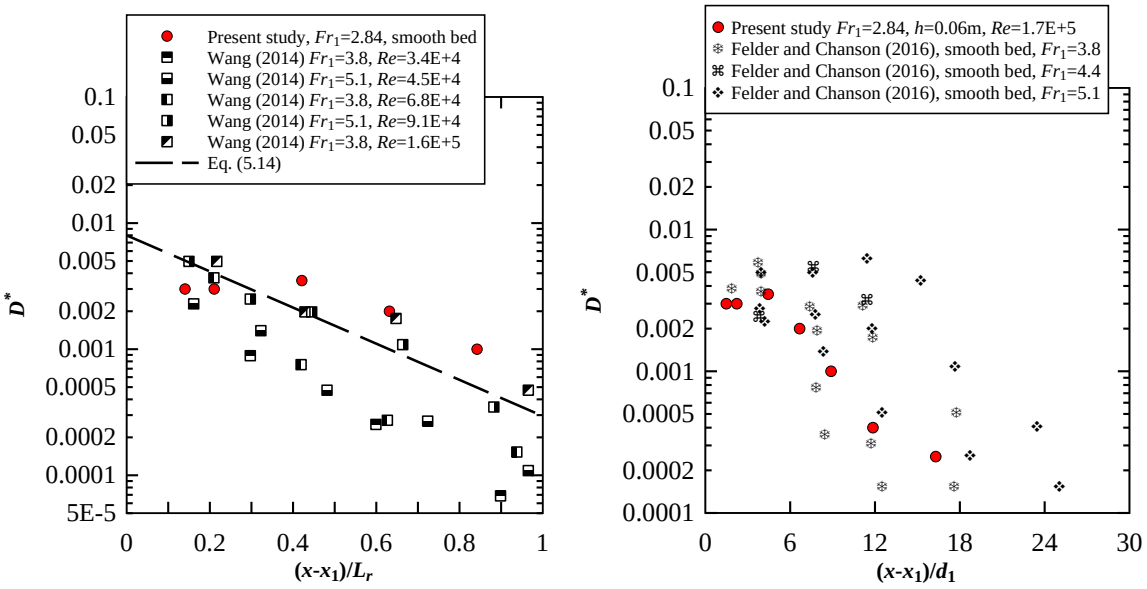

A: As functions of relative longitudinal position in jump roller, smooth bed

B: As functions of dimensionless longitudinal position, smooth bed

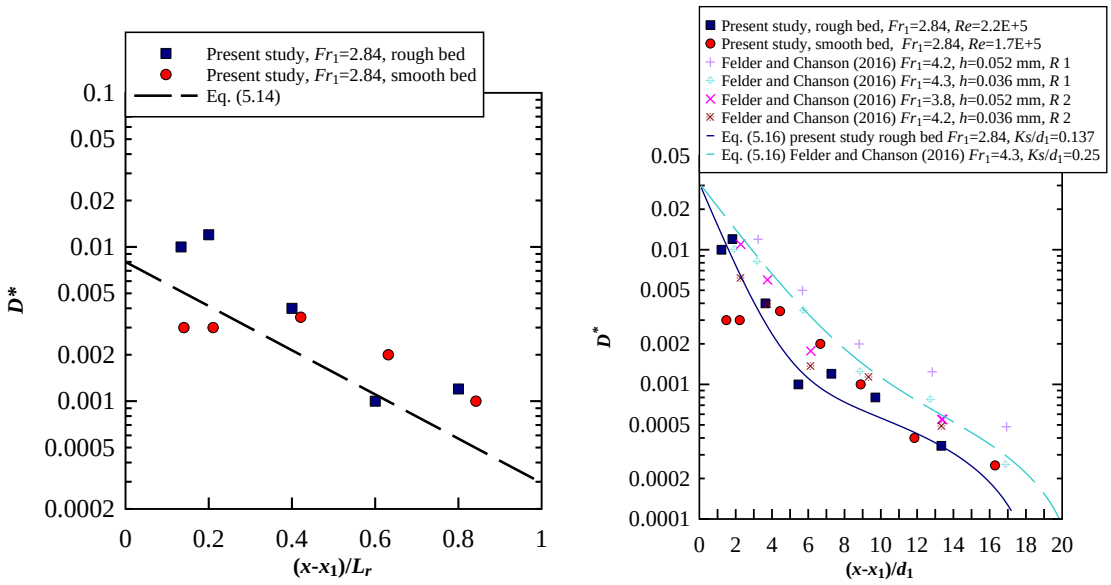

C: As functions of relative longitudinal position in jump roller, rough bed

D: As functions of dimensionless longitudinal position, rough bed

Figure 5.14 Dimensionless turbulent diffusivity in the recirculation region. *R*1 and *R*2 roughness types 1 and 2 of Felder and Chanson (2016)

In the shear region, the diffusion of air bubbles was observed with the broadening of the bell-shaped void fraction vertical profile with longitudinal distance as shown in Figure (5.8A and D) on rough and smooth bed, respectively. The turbulent diffusivity $D^{\#}$ increased along the roller length and reached a constant value at the end of roller. In the upper free-surface region, the diffusivity D^* decreased towards zero at the end of roller because of vanishing the

backward flow with negative velocity. The higher value of D^* for rough bed at first half of the roller length was associated with higher negative velocities of backward flow as well as higher rate of air entrainment. The gradual disappearance of air diffusion at the end of roller corresponded to the surface de-aeration and the vanishing of free-surface turbulence on both rough and smooth beds. This data trend was supported by the data of Chanson (2005, 2010), Wang (2014, 2015) Felder and Chanson (2016, 2018).

5.3.3 Bubble count rate

The bubble count rate F was linked to the air entrainment and diffusion, as well as to the formation, breaking-up, coalescence and collapse of air bubbles and air pockets in the turbulent shear region. Along the jump roller length, the vertical distributions of bubble count rates showed some typical characteristics, including two peaks, F_{max} in the air-water shear layer and F_{sec} in the recirculation region (Figure 5.2B) (Chanson and Brattberg 2000, Murzyn et al. 2007).

Figure 5.15 presents typical bubble count rate distributions for three Froude numbers on rough bed and one Froude number on smooth bed. The same intake aspect ratio h/W = 0.12 and inflow length x_1/h = 16.67 were used on both rough and smooth bed. For each set of flow conditions, the vertical profiles of bubble count rate were plotted at seven longitudinal positions on the channel centerline.

In Figure 5.15, the data showed that the maximum bubble count rate F_{max} in the turbulent shear region was distinctive on both rough and smooth bed configurations and its value decreased with increasing distance from the jump toe. The vertical elevations of the two peak values Y_{Fmax} and Y_{Fsec} increased along the jump roller, together with the increasing free-surface elevation.

A comparison between the upstream flow and the jump roller showed much smaller bubble count rates upstream of the jump toe for Fr_1 = 2.84 on both rough and smooth bed. For Fr_1 < 2 on rough bed, higher bubble count rates were observed upstream of the jump toe. The findings were overall in agreement with the results of Felder and Chanson (2016, 2018) on rough bed and Chanson (2011) on smooth bed.

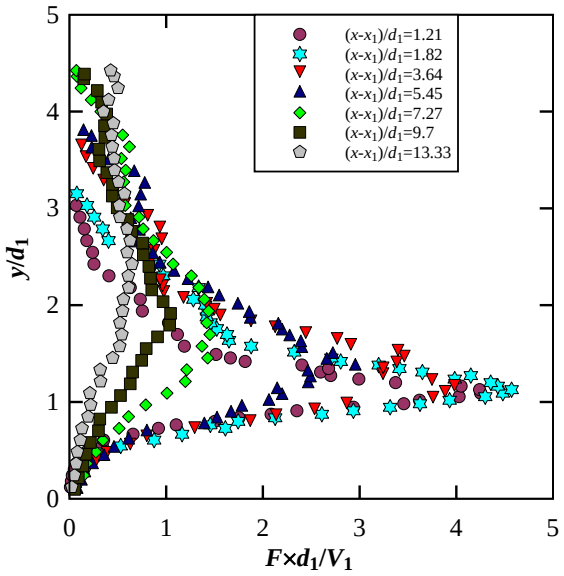

A: Rough bed, Run BR3, Q = 0.1 m^3/s,
d_1 = 0.0825 m, Fr_1 = 2.84, Re_1 = 2.2E+5

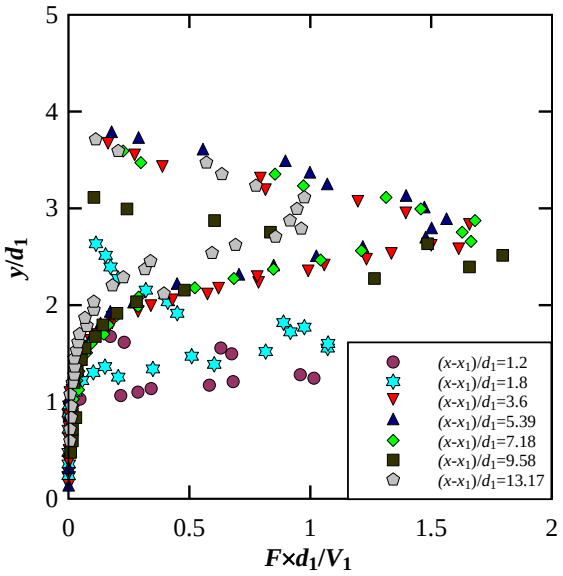

B: Rough bed, Run BR2, Q = 0.07 m^3/s,
d_1 = 0.0835 m, Fr_1 = 1.96, Re_1 = 1.6E+5

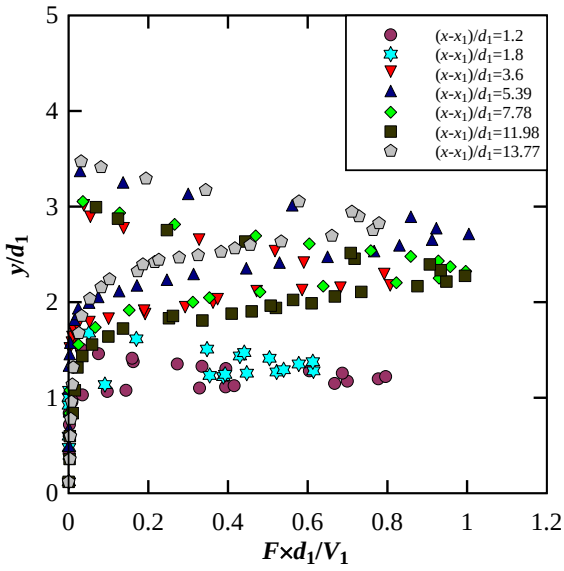

C: Rough bed, Run BR1, Q = 0.061 m^3/s,
d_1 = 0.0835 m, Fr_1 = 1.7, Re_1 = 1.4E+5

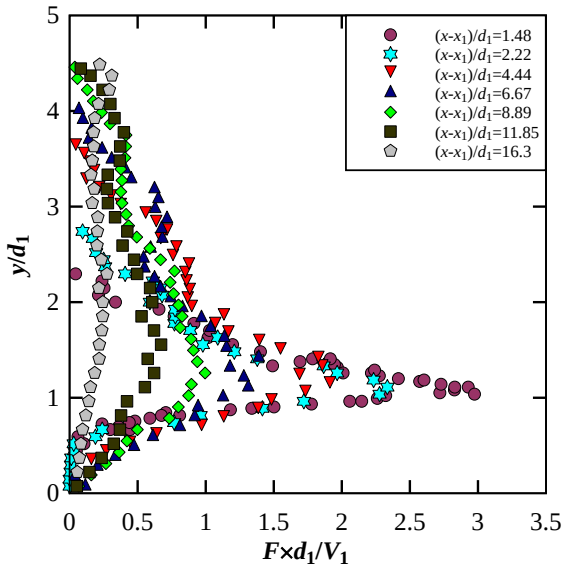

D: Smooth bed, Run BS1, Q = 0.078 m^3/s,
d_1 = 0.0675 m, Fr_1 = 2.84, Re_1 = 1.7E+5

Figure 5.15 Bubble count rate profiles on the channel centerline

The comparison between rough and smooth bed showed higher bubble flux on rough bed configuration, likely because of the roughness effect, while the shape of the bubble count rate distributions was the same. For the same Froude number, Fr_1 = 2.84, a higher bubble count rate profile was observed at second cross-section $(x-x_1)/d_1$ > 1.82 on rough bed and at first

cross-section $(x\text{-}x_1)/d_1 > 1.48$ on smooth bed (Figure 5.15A and D). For $Fr_1 < 2$ on rough bed, higher bubble count rates were measured further downstream of the jump toe, $(x\text{-}x_1)/d_1 > 3.6$ and $(x\text{-}x_1)/d_1 > 5.39$, for $Fr_1 = 1.96$ and $Fr_1 = 1.7$, respectively (Figure 5.15B and C). This confirmed the visual observations which showed that air bubbles entrained most likely downstream of the jump toe (Section 4.2).

The longitudinal variations of vertical profiles on both rough and smooth bed configurations with the same inflow Froude number, $Fr_1 = 2.84$ are presented in Figure 5.16. The characteristic elevations Y_{90} above the invert were added. The results showed higher bubbly flow on rough bed in the jump roller area as well as downstream. The reason could be the formation of more intense vortices in the shear layer on pebbled rough bed, resulting in higher rate of bubble flux into the flow. It is thought that, for the same inflow Froude number, the magnitude of bubble count rate was mostly affected by the roughness type.

The analyses of bubble count rate distributions revealed distinct effects of channel bed roughness on the bubble count rate data. A comparison between present rough and smooth bed configurations is presented in Figure 5-17A, while in Figure 5-17B the present data are compared with those from Felder and Chanson (2016). The comparison was undertaken for similar inflow Froude and Reynolds numbers.

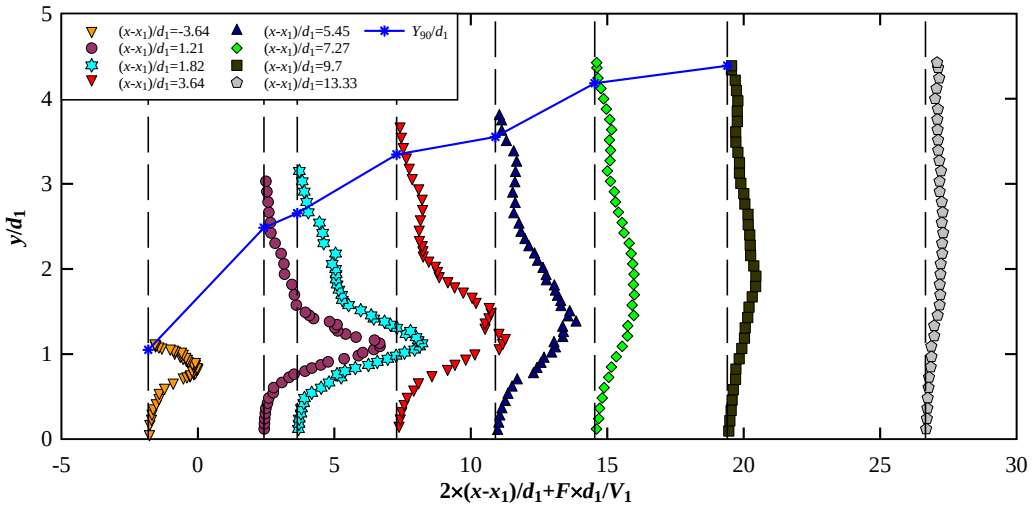

A: Rough bed, Run BR3, $Q = 0.1$ m^3/s, $d_1 = 0.0825$ m, $Fr_1 = 2.84$, $Re_1 = 2.2$E+5

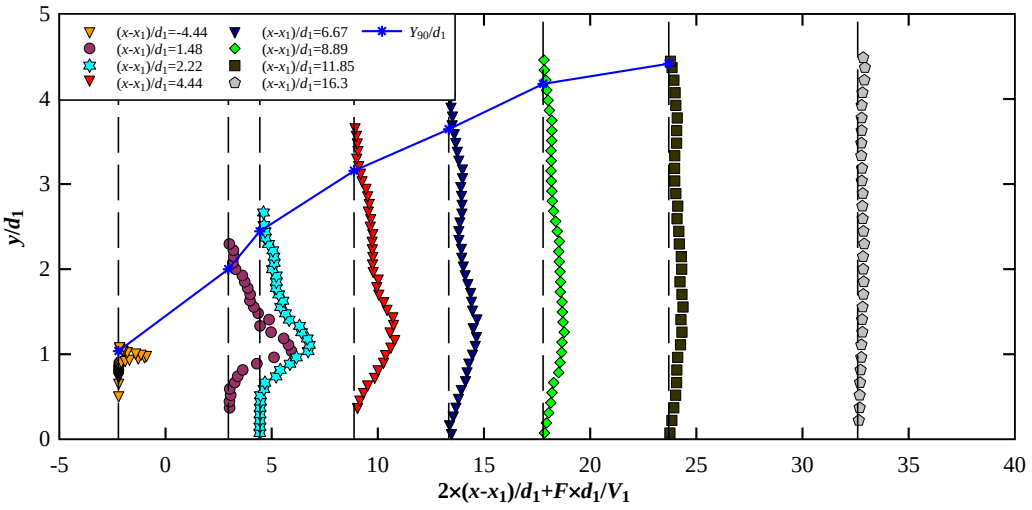

B: Smooth bed, Run BS1, Q = 0.078 m^3/s, d_1 = 0.0675 m, Fr_1 = 2.84, Re_1 = 1.7E+5

Figure 5.16 Bubble count rate distributions in hydraulic jump, comparison with characteristic flow depth Y_{90}/d_1

Felder and Chanson (2016) and Tastan and Yildirim (2014) stated that the bubble count rate was influenced by significant scale effects and the number of entrained air bubbles cannot be scaled in terms of only a Froude similitude. It is acknowledged that the present analysis did not achieve exact similitude based upon both Froude and Reynolds numbers, but that the comparison provided valuable information. The comparison between smooth and rough bed configuration showed a similar shape of the bubble count rate distributions with distinctive maxima in the shear layer and secondary peaks in the recirculation region (Figure 5-17A). While the bubble count rates were higher on the rough channel bed at the start of the roller, further downstream the bubble count rates were comparable on both bed configurations. A comparison between the present rough bed and rough bed configurations 1 and 2 by Felder and Chanson (2016) highlighted some differences in both magnitude and shape of the bubble count rate distributions (Figure 5-17B). On the present rough bed, the bubble count rates in the turbulent shear region were larger close to the jump toe. Wang (2014) highlighted that on smooth bed, a larger Reynolds number characterised a stronger turbulent flow with larger shear stress, resulting in shearing of the entrapped air packets into finer air bubbles and led to a larger number of bubbles and second, the decreasing rate was mostly controlled by the Froude number. As seen in Figure (5.17B) on rough bed, present rough bed and roughness type 1 of Felder and Chanson (2016) with the same Reynolds number $Re_1 \approx$ 2E+5, bubble count rate on pebbled rough bed was higher even with lower Froude number. This could be due to the effect of roughness type affecting the formation and advection of large vortices in

the roller area. The roller pattern was the same as on rough bed configuration 1 and different from rough bed configuration 2. As observed in the shear layer, the location of the peak in bubble count rate F_{max} was the same for the present study and the rough bed configuration 1 for $(x\text{-}x_1)/d_1 > 8$, while it was half at the location of F_{max} on rough bed configuration 2.

5.3.4 Characteristic bubble count rate parameters

A comparison in terms of maximum bubble count rate, void fraction at the location of maximum bubble count rate and secondary maximum bubble count rate is shown in Figures 5.18 – 5.20, between different beds roughness configurations for comparable Froude and Reynolds numbers.

Considering the present data on both rough and smooth bed configurations and those from Felder and Chanson (2018) on rough bed, an empirical relationship was developed in terms of inflow Froude number and roughness for $2.8 < Fr_1 < 4.3$:

$$\frac{F_{max} d_1}{V_1} = 5.5k \exp\left(-\frac{1}{3.6k\,(Fr_1 - 1)} \times \frac{x - x_1}{d_1}\right) + \left(0.7 \exp\left(\frac{K_s}{d_1}\right)^2\right) - b \qquad (5.17)$$

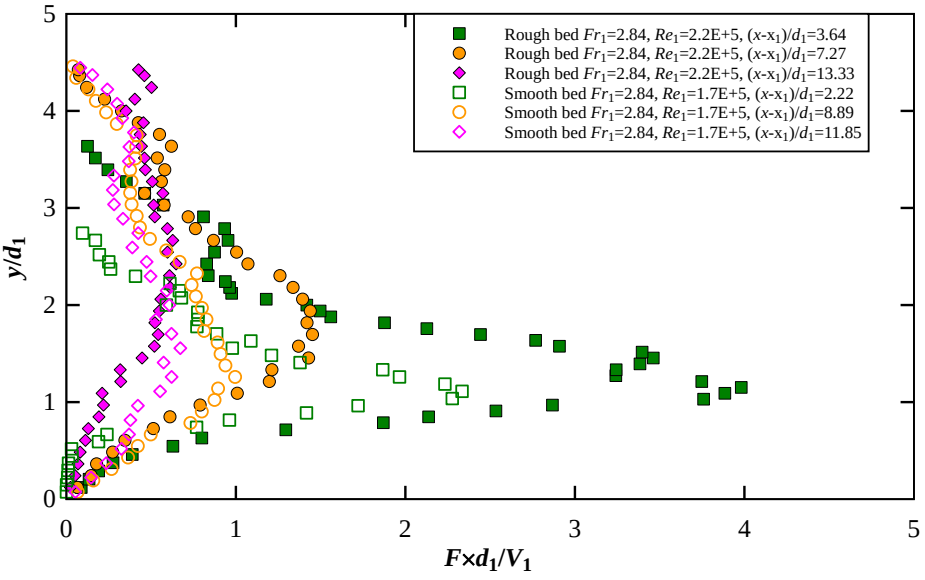

A: Present study, comparison between rough and smooth bed

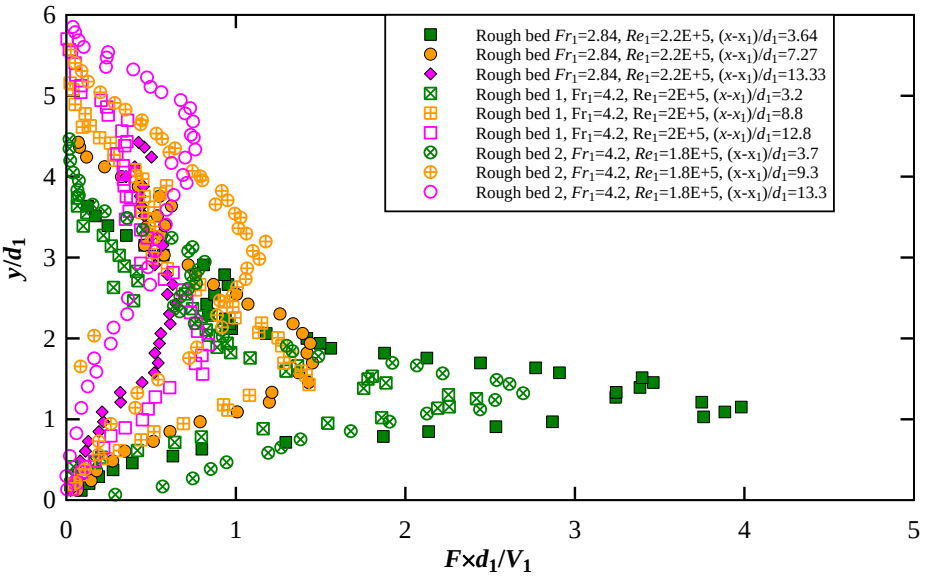

B: Comparison between present rough bed and two rough bed configurations of Felder and Chanson (2016). Colored symbols are present study.

Figure 5.17 Bubble count rate distribution in hydraulic jumps with different bed roughness configurations

where for smooth bed: b=0.0 and for rough bed: b=0.75+k with:

$$\left.\begin{array}{ll} k = 1 & \text{for pebbled rough bed} \\ k = \left(0.85 - K_s / d_1\right) & \text{uniform rough beds for } K_s / d_1 < 0.5 \\ k = \left(1.07 K_s / d_1\right)) \text{ and } K_s / d_1 = 0.5 K_s / d_1 & \text{uniform rough beds for } K_s / d_1 > 0.5 \end{array}\right\} \quad (5.18)$$

The application of Equation (5.17) to the present pebbled rough bed with Fr_1 = 2.84 yielded R = 0.95 and SE = 0.57. The data on pebbled rough bed and uniform rough bed, such as rubber mat as used by Felder and Chanson (2016), resulted in different values of bubble count rate (Figure 5.18C). It is believed that, for a given void fraction, the number of bubbles was largely determined by the turbulent shear stress, and linked to the turbulence level and bed roughness. For the present rough bed with Fr_1 < 2, the distribution of dimensionless maximum bubble count rate showed different profiles close to the jump toe because of different type of hydraulic jump which was undular for Fr_1 < 2 (Figure 5.18C).

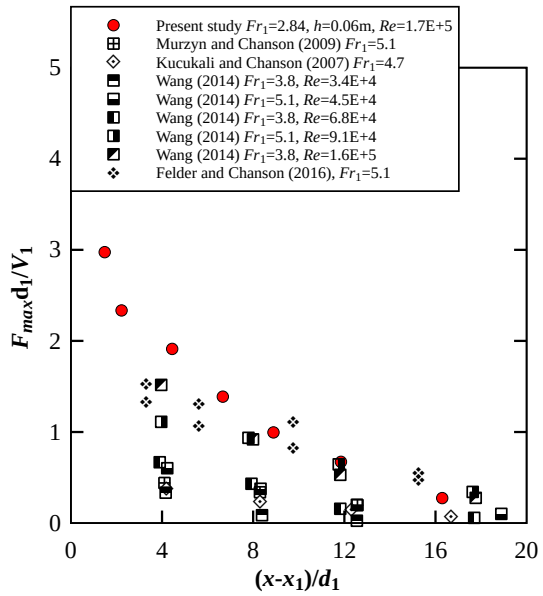

A: Dimensionless longitudinal distribution of the maximum dimensionless bubble count rate, smooth bed

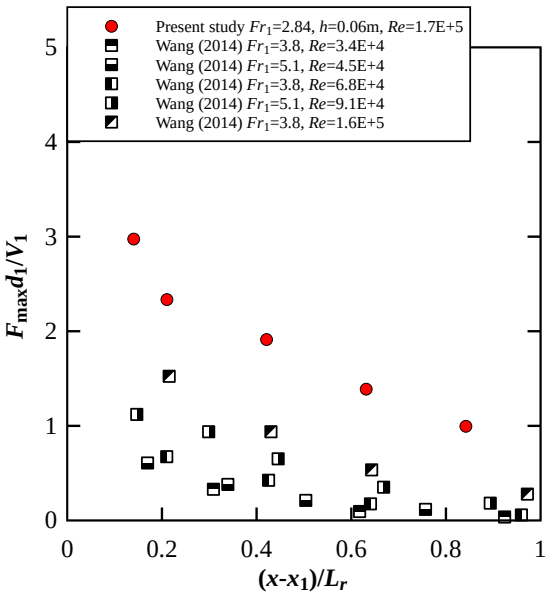

B: Dimensionless longitudinal distribution related to the jump roller of the maximum dimensionless bubble count rate, smooth bed

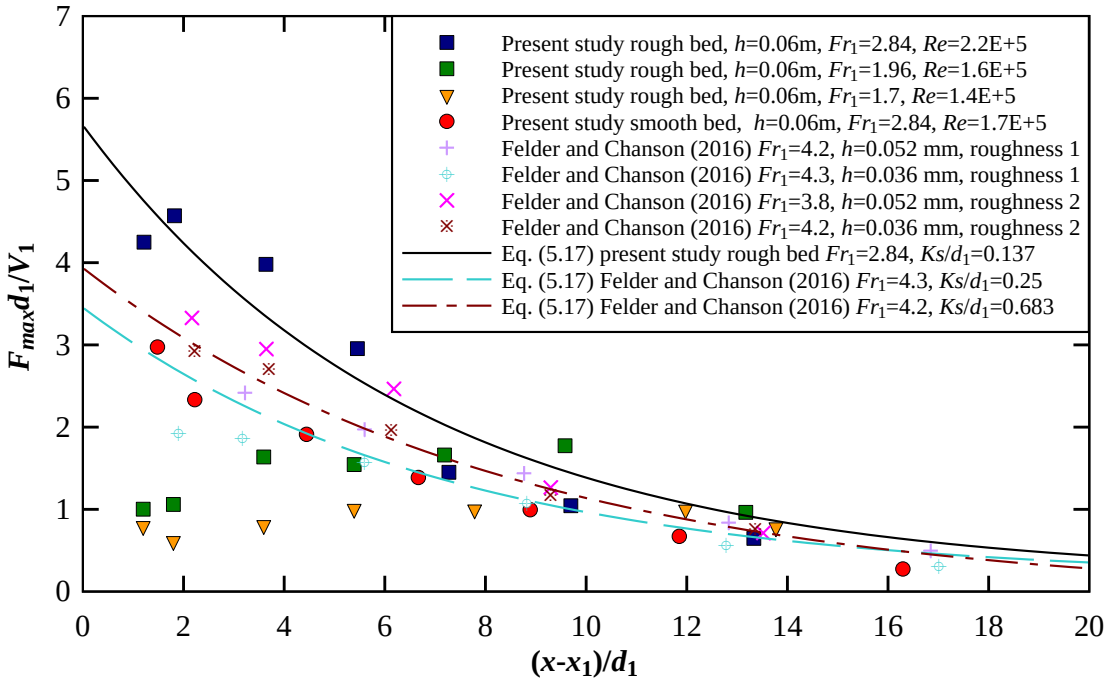

C: Dimensionless longitudinal distribution of the maximum dimensionless bubble count rate, rough bed

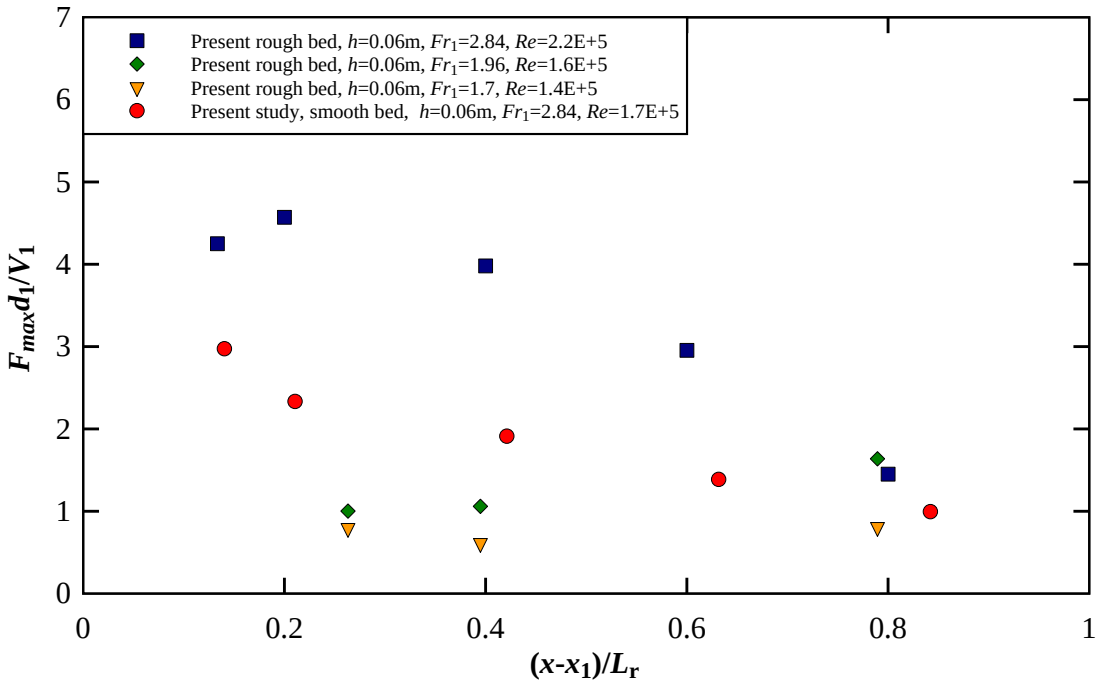

D: Dimensionless longitudinal distribution related to the jump roller of the dimensionless bubble count rate, rough bed

Figure 5.18 Dimensionless maximum bubble count rate for different bed roughness configurations, comparison with previous studies on smooth and rough beds

The data presented in Figure 5.18 indicated that the dimensionless maximum bubble count rates F_{max} on both smooth and rough bed configurations were at the beginning of the roller larger than downstream. Further downstream, this parameter decreased with a comparable maximum bubble frequency for all the bed configurations. The dimensionless F_{max} on smooth bed had comparatively the same trend along the channel length as well as in previous literature studies (Figure 5.18A and B). In the jump roller length, the higher values of dimensionless F_{max} for the present study were related to the higher Reynolds number (Figure 5.18B). A comparison between rough and smooth bed showed that the roughness increased the momentum exchange between the boundary layer and the overlying shear layer, especially in the first part of the jump. The bed roughness provoked the formation of large-scale eddies which were transported downstream entrapping the air bubbles. A comparison between the present results on rough bed and those from Felder and Chanson (2016) revealed that dimensionless F_{max} was higher on pebbled rough bed in the jump roller length. As discussed in Section (5.3.3), on smooth bed, larger Reynolds number characterised a highly turbulent flow with larger shear stress, resulting in a larger bubble count rates while Froude

number controlled the longitudinal decreasing rate of bubbles (Wang 2014), but on rough bed, roughness type was the most important factor. For $Fr_1 < 2$, the maximum value of dimensionless F_{max} on rough bed was observed in the middle region of jump roller because of the different process of air entrainment in undular hydraulic jump on rough and smooth bed configurations (Figure 5.18C). As discussed in Section (4.2), for $Fr_1 < 2$ on rough bed, the entrainment of air occurred at the first undular wave crest downstream of the jump toe position which gradually vanished in following wave crests. Furthermore, at the first and second wave crests, ripples were sliding toward backward. The entrained air consisted of groups of bubbles being transported downstream before rising to the free-surface.

Figure 5.19 compares the local maximum bubble count rate $F_{sec\text{-}max}$ in the recirculation region for the different bed configurations including present rough and smooth bed and the rough bed data by Felder and Chanson (2016). Features similar to those for the maximum bubble count rate F_{max} were observed (Figure 5.19). In the present study, the trend of variation was comparable to that of Felder and Chanson (2016), who used a different bed roughness configuration. In the region close to the beginning the roller, the rough bed configuration data showed bubble frequencies larger than those on a smooth bed for similar inflow conditions. The differences between rough and smooth bed decreased with increasing distance from the jump toe. Wang (2014) stated that on smooth bed, the magnitude of local maximum bubble count rate in the free-surface region was affected by both Froude and Reynolds numbers, and its streamwise decay rate was related to the inflow Froude number. Based upon present data and those from Felder and Chanson (2016), an empirical relationship was derived:

$$\frac{F_{sec-max} d_1}{V_1} = \exp\left(\frac{\frac{x - x_1}{d_1} - 1.94}{Fr_1 - 15.1}\right) \qquad 2.8 < Fr_1 < 4.3 \qquad (5.19)$$

Equation (5.18) implied that for rough bed condition, only Fr_1 affected the local maximum bubble count rate. For present rough bed with $Fr_1 = 2.84$ Equation (5.19) yielded $R = 0.91$, $SE = 0.16$. Except for second cross-section $x\text{-}x_1 = 1.82$ on the present rough bed, Equation (5.19) showed good agreement with the experimental data.

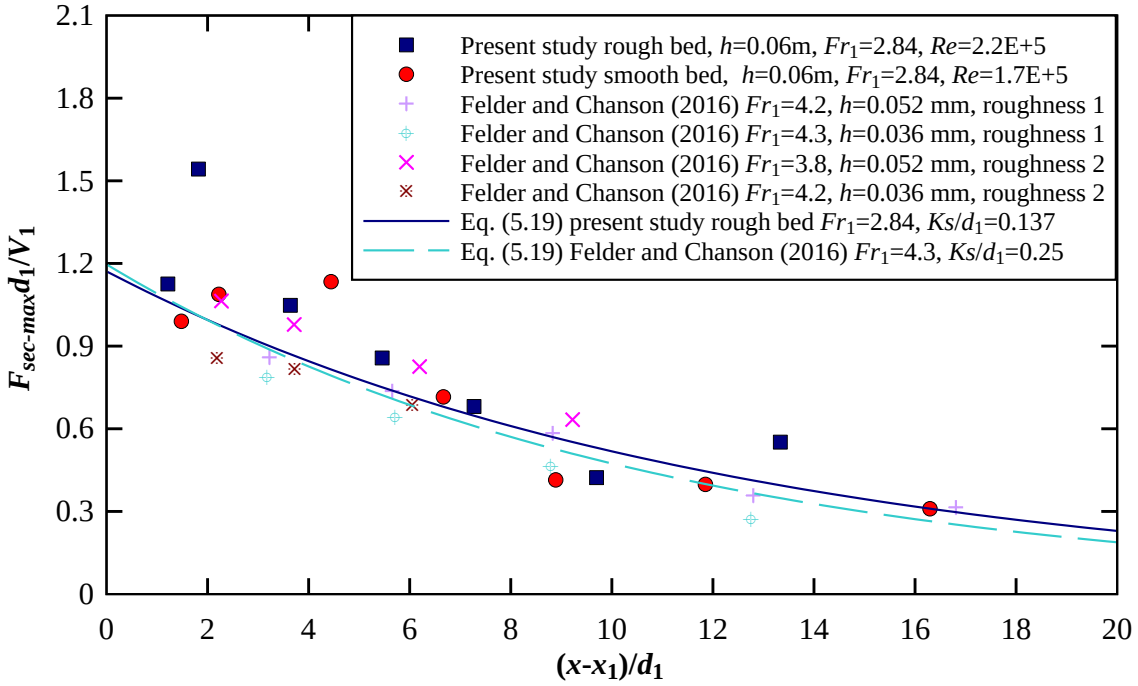

Figure 5.19 Local maximum bubble count rate in the recirculation region on both rough and smooth bed configurations, comparison with Felder and Chanson (2016)

Discussion

The maximum bubble count rate F_{max} in the turbulent shear layer was measured and its longitudinal decay was well correlated with the Equation (5.17). Most data were obtained at relative longitudinal positions between $(x\text{-}x_1)/L_r$ = 0.1 and $(x\text{-}x_1)/L_r$ = 1 on both rough and smooth bed configurations. It should be noted that the accurate two-phase flow measurements close to the mean jump toe position e.g. within $0 < (x\text{-}x_1)/L_r < 0.05$, was hindered by the longitudinal jump toe oscillations.

Air entrainment properties were investigated previously for supported plunging water jets (Cummings and Chanson 1997, Brattberg and Chanson 1998). The longitudinal distributions of maximum bubble count rate implied a quick increase in F_{max} along a short distance from the impingement point before it decreased with further increasing distance. Close to the jump toe, the increase in maximum bubble count rate reflected a bubble break-up process. Wang (2014) indicated that the entrapped air pockets at jump toe were broken into small bubbles by the turbulent shear stress which was larger than the air-water interfacial resistance. Herein, the observations on rough and smooth beds suggested that the process of bubble break-up within the roller was contrived by the interactions between turbulent shear and the underlying

boundary layer. The pebbled rough bed led to increasing the momentum exchange between the overlying shear layer and the boundary layer, especially in the first part of the jump, as observed by Felder and Chanson (2016) on uniform rubber mat roughness. The formation of large-scale eddies provoked by roughness which was transported downstream entrapping the air bubbles.

5.3.5 Relationship between maximum void fraction and bubble count rate

The relationship between maximum void fraction and the maximum bubble count rate could give some information about air entrainment properties at the critical vertical points in the turbulent shear layer of hydraulic jumps. An insight into these relationships may provide a better understanding of the flow physics.

The void fraction corresponding to the maximum bubble count rate in the turbulent shear region C_{Fmax} was investigated. The present results were compared to previous studies on different bed configurations (Figure 5.20). The void fraction corresponding to the maximum bubble count rate decreased with increasing inflow Froude number for all studies. The void fraction at the position of maximum bubble count rate was not affected by the differences in the magnitude of bubble count rates (Figures 5.17 and 5.18). This feature was most apparent in the present study as well as on roughness type 2 by Felder and Chanson (2018), showing very similar values of void fractions C_{Fmax} compared to other bed configurations, despite the observed differences in magnitude of F_{max} and the different shape of the bubble count rate distributions at the downstream end of the jump. The data of C_{Fmax}/C_{max} were in the range from 0.6 to 1.0. On rough bed, despite some scatter, C_{Fmax}/C_{max} was in average 0.83, while the data for the smooth bed showed a larger scatter. (Figure 5.20B). Chanson and Brattberg (2000) proposed an empirical relationship for a hydraulic jump on smooth bed:

$$\frac{C_{F\max}}{C_{\max}} = 0.587 + 0.0135\frac{(x - x_1)}{d_1} \qquad 3.6 \leq (x - x_1)/d_1 \leq 28.7 \qquad (5.20)$$

Overall, on rough and smooth bed configurations, independently of Froude number and longitudinal distances from the jump toe, a value of 0.8 might be considered as typical of C_{Fmax}/C_{max}, although the data showed some scatter. Herein, this feature was valid for $2.8 < Fr_1 < 5.1$ on both rough and smooth bed configurations.

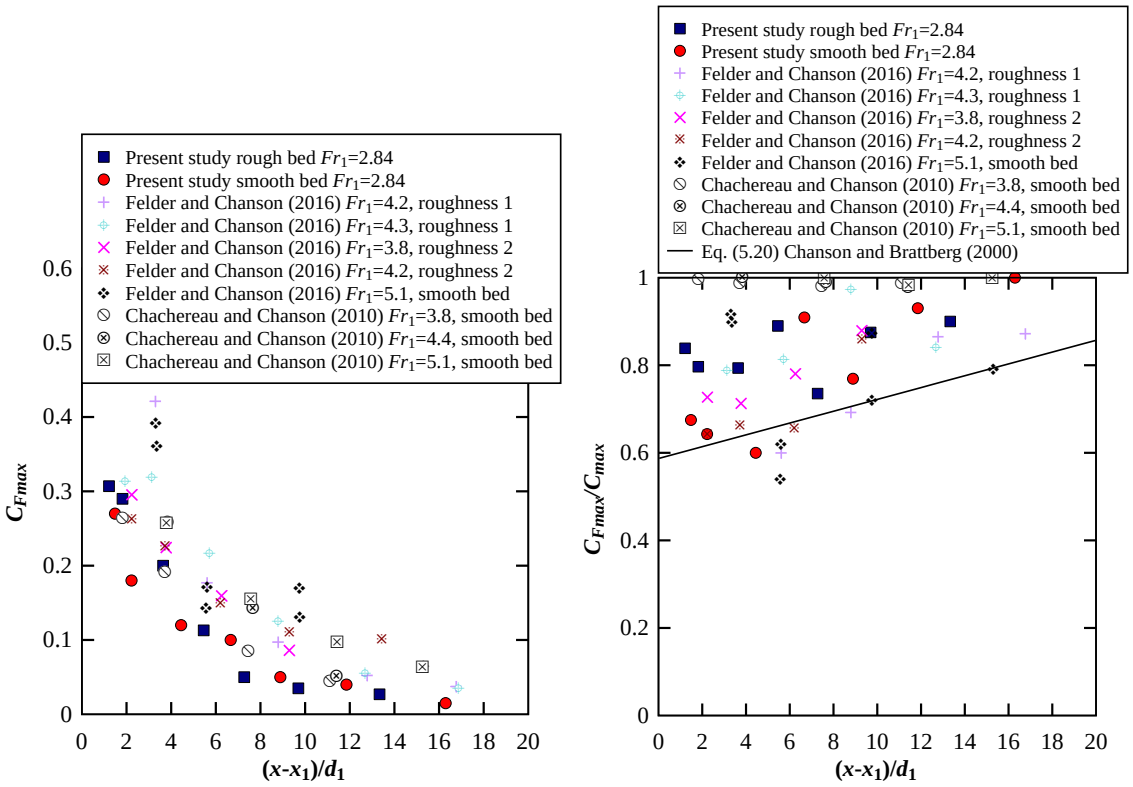

A: Void fraction corresponding to the maximum bubble count

B: Void fraction corresponding to the maximum bubble count

Figure 5.20 Void fraction at location with maximum bubble count rate; comparison with rough and smooth channel bed data from previous study (Felder and Chanson 2016, Chachereau and Chanson 2010)

5.3.6 Interfacial velocity distributions in hydraulic jumps

5.3.6.1 Presentation

In a hydraulic jump with a marked roller, the velocity field may be defined in three regions: positive and monotonically increasing within the boundary layer immediately above the channel bed, positive or negative in the turbulent shear region, and negative in the recirculation region. Figure 5.21 plots a sketch of the typical velocity profile in these regions, including the no-slip boundary condition applied at the channel bed (y = 0). In the boundary layer, the time-averaged velocity V increases rapidly, reaching a maximum V_{max} at the elevation Y_{Vmax}. And in the shear layer region, decreasing gradually with increasing distance from the bottom. The negative velocity in the reversed flow V_{rec} was relatively uniform along the recirculation region.

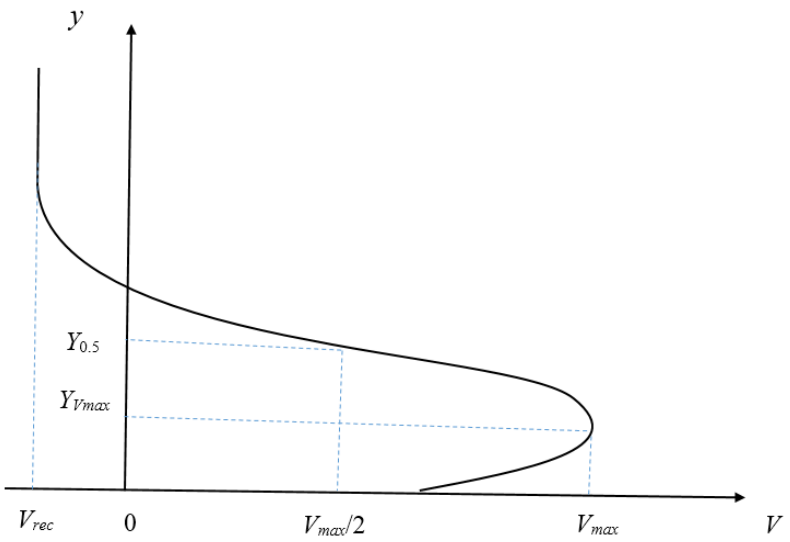

Figure 5.21 Air-water interfacial velocity profile in a vertical cross-section of jump roller (based on Chanson 2009c)

Figure 5.22 presents typical distributions of dimensionless interfacial velocity V/V_1 for the rough and smooth bed configurations with the same inflow Froude number. The data included both upstream flow and hydraulic jump roller. The characteristic dimensionless flow depth Y_{90}/d_1 was added to Figure 5.22. In the turbulent shear flow, the magnitude of positive velocities decreased in the longitudinal direction with increasing distance from the jump toe. In the recirculation region, higher negative velocities were observed near the jump toe. Overall, the negative velocities did not occur over the full roller length. Once the flow reversal disappeared, a quasi-uniform velocity distribution was observed. Next to the channel bed, a boundary layer developed with a rapid increase of velocity over a short distance normal to the invert. A comparison between the observation on rough and smooth beds showed that, in the jump roller region, the negative velocity covered on rough bed a dimensional distance longer than on smooth bed: $1.21 < (x-x_1)/d_1 < 5.45$ and $1.48 < (x-x_1)/d_1 < 4.44$ on rough and smooth beds, respectively.

In the turbulent shear flow region as well as downstream of the jump roller, the vertical distribution of positive velocity was more uniform on smooth bed than on rough bed. A reason could be the larger eddies generated in the turbulent shear layer on rough bed. Overall, the present observations were generally consistent with previous findings on both rough and smooth bed hydraulic jumps (Chanson 2007, Murzyn et al. 2007, Wang et al. 2014a, Wang and Chanson 2015, Felder and Chanson 2016).

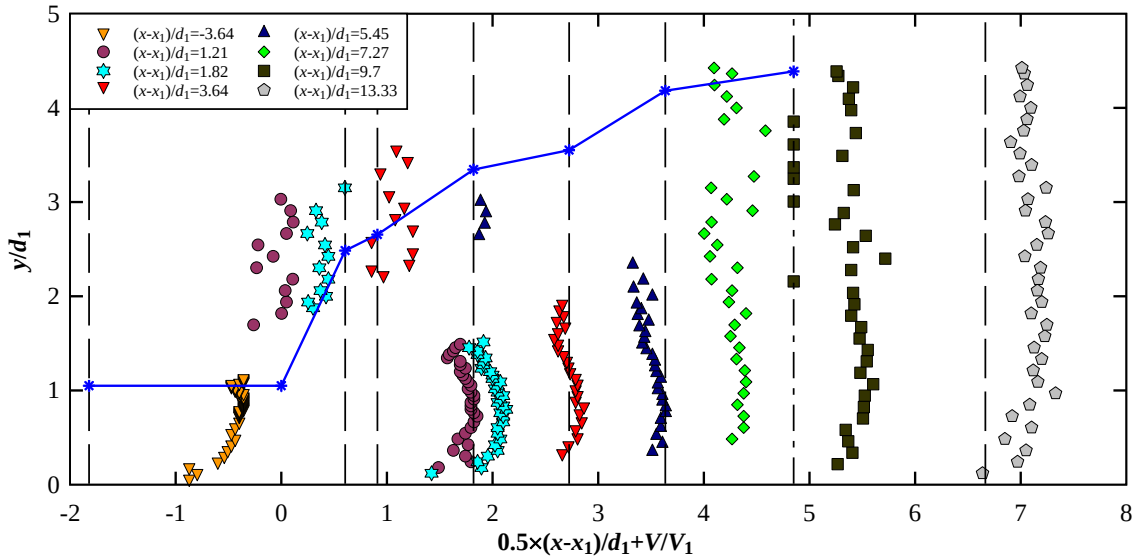

A: Rough bed, Run BR3, Q = 0.1 m^3/s, d_1 = 0.0825 m, Fr_1 = 2.84, Re_1 = 2.2E+5

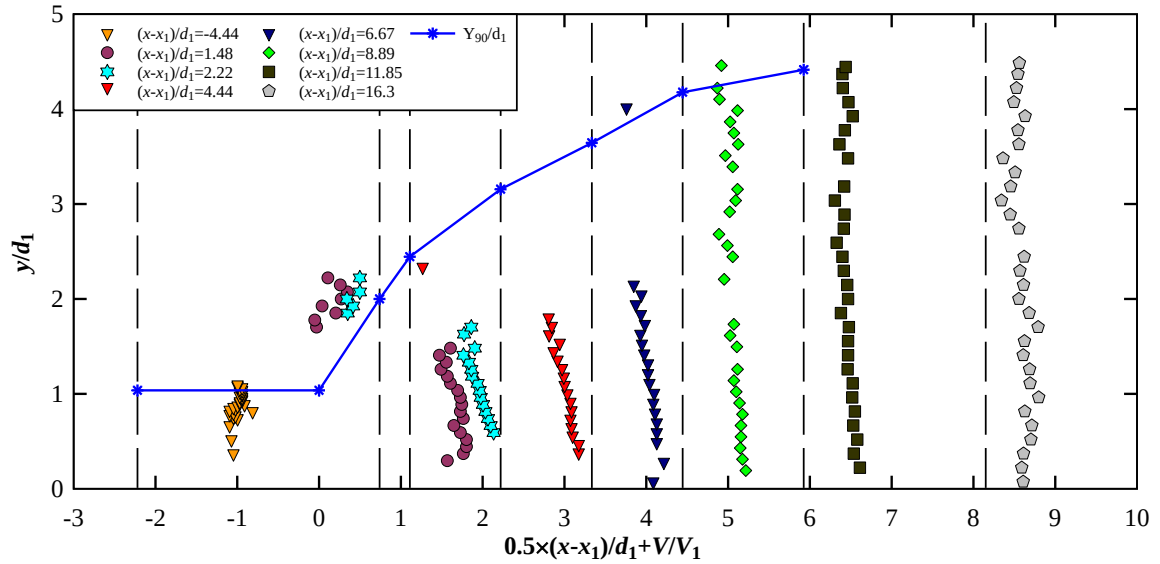

B: Smooth bed, Run BS1, Q = 0.078 m^3/s, d_1 = 0.0675 m, Fr_1 = 2.84, Re_1 = 1.7E+5

Figure 5.22 Dimensionless interfacial velocity distributions upstream and in the hydraulic jump, dashed vertical lines illustrate *y*-axis for the respective velocity data; comparison with characteristic flow depth Y_{90}/d_1

5.3.6.2 Comparative analyses of interfacial velocity distributions

Figure 5.23 presents a comparison of the interfacial velocity distributions between rough and smooth bed configurations for a similar inflow Froude number, Fr_1 = 2.84. Despite some

scattered data, the overall velocity distribution was similar for both bed configurations, showing a boundary layer close to the channel bed. At the start of the jump roller, the comparison showed the larger interfacial velocities on rough bed, slightly shifted upwards.

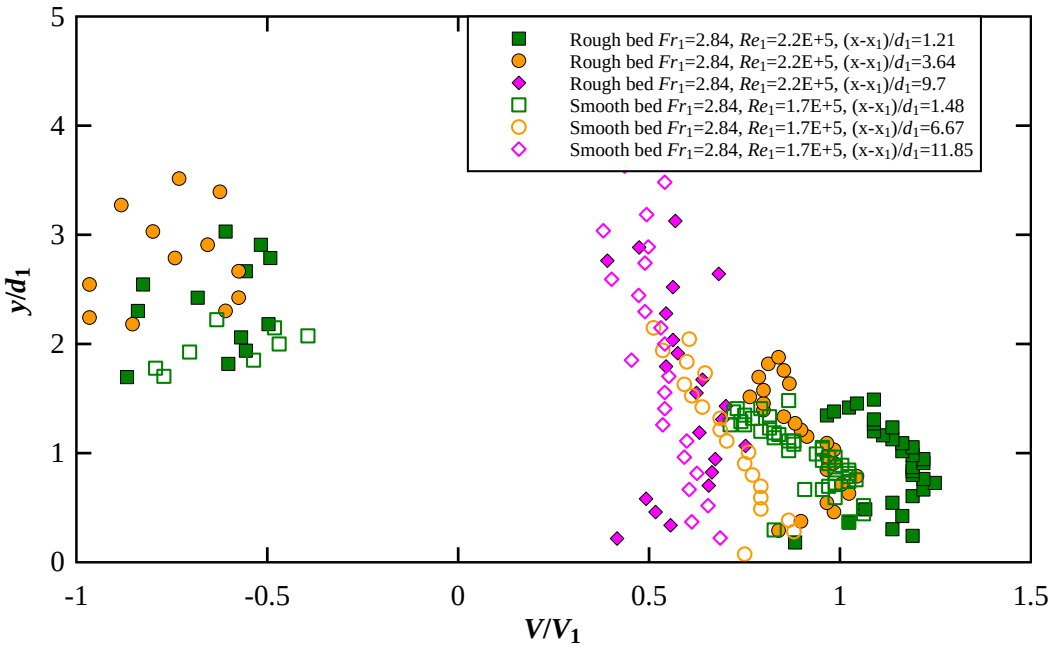

Figure 5.23 Comparison of interfacial velocity in hydraulic jumps with different bed roughness

In the recirculation region, negative velocities were observed for both bed configurations at the start of the jump, $(x\text{-}x_1)/d_1 < 4$, with larger recirculation velocities on rough bed but, more uniform distribution on smooth bed. In the shear layer, a similar trend was observed in terms of the interfacial velocity distributions between rough and smooth bed configurations.

The maximum velocity V_{max} in the shear layer decreased in the longitudinal direction on both rough and smooth bed as some momentum transfer took place in the water column. Apart from the flows close to the jump toe, the dimensionless interfacial velocities V/V_1 were larger on rough bed. Further downstream, the velocity profiles tended to exhibit a uniform profile on both bed configurations.

An analogy between a wall jet and the impinging flow into the jump roller suggested a self-similar shape (Rajaratnam 1965, Chanson 2010; Chachereau and Chanson 2011):

$$\frac{V}{V_{max}} = \left(\frac{y}{Y_{Vmax}}\right)^{\frac{1}{N}} \qquad \frac{y}{Y_{Vmax}} < 1 \qquad (5.21)$$

$$\frac{V - V_{rec}}{V_{max} - V_{rec}} = \exp\left(-\frac{1}{2} \times \left[1.765 \times \left(\frac{y - Y_{Vmax}}{Y_{0.5}}\right)\right]^2\right) \qquad 1 < \frac{y}{Y_{Vmax}} < 3 \text{ to } 4 \qquad (5.22)$$

where V_{max} is the maximum velocity in the shear layer observed at $y = Y_{Vmax}$ and V_{rec} is the recirculation velocity. Note that self-similar velocity profile could be calculated based upon $Y_{0.5} = y(V = (V_{max}\text{-}V_{rec})/2)$ or $Y_{0.5} = y(V = V_{max}/2)$ while the latter was more physically and practically accessible (Wang 2014). All experimental data including a negative free-surface velocity are plotted in Figure 5.24 and compared to Equation (4.22). Consistent results were observed at various longitudinal positions for all inflow conditions on both rough and smooth bed configurations. Despite the different Reynolds numbers, on rough and smooth beds respectively, a reasonable agreement was seen between all data and the theoretical prediction in both shear layer and recirculation regions. Some scattered data were observed in the shear layer for Fr_1 = 1.96 and 1.7 on rough bed revealing vertical shifting of maximum interfacial velocity location, that could be because of undular type of hydraulic jump. Note that scattering in data was mainly related to the uncertainties of data processing. The cross-correlation analysis did not give meaningful results at the transition region where the time-averaged velocity was about zero.

Wang (2014) noted that the statistical analysis of instantaneous time lag from the raw probe signals showed small average velocities close to $y(V = 0)$ which supported the continuous velocity profile prediction at the transition region, where the time-averaged velocity was about zero. The idea was valid here for rough bed too, since the data on rough and smooth beds were comparable (Figure 5.24).

The characteristic interfacial velocity data, V_{max} and V_{rec}, are shown in Figures 5.25 and 5.26 as functions of the dimensionless jump toe position and jump roller. Data from previous studies are included for comparison. Overall, present data trend was comparable to the data previous data (Murzyn and Chanson 2009, Chanson 2010, Wang et al. 2014b, Felder and Chanson 2016). The ratio V_{max}/V_1 decreased with increasing distance from the jump toe, and the trend was affected by the Froude number. Close to the jump toe, the magnitude of the dimensionless maximum interfacial velocity was higher on rough bed than on smooth bed (Figure 5.25C and D).

An empirical relationship based upon present data and the data from Felder and Chanson (2016) was developed:

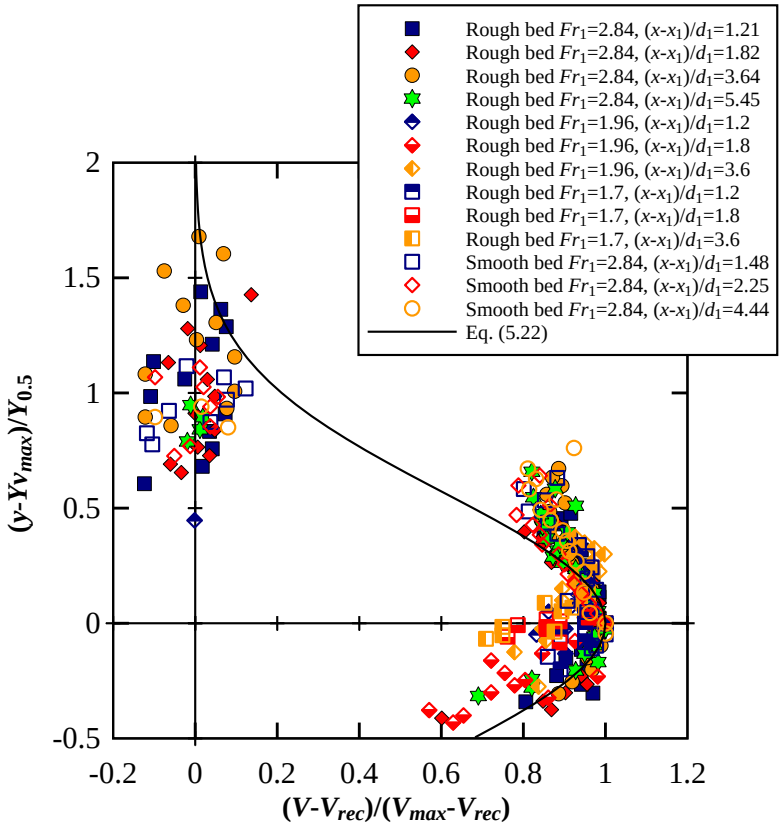

Figure 5.24 Dimensionless velocity distributions in hydraulic jump, comparison between experimental data and Equation (5.21)

$$V_{max}/V = \left(0.88 \times \exp\left(-\frac{1}{3.3 \times (Fr_1 - 1)} \times \frac{x - x_1}{d_1}\right)\right) + k \qquad 2.8 < Fr_1 < 4.3 \qquad (5.23)$$

where k=0.50, 0.55 and 0.3 for smooth, pebbled rough and uniform rough (rubber mat) bed configurations, respectively with R = 0.99, SE = 0.03. Note that several empirical correlations were derived for V_{max}/V_1 based on data on smooth bed, as an example Chanson and Brattberg (2000):

$$V_{max}/V = 1.083 - 0.0268 \frac{x - x_1}{d_1} \qquad \frac{x - x_1}{d_1} < 21.4 \qquad (5.24)$$

The maximum velocity at the jump toe ($x = x_1$) was higher than the cross-sectional average inflow velocity V_1 as observed in the upstream flow (Table 5.2). Note the scatter of data in the hydraulic jump roller which was caused by the highly turbulent nature of the jump roller (Chanson and Brattberg 2000).

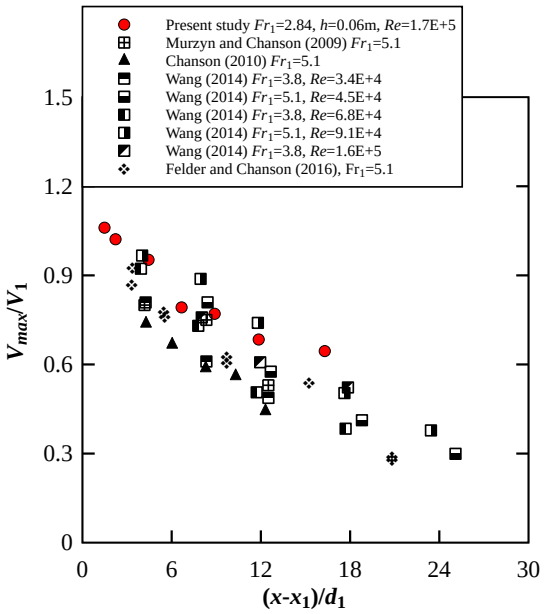

A: As functions of dimensionless longitudinal position, smooth bed

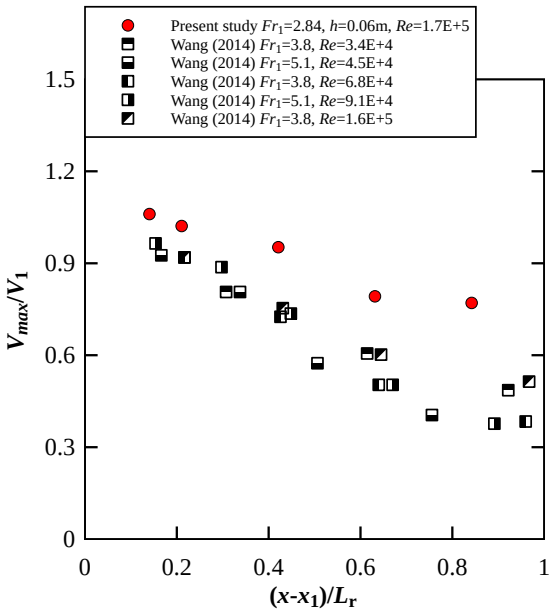

B: As functions of relative longitudinal position in jump roller, smooth bed

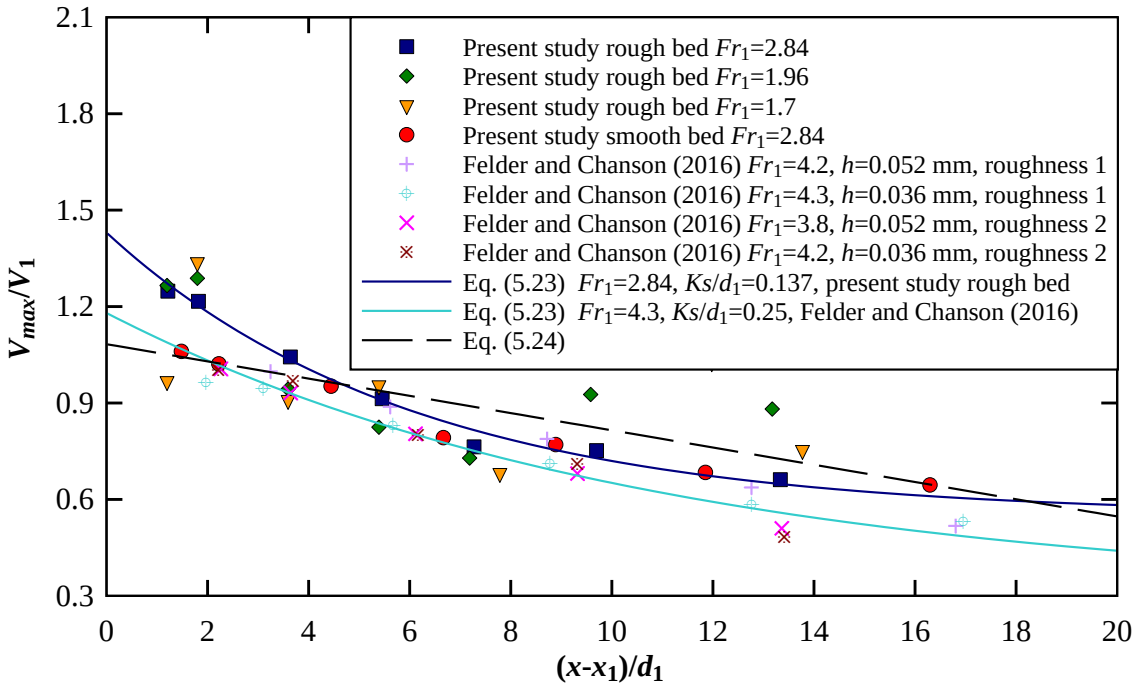

C: As functions of dimensionless longitudinal position, rough bed

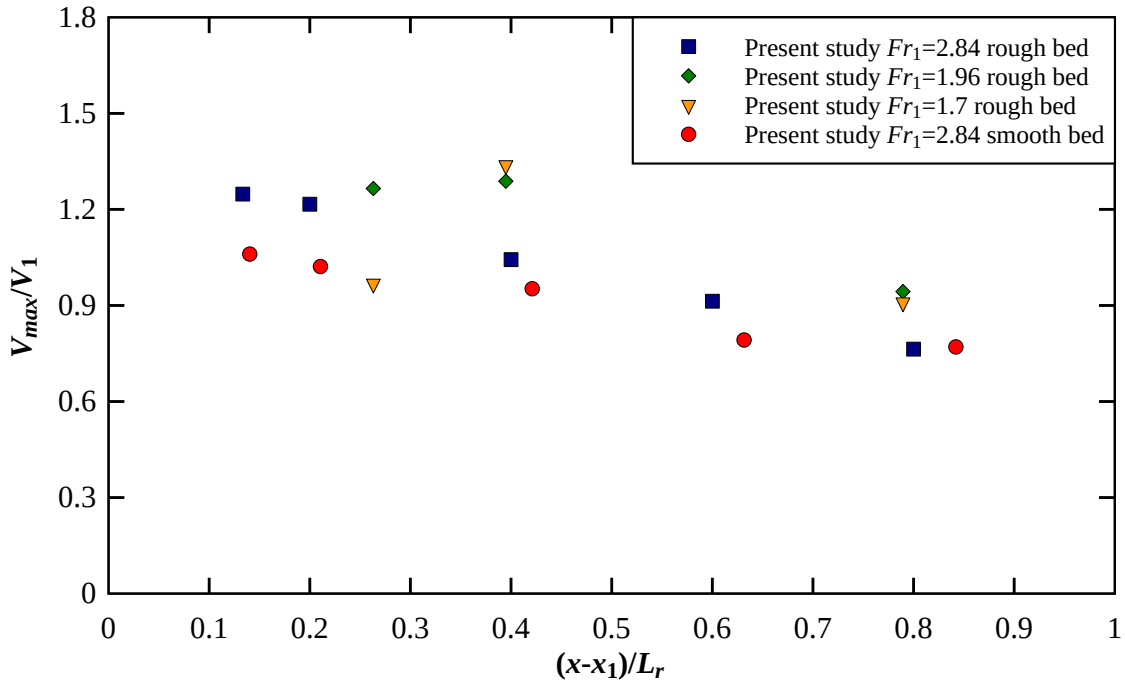

D: As functions of relative longitudinal position in the jump roller, rough bed

Figure 5.25 Maximum interfacial velocity in the shear region, comparison with previous studies and empirical correlations, colored symbols present data

At the end of roller, the ratio of maximum velocity to inflow velocity was 0.7 for both rough and smooth beds with Fr_1 = 2.87 (Figure 5.25D). For comparison, the Bélanger equation yielded V_2/V_1 = 0.28 for Fr_1 = 2.87, where V_2 is the downstream conjugate velocity. The difference between V_{max}/V_1 and V_2/V_1 at $(x\text{-}x_1)/L_r$ = 1 suggested a non-uniform velocity field at the end of jump roller, though the water depth reached a constant d_2. A similar result was reported by Wu and Rajaratnam (1996), who conducted some velocity measurements in the transition region between the roller end and fully developed downstream flow.

The recirculation velocity data are presented based on inflow Froude number in Figure (5.26). The results on smooth bed were quantitatively comparable to the findings of Chanson (2010) for 5.1 < Fr_1 < 11.2, Chachereau and Chanson (2011) for 3.1 < Fr_1 < 5.1 and Wang (2014) 3.1 < Fr_1 < 5.1. On rough bed, the data showed a decreasing trend of variation by increasing the distance from jump toe (Figure 5.26B). The trend was similar to that of Felder and Chanson (2016) for 3.8 < Fr_1 < 4.3 on rough bed.

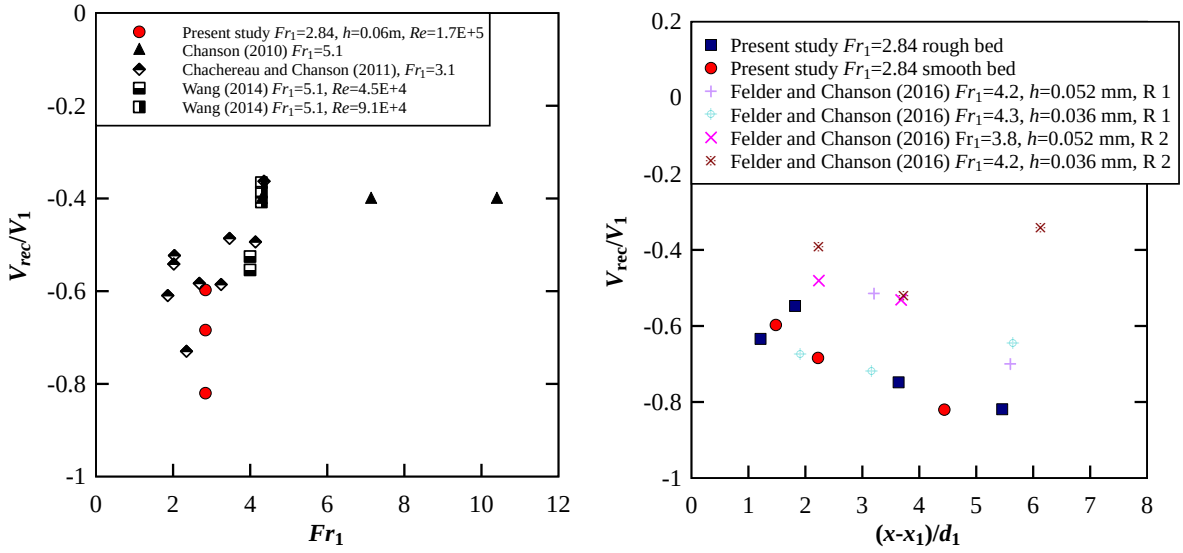

A: as function of the inflow Froude number, smooth bed

B: As functions of dimensionless longitudinal position, rough bed

Figure 5.26 Interfacial velocity in recirculation region, comparison with previous studies, colored symbols present data, *R*1 and *R*2 roughness types 1 and 2 of Felder and Chanson (2016)

The vertical averaged V_{rec}/V_1 was -0.6 and -0.7 on smooth and rough bed, respectively. No flow reversal was detected for the $Fr_1 < 2$ on both rough and smooth bed configurations with different Reynolds numbers from 1.4×10^5 to 1.7×10^5 in the present study since at upper part of the roller, no backward flow was detected by visual observation (Section 4.2).

5.3.7 Comparative analysis of characteristic air-water flow depths

The comparison of characteristic air-water flow depths in the hydraulic jumps with smooth and rough beds is presented in this Section. The dimensionless elevation of the maximum void fraction in the shear region Y_{Cmax}/d_1 is shown in Figure 5.27. The present results were compared to those from previous studies (Chanson 2007, Kucukali and Chanson 2007, Murzyn and Chanson 2009, Wang 2014, Felder and Chanson 2016). The longitudinal trend was comparable for all the data. That is Y_{Cmax}/d_1 increased with increasing longitudinal distance from the jump toe. It was believed that the large eddies within the turbulent shear layer were shifted upward, resulting in an increase in vertical position of the maximum void fraction. There was no significant difference between the rough and smooth bed results close to the jump toe. Further downstream, Y_{Cmax}/d_1 was higher for the rough bed. This was consistent with the reported upward shift of the jump roller (Chapter 4). The present data

were compared to an empirical correlation on smooth bed data proposed by Chanson and Brattberg (2000):

$$\frac{Y_{Cmax}}{d_1} = 1 + 0.108 \times \frac{(x - x_1)}{d_1} \qquad \frac{x - x_1}{d_1} < 29 \qquad (5.25)$$

An empirical relationship was derived using the present data and those from Felder and Chanson (2016) on rough and smooth bed configurations for 2.8 < Fr_1 < 4.3:

$$\frac{Y_{Cmax}}{d_1} = 1 + 0.108 \frac{(x - x_1)}{d_1} + \left(0.05 \frac{(x - x_1)}{d_1} \exp(\frac{K_s}{d_1}) \right) \qquad \frac{x - x_1}{d_1} < 20 \qquad (5.26)$$

The application of the Equations (5.25) and (5.26) for the present rough bed with Fr_1 = 2.84, yielded R = 0.80 and 0.99 and SE =0.065 and 0.044.

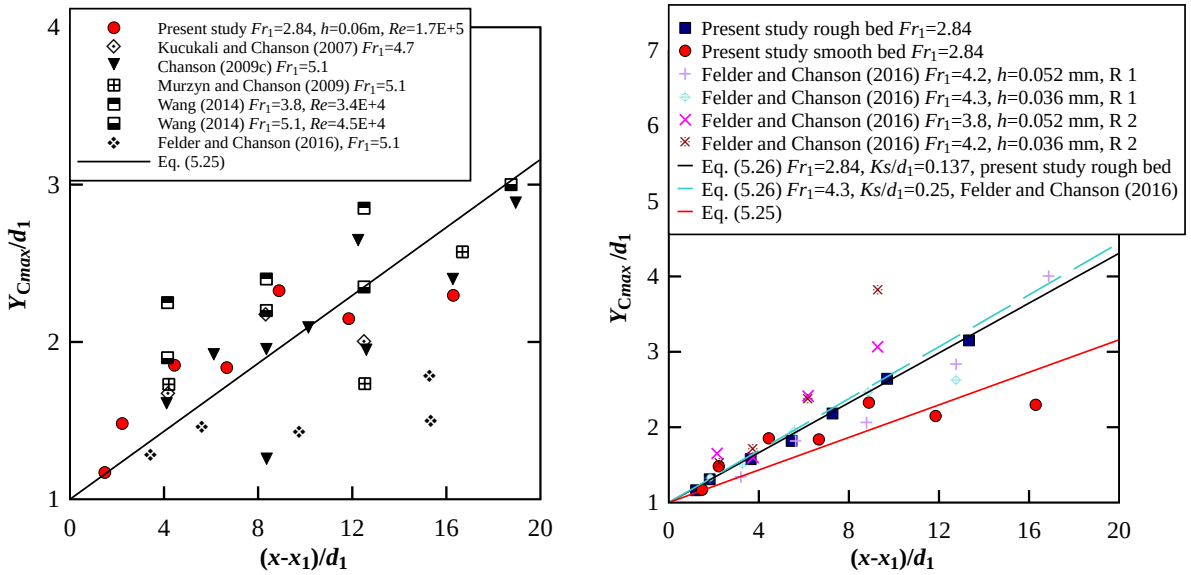

A: Dimensionless longitudinal distribution of the dimensionless elevation of maximum void fraction, smooth bed

B: Dimensionless longitudinal distribution of dimensionless elevation of the maximum void fraction, rough bed

Figure 5.27 Characteristic air-water flow depth in the shear region, comparison with previous studies, colored symbols present data, R_1 and R_2 roughness types 1 and 2 of Felder and Chanson (2016)

The characteristic flow depth with maximum bubble count rate Y_{Fmax} is presented in Figure 5.28 for both bed configurations. The magnitude of Y_{Fmax}/d_1 was lower on rough bed (Figure 5.28B). The increasing trend of Y_{Fmax}/d_1 with the increasing distance from the jump toe could be related to transferring the large eddies to downstream and shifting toward water surface. The results were compared to the empirical relation of Chanson and Brattberg (2000) for

hydraulic jumps on smooth bed:

$$\frac{Y_{Fmax}}{d_1} = 1 + 0.0346 \times \left(\frac{x - x_1}{d_1}\right)^{1.17} \qquad \frac{x - x_1}{d_1} < 29 \tag{5.27}$$

An empirical relationship was extracted from the present data and those from Felder and Chanson (2016) for $2.8 < Fr_1 < 4.3$:

$$\frac{Y_{Fmax}}{d_1} = 1 + 0.0346 \times \left(\frac{x - x_1}{d_1}\right)^{1.17} + \left(0.04 \frac{(x - x_1)}{d_1} \exp(\frac{K_s}{d_1})\right) \tag{5.28}$$

The application of the Equations (5.27) and (5.28) for the present rough bed with Fr_1 = 2.84, yielded R = 0.67 and 0.99 and SE = 0.2 and 0.08.

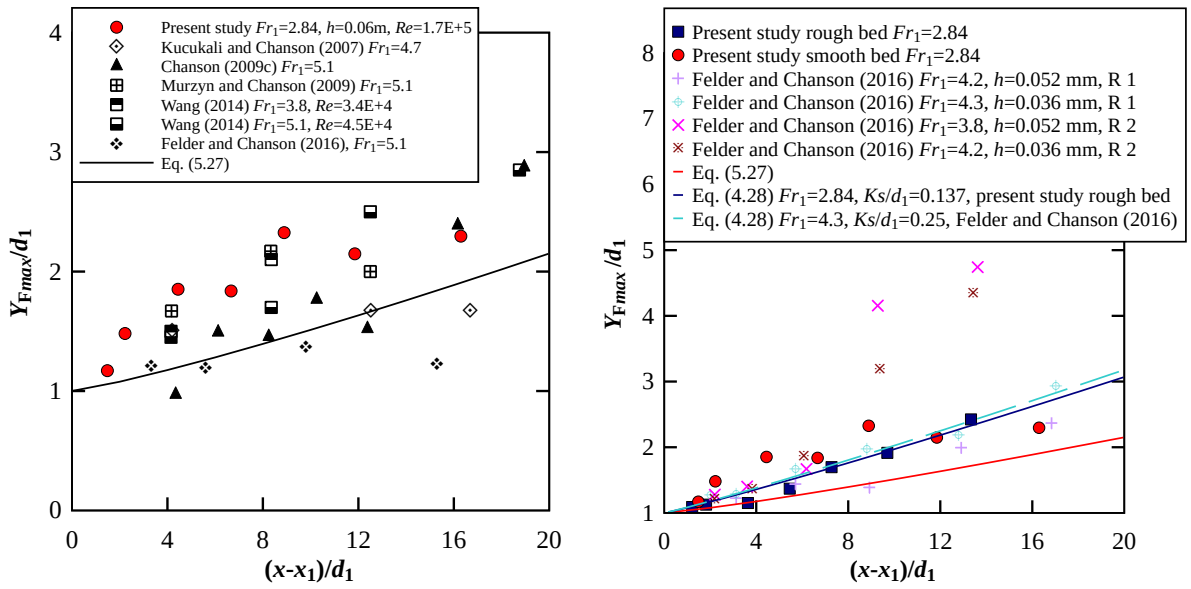

A: Dimensionless longitudinal distribution of the dimensionless elevation of maximum bubble count rate, smooth bed

B: Dimensionless longitudinal distribution of the dimensionless elevation of maximum bubble count rate, rough bed

Figure 5.28 Characteristic flow depth at location with maximum bubble count rate in the shear region, comparison with previous studies, colored symbols present data

Figure 5.29 shows the characteristic flow depth Y_{C*} at the location of the minimum void fraction at the boundary between the shear and recirculation regions. For all configurations, a linear relationship was observed between the dimensionless distance from the jump toe and the dimensionless flow depth at the location of the minimum void fraction.

Furthermore, in the present study the magnitude of Y_{C*}/d_1 was higher on rough bed demonstrating the higher depth of the shear layer. The higher depth of the turbulent shear layer could be linked to the formation of larger vortices in the turbulent shear layer that was associated with larger positive interfacial velocities in the shear layer (Figure 5.25B) and higher negative interfacial velocities in recirculation region (Figure 5.26B).

An empirical relationship was developed based upon the present data and those from Felder and Chanson (2016) on rough and smooth bed configurations for $2.8 < Fr_1 < 4.3$:

$$\frac{Y_{C*}}{d_1} = 1 + 0.007 \times \left(\frac{x - x_1}{d_1}\right) + \left(0.24 \frac{(x - x_1)}{d_1} \exp\left(\frac{K_s}{d_1}\right)\right) \quad (5.29)$$

The application of the Equations (5.29) for the present rough bed with Fr_1 = 2.84, yielded R = 0.94 and SE = 0.09.

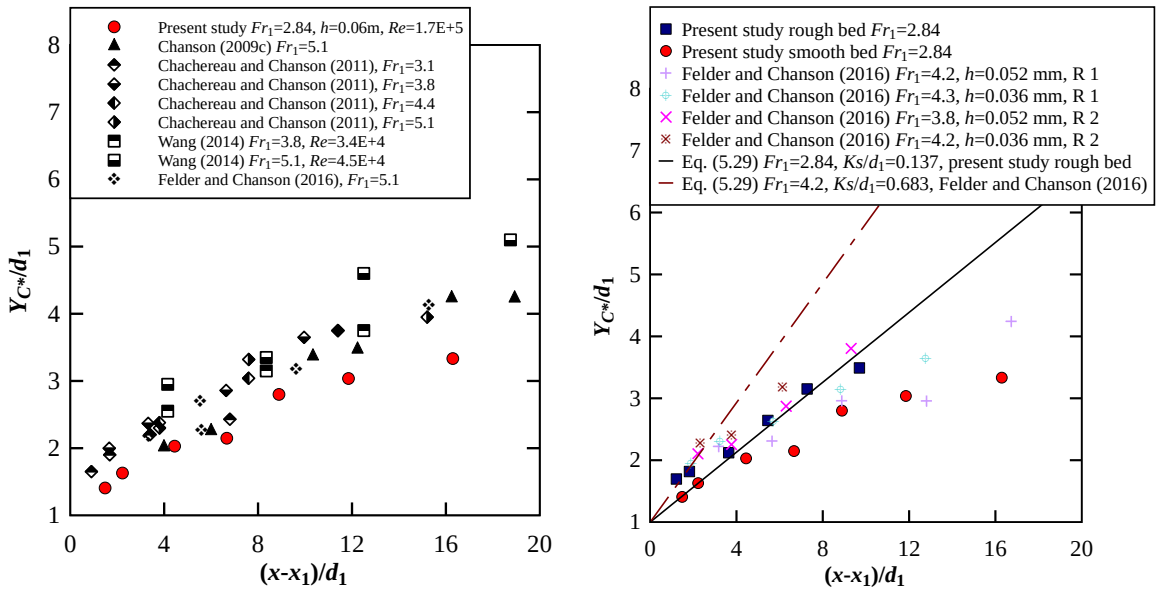

A: As functions of dimensionless longitudinal position, smooth bed

B: As functions of dimensionless longitudinal position, rough bed

Figure 5.29 Characteristic flow depth at local minimum void fraction C* at boundary of shear and recirculation regions, comparison with previous studies, colored symbols present data, $R1$ and $R2$ roughness types 1 and 2 of Felder and Chanson (2016)

The characteristic flow depth Y_{50}, i.e. the flow depth where C = 0.5 and the characteristic flow depth Y_{90} are shown in Figure 5.30 on both rough and smooth bed configurations. Previous studies of Chanson (2009c), Chachereau and Chanson (2010), Wang (2014), and Felder and Chanson (2016) were added for comparison. A pseudo-linear relationship was

observed between the dimensionless distance from the jump toe and the dimensionless flow depth at the locations of C = 0.5 and C = 0.9. Additionally, the magnitude of Y_{90}/d_1 was higher on rough bed (Figure 5.30B left). The characteristic depths Y_{50}, Y_{90} were related to the recirculation region while Y_{C*} is the characteristic flow depth in the lower boundary of the recirculation region.

An empirical relationship was extracted from the present data and those from Felder and Chanson (2016) on rough and smooth bed configurations for 2.8 < Fr_1 < 4.3:

$$Y_{90}/d_1 = \left(\frac{x - x_1}{d_1}\right)^{0.512} + \exp\left(\frac{K_s}{d_1}\right) \quad (5.30)$$

$$Y_{50}/d_1 = \exp\left(-\frac{\frac{x - x_1}{d_1}}{Fr_1}\right)^{0.236} \quad (5.31)$$

A good agreement was found between the empirical relationships and the experimental data. The application of the Equations (5.30) and (5.31) for the present rough bed with Fr_1 = 2.84, yielded R = 0.96 and 0.97, SE = 0.11 and 0.13 for Y_{90}/d_1 and Y_{50}/d_1, respectively.

Figure 5.31 depicts the characteristic flow depth Y_{Vmax}, i.e. the flow depth where interfacial velocity had the maximum value. The comparison was made only with studies on smooth bed including Chanson and Brattberg (2000), Murzyn and Chanson (2009), Chachereau and Chanson (2010), Wang (2014).

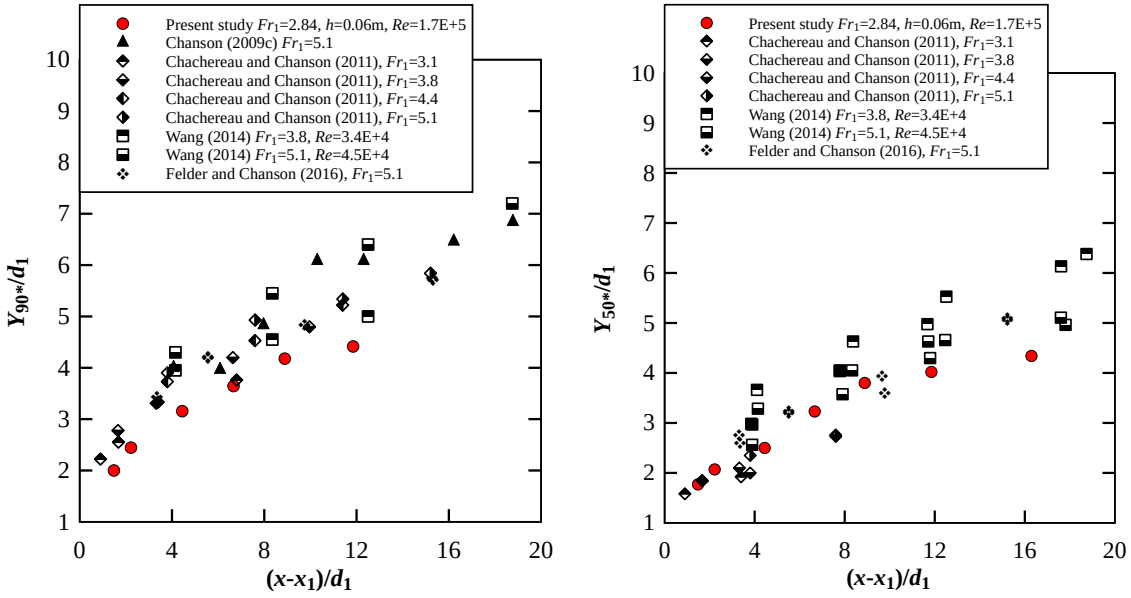

A: As functions of dimensionless longitudinal position, smooth bed

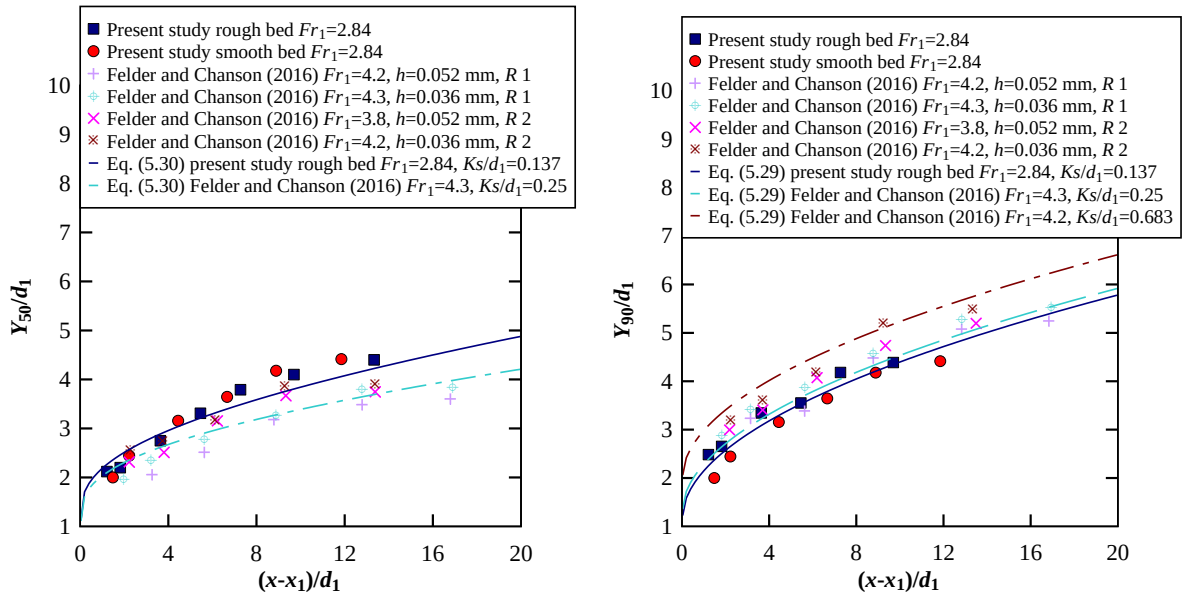

B: As functions of dimensionless longitudinal position, rough bed

Figure 5.30 Characteristic flow depths Y_{90} and Y_{50}, comparison with previous studies, colored symbols present data. R_1 and R_2 stands for the roughness type 1 and 2

The average value of Y_{Vmax}/d_1 was 0.85 and 0.8 for rough and smooth bed configurations, respectively, with slightly higher values on rough bed.

Overall, based on the void fraction and bubble count rate profiles measured with phase-detection probes, a series of characteristic elevations were specified through the vertical cross section of jump roller, so that:

$$1 < \frac{Y_{V\max}}{d_1} < \frac{Y_{F\max}}{d_1} < \frac{Y_{C\max}}{d_1} < \frac{Y_{C^*}}{d_1} < \frac{Y_{50}}{d_1} < \frac{Y_{90}}{d_1} \quad (5.32)$$

These findings were in agreement with previous studies on smooth bed (Chanson and Brattberg 2000, Murzyn and Chanson 2007, Wang 2014, 2015) and on rough bed (Felder and Chanson 2016, 2018). The difference between smooth and rough bed was the higher depth of turbulent shear layer because of formation of larger eddies which were advected in the turbulent shear layer resulting in higher characteristic depths.

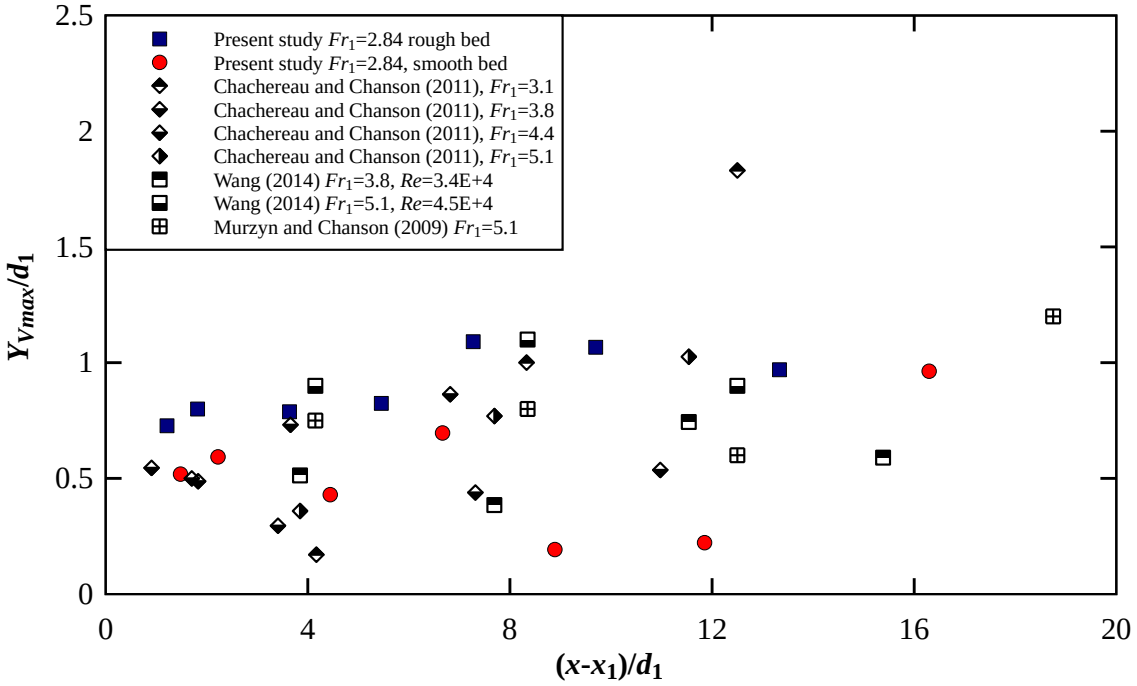

Figure 5.31 Characteristic flow depths Y_{Vmax} as functions of dimensionless longitudinal position, comparison with previous studies, colored symbols present data

5.4 Summary

The time-averaged void fraction, bubble count rate, air-water interfacial velocity, and characteristics flow depths were studied. The spatial distributions of these two-phase flow properties, as well as the effects of Froude and Reynolds numbers, were investigated on both rough and smooth bed configurations. A comprehensive comparative analysis of hydraulic jumps between the results of present study with those from literature showed the following features:

- Upstream of the jump toe, the time-averaged void fraction and bubble count rate as well as the interfacial velocity and turbulent intensity distributions were presented in terms of profile shapes in a vertical cross-section;
- Downstream of the jump toe, the distributions of two-phase flow properties observed in hydraulic jumps on both rough and smooth bed configurations were comparable. A shear layer region close to the channel bed and a recirculation region in the upper part of the hydraulic jump was observed;
- In both shear layer and recirculation regions, some differences were observed for hydraulic jumps properties between rough and smooth bed configurations;

- The roughness resulted in larger maximum and mean void fractions within a cross-section. In terms of local void fraction minimum values, between the shear layer and the recirculation regions, no significant difference was observed between rough and smooth bed. Further downstream, the void fraction in a cross-section were comparable on rough and smooth bed configurations;
- The effect of roughness led to increasing the momentum exchange between the boundary layer and the overlying shear layer, especially close to the jump toe. The bed roughness induced the bubble break-up processes into smaller bubbles and the formation of large-scale eddies which were transported downstream entrapping the air bubbles. Comparing to smooth bed and rubber mat roughness (Felder and Chanson 2016, 2018), the pebbled roughness resulted in larger dimensionless maximum bubble count rate;
- Some characteristic air-water flow parameters were comparable on both rough and smooth bed configurations. This included several characteristic flow depths, the magnitude of maximum interfacial velocities in a cross-section and the mean void fraction in a cross- section. Furthermore, all the void fraction distributions were in relatively close agreement with the advection-diffusion equation for the hydraulic jump;
- The increasing trend in characteristic elevations along the roller was a pseudo-linear process in the shear region and followed a self-similar depth increase trend above the roller.

6 TURBULENCE IN THE AIR-WATER FLOW REGION

6.1 Presentation

Energy dissipation and fluid mixing in the highly turbulent flow motion might be considered advantageous processes. The turbulence in hydraulic jump has two noteworthy features: (a) its strong interaction with air entrainment and (b) its wide range of time and length scales. Herein the turbulence in the jump roller was investigated based upon intrusive air-water flow measurements. The signals of phase-detection probes were analysed statistically using auto- and cross-correlation functions, and the turbulence properties were derived from the correlation analysis (Chanson and Carosi 2007a,b). It should be considered that the turbulence process was not a truly random process because it involved the pseudo-periodic motions of the flow such as deformations of free-surface and advections of large eddy (Wang 2014), Wang et al. (2014). The effects of such instabilities in flow could led to unusual large turbulence levels and characteristic turbulent scales, especially in the free-surface region. Wang et al. (2014) quantified the effect of the flow instabilities and fast random turbulence by means of a triple decomposition of the phase-detection probe signal.

In this Chapter, the basic turbulence properties derived from the raw phase-detection probe signal are presented. The investigated turbulent properties included turbulence intensity, correlation time scales, advection and length scale. These parameters were measured in longitudinal direction for both rough and smooth bed configurations.

6.2 Turbulence intensity

6.2.1 Turbulence intensity upstream of jump toe

The upstream turbulent intensity distributions is presented in Figure 6.1 for both rough and smooth beds. On rough bed, some small turbulence levels appeared in the bubbly flow region close to the bed as well as in the spray region close to the free-surface. The turbulence levels close to the channel bed showed a larger magnitudes compared to turbulence intensities in mono-phase flows and in air-water flows on spillways with smooth bed (Felder and Chanson 2013).

The largest turbulence levels were observed in the intermediate flow region which correspond

to void fractions of 0.45 < C < 0.75, independent of the bed roughness. Furthermore, on smooth bed, the turbulent intensity near the water surface was linked to the bubble count rate distribution (Figure 5.4). For the same inflow Froude number, *Tu* on rough bed was slightly greater than smooth bed. A comparison of the turbulence intensity distributions for different discharges suggested that the turbulence intensities were elevated in the regions with the largest bubble count rate. Overall, vertical *Tu* profiles were relatively similar to bubble count rates as observed in the study by Felder and Chanson (2016).

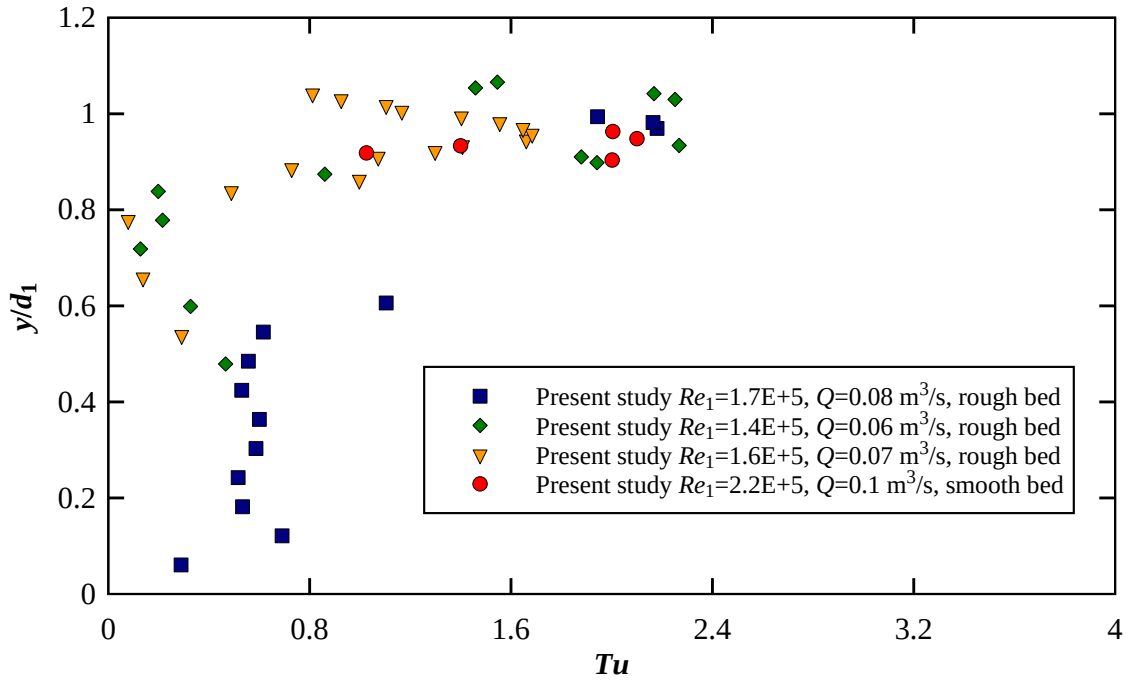

Figure 6.1 Turbulence intensity distributions upstream of hydraulic jump with bed roughness

6.2.2 Turbulence intensity downstream of jump toe

Turbulence intensities were investigated for three inflow Froude numbers with the same intake aspect ratio h/W = 0.13 and inflow length x_1/h = 16.67 on rough bed and one inflow Froude number on smooth bed with the intake aspect ratio h/W = 0.12 and inflow length x_1/h = 16.67 (Figure 6.2). The data were measured at seven cross sections of the jump roller on the centreline of the channel. Typical distributions for both rough and smooth bed configurations, revealed an increase in turbulence intensity with increasing elevation in the lower part of shear flow, approximately between the channel bed and the elevation of local maximum void fraction Y_{Cmax}. In this region, for Fr_1 = 2.84 for both bed type, *Tu* increased rapidly from about 0 to 1 within a thin boundary layer next to the invert then increased

progressively till $y \approx Y_{Cmax}$. The increasing rate varied at different longitudinal positions, giving the largest turbulence intensity $Tu \approx 2.5$ close to the jump toe. In the upper part of shear flow ($Y_{Cmax} < y < y^*$) as well as in the entire recirculation region ($y > y^*$), the turbulence intensity became unusually large and scattered including the values over 4 to 5. Such large velocity turbulence could be associated to the impact of large-scale fluctuating motions of the jump roller which led to some computation errors. Due to uncertainty in the cross-correlation function, the correlation method cannot solve properly the velocity data about zero velocity and likely led to inaccurate estimation of Tu magnitude. The largest anomaly was observed about $y \approx Y_{50}$, namely near the time-averaged water elevation above the roller.

For $Fr_1 = 2.84$ on both rough and smooth bed, larger magnitudes of Tu were observed in both shear layer and recirculation regions. For $Fr_1 = 1.96$ and 1.7 on rough bed, close to the jump toe larger magnitudes of Tu were observed in the shear layer while further downstream larger magnitudes of Tu were observed near the surface. Larger magnitudes of Tu in the turbulent shear layer possibly corresponded to the maximum bubble count rate while in the recirculation region as well as near the surface were linked to the impact of large-scale fluctuating motions of the jump roller.

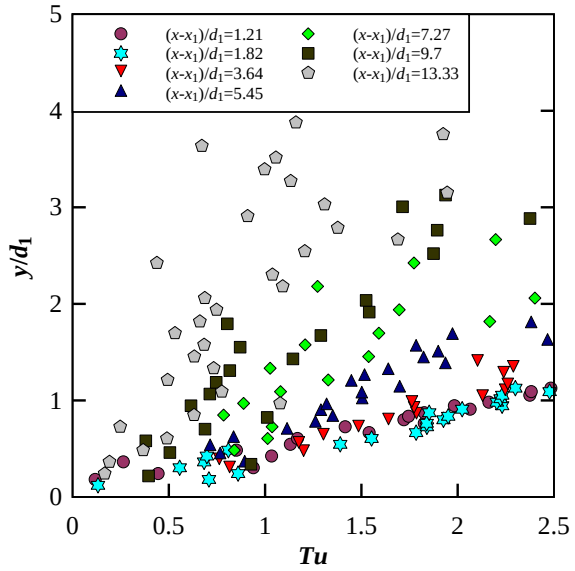

A: Rough bed, Run BR3, $Q = 0.1$ m^3/s,
$d_1 = 0.0825$ m, $Fr_1 = 2.84$, $Re_1 = 2.2$E+5

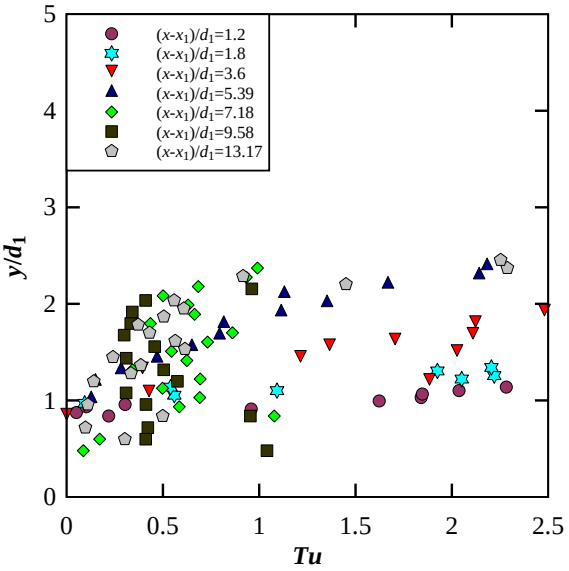

B: Rough bed, Run BR2, $Q = 0.07$ m^3/s,
$d_1 = 0.0835$ m, $Fr_1 = 1.96$, $Re_1 = 1.6$E+5

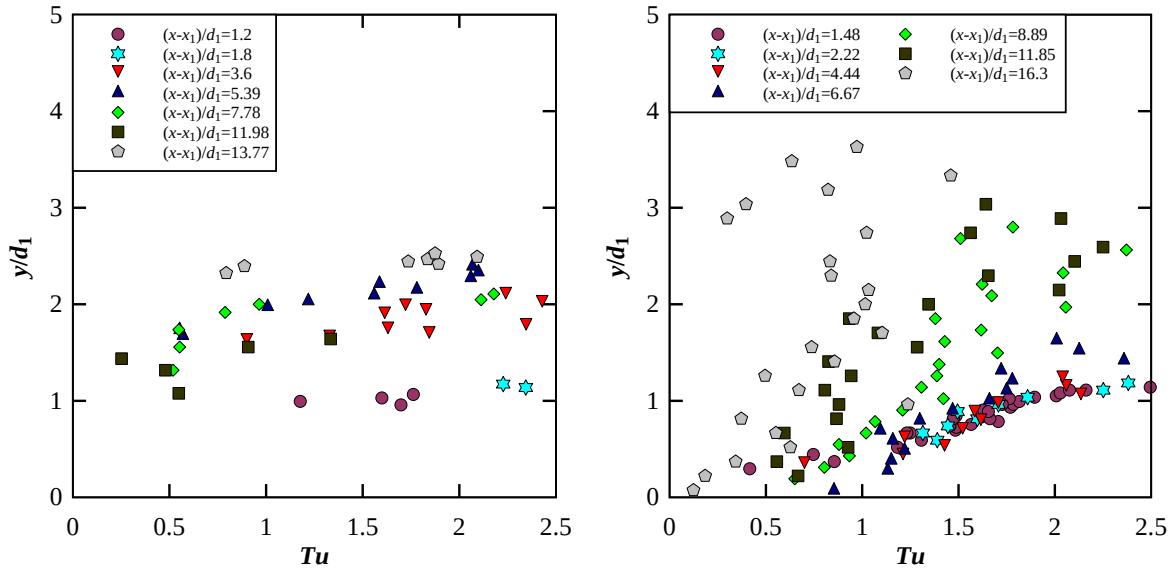

C: Rough bed, Run BR1, Q = 0.061 m^3/s, d_1 = 0.0835 m, Fr_1 = 1.7, Re_1 = 1.4E+5

D: Smooth bed, Run BS1, Q = 0.078 m^3/s, d_1 = 0.0675 m, Fr_1 = 2.84, Re_1 = 1.7E+5

Figure 6.2 Turbulence intensity measured on the channel centerline downstream of the hydraulic jump

A comparison of turbulence intensity distributions in the jump roller for Fr_1 = 2.84 on both rough and smooth bed is presented in Figure 6.2. The data included both upstream of the roller toe and in the hydraulic jump roller. The characteristic dimensionless flow depth Y_{90}/d_1 was added to the Figure 6.3. On both rough and smooth bed with the same inflow Froude number, the turbulence intensity was investigated in the turbulent shear layer. The results highlighted some very high levels of turbulence, possibly linked with the bubble induced turbulence in the jump shear region. Higher magnitudes of *Tu* were observed on rough bed in the turbulent shear layer especially close the jump toe that could be associate to higher rate of bubble count on rough bed (Section 5.3.3).

Overall, on both rough and smooth bed configurations, in the areas with higher bubble count rate, the turbulent intensity was higher. Further downstream of the jump toe, the distribution and the maximum value in the vertical direction were comparable on both rough and smooth bed configurations.

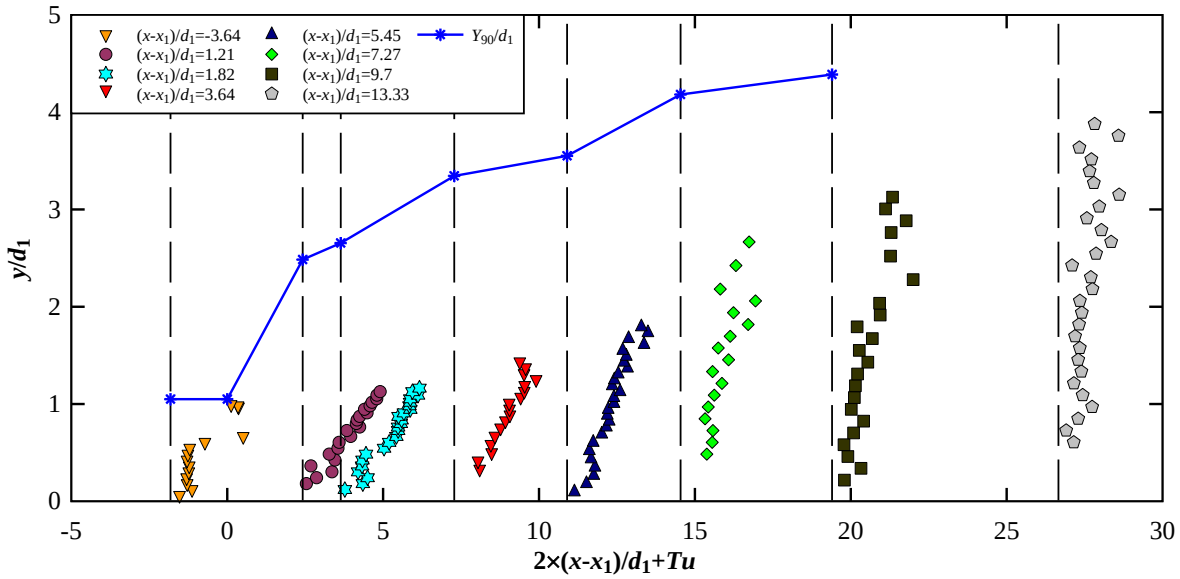

A: Rough bed, Run BR3, Q = 0.1 m^3/s, d_1 = 0.0825 m, Fr_1 = 2.84, Re_1 = 2.2E+5

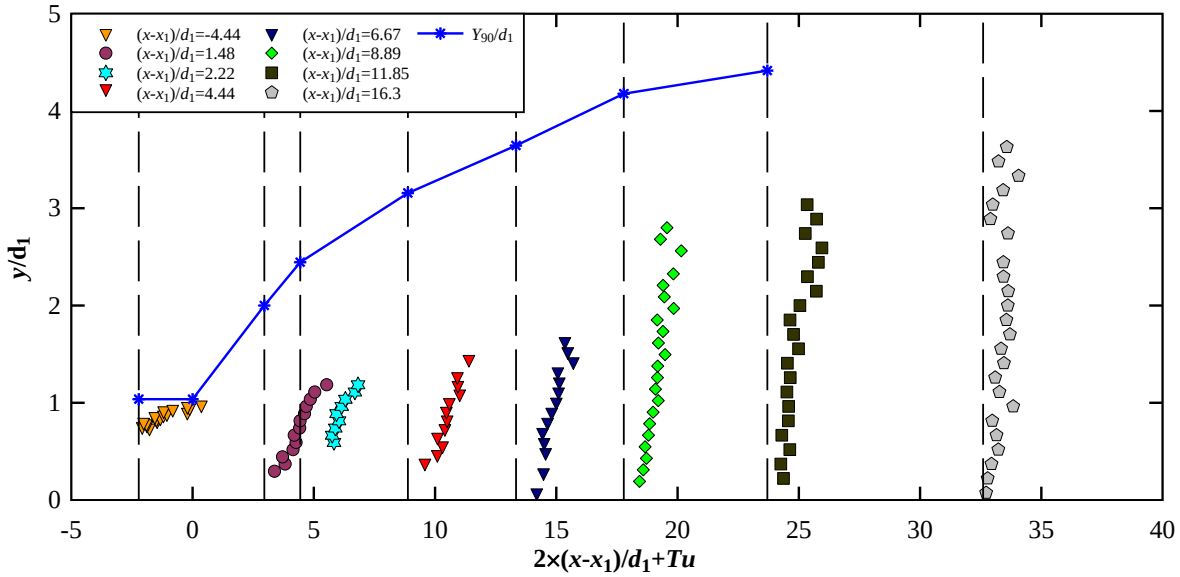

B: Smooth bed, Run BS1, Q = 0.078 m^3/s, d_1 = 0.0675 m, Fr_1 = 2.84, Re_1 = 1.7E+5

Figure 6.3 Turbulent intensity distributions upstream and in hydraulic jumps, dashed vertical lines illustrate y-axis for the respective velocity data; comparison with characteristic flow depth Y_{90}/d_1

Recent investigations demonstrated that the roller was a highly unsteady turbulent region and both the roller toe and free surface constantly fluctuated with time and space (Wang and Chanson 2015, Chanson 2010, 2015, Felder and Chanson 2016). The roller was a source of both air entrainment and vorticity. Strong interactions occurred between entrained bubbles

and turbulent structures. This process led to a complex interplay between instantaneous free-surface deformations, velocity fluctuations, interfacial processes including breakup and coalescence and dissipative processes as observed in breaking bores (Wang et al. 2015, 2017).

The turbulence intensity at the characteristic elevations of maximum bubble count rate, $Tu(y = Y_{Fmax})$ is depicted in Figures 6.4. Larger magnitudes of $Tu(y = Y_{Fmax})$ were consistently observed in the first half of the roller with the average magnitude of $Tu(y = Y_{Fmax})$ = 2.3 and 2.2 on present rough and smooth bed, respectively. For the second half of roller, the magnitude of *Tu* longitudinally decreased to 1.4 at the end of roller (Figure 6.4A). Further downstream of the jump toe, the decreasing rate on present rough bed, as well as on roughness type 2 (Fr_1=3.8) for Felder and Chanson (2016), was higher than that on smooth bed (Figure 6.4B). This could be associated with a higher rate of energy dissipation on rough bed, resulting in a shorter length of roller on rough bed (Section 4.4).

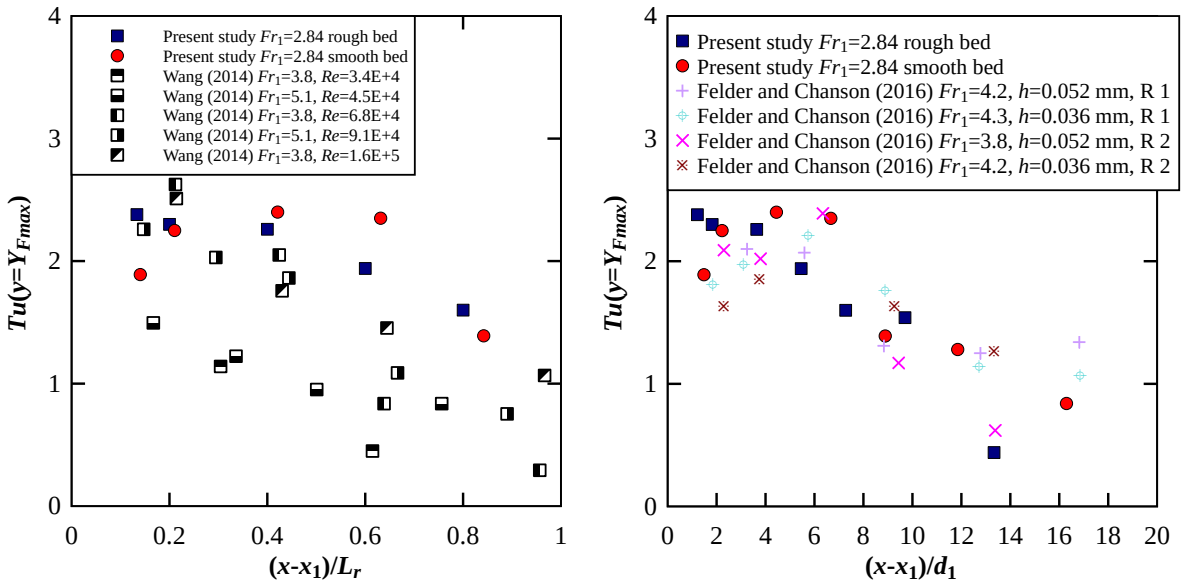

A: As functions of dimensionless roller length

B: As functions of dimensionless distance from the jump toe

Figure 6.4 The turbulence intensity at the characteristic elevations of maximum bubble count rate. *R*1 and *R*2 roughness types 1 and 2 by Felder and Chanson (2016)

Figure 6.5 highlighted the turbulence intensity at the characteristic elevations of maximum velocity $Tu(y = Y_{Vmax})$, on both rough and smooth bed configurations. The results were compared with Wang (2014) and Felder and Chanson (2016) on different channel beds.

Overall, the trend was the same on both bed configurations. Within the jump roller, the characteristic turbulence level decreased with increasing distance from the jump toe. Furthermore, $Tu(y = Y_{Vmax})$, on rough bed was higher than on smooth bed, especially close to the jump toe.

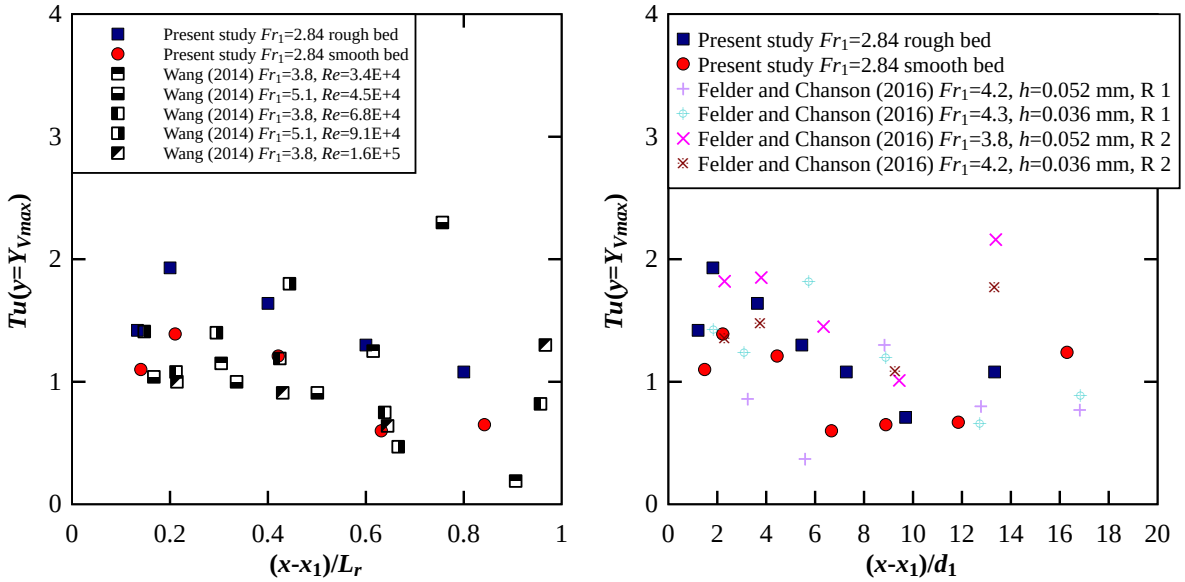

A: As functions of dimensionless roller length

B: As functions of dimensionless distance from the jump toe

Figure 6.5 The turbulence intensity at the characteristic elevations of maximum interfacial velocity. *R*1 and *R*2 roughness types 1 and 2 by Felder and Chanson (2016)

Figure 6.6 presents turbulence intensity data as a function of the dimensionless bubble count rate. The turbulence data were correlated to the dimensionless bubble frequency by (Chanson and Toombes 2002):

$$Tu = k'(\frac{Fd_c}{V_c})^{0.295} \quad (6.2)$$

where k' is a constant which was a function of the longitudinal distance from the jump toe. In a rectangular channel, $d_c = (q_w^2/g)^{1/3}$ and $V_c = (gd_c)^{0.5}$ where q_w is the water discharge per unit width and g is the gravity acceleration. Equation 6.2 implied an increase in turbulence associated with the number of entrained particles so that the maximum turbulent intensity was corresponded to the maximum bubble count rate. For bubble count rates $2 < Fd_c/V_c < 18$, the result of Equation 6.2 and Figure 6.5 yielded $1 < Tu < 2.5$ which was close to the

observations of low bubble count rates in skimming flows on stepped chutes (Chanson and Toombes 2002) and in a hydraulic jump on rubber mat rough bed (Felder and Chanson 2016).

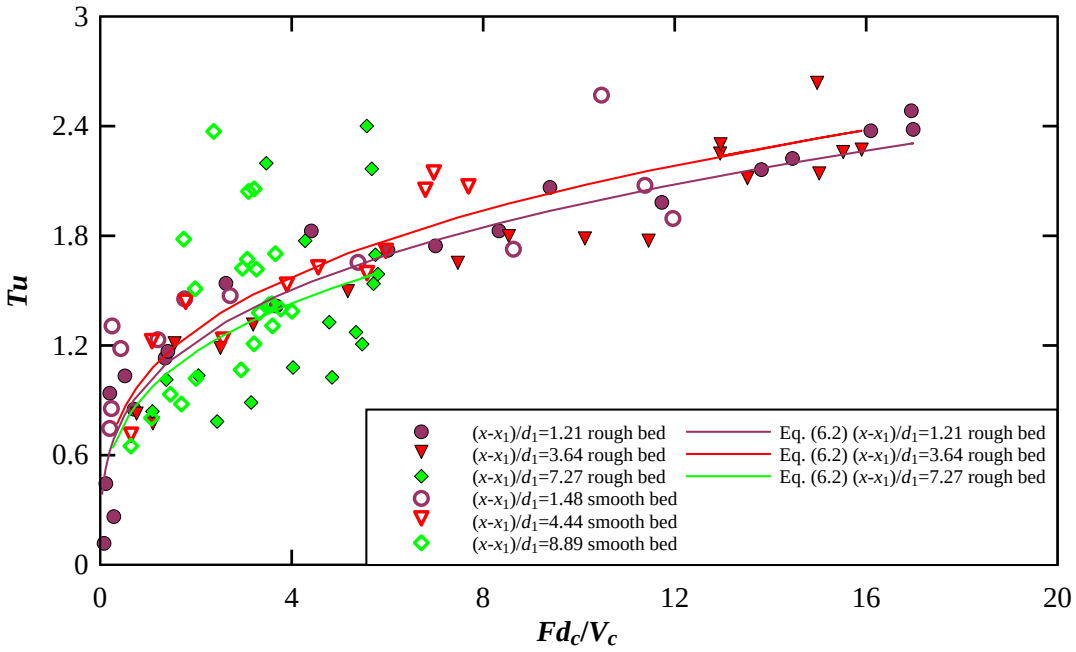

Figure 6.6 Relationship between turbulent intensity and dimensionless bubble count rate

6.3 Correlation time scales in the jump roller

The correlation time scales were derived from the integration of the correlation functions from the maximum to the first zero-crossing point as explained in Equations 3.9-3.10. The auto-correlation time scale T_{xx} provided some information on the air-water flow characteristic in the form of a measure of memory time scale. The longitudinal cross-correlation time scale $T_{xx'}$ was some kind of "lifetime" of the structures over a separate distance Δx.

Figure 6.7 presents the dimensionless auto-correlation time scale $T_{xx} \times V_1/d_1$, and longitudinal cross-correlation time scale $T_{xx'} \times V_1/d_1$ on both bed configurations. The characteristic dimensionless flow depth Y_{90}/d_1 was added to the Figure 6.7. T_{xx} and $T_{xx'}$ were investigated in the vertical direction on both rough and smooth bed configurations with the same inflow Froude number.

As seen in Figure 6.7, in the turbulent shear layer with high rate of bubbles, both correlation time scales increased gradually with increasing vertical elevation, showing the largest values

corresponded to the large-size vortices. In the recirculation region, the significant observed increases in T_{xx} and $T_{xx'}$ might be related to the free-surface dynamics. The largest values were seen near the mean water elevation, in the order of 10 ms. That was one order of magnitude larger than the values in the lower shear region (~ 1 ms). Note that the recirculation region consisted of a bubbly flow region below and a splashing free-surface area above the mean water elevation. The mean water elevation was recorded based upon the time-averaged free-surface profiles above the invert. The ratio of auto-correlation time scale to cross-correlation time scale $T_{xx}/T_{xx'}$ showed the maximum value of 1.2 and 1.17 at $(x\text{-}x_1)/d_1$ = 1.21 and 1.48 on rough and smooth bed, respectively. Further downstream of the jump toe, the maximum rate of $T_{xx}/T_{xx'}$ decreased to about 1.0 on both rough and smooth bed configurations.

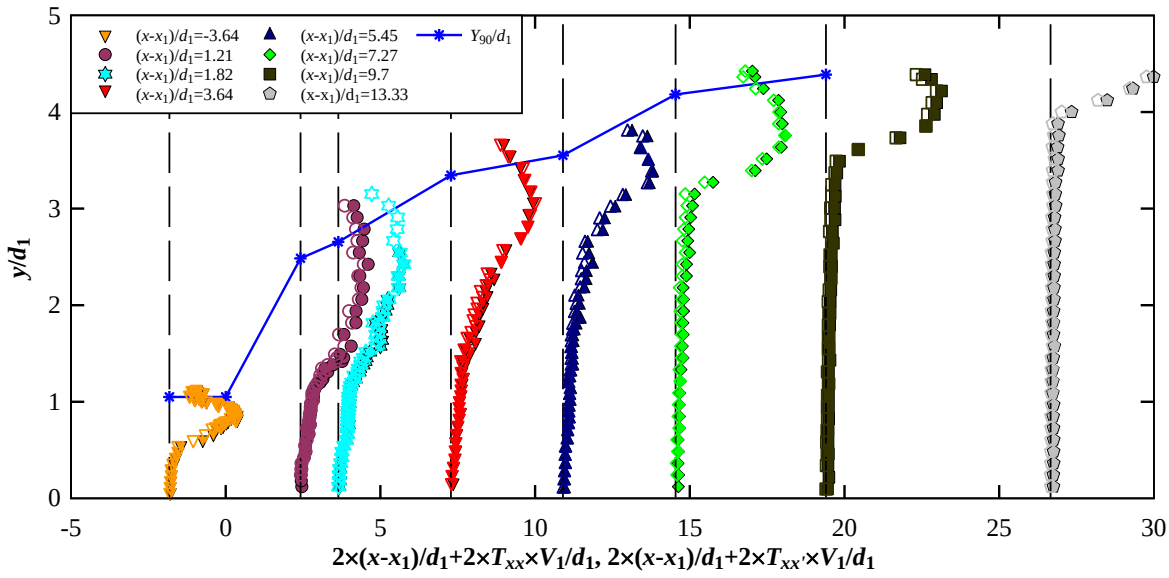

A: Rough bed, Run BR3, Q = 0.1 m^3/s, d_1 = 0.0825 m, Fr_1 = 2.84, Re_1 = 2.2E+5

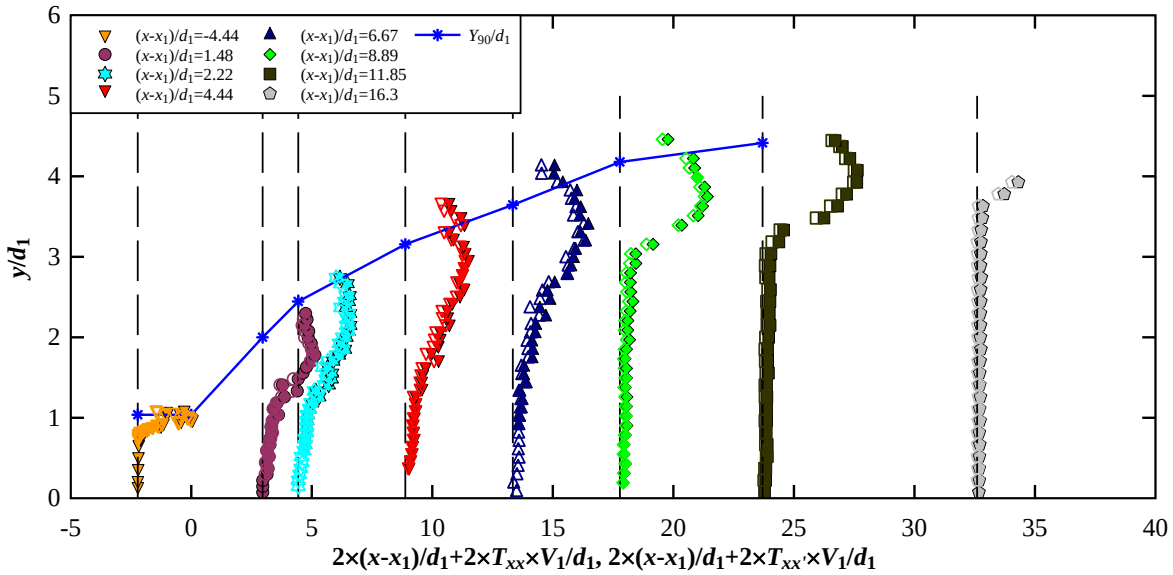

B: Smooth bed, Run BS1, Q = 0.078 m^3/s, d_1 = 0.0675 m, Fr_1 = 2.84, Re_1 = 1.7E+5

Figure 6.7 Auto-correlation time scale (filled symbols), longitudinal cross-correlation time scale (empty symbols), in longitudinal direction, dashed vertical lines illustrate y-axis for the respective velocity data; comparison with characteristic flow depth Y_{90}/d_1

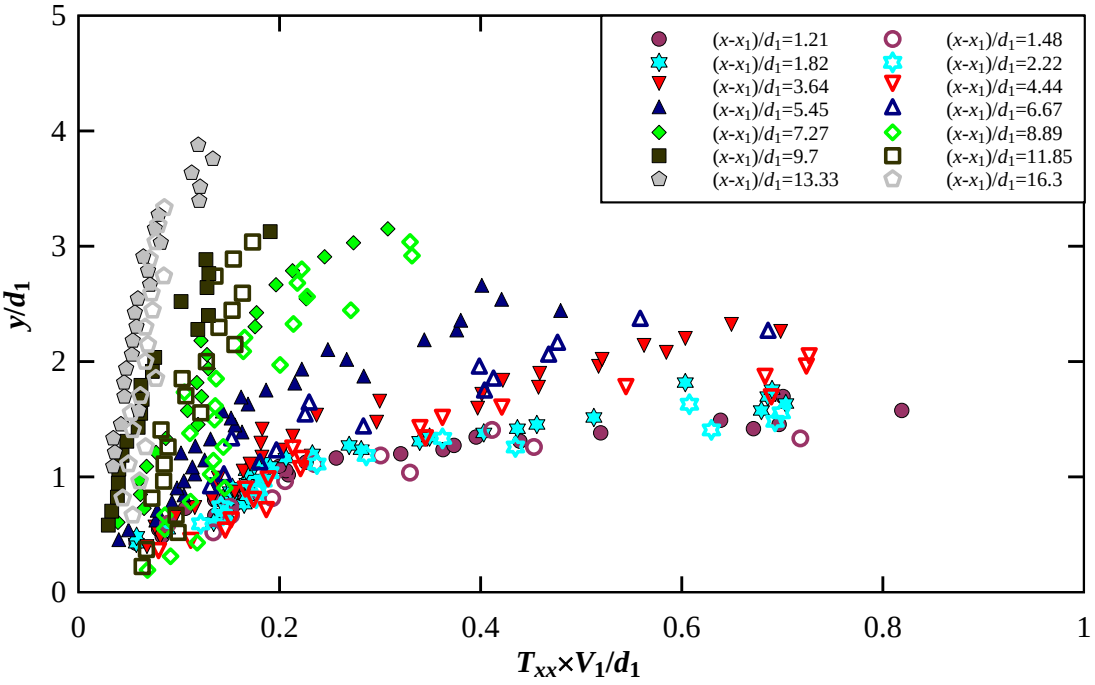

A: Dimensionless auto-correlation time scales

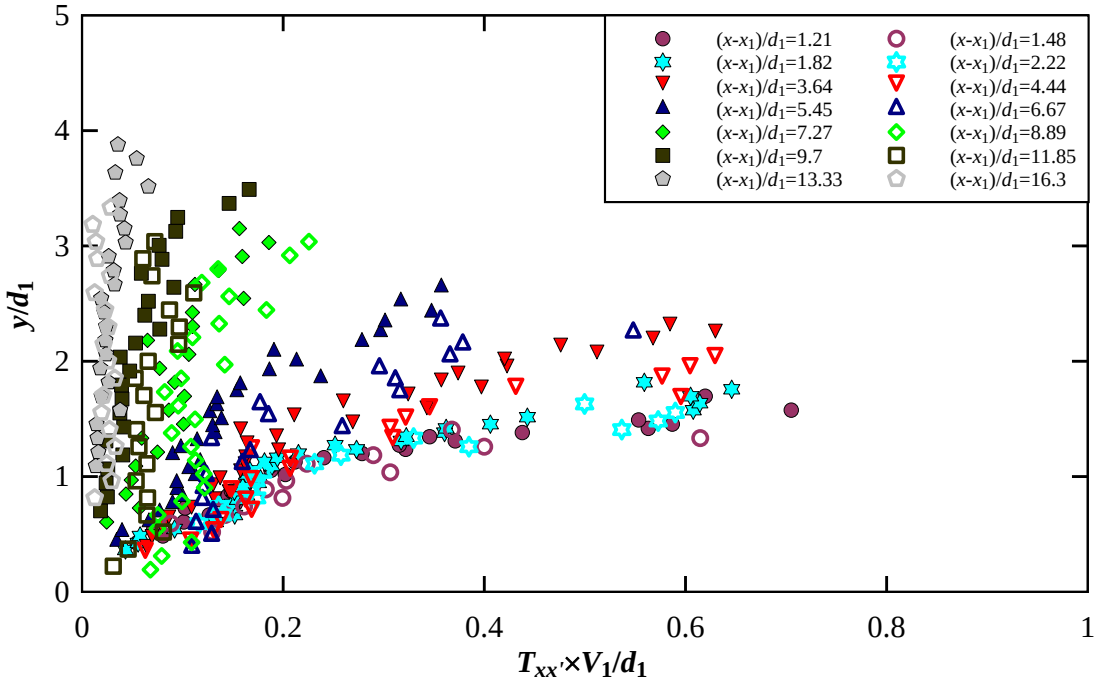

B: Dimensionless cross-correlation time scales

Figure 6.8 Dimensionless correlation time scales between rough bed (Run BR3, Q = 0.1 m^3/s, d_1 = 0.0825 m, Fr_1 = 2.84, Re_1 = 2.2E+5) and smooth bed (Run BS1, Q = 0.078 m^3/s, d_1 = 0.0675 m, Fr_1 = 2.84, Re_1 = 1.7E+5). Filled symbols rough bed

Figure 6.8 shows the comparison between the dimensionless auto-correlation time scale $T_{xx}\times V_1/d_1$, and longitudinal cross-correlation time scale $T_{xx'}\times V_1/d_1$ in different cross section downstream of jump toe. Overall the trend of variation was the same for both correlation time scales, decreased with increasing distance from the jump toe. Furthermore, close to the jump toe, both correlation time scales $T_{xx}\times V_1/d_1$ and $T_{xx'}\times V_1/d_1$ increased rapidly to the maximum values in the turbulent shear layer. Close to the jump toe, at $(x\text{-}x_1)/d_1$ = 1.21 and 1.48 on rough and smooth bed, respectively, the maximum magnitude of $T_{xx}\times V_1/d_1$ was 0.82 and 0.73 on rough and smooth bed configurations, respectively, while the maximum magnitude of $T_{xx'}\times V_1/d_1$ was 0.7 and 0.63 on rough and smooth bed, respectively. Further downstream of the jump toe at $(x\text{-}x_1)/d_1$ = 13.3 and 16.3 on rough and smooth bed, respectively, $T_{xx}\times V_1/d_1$ showed the maximum magnitude of 0.13 and 0.1, $T_{xx'}\times V_1/d_1$ showed the maximum magnitude 0.08 and 0.05 on rough and smooth bed, respectively. These findings were in agreement with distribution of turbulent intensity (Figure 6.2), especially close to the jump toe. The results presented here were consistent with previous results on hydraulic such as Chanson (2007) and Wang (2014) on smooth bed and Felder and Chanson (2016) on rough bed.

6.4 Advective length scale in jump roller

The advective length scale L_{xx} was the product of the auto-correlation time scale and local time-averaged interfacial velocity. It represented a characteristic size of the turbulent structures advected in the longitudinal direction. Figures 6.9 and 6.10 present the vertical distributions of advection length scales on smooth and rough bed with the same inflow Froude numbers.

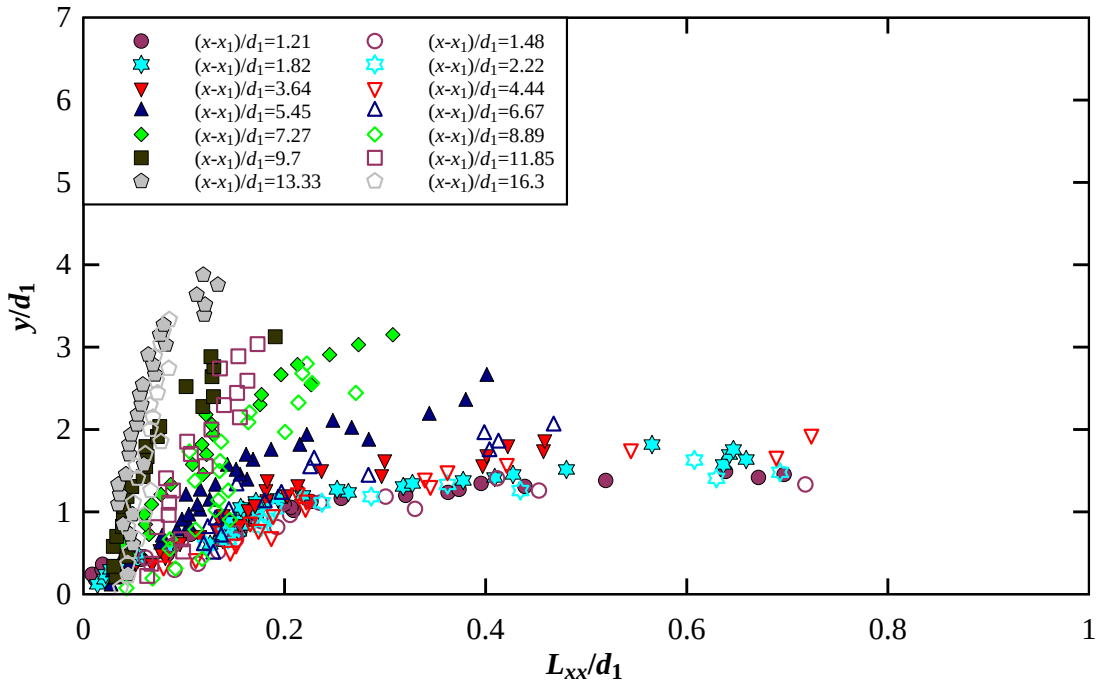

Figure 6.9 Dimensionless advective length scale measured on the channel centreline, filled symbols rough bed (rough bed, Run BR3, Q = 0.1 m^3/s, d_1 = 0.0825 m, Fr_1 = 2.84, Re_1 = 2.2E+5, and smooth bed, Run BS1, Q = 0.078 m^3/s, d_1 = 0.0675 m, Fr_1 = 2.84, Re_1 = 1.7E+5)

As seen in Figure 6.9 on both bed configurations, within a boundary layer next to the channel bed, the increase in both velocity and auto-correlation time scale resulted in a rapid increase in the advection length scale with increasing the vertical elevation. The vertical increasing in length scale L_{xx} was related to the interaction between the turbulent air-water flow and the channel bed within the boundary layer. This kind of interaction on rough bed was higher than on smooth bed and associated with the formation of larger eddies. As the vortical structures were dispersed further downstream, the impact of large eddies in the upper shear region vanished. A longitudinal decrease in the dimensionless advective length scale was observed in the turbulent shear region. Comparison between flow conditions on both rough and smooth

bed configurations showed larger length scales on rough bed at a given flow depth within the jump roller length. Overall, within the roller length, larger length scales were associated with the higher bubble count rate in the turbulent shear layer. However, further downstream, larger length scales were related to the roller length (Section 4.4). The former was higher on rough bed while the latter was higher on smooth bed. These findings were in agreement with the variation of auto- and cross-correlation time scales (Figure 6.8) as well as with results of Wang (2014) on smooth bed channel with comparable inflow Reynolds numbers.

The maximum advection length scale was observed in the turbulent shear layer, $L_{xx}/d_1 \approx 0.7$ and 0.72 on rough and smooth bed configurations, respectively. It was slightly lower than the maximum advection length scale in the plunging jet, i.e. $L_{xx}/d_1 \approx 0.8$ reported by Shi et al. (2018). This demonstrated that the large turbulent structures seemed to dissipate more rapidly, i.e. over a shorter distance in the horizontal direction, indicating a well-separated advection and diffusion of bubbles further downstream.

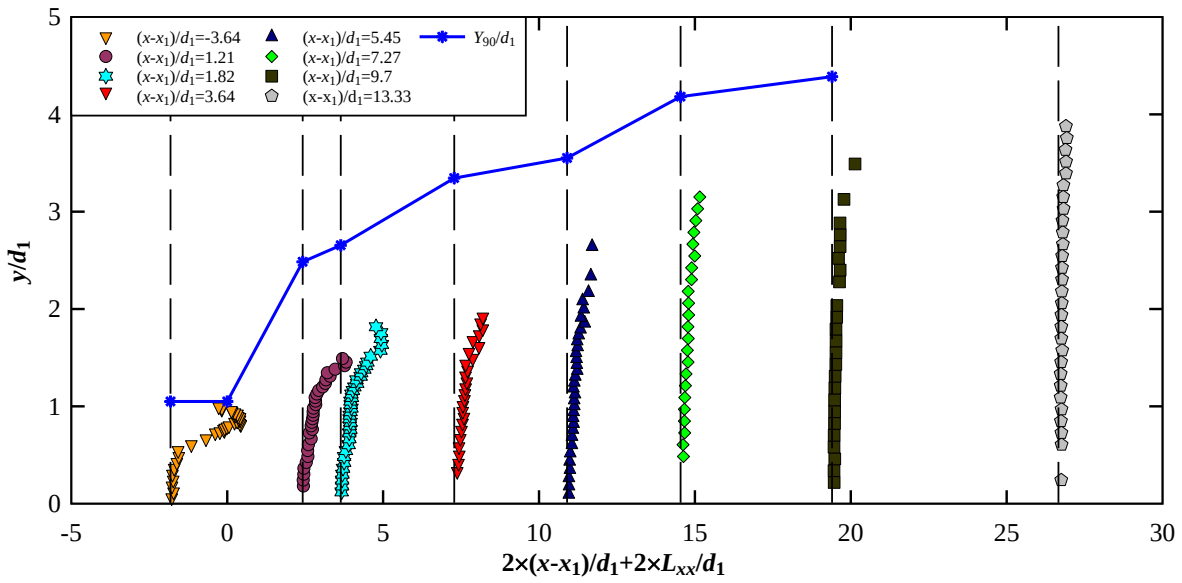

A: Rough bed, Run BR3, Q = 0.1 m^3/s, d_1 = 0.0825 m, Fr_1 = 2.84, Re_1 = 2.2E+5

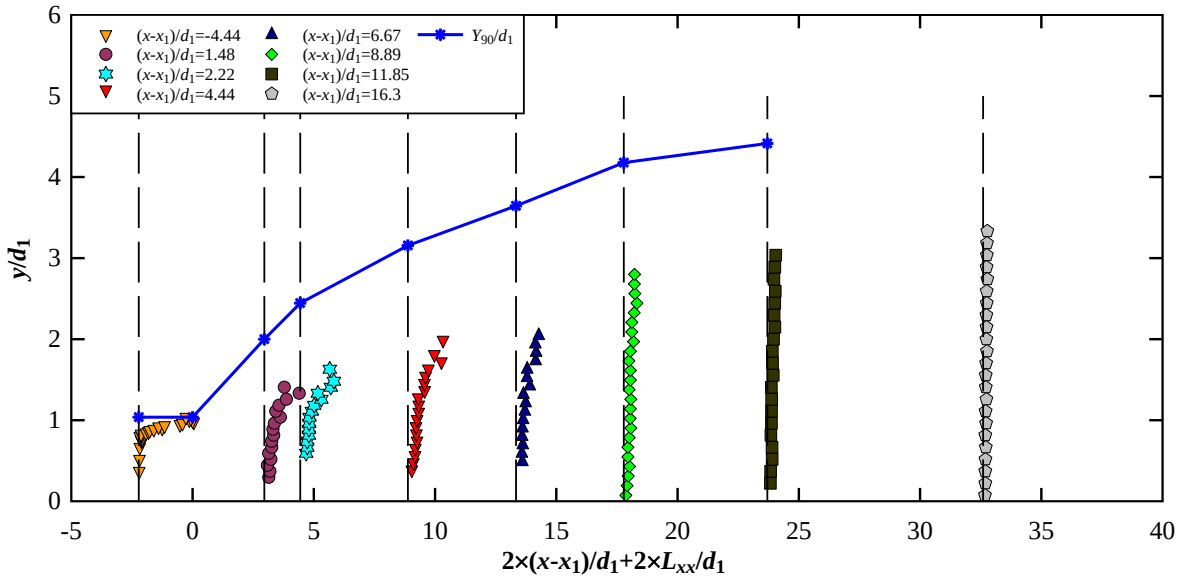

B: Smooth bed, Run BS1, Q = 0.078 m^3/s, d_1 = 0.0675 m, Fr_1 = 2.84, Re_1 = 1.7E+5

Figure 6.10 Vertical distribution of advection length scale in longitudinal direction; comparison with characteristic flow depth Y_{90}/d_1

6.5 Summary

Turbulent properties of the hydraulic jump roller were discussed in terms of turbulence intensity, characteristic turbulent length and time scales. The turbulence intensity, correlation time scales, and advection length scale were derived from a statistical analysis of the dual-tip phase-detection probe signal. High turbulence levels were detected in the roller free-surface region, which were related to the existence of self-sustained instabilities of the flow.

Larger magnitudes of *Tu* were observed in both shear layer and recirculation regions. Close to the jump toe larger magnitudes of *Tu* were observed in the shear layer while further downstream larger magnitudes of *Tu* were seen near the surface. Larger magnitudes of *Tu* in the turbulent shear layer was possibly corresponded to maximum bubble count rate while in the recirculation region as well as near the surface was linked to the impact of large-scale fluctuating motions of the jump roller. Comparison showed the higher magnitude of turbulent intensity on rough bed. Furthermore, the turbulence dissipation process was affected by the Froude number.

The relationship between turbulent intensity and dimensionless bubble count rate reflected an increase in turbulence associated with the number of entrained particles. The findings in

terms of magnitude were in agreement with the data of skimming flow on stepped chutes and of hydraulic jump on rubber mat rough bed.

The correlation time scales were deduced from the integration of the correlation functions from the maximum to the first zero-crossing point. The results showed that in the flow region immediately downstream of the jump toe, the maximum magnitude of $T_{xx} \times V_1/d_1$ was 0.82 and 0.73 on rough and smooth bed configurations, respectively, while the maximum magnitude of $T_{xx'} \times V_1/d_1$ was 0.7 and 0.63 on rough and smooth bed configurations, respectively.

Results showed that, on both bed configurations, the increase in both velocity and auto-correlation time scale resulted in a rapid increase in the advective length scale with the increasing vertical elevation. The vertical increasing in length scale L_{xx} was related to the interaction between the turbulent air-water flow and the channel bed within the boundary layer. This kind of interaction on rough bed was higher than on smooth bed and associated with the formation of larger eddies. Further downstream, vortical structures tended to be dispersed, since the impact of large eddies in the upper shear region vanished.

7 PARTICLE GROUPING AND CLUSTERING

7.1 Presentation

In hydraulic jump, within the turbulent shear layer, momentum transfer from the high-velocity jet flow to the circulation region may be occurred, as well as significant interactions between the entrained air and turbulence. These lead to some complicated processes including bubble break-up, coalescence and clustering. The time-averaged air-water properties such as void fraction, bubble count rate, and interfacial velocity did not impart any information on the microscopic structure of the two-phase flow. However, the analysis of clustering may provide some relevant insights about the interaction between turbulence and bubbly flow (Figueroa-Espinoza and Zenit 2005). Overall, the clustering process is linked to the non-uniform bubble distribution in flow, with preferential concentration, forming coherent structures termed clusters. In a bubbly flow, a cluster characterized as a group of two or more bubbles that clearly separated from other bubbles up- and downstream of the cluster (Chanson and Toombes 2002, Chanson 2007a, Gualtieri and Chanson 2010). In hydraulic engineering, previous investigations studied the one dimensional clustering process in plunging jets (Chanson et al. 2006), stepped chutes (Chanson and Toombes 2002), a dropshaft (Gualtieri and Chanson 2004, 2007b), and the hydraulic jump on smooth bed (Chanson 2007a, Gualtieri and Chanson 2007b, Gualtieri and Chanson 2010, Wang 2014). The clustering process was analysed in 2D in skimming flows on a stepped spillway (Sun and Chanson 2013) and in hydraulic jump on smooth bed (Wang et al. 2015).

In the present study, a 1D clustering analysis was conducted. Despite some limitations associated with the 1D analysis, the results suggested that the clustering index may provide a measure of the vorticity production rate and associated energy dissipation (Sun and Chanson 2013). In this Chapter, first the characteristic air-water time scale including particle chord time and length and their PDF are presented and discussed. Then the basic features of particle grouping and clustering derived from the raw phase-detection probe signal are reported. Properties including the number of clusters, the dimensionless number of clusters per second, the percentage of clustered bubbles and the number of bubbles per cluster were first investigated based upon two criteria: one is based on a comparison between the local instantaneous water chord time and a time-averaged characteristic water timescale, whereas the second identified a cluster if the bubble is in the near-wake of the preceding bubble.

Furthermore, the clustering process is studied using a different approach, the analysis of the interparticle arrival time (IAT) of the bubbles.

7.2 Characteristic air-water time scale: particle chord time and pseudo-length

7.2.1 Particle chord time

In the bubbly flow region, the air chord time $(t_{ch})_a$ was defined as the time that an air bubble spent on the phase-detection probe sensor tip, and the water chord time $(t_{ch})_w$ was the time that the sensor tip was in water between two adjacent bubbles. In the spray region above the bubbly flow, the water chord time referred to the time that a water droplet spent on the sensor tip, and the air chord time linked to the time of the sensor tip being in air between two droplets. The air chord time is proportional to the air chord length $(l_{ch})_a$, which, however, statistically reveals the size of the entrapped air bubbles, and it is inversely proportional to the bubble velocity. Since the phase-detection probe could not recognize the velocity direction, no information on the air chord length can be accurately acquired in the recirculation region with flow reversal. Therefore, the chord time data presented herein are in the positive flow region ($y < y(V = 0)$). Note that in case of $V = 0$ since the bubble velocity was zero, although physically bubbles were exist in flow and had chord length, the magnitude of t_{ch} tended to infinity.

The mean air bubble chord time is defined as the ratio of the time-averaged void fraction C to the bubble count rate F. It simply yielded an average time that a bubble spent on the phase-detection probe tip:

$$(t_{ch})_{a,mean} = \frac{C}{F} \tag{7.1}$$

If the relation between C and F follows a parabolic low, i.e. $F = 4 \times F_{max}. C(1\text{-}C)$ (Chanson and Toombes 2002), Equation 7.1 could be simplified into:

$$(t_{ch})_{a,mean} = \frac{1}{4 \times F_{max} \times (1-C)} \tag{7.2}$$

The mean air chord time was investigated for all inflow conditions on both bed configurations in the bubbly flow region where the void fraction was smaller than 0.3. Figure 7.1 shows the vertical distributions of dimensionless mean air chord time within two vertical cross sections at the same inflow Froude number, $Fr_1 = 2.84$ on both rough and smooth bed

configurations, comparing to the void fraction and the dimensionless bubble count rate profiles.

Overall, on both smooth and rough bed configurations, the dimensionless mean air chord time increased with the dimensionless elevation.

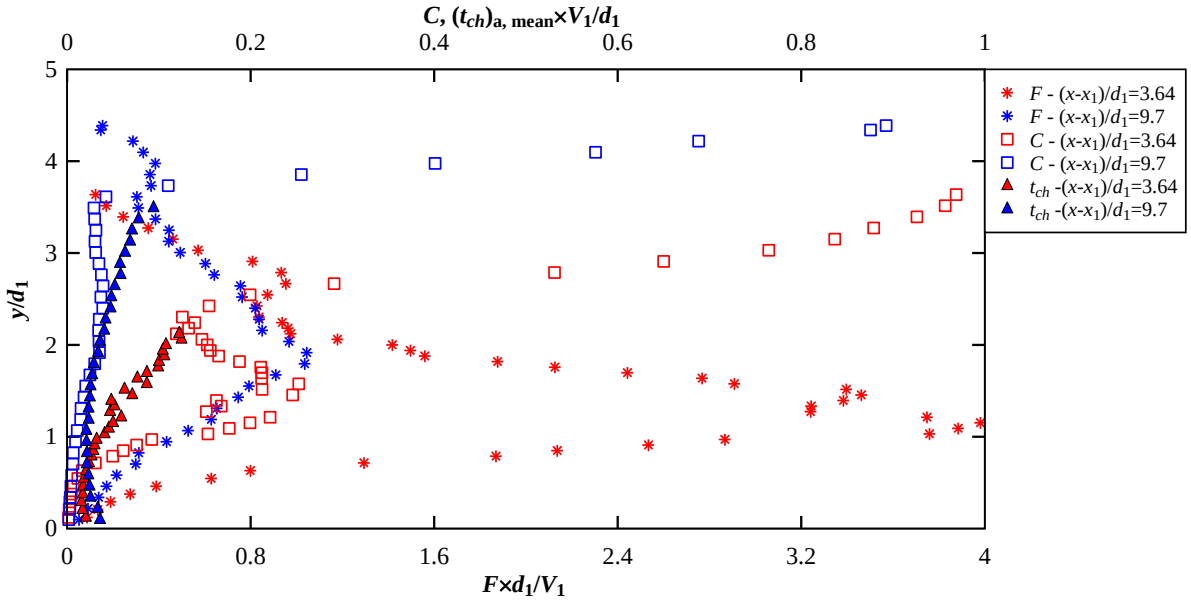

A: Rough bed, Fr_1 = 2.84, d_1 = 0.0825m

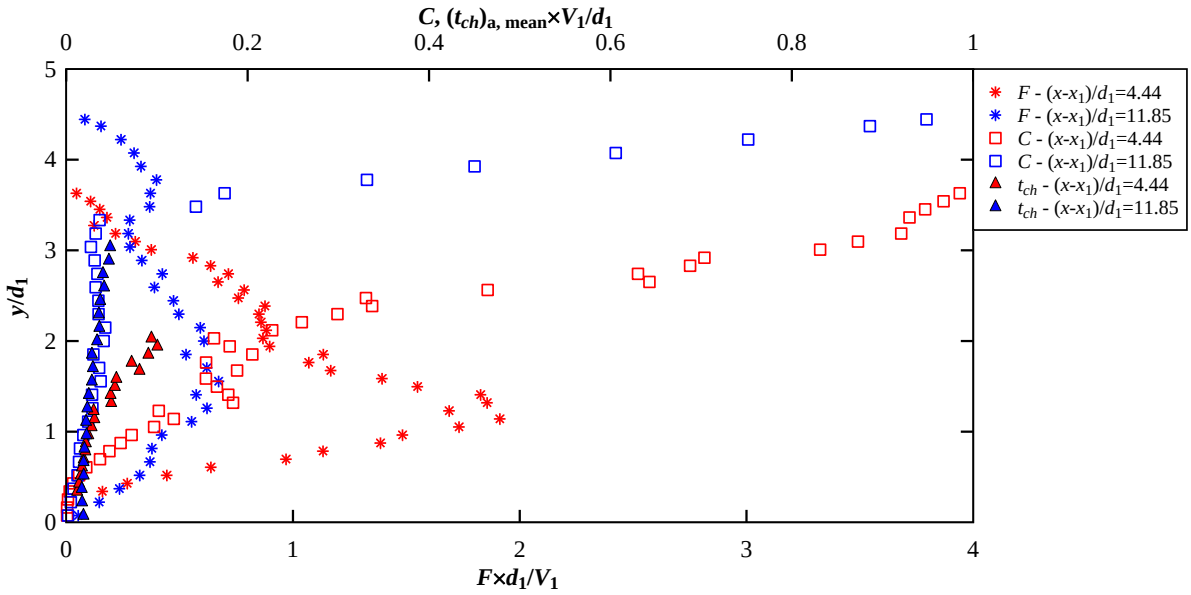

B: Smooth bed, Fr_1 = 2.84, d_1 =0.0675

Figure 7.1 Average air chord time compared with void fraction and bubble count rate distributions

Figure 7.2 presents the vertical distribution of average air chord time at several dimensionless longitudinal positions $(x\text{-}x_1)/d_1$ at the same inflow Froude number, $Fr_1 = 2.84$, on both rough and smooth bed configurations. Based upon the vertical elevation, regardless of the bed configuration, three regions with different rates of variation were observed for average air chord time (Figure 7.2). In the first region, $0 < y < Y_{Fmax}$, the average bubble chord time increased gradually with increasing elevation from the channel bed to approximately the elevation of the maximum bubble count rate. In the second region, $Y_{Fmax} < y < y^*$, the average air chord time increased rapidly in the upper turbulent shear region. In the third region, $y^* < y < y_{(C = 0.3)}$, the average air chord time increased more rapidly in the bubbly flow of the recirculation region. It should be considered that, in this region, the velocity is basically negative. Note that

Regardless of bed type, the smallest and the largest average bubble chord time were observed in the lower shear flow (i.e., $y/d_1 < 0.9$, close to the jump toe, to $y/d_1 < 3.9$, far from the jump toe) and next to the free-surface (i.e., $y/d_1 > 1.0$, close to the jump toe, to $y/d_1 > 4.0$, far from the jump toe), respectively. In the lower shear flow, the void fraction was relatively low resulted in lower magnitudes of average bubble chord time. Next to the free-surface, because of the larger bubbles and lower shear stresses, the average air chord time was at least one order of magnitude larger than in the shear layer. These findings supported the results presented by Wang (2014) on smooth bed. Overall, at the same elevation, the magnitude of average air chord time was higher on smooth bed than on rough bed. That was, near the jump toe and on rough bed, for $y/d_1 < 2$ and $2 < y/d_1 < 3$: $((t_{ch})_{a,mean})_{max} \times V_1/d_1 = 0.2$ and 0.3, respectively, while on smooth bed $((t_{ch})_{a,mean})_{max} \times V_1/d_1 = 0.4$ and 0.39, respectively. For $y/d_1 < 2$ and $2 < y/d_1 < 3$, the average air chord time on smooth bed was 2 and 1.5 times greater than on rough bed, respectively. Regarding the higher bubble count rates on rough bed (Sections 5.3.3 to 5.3.5), a lower rate of the average air chord time on rough bed could imply a smaller size of the bubbles.

The probability density functions (*PDF*s) of the air chord time for both bed configuration are presented in Figures from 7.3 to 7.5. The time interval was from 0 to 10 ms and a bin size of 0.25 ms was applied. The label in the plots referred to the smaller number of the interval, that was the probability of air chord time from 1 to 1.25 ms was indicated as 1 ms. Air chord time larger than 10 ms were regrouped and presented in an individual column.

Figure 7.3 presents the *PDF*s of air chord time measured at the elevation of the maximum bubble count rate ($y = Y_{Fmax}$) in the air-water shear layer, while Figure 7.4 shows the *PDF*s of

air chord time at the elevations of maximum bubble count rate (Y_{Fmax}) and maximum void fraction (Y_{Cmax}) in the shear layer, the elevation of secondary maximum bubble count rate (Y_{Fsec}) in the recirculation region and the boundary between these two regions (y^*). For each figure, the legend included the location (x-x_1, y/d_1) and the local air-water flow properties (C, F, V).

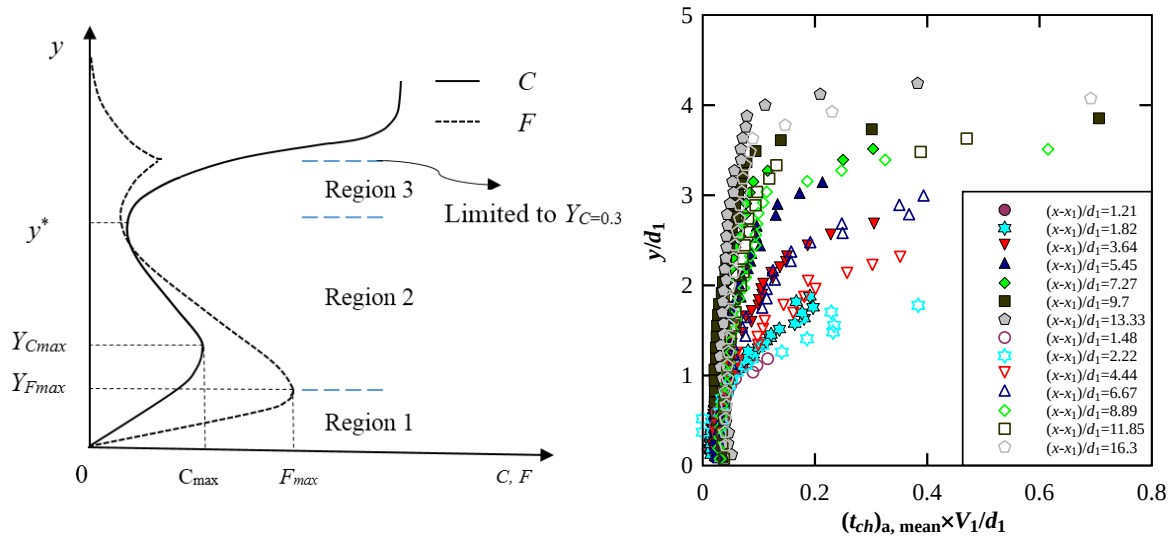

A: Sketch of three regions

B: Vertical distribution of average air chord time

Figure 7.2 Vertical distribution of average air chord time, Rough bed, Fr_1 = 2.84, d_1 = 0.0825m, Smooth bed, Fr_1 = 2.84, d_1 =0.0675. Filled symbols rough bed

Figure 7.3 presents the results at different longitudinal positions for Fr_1 = 2.84, 1.96 and 1.7 on rough bed and Fr_1 = 2.84 on smooth bed. Table 7.1 presents the percentage of the chord time in the ranges from 0 to 1 ms, from 0 to 2 ms and greater than 5 ms for any flow conditions, together with the corresponding total number of bubbles. These ranges were also chosen by Wang (2014) in hydraulic jump on smooth bed conditions.

Although in the present study only a limited number of inflow conditions were investigated, the data in Figures 7.3 and Table 7.1 suggested that an increase in Reynolds number (Re_1 from 1.4E+5 to 2.2E+5) resulted in a larger proportion of small bubbles. This might due to the break-up of large bubbles by the enhanced turbulent shear force and it is consistent with Wang (2014) experiments on smooth bed. The longitudinal trend of the air chord time indicated an increasing percentage of small bubbles in the downstream direction. It might suggest that large bubbles de-aerated first by buoyancy effect.

For Fr_1 = 2.84, on rough bed, near the jump toe was the lowest, e.g. for (x-x_1)/d_1 = 1.21 and

$(x\text{-}x_1)/d_1$ = 13.33, the percentage of smaller air chord times, i.e. $(t_{ch})_a$ < 2 ms, was 72% and 80%, respectively. For Fr_1 = 2.84, on smooth bed the percentage of smaller air chord times near the jump toe was higher than downstream, e.g. for $(x\text{-}x_1)/d_1$ = 1.48 and $(x\text{-}x_1)/d_1$ = 16.3, the percentage of $(t_{ch})_a$ < 2 ms was 70% and 77%, respectively (Table 7.1). This could be explained by the larger air entrainment and the higher air count rates on rough bed. The number of bubble near jump toe, i.e. at $(x\text{-}x_1)/d_1$ = 1.21 was 11121 and at $(x\text{-}x_1)/d_1$ = 1.48 was 9095 on rough and smooth beds, respectively (Table 7.1 and also Section 5.3).

At lower inflow Froude numbers, Fr_1 = 1.96 and 1.7, on rough bed, no remarkable difference was observed between smaller and larger air chord times. This was due to the lower air entrainment (see *C* and *F* distributions in Section 5.3.1 to 5.3.4) and lower shear stress, which resulted in a lower rate of bubbles break-up. The average number of bubbles was 2655 and 1439 for Fr_1 = 1.96 and 1.7, respectively (Figure 7.3B and C and Table 7.1). Note that a large amount of air chord time larger than 10 ms was recorded at Y_{Fmax}. Since for two flow conditions, the void fraction at Y_{Fmax} was from 0.3 to 0.5, the local air chord time might sometimes related to the air phase between water droplets. The decrease in the number of largest bubbles, $(t_{ch})_a$ > 10 ms with the increasing downstream distance is linked to the break-up of large air entities and their upward advection by buoyancy (Figure 7.3 and Table 7.1). Overall the range of air chord times covered one order of magnitude, as previously presented by Chanson (2007a, 2010), Gualtieri and Chanson (2013) and Wang and Chanson (2016).

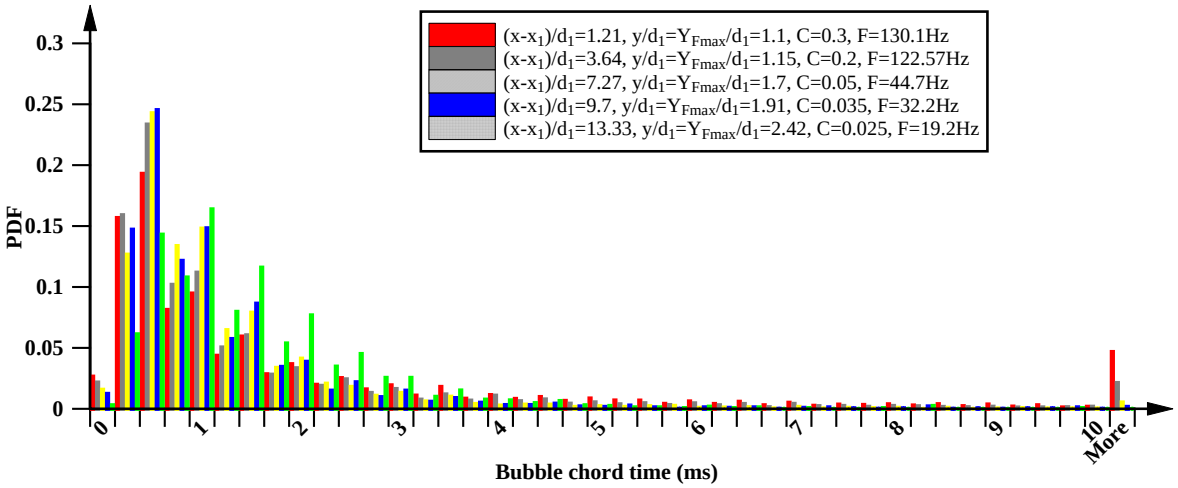

A: Rough bed, Fr_1 = 2.84, Re_1 = 2.2E+5

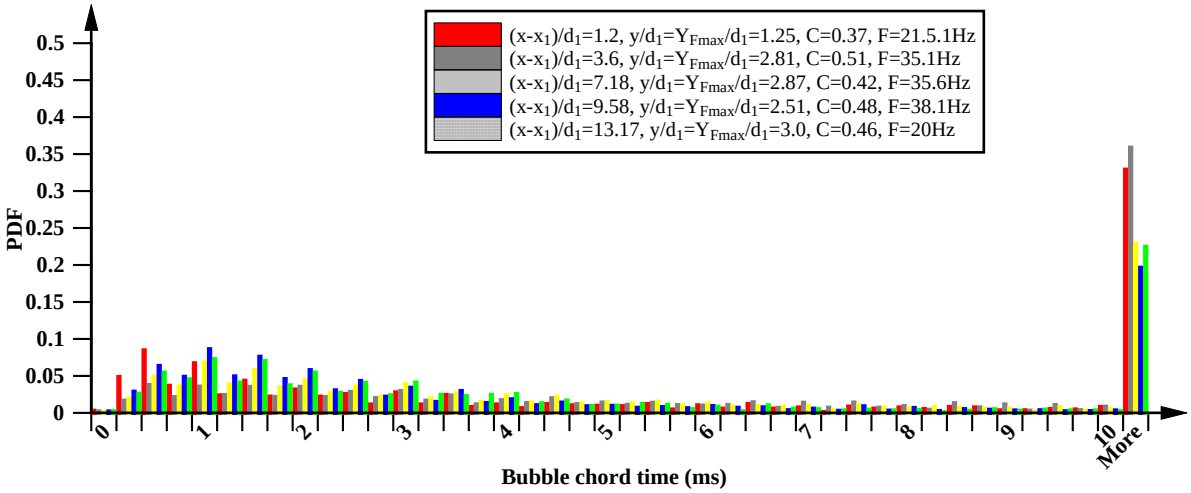

B: Rough bed, Fr_1 = 1.96, Re_1 = 1.6E+5

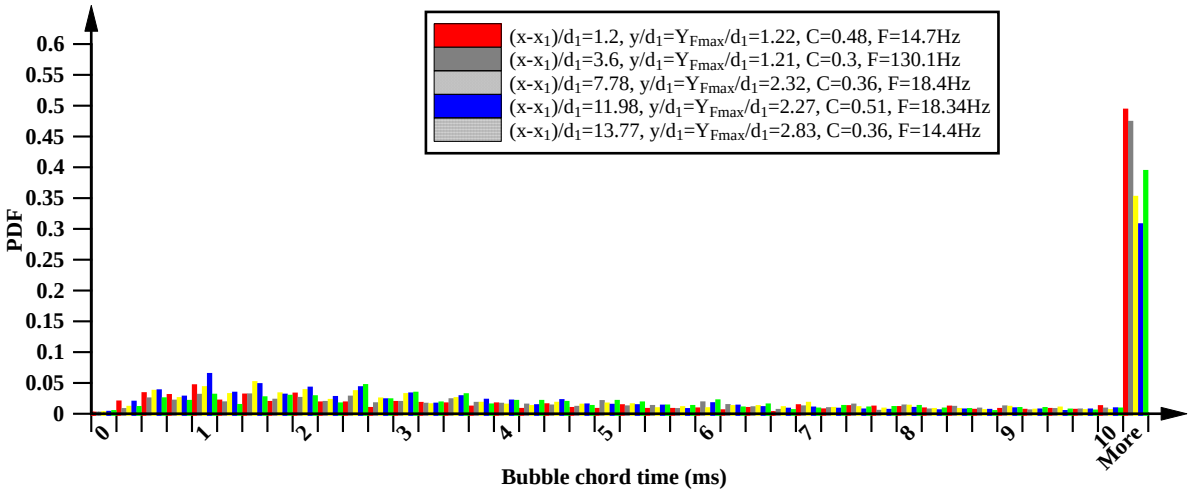

C: Rough bed, Fr_1 = 1.7, Re_1 = 1.4E+5

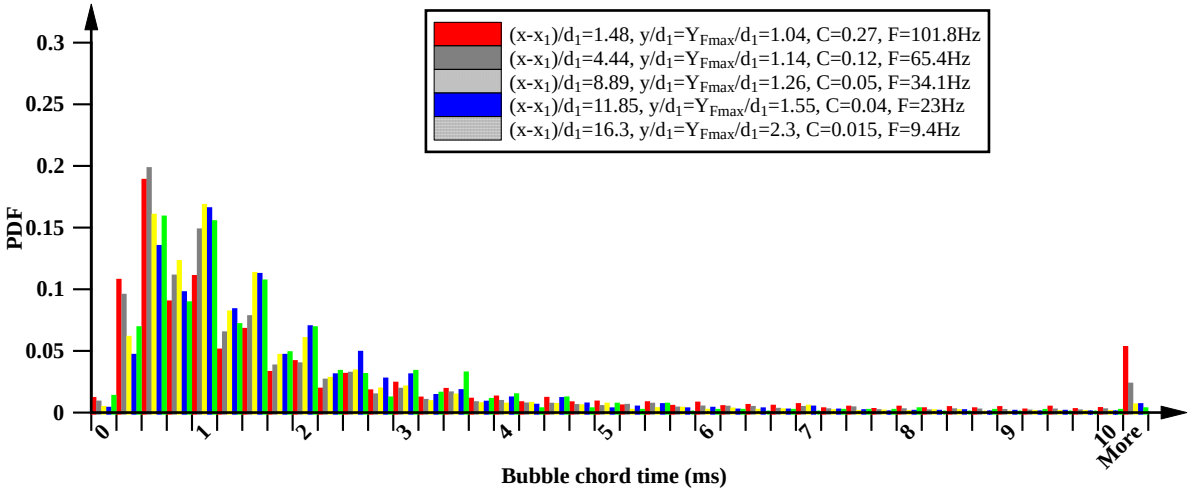

D: Smooth bed, Fr_1 = 2.84, Re_1 = 1.7E+5

Figure 7.3 Probability density functions of air chord time as functions of longitudinal positions in hydraulic jumps, data selected at the characteristic elevation Y_{Fmax} of maximum bubble count rate F_{max}

Table 7.1 Percentage of the bubble chord time at $y = Y_{Fmax}$

Bed type	Fr_1	$(x\text{-}x_1)/d_1$	$0<(t_{ch})_a<1$ ms	$0<(t_{ch})_a<2$ms	$(t_{ch})_a>5$ ms	Number of bubbles	Sampling duration (s)
Rough	2.84	1.21	0.55	0.72	0.12	11121	90
		3.64	0.63	0.80	0.07	10794	
		7.27	0.67	0.88	0.02	3842	
		9.7	0.67	0.89	0.01	2619	
		13.33	0.48	0.80	0.01	1735	
	1.96	1.2	0.24	0.36	0.46	1776	180
		3.6	0.11	0.23	0.54	3160	
		7.18	0.17	0.35	0.38	3088	
		9.58	0.23	0.46	0.30	3394	
		13.17	0.20	0.40	0.32	1858	
	1.7	1.2	0.12	0.22	0.63	1330	180
		3.6	0.08	0.17	0.6	1386	
		7.78	0.11	0.26	0.51	1696	
		11.98	0.14	0.29	0.45	1577	
		13.77	0.08	0.17	0.57	1206	
Smooth	2.84	1.48	0.50	0.70	0.13	9095	90
		4.44	0.56	0.77	0.07	5772	
		8.89	0.51	0.75	0.03	3009	
		11.85	0.44	0.89	0.04	2027	
		16.3	0.48	0.77	0.02	791	

Figure 7.4 shows some probability distributions of air chord time at several characteristic elevations in the same vertical cross section of roller for Fr_1 = 2.84 on both rough and smooth bed configurations. The data for C < 0.3 and at the elevations of maximum void fraction (Y_{Cmax}) in the shear layer and the boundary between these two regions (y*) are presented. Two vertical cross section, one close to the jump toe and one at far downstream were considered on each bed type. Overall, Figure 7.4 showed that that, despite the bed roughness type and the longitudinal distance from jump toe, the percentage of small and large air chord times decreased and increased, respectively, as the vertical elevation increased. Close to the jump toe, $(x\text{-}x_1)/d_1$ = 1.21 and 1.48, the percentage of air chord time lower than 3 ms was the largest at Y_{Fmax} and Y_{Cmax} on rough and smooth bed, respectively (Figures 7.3 and 7.4A). On smooth bed, the proportion of air chord time lower than 3 ms at Y_{Fmax} was significantly higher than that at the other elevations (Figures 7.3 and 7.4C). This might be related to the large air entities and larger vortices on rough bed. The longitudinal position did not affect the shape of the probability density functions on both bed configurations. Furthermore, the *PDF* data were in agreement with the increasing average air chord time $(t_{ch})_{a,\text{mean}} = 1/4 \times F_{max} \times (1\text{-}C)$ with increasing elevation (Figure 7.2). Generally, the findings confirmed the results of Wang and Chanson (2016) on smooth bed conditions.

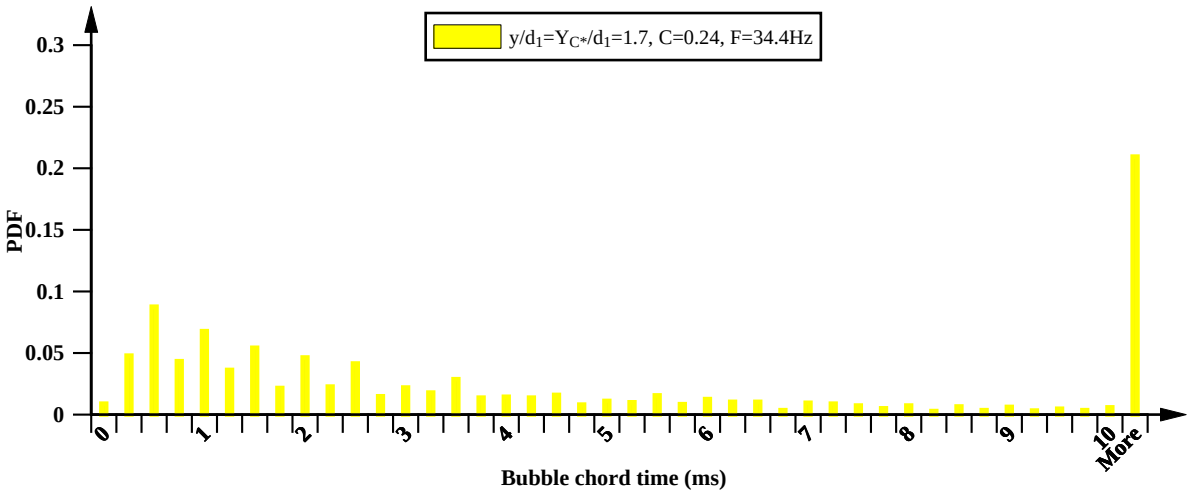

A: Rough bed, Fr_1 = 2.84, Re_1 = 2.2E+5, $(x\text{-}x_1)/d_1$ = 1.21

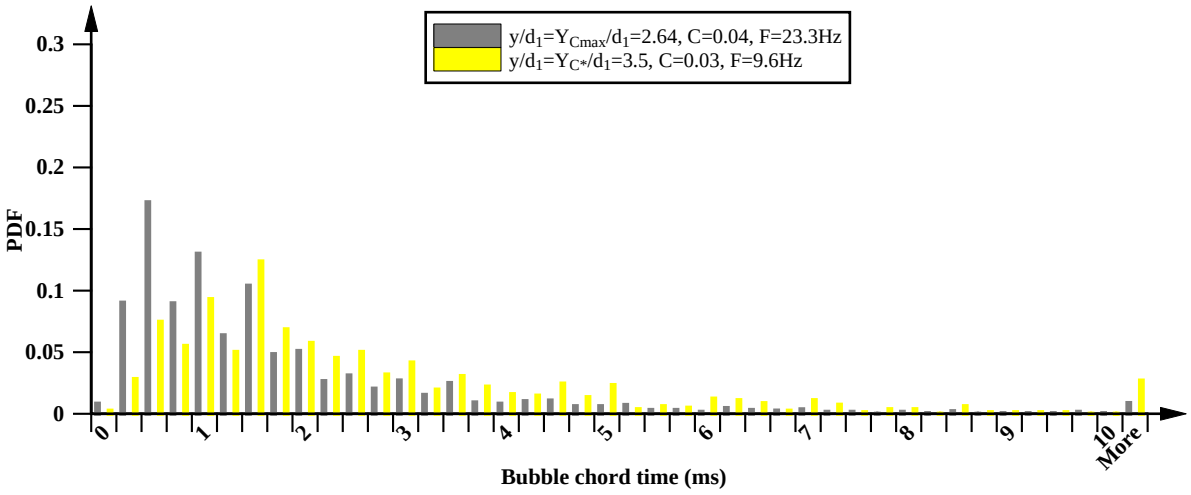

B: Rough bed, Fr_1 = 2.84, Re_1 = 2.2E+5, $(x\text{-}x_1)/d_1$ = 9.7

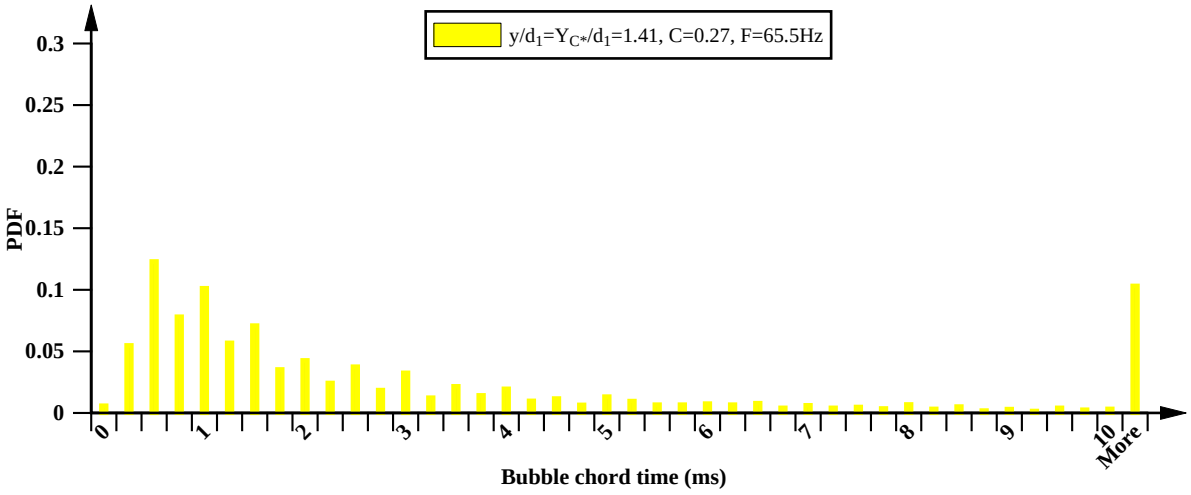

C: Smooth bed, Fr_1 = 2.84, Re_1 = 1.7E+5, $(x\text{-}x_1)/d_1$ = 1.48

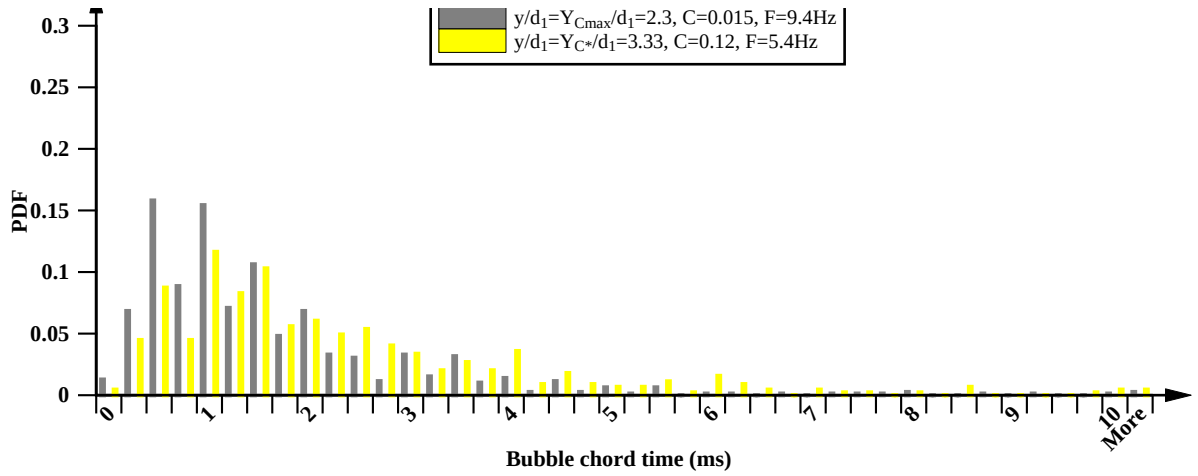

D: Smooth bed, Fr_1 = 2.84, Re_1 = 1.7E+5, $(x\text{-}x_1)/d_1$ = 16.3

Figure 7.4 Probability density functions of bubble chord time measured at different characteristic elevations with the same longitudinal position

7.2.2 Particle chord length

Considering a positive flow direction parallel to the channel bed, the air chord length was calculated from the air chord time and the corresponding local velocity: $(l_{ch})_a = (t_{ch})_a \times V$, where V is the time-averaged interfacial velocity.

Air chord length was investigated only in lower flow region, i.e. where the time-averaged interfacial velocity is positive, $V > 0$. Hence, Figure 7.5 presents the PDFs of the bubble chord length at Y_{Fmax} in the shear layer, in the locations closest and farthest to the jump toe for both rough and smooth bed configurations. The chord lengths were grouped in 0.5 mm bins from 0 to 20 mm, and those larger than 20 mm were regrouped in the last column. The data showed that there was no significant difference between the magnitudes of PDF on rough and smooth bed configurations. A comparison between the air chord length (Figure 7.5) and the air chord time (Figure 7.4) suggested that the different probability distributions of air chord length for different flow conditions may be related to the different interfacial velocities rather than to any change in chord size proportion. Similarly, the data of Wang (2014) on smooth bed and Pagliara et al. (2011) on rough bed showed the same range of variation for air chord length. The present data were comparable to those from Bertola et al. (2018) for supported plunging water jet and Wei et al (2018a, 2018b) for supercritical chute flow. It should be considered that the present investigation was conducted using a very limited number of inflow conditions.

7.3 Clustering characterisation

7.3.1. Introduction

In the bubbly flow region, the phase-detection probe signal consistently suggested a concentration of air bubbles in a short interval of time rather than a uniform bubble distribution. An investigation of clustering events may provide some information to conclude if the formation frequency responds to some particular frequencies of the flow (Loung and Sojka 1999, Noymer 2000).

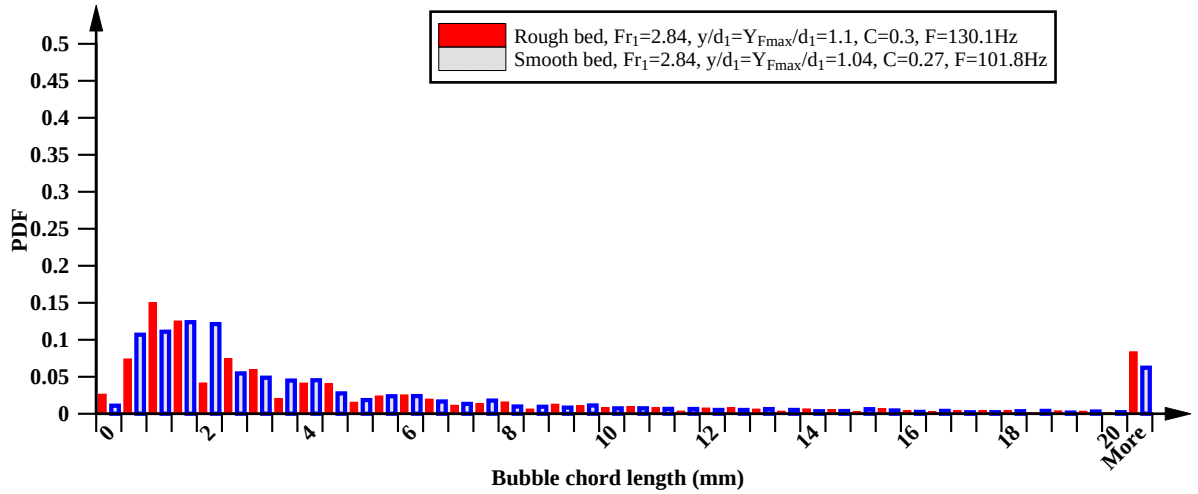

A: Rough bed, $(x\text{-}x_1)/d_1$ = 1.21 and smooth bed, $(x\text{-}x_1)/d_1$ = 1.48

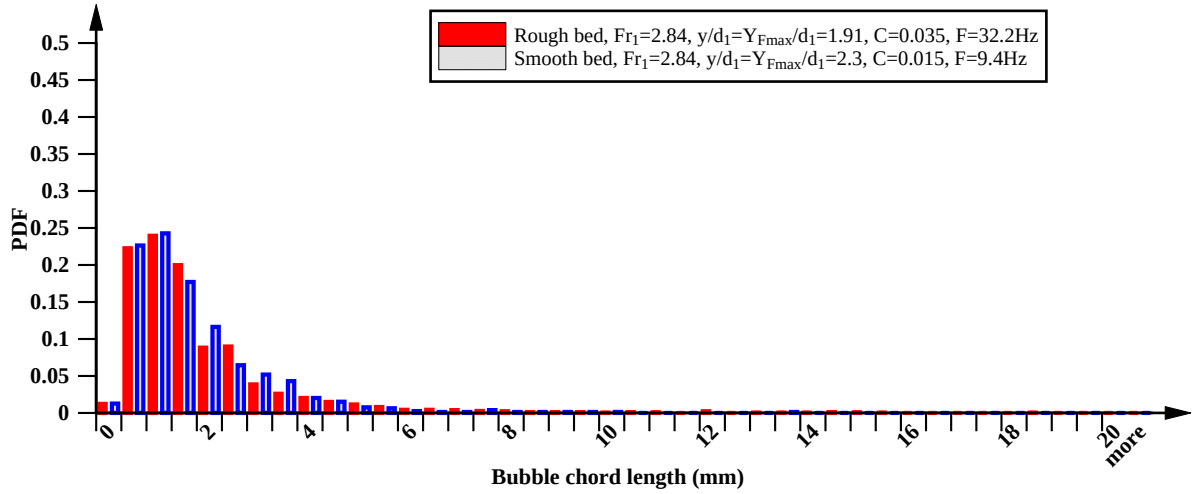

B: Rough bed, $(x\text{-}x_1)/d_1$ = 9.7 and smooth bed, $(x\text{-}x_1)/d_1$ = 16.3

Figure 7.5 Comparison of probability density functions of bubble chord length, Rough bed, Fr_1 = 2.84, Re_1 = 2.2E+5 and smooth bed, Fr_1 = 2.84, Re_1 = 1.7E+5

A definition sketch of a bubbles cluster is presented in Figure 7.6, while Figure 7.7 shows a signal segment received by leading probe tip, some bubble groups can be observed in the

longitudinal direction with small intervals between adjacent bubbles. Basically, the notion of cluster applied to dispersed particles advected in a carrier phase (Chanson 2007a). The presence of bubble groups in flow may result in the interaction between individual bubbles with other bubbles when they travelled one after another or side by side. Furthermore, it might demonstrate that the flow was not fully dispersed, and the advection of bubbles was not a random process (Chanson 2007a). Similarly grouping of water droplets were observed in the free surface region above the jump roller.

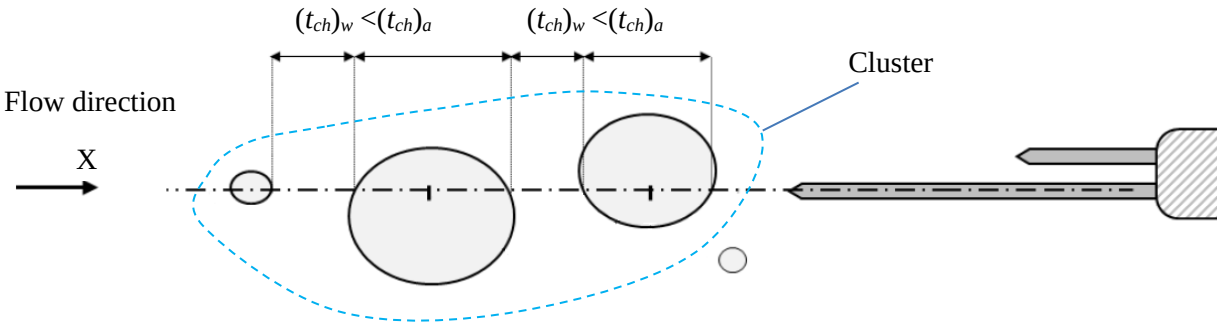

Figure 7.6 Definition sketch of the detection of 1D bubble cluster

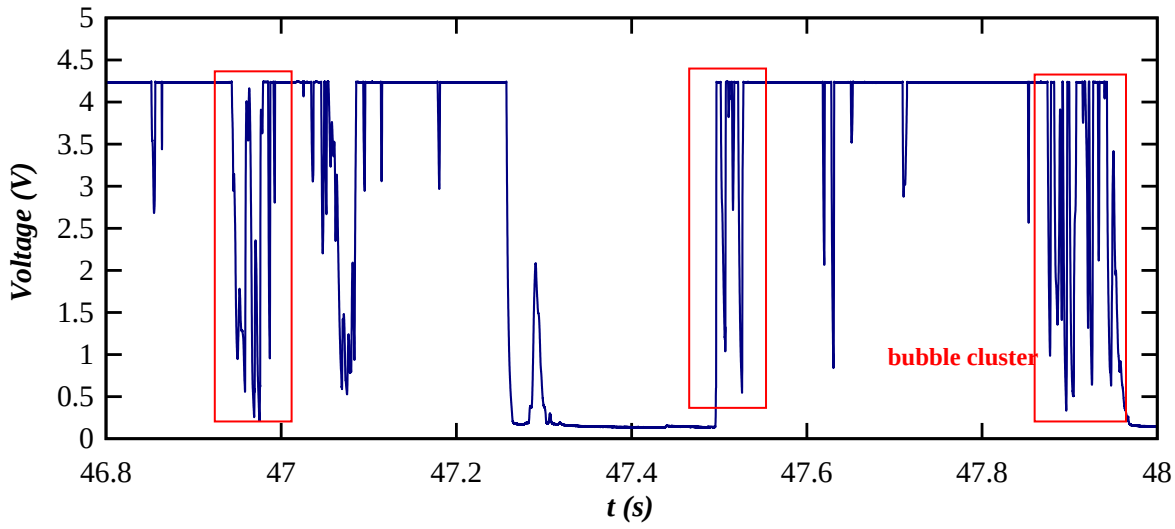

Figure 7.7 Phase-detection probe signal indicating longitudinal bubble grouping, rough bed, Run BR3, Q = 0.1 m^3/s, d_1 = 0.0825 m, Fr_1 = 2.84, Re_1 = 2.2E+5, x-x_1 = 0.6m, y = 0.3m

Different methods were proposed to identify a cluster structure within the air–water flow. The approach in the present study was first based upon the analysis of water chord between two subsequent air particles. Two adjacent bubbles can be considered as a cluster if they are closer than a characteristic time/length scale, as depicted in Figure 7.6 (Chanson and Toombes 2002, Gualtieri and Chanson 2004, 2007b, Gualtieri and Chanson 2010). The

time/length scale may be linked to the water chord statistics or to the bubble size itself because the bubbles within that distance are in the near-wake and may be affected by the leading particle (Chanson and Toombes 2002, Chanson et al. 2006, Gualtieri and Chanson 2007b). In the hydraulic jump, since it is difficult to ascertain the direction of motion of each individual bubbles, the analysis must be conducted in terms of chord times. Herein, based on Gualtieri and Chanson (2010), two criteria were chosen to detect the occurrence of clusters in the air–water flow:

1. Criterion A. Water chord time between two subsequent air bubbles was considered to be compared with the median water chord time recorded in the point of measurement. Accordingly, a cluster was detected if (Chanson and Toombes 2002):

$$(t_{ch})_w < \left(\frac{1}{10}\right)(t_{ch})_{w-median} \tag{7.3}$$

2. Criterion B. Water chord time between two subsequent air particles was considered to be compared with the air chord of the preceding bubble recorded in the point of measurement. Accordingly, a cluster was detected if (Chanson 2002, Chanson et al. 2006):

$$(t_{ch})_w < \lambda(t_{ch})_a \tag{7.4}$$

where $(t_{ch})_a$ is the air chord time of the leading bubble, λ is the dimensionless parameter characterizing the wake timescale of the leading bubble, which for pseudo-spherical particles is in the range 0.5–2.0 (Gualtieri and Chanson 2013). It was assumed herein that λ = 1 following Chanson et al. (2006) and Gualtieri and Chanson (2010). Equation (7.4) indicated that the leading particle has an effect on the behaviour of trailing particle because the latter travels in the near-wake of the latter. The analysis was conducted only in the longitudinal direction (1D analysis) and it did not consider those clusters consisting of transverse or vertical particle pairs.

As the concept of clustering holds for dispersed particles advected in a carrier phase, the clustering analysis was carried out only in the bubbly shear flow region where the time-averaged void fraction was smaller than 0.3. The investigated properties included the cluster count rate F_{clu}, cluster size N_{clu} and cluster proportion P_{clu}., defined in the next sections.

7.3.2 Cluster count rate

The cluster count rate F_{clu} is the number of clusters per second, i.e. N_c/T_{scan} where N_c is the number of clusters and T_{scan} is the scanning duration. The vertical distribution of dimensionless cluster count rate for different inflow Froude numbers is presented in Figure 7.8 for both rough and smooth bed configurations. Figure 7.8 compares the results from Criterion A and B (Equations 7.3 and 7.4) at different locations downstream the of jump toe. At each location, the cluster count rate profiles exhibited shapes similar to the bubble count rate profiles (Figure 5.15), with a smaller magnitude, that was $F_{clu} < F$. On both rough and smooth bed configurations and for both Criteria A and B , the cluster count rate was about zero at the channel bed and quickly increased with the elevation to a maximum $(F_{clu})_{max}$, then decreased in the upper shear flow region. Note that the data refer to air bubble clusters in the shear flow region and for $C < 0.3$. Generally, the lowest magnitudes were detected at the farthest distance from the jump toe for all the inflow conditions on both rough and smooth bed and for both clustering criteria. Independently of the clustering criterion and bed type, the maximum number of clusters per second decreased with the distance from the jump toe and decreased with the decreasing inflow Froude number Fr_1 at a given dimensionless distance $(x\text{-}x_1)/d_1$. Overall, Criterion B showed much larger cluster count rate for all flow conditions on both rough and smooth bed configurations.

For $Fr_1 = 2.84$, a comparison between rough and smooth data showed larger magnitudes of cluster count rates on rough bed for both Criteria A and B, especially close to the jump toe. On the rough bed, the dimensionless number of clusters per second ranged from 0.001 to 0.227 and from 0.002 to 0.9 for the Criteria 1 and 2, respectively. On the smooth bed, the dimensionless number of clusters per second ranged from 0.001 to 0.148 and from 0.002 to 0.6 for the Criteria A and B, respectively.

For $Fr_1 = 1.96$ and 1.7 on rough bed, higher cluster count rates were detected farther downstream of the jump toe, $(x\text{-}x_1)/d_1 > 3.6$ for both $Fr_1 = 1.7$ and 1.96 (Figure 7.7B and C). This was associated with the larger bubble count rates at the same locations and it confirmed the visual observations which highlighted the air bubbles entrapped most likely downstream of the jump toe. These findings were in agreement with the data from Gualtieri and Chanson (2007b), Murzyn et al. (2007), Wang et al. (2015) in hydraulic jump on smooth bed and Bertola et al. (2018) in planar plunging water jet flow.

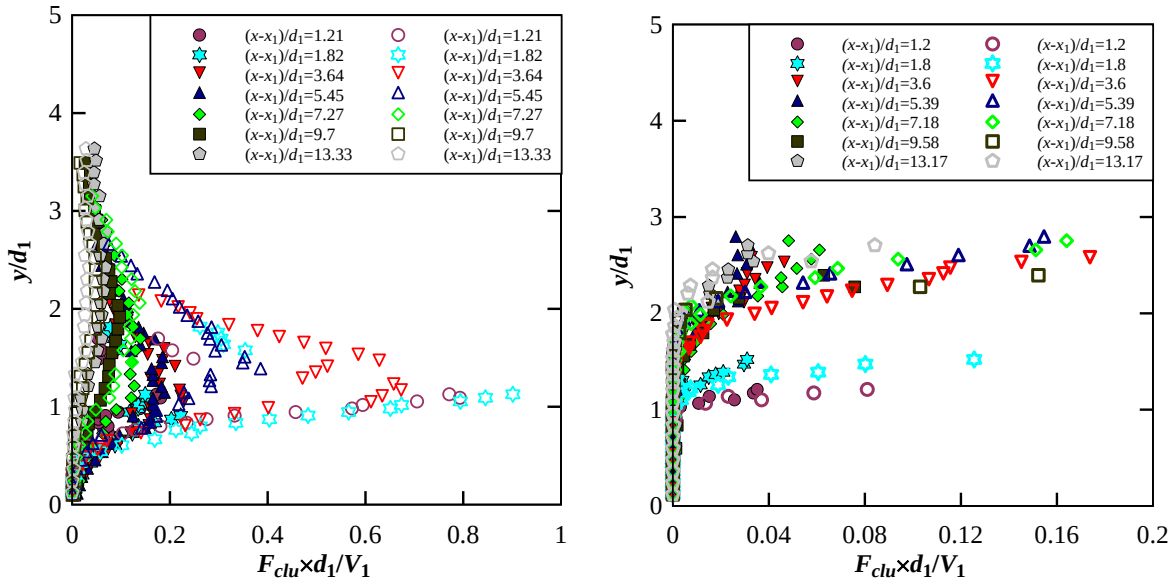

A: Rough bed, Fr_1 = 2.84, Re_1 = 2.2E+5

B: Rough bed, Fr_1 = 1.96, Re_1 = 1.6E+5

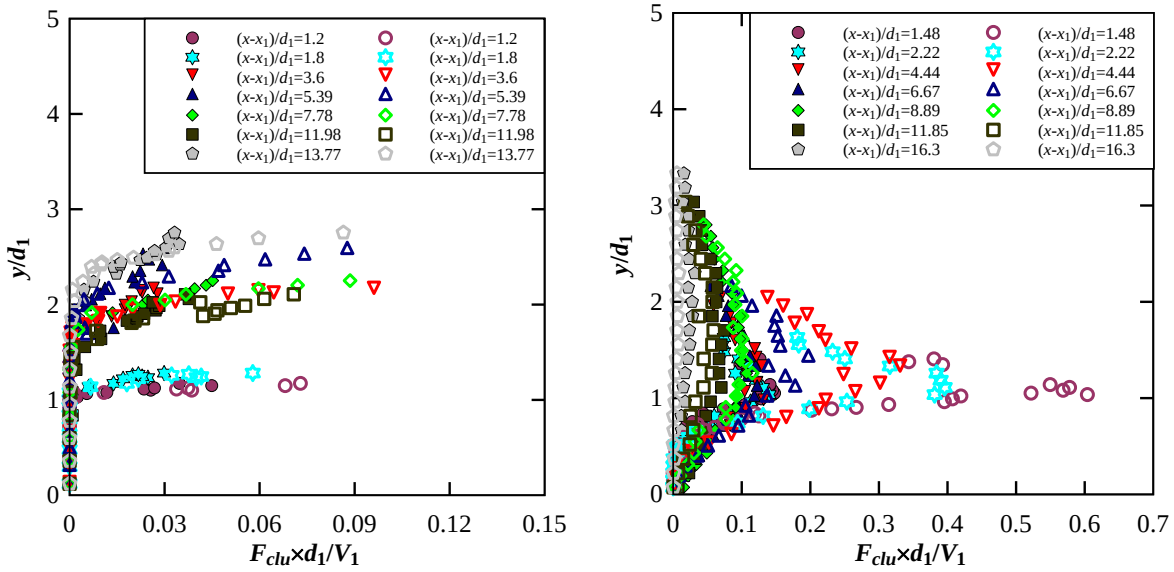

C: Rough bed, Fr_1 = 1.7, Re_1 = 1.4E+5

D: Smooth bed, Fr_1 = 2.84, Re_1 = 1.7E+5

Figure 7.8 Vertical distributions of one-dimensional cluster count rate on the channel centreline. Filled symbols, Criterion A (Equation 7.2), empty symbols, Criterion B (Equation 7.3)

Figure 7.9 presents the longitudinal distribution of the dimensionless maximum cluster count rate $(F_{clu})_{max}\times d_1/V_1$ in the turbulent shear region considering C < 0.3 for both rough and smooth bed configurations, using both Criteria A and B. For the hydraulic jump with a marked roller, i.e. Fr_1 = 2.84, for both bed type and clustering criterion, the dimensionless magnitude of $(F_{clu})_{max}$ decreased with the distance from the jump toe. The reduced cluster count rate was associated with the diffusion of bubbles and the dissipation of turbulent

structures along the roller. For both Criteria, the data on rough bed were larger than those on smooth bed, suggesting higher levels of interaction between turbulence and bubbly flow on rough bed. According to Criterion A, the dimensionless maximum cluster count rate was 0.23 and 0.15 at $(x\text{-}x_1)/d_1$ = 3.64 and 1.48 on rough and smooth bed, respectively. According to Criterion B, the dimensionless maximum cluster count rate was 0.9 and 0.6 at $(x\text{-}x_1)/d_1$ = 1.82 and 1.48 on rough and smooth bed, respectively. For both Criteria, for $Fr_1 < 2$ on rough bed, corresponding to an undular hydraulic jump, the distribution of dimensionless maximum cluster count rate exhibited different profiles and lower magnitudes than for Fr_1 = 2.84 (Figure 5.18C). Furthermore, the data for the undular hydraulic jump not exhibited a clear decay, but were almost constant with the distance from the jump toe.

The data from the present study were also compared with those from Gualtieri and Chanson (2007b) for Criterion A and Gualtieri and Chanson (2010) and Wang (2014) for Criteria B. Considering the Criterion A, the present data on smooth bed were higher than those from Gualtieri and Chanson (2007b). The former was conducted with lower inflow Froude number Fr_1 = 2.84 but higher Reynolds number Re_1 = 1.7E10+5 while the latter referred to a higher inflow Froude number from 6.5 to 14.3 but lower Reynolds numbers from 2.7E10+4 to 5.8E10+4. The comparison suggested some effect of Reynolds number upon the cluster count rate. For Criterion B, the data of Gualtieri and Chanson (2010) and Wang (2014), corresponding to higher inflow Froude numbers from 3.8 and 14.3, but lower Reynolds numbers from 2.7E10+4 to 9.1E10+4 were generally lower than the present data. Only Wang (2014) data with Fr_1 = 3.8 and Re_1 = 1.6E10+5 were comparable to the present data with Fr_1 = 2.84 and Re_1 = 1.7E10+5 on smooth bed.

At the end, the comparison between the present data on smooth bed with those from Gualtieri and Chanson (2007b, 2010) and Wang (2014) confirmed the effect of Reynolds number on clustering level.

The longitudinal decay of dimensionless maximum cluster count rate was correlated by Wang (2014) as:

$$\frac{\left(F_{clu}\right)_{\max} \times d_1}{V_1} = \phi_{F_{clu}} \times \exp(-\Psi \times \frac{x - x_1}{d_1}) \quad (7.5)$$

where Φ_{Fclu} and Ψ_{Fclu} are dimensionless coefficients corresponded to the flow conditions. Based on the present data and the data of Chanson (2010), Chachereau and Chanson (2011a) and Wang (2014), the following correlations for Φ_{Fclu} and Ψ_{Fclu} were proposed for Criterion A:

$$\phi_{F_{clu}} = 0.015 \times \frac{Re_1}{10^4} \qquad 4.5\times10^4 < Re_1 < 2.2\times10^5 \qquad (7.6a)$$

$$\Psi_{F_{clu}} = 0.25 \times \frac{1}{Fr_1 - 1} \qquad 2.8 < Fr_1 < 11.2 \qquad (7.6b)$$

and for Criterion B:

$$\phi_{F_{clu}} = 0.06 \times \frac{Re_1}{10^4} \qquad 4.5\times10^4 < Re_1 < 2.2\times10^5 \qquad (7.7a)$$

$$\Psi_{F_{clu}} = 0.5 \times \frac{1}{Fr_1 - 1} \qquad 2.8 < Fr_1 < 11.2 \qquad (7.7b)$$

By applying Equations (7.6) and (7.7), Equation (7.5) could be rewritten as it follows for Criterion A:

$$\frac{(F_{clu})_{\max} \times d_1}{V_1} = \left(0.015 \times \frac{Re_1}{10^4}\right) \times \exp\left(-\frac{1}{4\times(Fr_1 - 1)} \times \frac{x - x_1}{d_1}\right) \qquad (7.8)$$

and for Criterion B:

$$\frac{(F_{clu})_{\max} \times d_1}{V_1} = \left(0.06 \times \frac{Re_1}{10^4}\right) \times \exp\left(-\frac{1}{2\times(Fr_1 - 1)} \times \frac{x - x_1}{d_1}\right) \qquad (7.9)$$

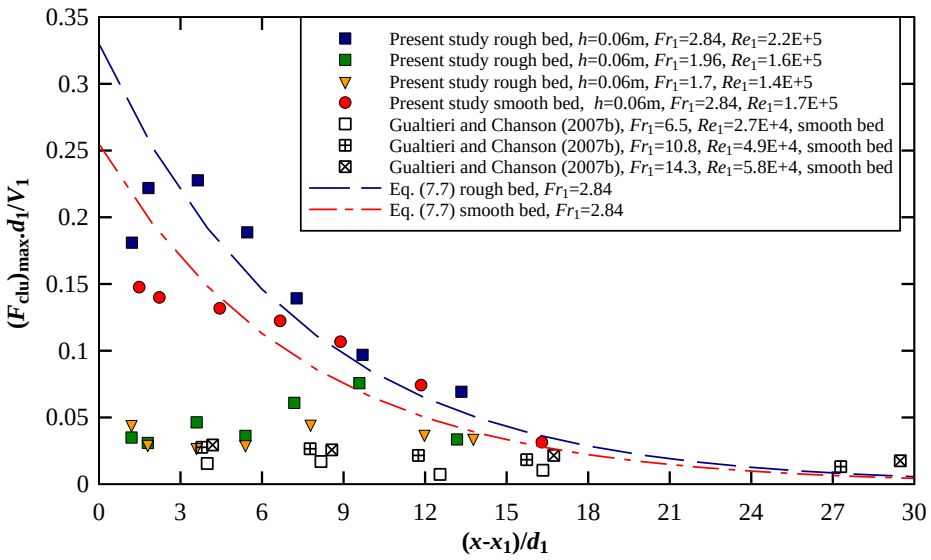

A: Based on Criterion A (Equation 7.2)

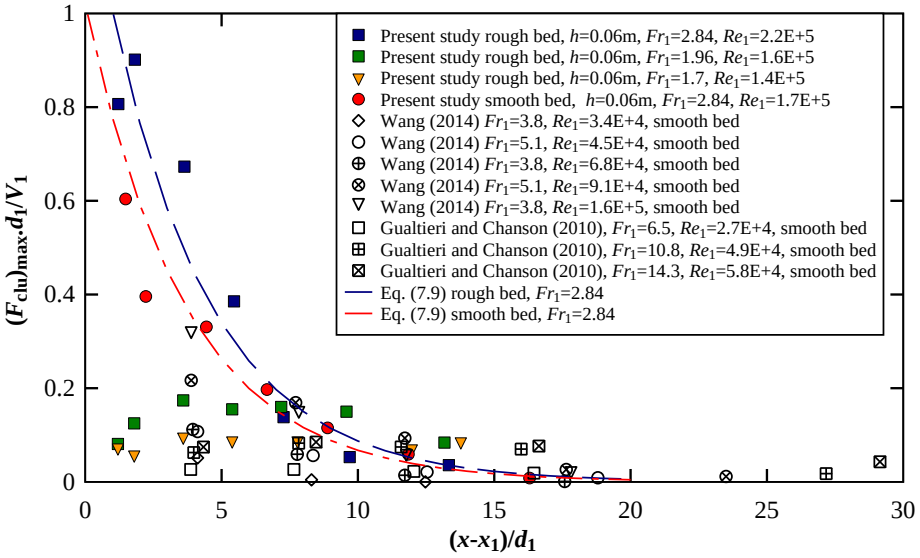

B: Based on Criterion B (Equation 7.3)

Figure 7.9 Maximum bubble cluster count rate in turbulent shear region as a function of the longitudinal distance from jump toe, comparison with empirical correlations

Based upon both Criteria A and B, comparisons were made between the maximum cluster count rate $(F_{clu})_{max} \times d_1/V_1$ and maximum bubble count rate $F_{max} \times d_1/V_1$ in the turbulent shear region on both rough and smooth bed configurations. The results are presented in Figure 7.10. For Criterion B, the present data were successfully compared with the available data of Wang (2014) in hydraulic jump on smooth bed. The relationship between the dimensionless maximum cluster count rate and bubble count rate followed a power correlation for Criterion A:

$$\frac{(F_{clu})_{max} \times d_1}{V_1} = 0.05 \left(\frac{F_{max} \times d_1}{V_1} \right)^{1.12} \quad (7.10)$$

and for Criterion B:

$$\frac{(F_{clu})_{max} \times d_1}{V_1} = 0.13 \left(\frac{F_{max} \times d_1}{V_1} \right)^{1.22} \quad (7.11)$$

In terms of both Criteria, the data presented in Figure (7.10) implied that the ratio between maximum numbers of clusters and bubbles was not a constant in the same flow. On rough bed close to the jump toe, the maximum value of $F_{max}/(F_{clu})_{max}$ was 23.5 and 5.3 which longitudinally changed to 9.3 and 18.1 at location far from the jump toe, for Criterion A and B, respectively. However, on smooth bed, close to the jump toe, the maximum value of $F_{max}/(F_{clu})_{max}$ was 20.1 and 4.9 which longitudinally changed to 8.7 and 33.8 at location far from the jump toe, for Criterion A and B, respectively. Regardless of bed type, a longitudinal

decay for the dimensionless maximum bubble and cluster count rate was observed. For Criterion A, the bubble count rate decayed more rapidly than the cluster count rate, the opposite if Criterion B was applied, in the shear flow region. Regarding the Criterion B, as reasoned by Wang (2014), it was likely due to the dissipation of turbulent structures more rapid than the flow de-aeration process. Overall, these findings were in agreement with the data of Gualtieri and Chanson (2007b), Chanson (2010) and Wang (2014) in hydraulic jump on smooth bed.

The locations with the maximum clustering rate were compared with those with the maximum local void fraction and maximum bubble count rate, Y_{Cmax} and Y_{Fmax}, respectively. Figure 7.11 compares the vertical elevations of maximum cluster count rate and the maximum bubble count rate. The present data were compared with the available data of Gualtieri and Chanson (2010) and Wang (2014) in hydraulic jump on smooth bed. The comparison reveals a good agreement between the data from the present study and those from Wang (2014). Independently of bed type and cluster criteria, the present data and those data from Wang (2014) tended close to the 1:1 line, implying almost the same vertical positions of $(F_{clu})_{max}$ and F_{max}, i.e. $Y_{(Fclu)max} \approx Y_{Fmax}$. Only the data of Fr_1 = 1.96 exhibited some scatter that might be associated with the undular behaviour of hydraulic jump.

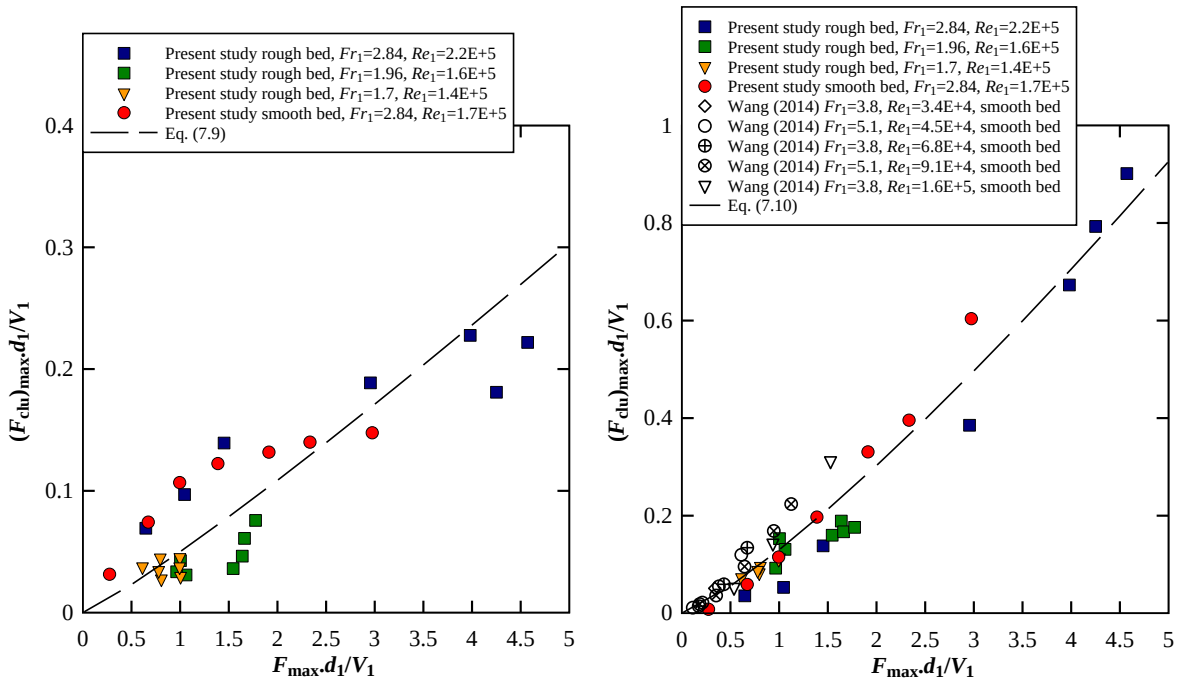

A: Based on Criterion A (Equation 7.2) B: Based on Criterion B (Equation 7.3)

Figure 7.10 Relationship between the maximum cluster count rate and the maximum bubble count rate

Figure 7.12 compares the vertical elevations of maximum cluster count rate and bubble count rate corresponding to maximum void fraction $Y_{F(Cmax)}$. The data are presented only for the highest inflow Froude number, i.e. Fr_1 = 2.84, which was related to hydraulic jump with the maximum void fraction in the shear region. The present data were compared with the data of Gualtieri and Chanson (2010) on smooth bed. Overall, regardless of bed type and clustering criteria, the ratio between the vertical elevations of maximum cluster count rate and cluster count rate corresponding to the maximum void fraction was not constant in the same flow. It implied a vertical position of maximum cluster count rate higher than that of the bubble count rate corresponding to the maximum void fraction in the shear flow region. The comparison between the vertical elevations of maximum cluster count rate and the maximum bubble count rate (Figure 7.11) as well as between the elevation of maximum cluster count rate and bubble count rate corresponding to maximum void fraction (Figure 7.12) indicated that the air bubbles mostly clustered at the elevation of the maximum bubble count rate in the shear region. These findings were in agreement with the data of Gualtieri and Chanson (2007a), Murzyn et al. (2007) and Gualtieri and Chanson (2010) in hydraulic jump on smooth bed.

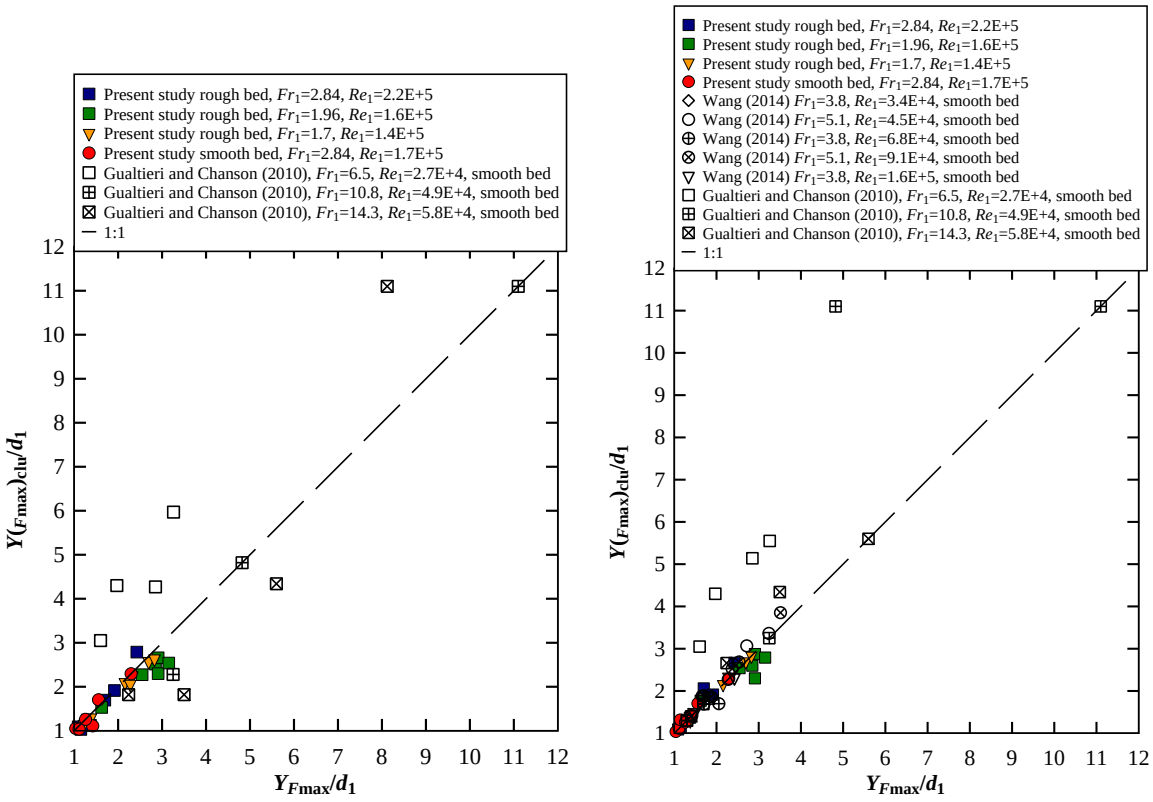

A: Based on Criterion A (Equation 7.2) B: Based on Criterion B (Equation 7.3)

Figure 7.11 Relationship between the vertical positions of maximum cluster count rate and the maximum bubble count rate

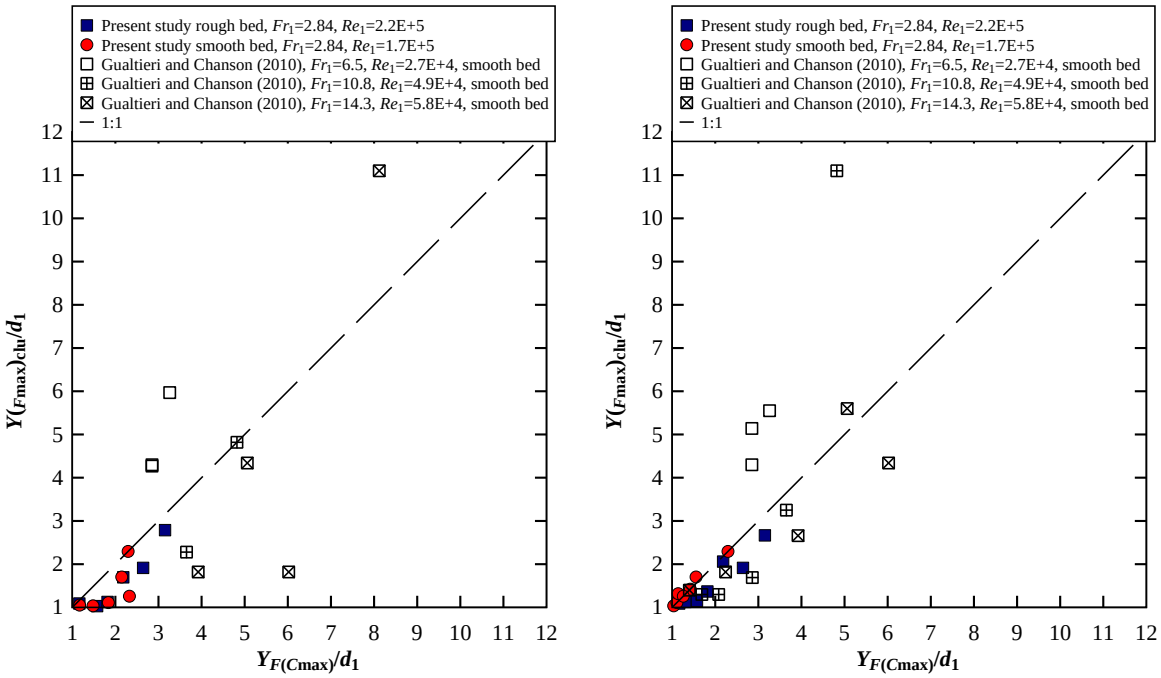

A: Based on Criterion A (Equation 7.2) B: Based on Criterion B (Equation 7.3)

Figure 7.12 Relationship between the vertical elevations of maximum cluster count rate and bubble count rate corresponding to maximum void fraction

Figure 7.13 compares the magnitude of cluster count rate and turbulent intensity corresponding to the elevation of maximum bubble count rate Y_{Fmax}. The data are presented only for Fr_1 = 2.84 on both rough and smooth bed configurations. Both criteria highlighted that higher rates of turbulent intensity were linked to higher clustering count rate. For turbulent intensity larger than 2, for the same value of *Tu* the magnitude of cluster count rate on rough bed was generally larger than that on smooth bed. Furthermore, for the same turbulent intensity, the number of clustered bubbles on rough bed was generally larger than that on smooth bed. Figure 7.13C compares the longitudinal distribution of the clustering rate and of the turbulent intensity. Close to the jump toe, in the first half of the roller, larger magnitudes of $Tu(y = Y_{Fmax})$ were consistently observed together with larger clustering count rates on rough bed. The average magnitude of $Tu(y = Y_{Fmax})$ = 2.3 and 2.2 on rough and smooth bed, respectively. In the second half of roller, the clustering rate decreased on rough bed more quickly than on smooth bed due to the higher rate of energy dissipation on rough bed.

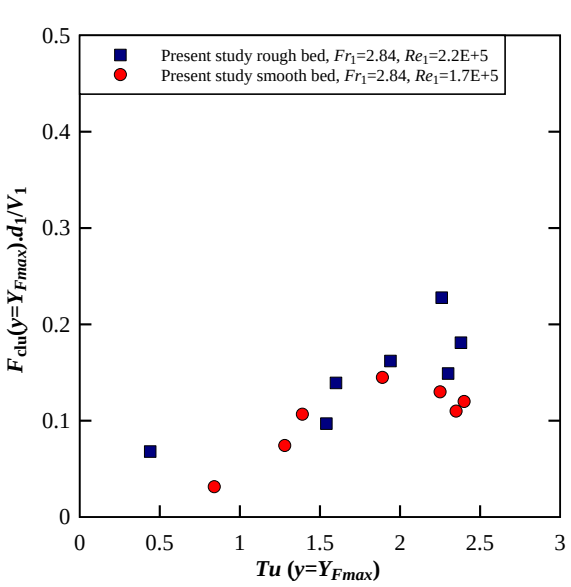

A: Based on Criterion A (Equation 7.2)

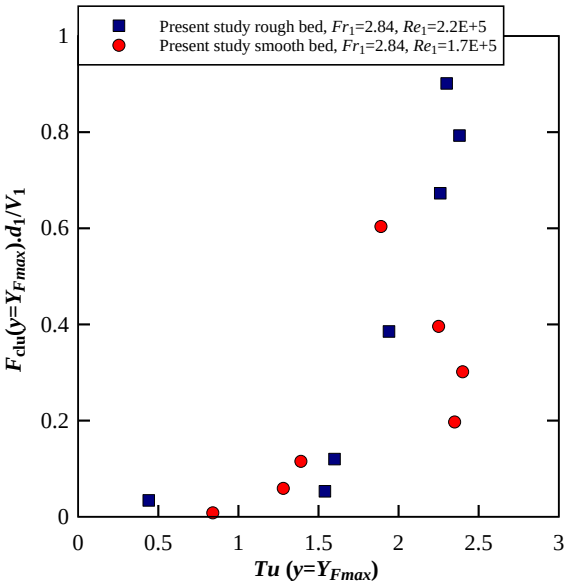

B: Based on Criterion B (Equation 7.3)

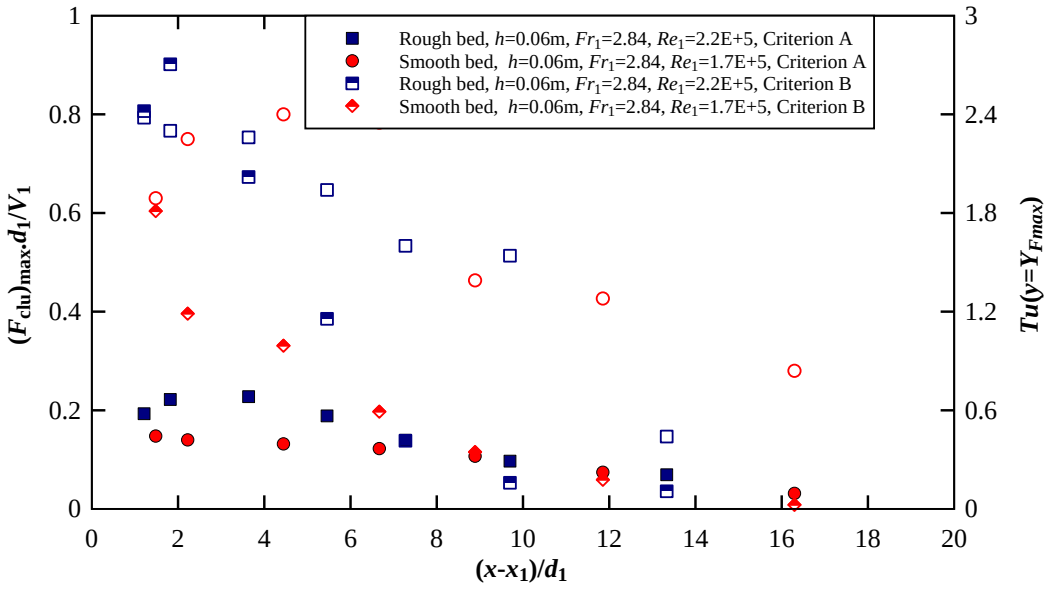

C: Longitudinal distribution of maximum cluster count rate and turbulent intensity. Filled symbols maximum cluster count rate, empty symbols turbulent intensity

Figure 7.13 Relationship between the maximum cluster count rate and turbulent intensity corresponded to the elevation of maximum cluster count rate Y_{Fmax}

Clustering count rate was compared with the interfacial velocity at the elevation of maximum bubble count rate Y_{Fmax}. Herein, the data are presented in Figure 7.14 for Fr_1 = 2.84 on both rough and smooth bed configurations. As the interfacial velocity increased, the clustering count rate increased. Since the elevation of maximum bubble count rate Y_{Fmax} was located in the developing shear layer, the magnitude of interfacial velocity should be positive. For Criterion A, at the same magnitude of interfacial velocity, the number of clustered bubbles on

rough bed was remarkably larger than that on smooth bed. For Criterion B, no significant difference was observed between rough and smooth bed data. The larger magnitude of interfacial velocity was observed close to the jump toe while its magnitude decreased in the longitudinal direction as some kinetic energy was dissipated (Figure 7.14C). Furthermore, both the interfacial velocity and cluster count rate decreased with the distance from the jump toe (Figure 7.14C).

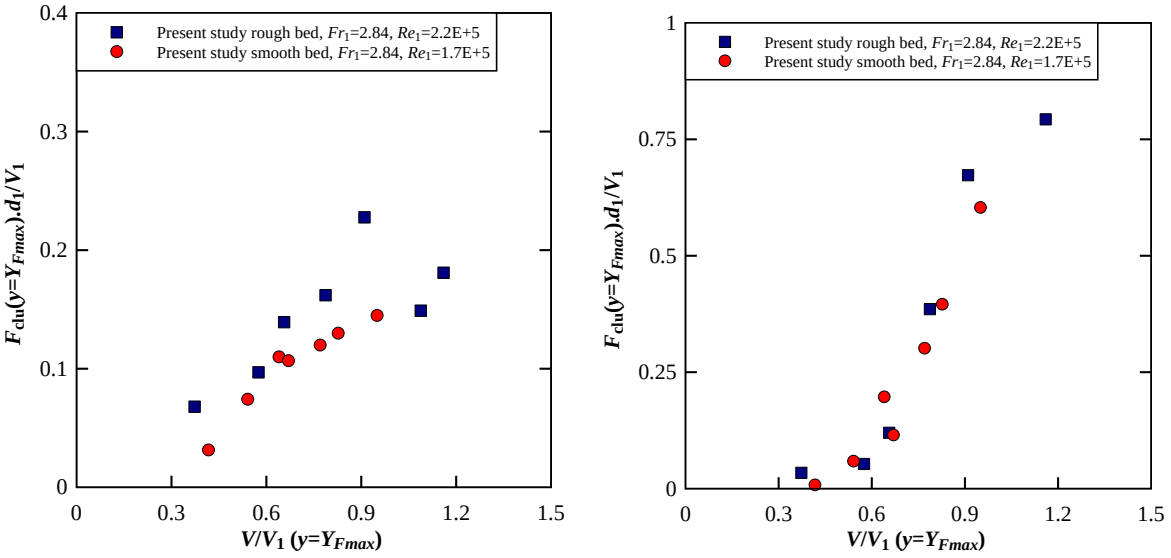

A: Based on Criterion A (Equation 7.2)

B: Based on Criterion B (Equation 7.3)

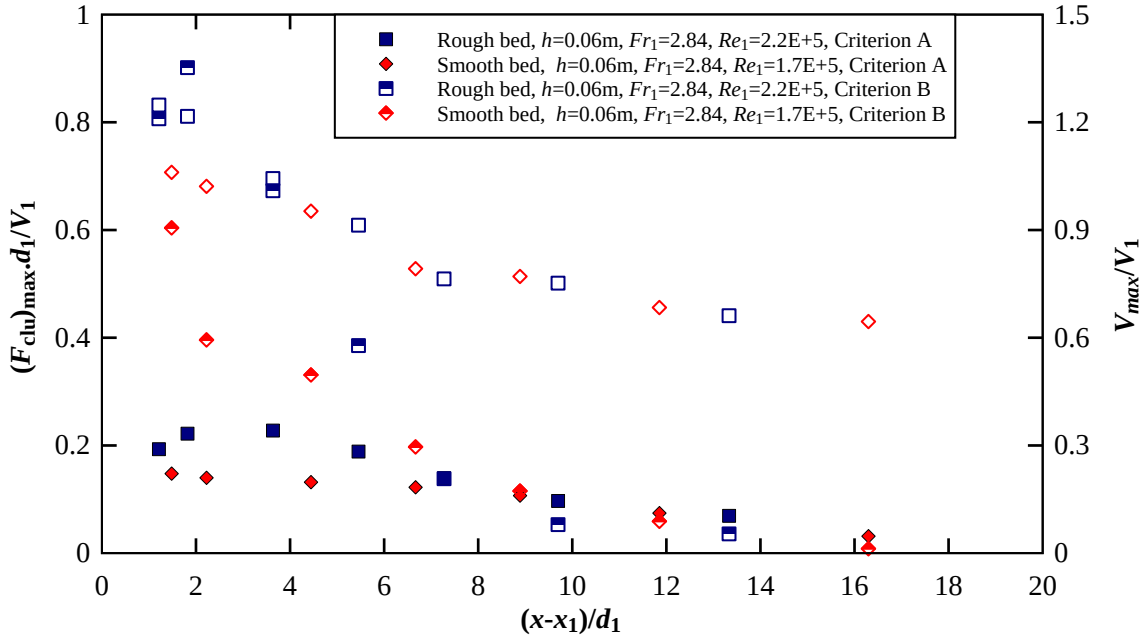

C: Longitudinal distribution of maximum cluster count rate and interfacial velocity. Filled symbols maximum cluster count rate, empty symbols interfacial velocity

Figure 7.14 Relationship between the maximum cluster count rate and interfacial velocity corresponding to the elevation of maximum cluster count rate Y_{Fmax}

Cluster count rate was also compared with the advection length scale at Y_{Fmax}. The advection length scale represented a characteristic size of the turbulent structures advected in the longitudinal direction. Figure 7.15 shows the data for Fr_1 = 2.84 on both rough and smooth bed configurations. Overall, high cluster count rates were associated with high values of the advection length scale. Using Criterion A, for the same magnitude of advection length scale, the number of clustered bubbles on rough bed was remarkably larger than that on smooth bed. Using Criterion B, for $L_{xx}/d_1 < 0.1$, there was no significant difference between rough and smooth bed data while, for $L_{xx}/d_1 > 0.1$, for the same magnitude of advection length scale, the number of clustered bubbles on rough bed was notably larger than that on smooth bed. It should be noted that larger advection length scales on rough bed were associated with the formation of large eddies. Close to the jump toe, larger length scales were associated with the higher bubble count rate in the turbulent shear layer while, further downstream, larger length scales were related to the roller length (Section 6.4). Hence, close to the jump toe, the formation of large eddies on rough bed resulted in a rate of clustered bubbles higher than that on smooth bed. Although close to the jump toe the maximum advection length scale on rough bed was larger than that on smooth bed (Section 6.4), at Y_{Fmax} the advection length scale was larger on smooth bed than on rough bed.

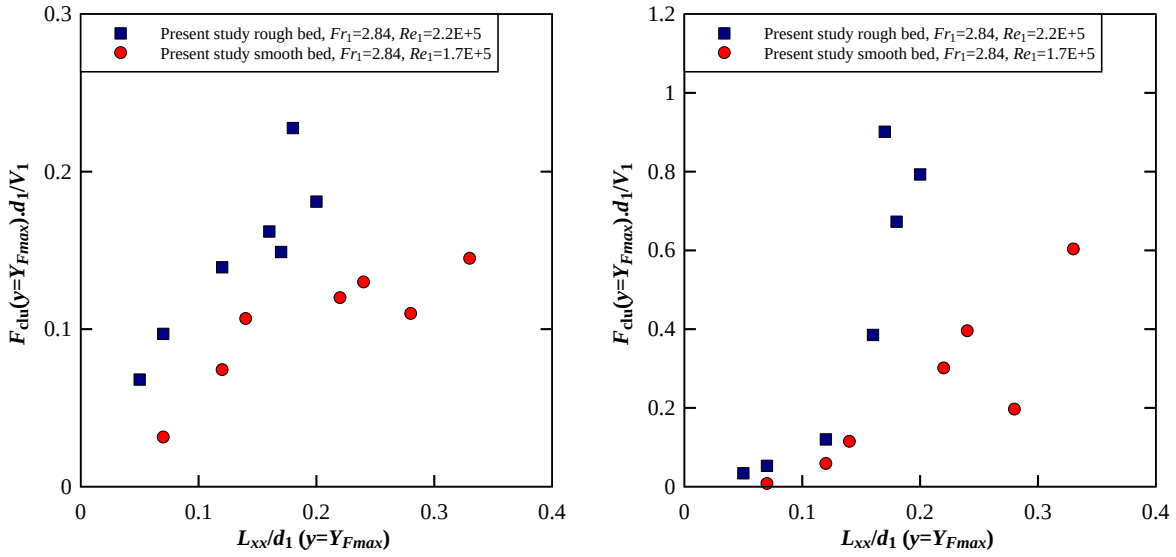

A: Based on Criterion A (Equation 7.2) B: Based on Criterion B (Equation 7.3)

Figure 7.15 Relationship between the maximum cluster count rate and advection length scale corresponding to the elevation of maximum cluster count rate Y_{Fmax}

7.3.3 Cluster size and cluster proportion

The cluster size defined as the number of bubbles in a cluster, and the cluster proportion refers to the percentage of clustered bubbles relative to the total number of the detected bubbles. Figure 7.16 presents the vertical distributions of cluster size N_{clu} for different longitudinal locations on both rough and smooth bed configurations with the same inflow Froude number Fr_1 = 2.84. The time-averaged void fraction is plotted for comparison only in the shear layer region. Note that N_{clu} referred to the number of bubbles for C < 0.3. Independently of the bed type, according to Criterion A, the vertical elevation of maximum cluster size was lower than Y_{Cmax}. However, according to Criterion B, the vertical elevation of maximum cluster size was same as the dimensionless elevation of Y_{Cmax} in the shear region. Since the larger magnitudes of cluster size corresponded to the highly-aerated flow, Criterion B was more consistent with the rate of flow aeration at the elevation of maximum void fraction in the shear region.

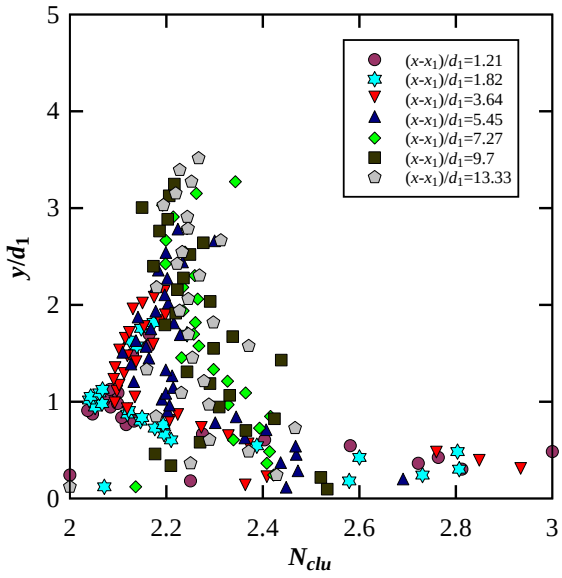

A1: Rough bed, based on Criterion A

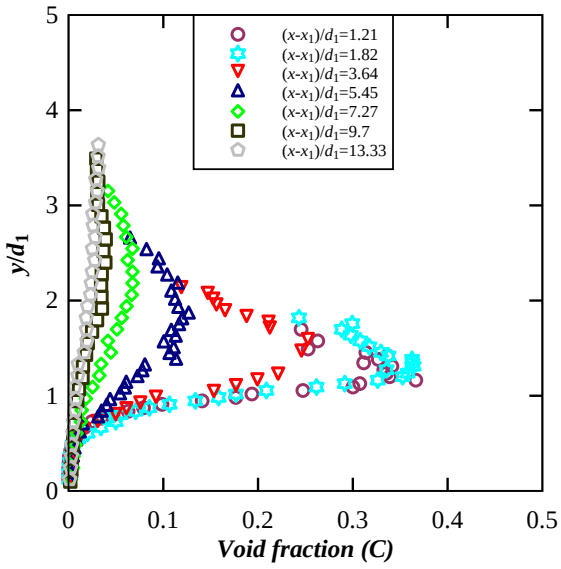

A2: Corresponding void fraction distribution

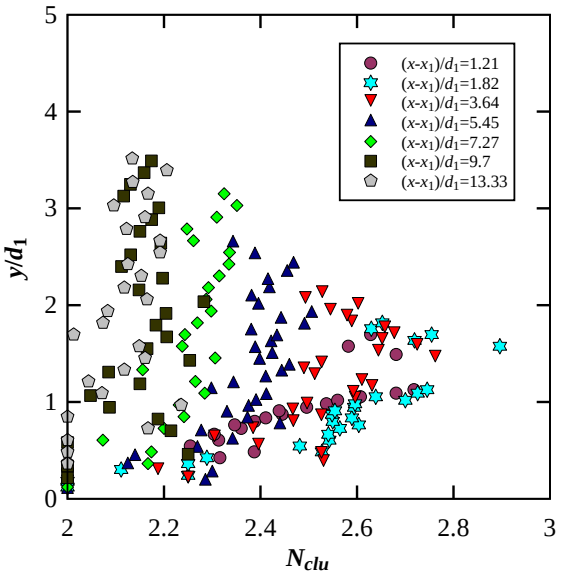

B1: Rough bed, based on Criterion B

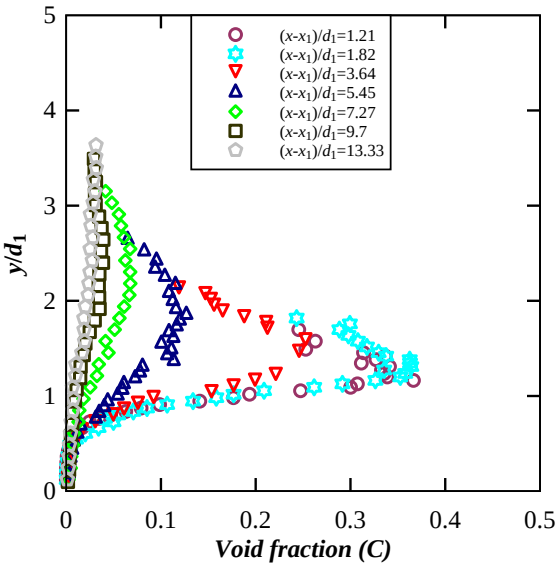

B2: Corresponding void fraction distribution

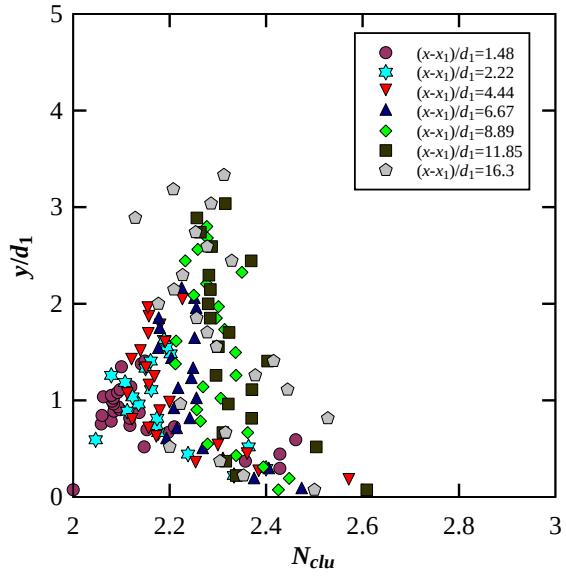

C1: Smooth bed, based on Criterion A

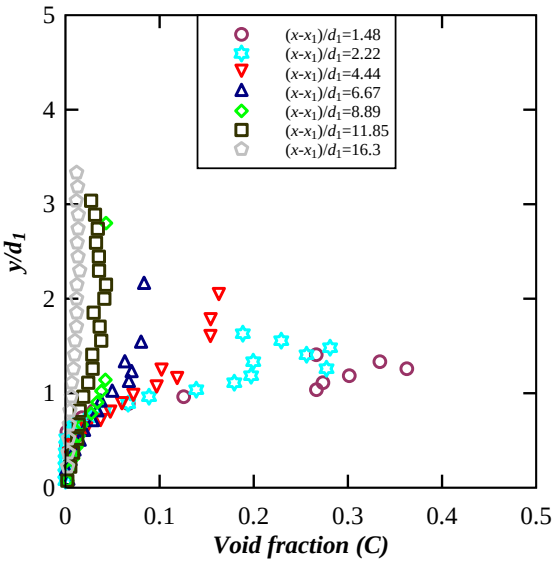

C2: Corresponding void fraction distribution

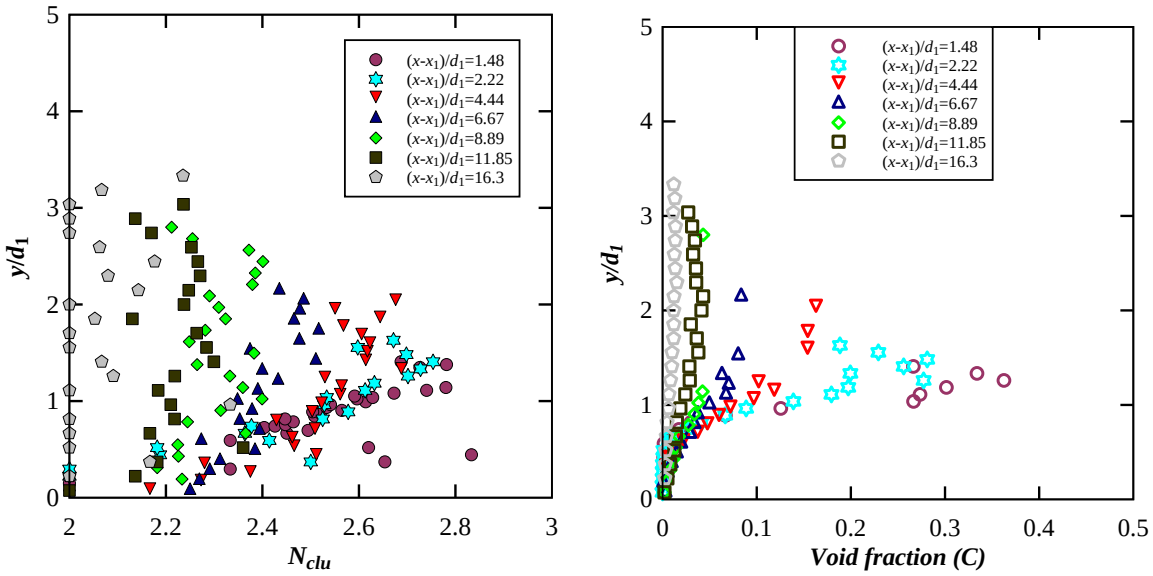

D1: Smooth bed, based on Criterion A D2: Corresponding void fraction distribution

Figure 7.16 Vertical distributions of cluster size (left), comparison with the time-averaged void fraction (right). Rough bed with Fr_1 = 2.84 and Re_1 = 2.2E+5, smooth bed with Fr_1 = 2.84 and Re_1 = 1.7E+5 Filled symbols cluster size, empty symbols void fraction

Figure 7.17 shows the longitudinal distribution of average cluster size for both Criteria on both rough and smooth bed configurations. Note that for Fr_1 = 2.84, the data refer to the shear region, while for Fr_1 = 1.96 and 1.7 the data refer to the vertical depth with C < 0.3 (Section 5.3.1). For Fr_1 = 1.96 and 1.7, visual observations suggested that a splashing droplet or water spray above the roller often contained a number of air entities inside (Section 4.2). In such a condition, the foamy structure of the air-water entities could be identified as a droplet/bubble cluster. Overall, regardless of bed type, Criterion A provided a longitudinally constant value of 2.3 bubbles for each cluster. While, Criterion B resulted in a longitudinal decreasing of the cluster size, with average of 2.4 bubbles for each cluster. The difference was likely related to the different definition of cluster in Criterion A and B. Gualtieri and Chanson (2007b) found that the average number of bubbles per cluster was about 2.5 in the dropshaft and about 2.3 in the hydraulic jump, demonstrating that cluster structures were mostly formed by two bubbles. The findings were in agreement with Chanson and Toombes (2002) in transition and skimming flows over stepped chute and Gualtieri and Chanson (2007b) and Wang (2014) in hydraulic jump on smooth bed.

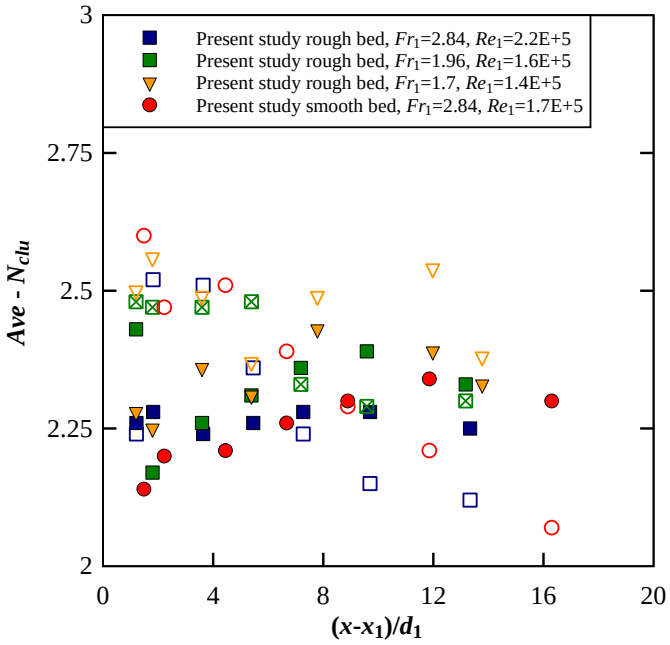

Figure 7.17 Longitudinal distribution of average cluster size. Filled symbols, Criterion A, empty symbols, Criterion B

Figure 7.18 presents the vertical distributions of cluster proportion using both criteria on both rough and smooth bed. Vertical distribution of time-averaged void fraction was added for comparison. Note that P_{clu} referred to the percentage of bubbles for $C < 0.3$. The distributions of cluster proportion showed trend a similar to that of the cluster size. Large cluster proportion suggested a combination of high aeration level and intense turbulent structures in the shear flow region on both rough and smooth bed configurations. In other words, a larger cluster proportion was associated to the larger magnitude of void fraction (Figure 7.16) and to the larger magnitude of turbulent intensity (Figure 7.13). Overall, using Criterion B, the maximum magnitude of cluster proportion was observed at Y_{Cmax} in the shear region. Regardless of bed type, close to the jump toe, the maximum P_{clu} was approximately 0.56 and 0.31 at the dimensionless elevation of Y_{Cmax} for Criterion A and B, respectively. Therefore, Criterion B was more consistent with the highly aerated flow at the local elevation of maximum void fraction in the shear region.

Figure 7.19 illustrates the distribution of average cluster proportion as function of longitudinal distance from the jump toe for both Criteria on both rough and smooth bed. Comparatively, for the same inflow Froude number Fr_1 = 2.84, no noticeable difference between rough and smooth bed was observed with an average $Ave.P_{clu}$ = 0.22% using Criterion A. However, according to Criterion A, the average cluster proportion on smooth

bed was larger than that on rough bed. Regardless of the bed type, Criterion B highlighted a longitudinally decay for the average cluster proportion. The findings were in agreement with the data trend and magnitude from Gualtieri and Chanson (2007b) and Wang (2014) in a hydraulic jump on smooth bed, which showed $0.14 < Ave.P_{clu} < 0.34$ for $3.8 < Fr_1 < 14.3$.

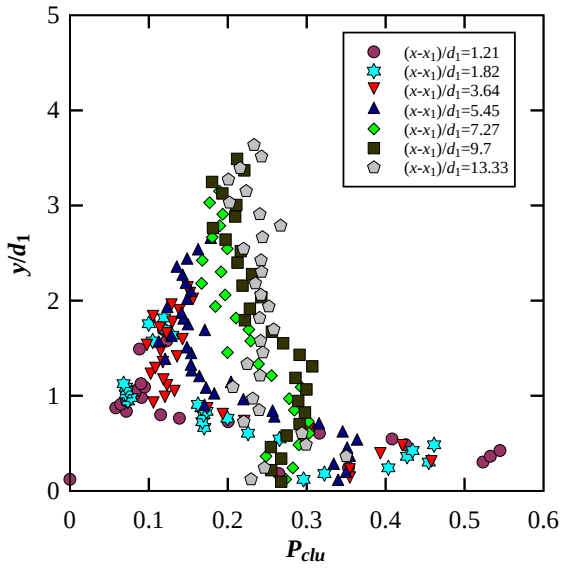

A1: Rough bed, based on Criterion A

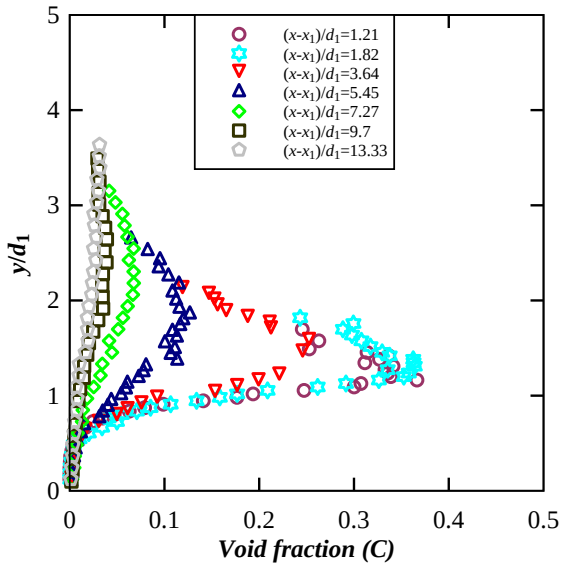

A2: Corresponding void fraction distribution

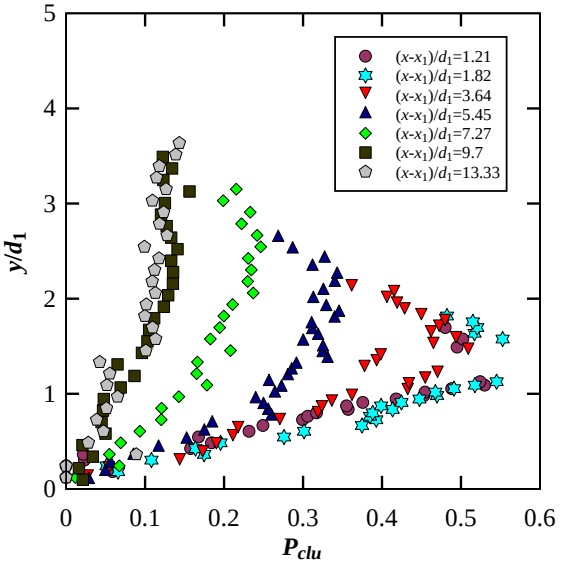

B1: Rough bed, based on Criterion B

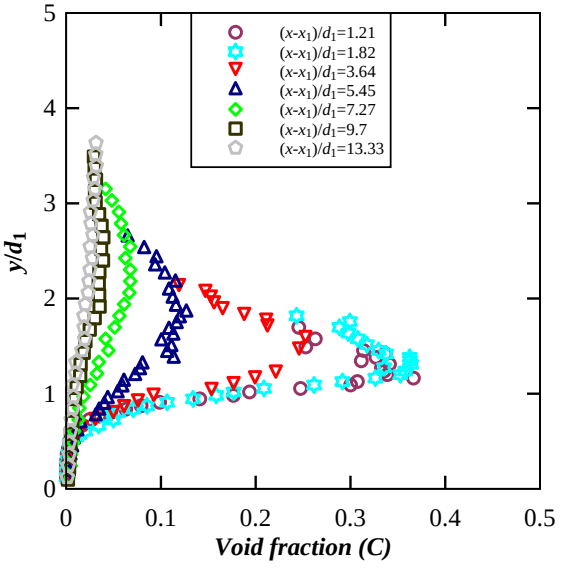

B2: Corresponding void fraction distribution

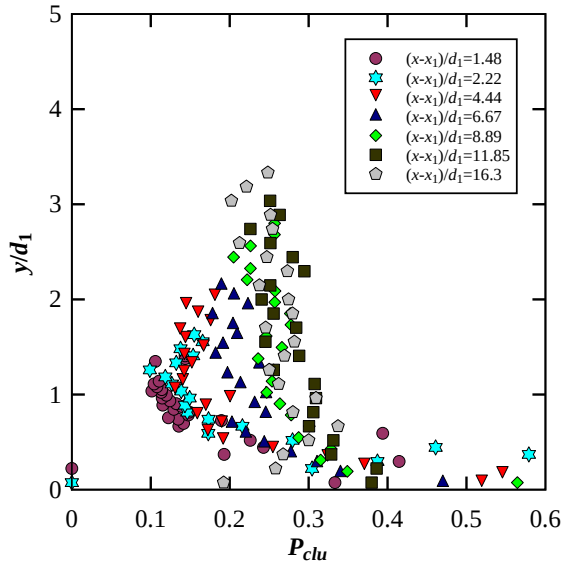

C1: Smooth bed, based on Criterion A

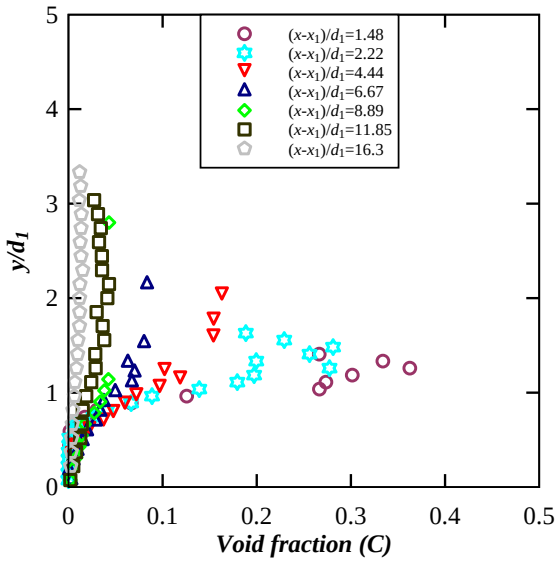

C2: Corresponding void fraction distribution

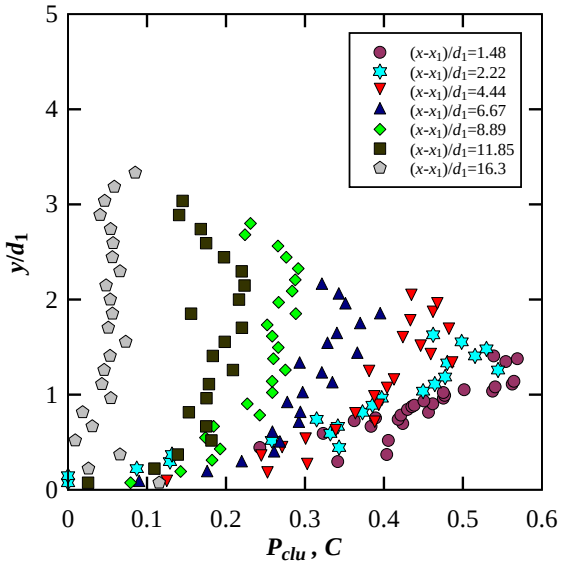

D1: Smooth bed, based on Criterion A

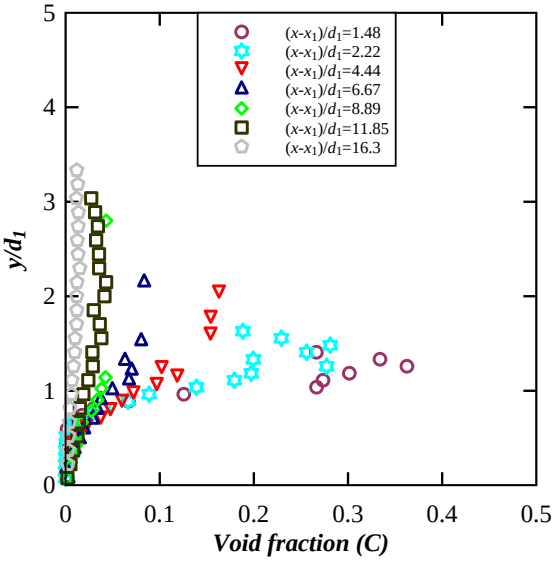

D2: Corresponding void fraction distribution

Figure 7.18 Vertical distributions of cluster proportion (left), comparison with the time-averaged void fraction (right). Rough bed with Fr_1 = 2.84 and Re_1 = 2.2E+5, smooth bed with Fr_1 = 2.84 and Re_1 = 1.7E+5 Filled symbols cluster size, empty symbols void fraction

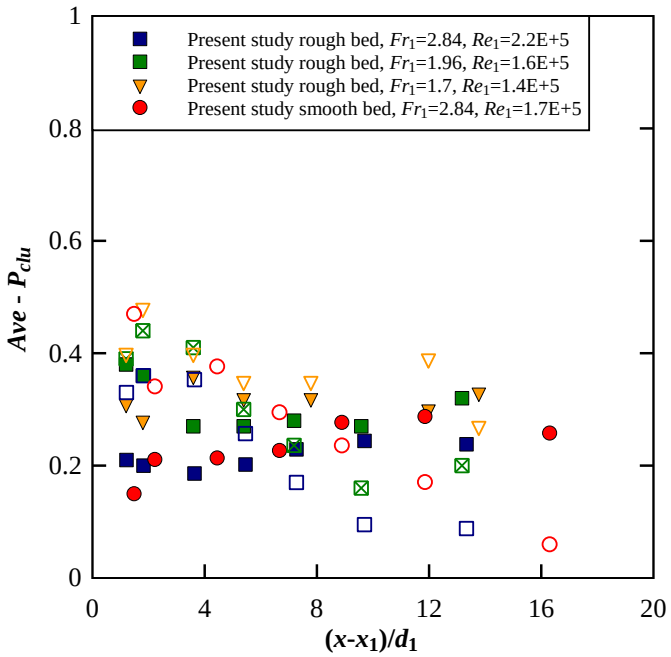

Figure 7.19 Longitudinal distribution of average cluster proportion. Filled symbols Criterion A, empty symbols Criterion B

Figure 7.20 compares the average cluster size and cluster proportion for both Criteria on rough and smooth bed. The ratio of P_{clu}/N_{clu} is equivalent to the ratio of cluster and particle count rates F_{clu}/F. The average cluster size N_{clu} and the cluster proportion P_{clu} are related as:

$$P_{clu} = \frac{F_{clu}}{F} \times N_{clu} \tag{7.12}$$

It was expected that, for a cluster count rate quasi-proportional to the bubble count rate, the distributions of average cluster size and cluster proportion imply similar trends of variation. Figure 7.20 presents a relationship between cluster size and proportion for bubbles in water for both Criteria. For Fr_1 = 2.84 on both rough and smooth bed configurations, the data are presented in the shear layer with $C < 0.3$. Generally, independently of bed type and clustering Criterion, the bubble cluster proportion was typically under 60%, with an average cluster size smaller than 3. Some scatter data were observed on rough bed for Fr_1 = 1.96 and 1.7, which might be associated with the undular behaviour of hydraulic jump. The data distribution was correlated as:

$$P_{clu} = 0.68 \times (N_{clu} - 2)^{0.73} \tag{7.13}$$

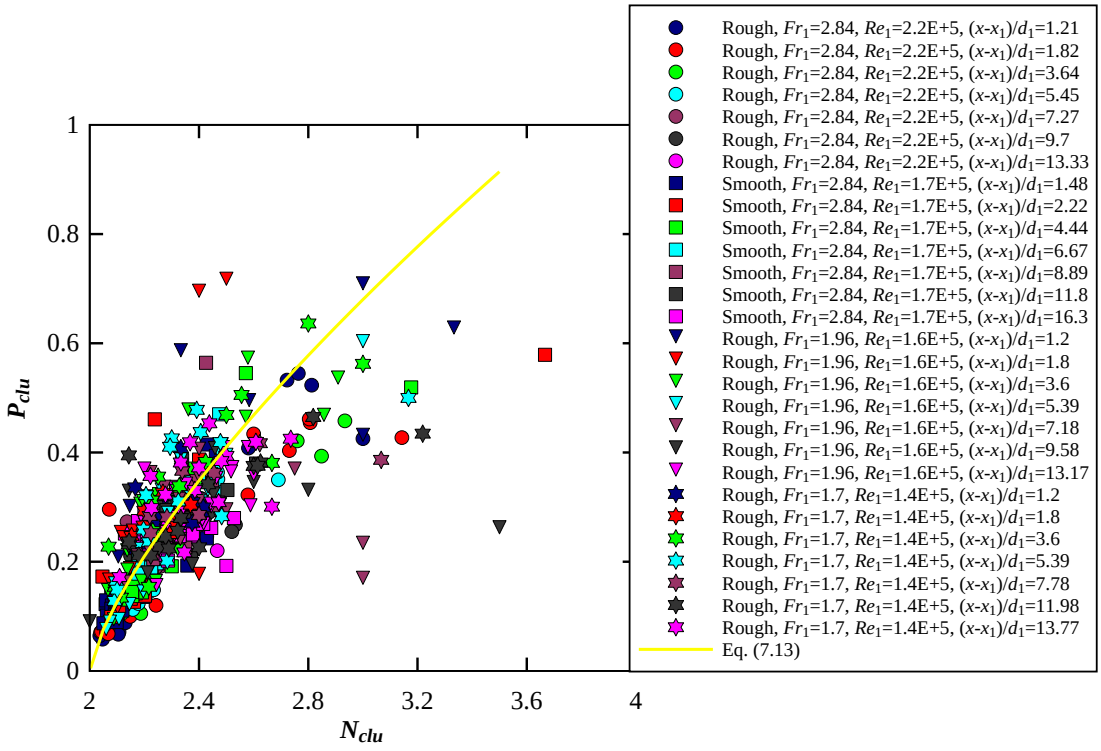

A: Based on Criterion A

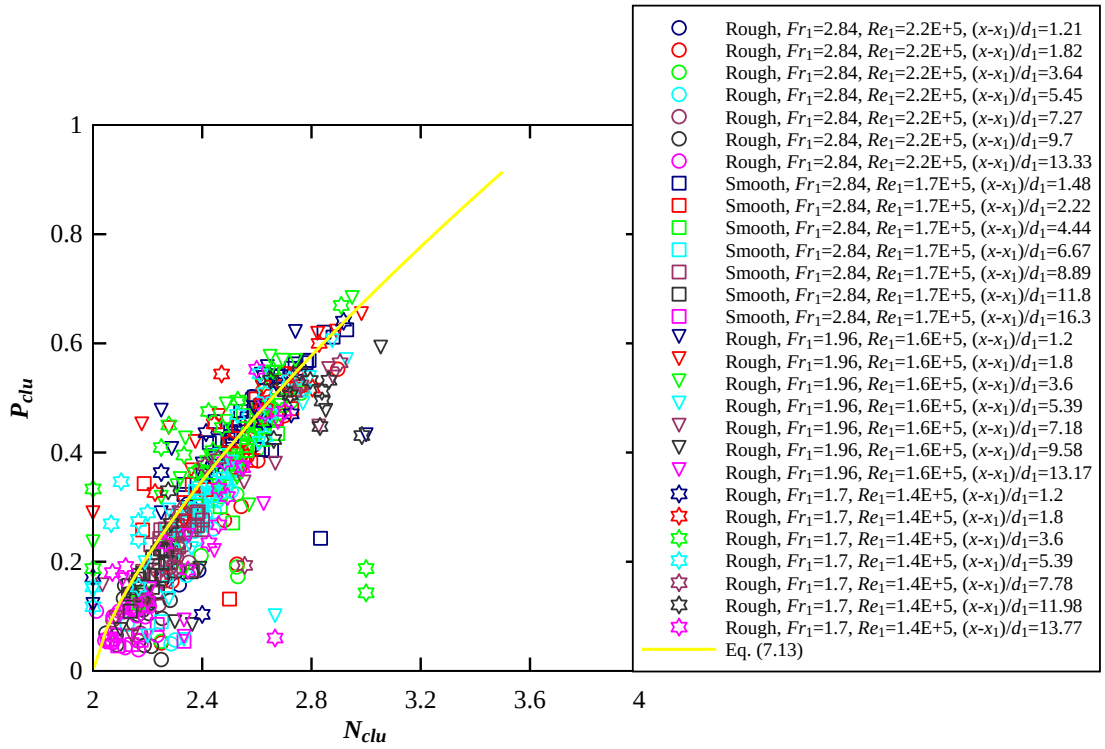

A: Based on Criterion B

Figure 7.20 Relationship between average cluster size and cluster proportion, comparison with the correlations (Equation 7.13)

7.4 Interparticle arrival time

Air bubbles were trapped in large-scale vortical structures generated in the turbulent shear layers. As vortical structures were advected downstream, they grew up in size by vortex pairing and contribute to further clustering. The presence of bubble groups showed that an individual bubble might interact with other bubbles when they travelled downstream one after another or side by side. It also suggested that the advection of bubbles was not a random process (Chanson 2007a). Herein, a complementary approach based upon interparticle arrival time, *IAT*, was applied to identify a cluster. The $IAT_{\tau IA}$ was defined as the time between the arrival of two consecutive bubbles measured by a probe sensor fixed in specific position (Gualtieri and Chanson 2013). Analysing the τ_{IA} may give some information about the occurrence or not of clustering within the flow structure. In a randomly-dispersed flow, the interparticle arrival time distributions follow inhomogeneous Poisson statistics, giving an interparticle time distribution function (Edwards and Marx 1995a,b, Martinez-Bazan et al. 2002, Aliseda and Lasheras 2011):

$$f\ (\tau\,\mathrm{IA}) = \frac{\lambda(T_{scan} - \tau\,\mathrm{IA})\exp(-\lambda\,\tau\,\mathrm{IA})}{\lambda T_{scan} - 1 + \exp(-\lambda T_{scan})} \tag{7.14}$$

where τ_{IA} is the interparticle arrival time, T_{scan} is the scanning duration (herein 90 or 180 s) and $\lambda = N_{ab}/T_{scan}$ and N_{ab} is the number of particles (Heinlein and Fritsching, 2006). Equation (7.14) addresses an ideal randomly-dispersed flow driven by a superposition of Poisson point processes of bubble sizes. The assumption behind Equation (7.14) is that there is no interactions between dispersed particles (Chanson 2007a) and the analysis was 1D. However, in shear bubbly flows, this assumption might be not respected as bubbles coalescence and breakup are common processes. Furthermore, the bubbles might not precisely follow the same trajectory to be measured by the probe. Anyway, it was believed that, although the analysis of clustering based upon both Criteria A and B (Section 7.3) and IAT are complementary, the latter is able to provide a better picture of the range of particle classes influenced by non-random clustering (Chanson 2007a). Furthermore, for the methods based upon the particle intervals, i.e. the water chord time between adjacent bubbles, the reference length/time scale could be a constant magnitude, a statistical particle interval or a dimension of the leading particle itself (Chanson and Toombes 2002a, Chanson et al. 2006, Chanson 2007a, Gualtieri and Chanson 2010).

Any non-randomness introduced by particle grouping or clustering could be result in deviation of interparticle time distributions from Equation (7.14), and may be quantified by a

chi-square analysis (Chanson and Gualtieri 2007b). Edwards and Marx (1995b) reasoned that breaking down the bubbly flow into narrow classes of particles with comparable sizes that have the same behaviour could result in a best analysis. As a simple way, the bubble population was divided in terms of $(t_{ch})_a$ or $(l_{ch})_a$. The probability distribution of interparticle arrival time was compared to the Poisson distribution for different classes of bubble chord time. At each location, on both rough and smooth bed configurations, the detected bubbles were subdivided into four classes in terms of $t_{ch\text{-}ab}$ (Table 7.2). The number of points of measurement selected for the IAT analysis were 6 and 6 on rough and smooth bed, respectively. Note that at the vertical elevation of Y_{Cmax} for $(x\text{-}x_1)/d_1$ = 1.21 and 1.48, C = 0.37 and 0.4, i.e. larger than 0.3, on rough and smooth bed, respectively. Hence, these points were not considered in the IAT analysis. Table 7.3 listed the points of measurement together with their C and F values. The interparticle arrival time $IAT_{\tau IA}$, were subdivided into 80 classes from 0 to 40 ms (size 0.5 ms).

Table 7.2 Classes of bubbles for the IAT analysis

Class	**Air chord time $t_{ch\text{-}ab}$ (ms)**
1	[0.0, 0.5]
2	[0.5, 1.5]
3	[1.5, 3.0]
4	[3.0, 5.0]

Table 7.3 Measurement points chosen for the IAT analysis in the hydraulic jump

Bed type	Fr_1	$(x\text{-}x_1)/d_1$	Characteristic elevation	y/d_1	C	F (Hz)
Rough	2.84	1.21	Y_{Fmax}	1.1	0.3	130.0
			Y_{Cmax}	1.16	0.37*	134.7
			y*	1.7	0.24	34.4
		7.27	Y_{Fmax}	1.7	0.05	44.7
			Y_{Cmax}	2.18	0.07	41.2
			y*	3.15	0.04	14.2
Smooth	2.84	1.48	Y_{Fmax}	1.04	0.27	101.8
			Y_{Cmax}	1.18	0.4*	88.0
			y*	1.41	0.27	65.5
		8.89	Y_{Fmax}	1.26	0.05	34.1
			Y_{Cmax}	2.32	0.06	26.4
			y*	2.8	0.04	14.8

*The data for these elevations were not calculated, because C > 0.3.

Figures 7.21 and 7.22 show the comparison for four bubble chord time classes on rough bed for Fr_1 = 2.84 with two cross-sections $(x\text{-}x_1)/d_1$ = 1.21 and $(x\text{-}x_1)/d_1$ = 7.27, respectively.

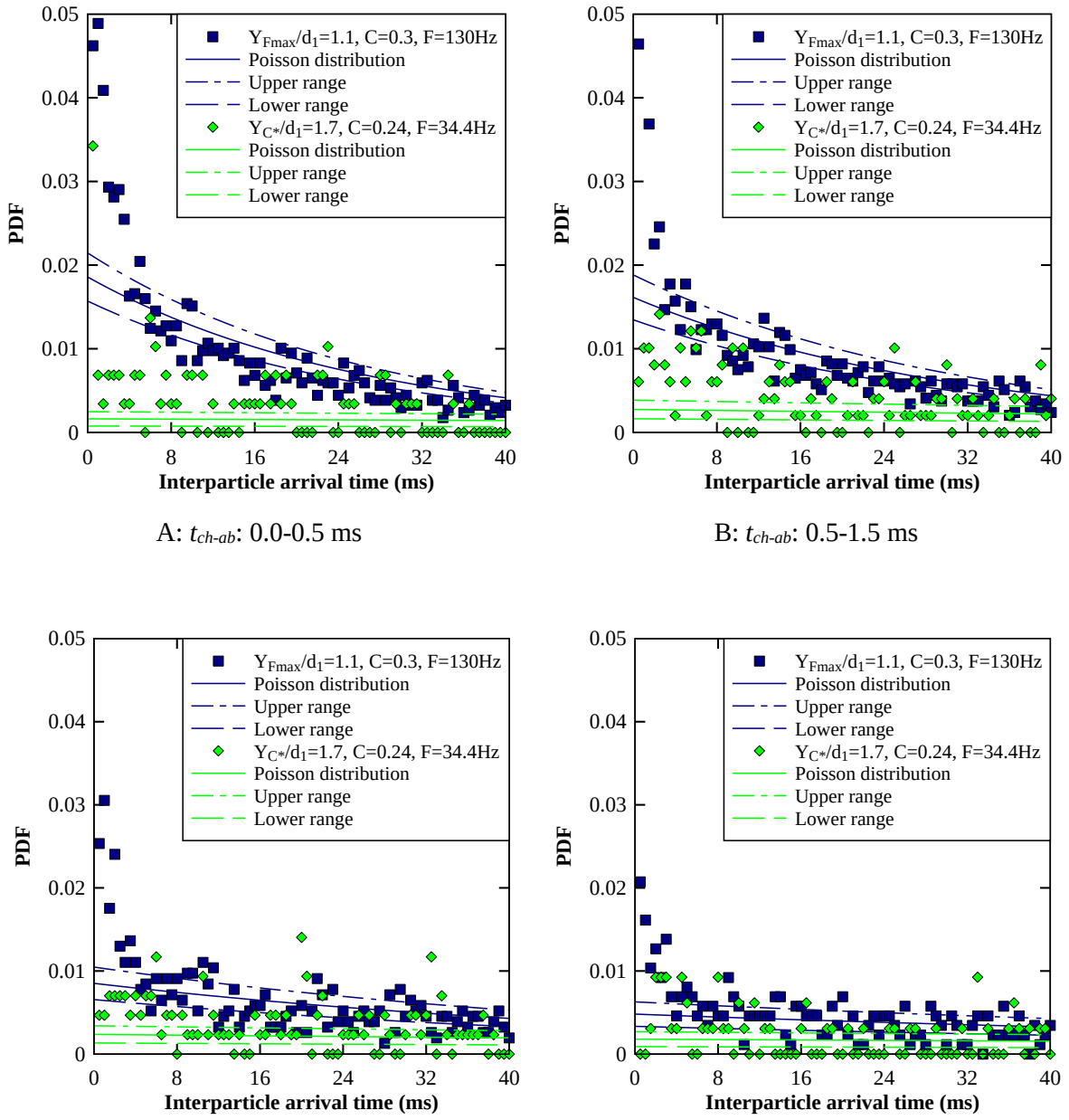

A: $t_{ch\text{-}ab}$: 0.0-0.5 ms

B: $t_{ch\text{-}ab}$: 0.5-1.5 ms

C: $t_{ch\text{-}ab}$: 1.5-3.0 ms

D: $t_{ch\text{-}ab}$: 3.0-5.0 ms

Figure 7.21 Probability density function of interparticle arrival time for different bubble chord classes at different characteristic elevations with the same longitudinal position. Rough bed, flow conditions: Fr_1 = 2.84, Re_1 = 2.2E+5, $(x\text{-}x_1)/d_1$ = 1.21

The experimental data were compared with Equation (7.14) and the expected deviation was also provided. Overall, regardless of the longitudinal distance from the jump toe and the class of bubble chord time, the difference between experimental and theoretical data showed the same magnitude for the characteristic elevations of Y_{Fmax} and Y_{Cmax} but it was higher than that for y^*. This suggested that the rate of bubble clustering for characteristic elevations of Y_{Fmax} and Y_{Cmax} was higher than that for y^*. Both Figures 7.21 and 7.22 demonstrates that the experimental distribution of bubbles was different from that expected for a random process.

Also, for both cases, the difference between experimental data and Poisson distribution decreased to zero as $IAT_{\tau IA}$ increased. This trend was similar to that observed in a dropshaft (Gualtieri and Chanson 2013). Close to the jump toe i.e. $(x\text{-}x_1)/d_1$ = 1.21, regardless of vertical elevation and bubble chord time class, bubbles with $IAT_{\tau IA}$ less than 5.0 ms did not show a true random behaviour (Figure 7.21). These bubbles had a frequency larger than that predicted by the Poisson law. The presence of large amount of small interparticle arrival time suggested a possible occurrence of bubble clustering. Farther downstream from the jump toe i.e. $(x\text{-}x_1)/d_1$ = 7.27, although the relative differences from the Poisson distribution for the second class of bubble chord time were higher than the other classes, generally, the difference between experimental and theoretical data was lower than that for $(x\text{-}x_1)/d_1$ =1.21. It demonstrated the lower rate of bubble clustering farther downstream of the jump toe.

Table 7.4 reported the expected deviation of a random bubbly mixture from the theoretical curve by Equation (7.14). The sixth column of Table (7.4) shows the range of $IAT_{\tau IA}$ that had difference with Poisson low. Large deviations highlighted that bubbles with smaller $IAT_{\tau IA}$ were in the bubbly flow zone with higher probability than it could be expected in a randomly-distributed bubbly flow. The last column of Table (7.4) listed the number of bubbles of each class of bubble chord time.

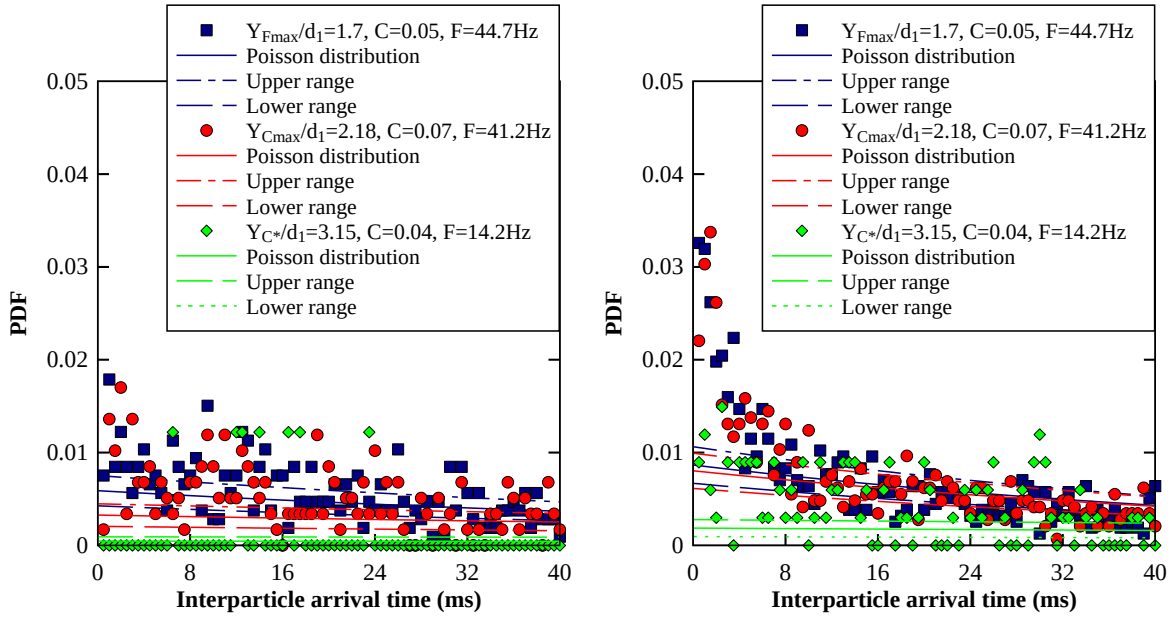

A: $t_{ch\text{-}ab}$: 0.0-0.5 ms

B: $t_{ch\text{-}ab}$: 0.5-1.5 ms

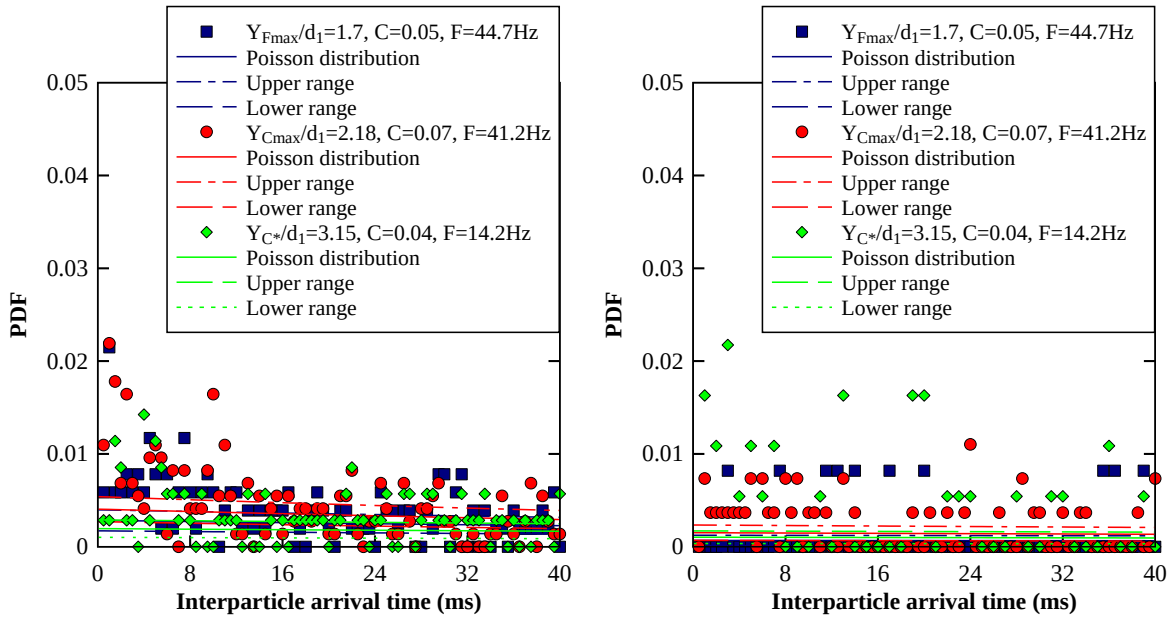

C: $t_{ch\text{-}ab}$: 1.5-3.0 ms D: $t_{ch\text{-}ab}$: 3.0-5.0 ms

Figure 7.22 Probability density function of interparticle arrival time for different bubble chord classes at different characteristic elevations with the same longitudinal position. Rough bed, flow conditions: Fr_1 = 2.84, Re_1 = 2.2E+5, $(x\text{-}x_1)/d_1$ = 7.27

Table 7.4 Details of IAT analysis for each flow condition

Bed type	Fr_1	$(x\text{-}x_1)/d_1$	Elevation	Expected deviation from Poisson law for 4 classes (%)				Number of bubbles			
Rough	2.84	1.21	Y_{Fmax}	15	17	23	30	3375	2929	1539	868
			Y_{Cmax}	-	-	-	-	-	-	-	-
			y^*	53	40	43	50	292	495	427	324
		7.27	Y_{Fmax}	28	23	40	81	1063	1565	512	122
			Y_{Cmax}	37	24	33	54	588	1452	730	272
			y^*	99	49	48	66	82	335	351	184
Smooth	2.84	1.48	Y_{Fmax}	20	17	24	32	2078	2723	1414	766
			Y_{Cmax}	-	-	-	-	-	-	-	-
			y^*	33	22	27	36	749	1679	1072	611
		8.89	Y_{Fmax}	42	24	37	70	447	1366	600	167
			Y_{Cmax}	64	34	35	48	194	677	659	349
			y^*	96	48	46	59	88	346	385	232

Fr_1 = 2.84 on rough bed, regardless of longitudinal distance from the jump toe, the expected deviation from Poisson law decreased with increasing the size of bubble chord time (Table 7.4). Note that the expected deviation from Poisson was related to the number of bubbles for each class of bubble chord time which decreased with the increasing number of class. Range of shorter $IAT_{\tau IA}$ deviated from Poisson law showed approximately the same magnitude for Y_{Fmax} and Y_{Cmax}, but they were higher than that for y^*. Overall, close to the jump toe, i.e. $(x\text{-}x_1)/d_1$ = 1.21, the percent of shorter $IAT_{\tau IA}$ deviated from Poisson law were higher than that far from the jump toe, i.e. $(x\text{-}x_1)/d_1$ = 7.27, revealing the larger rate of clustering.

Figures 7.23 presents the comparison for classes 1 and 4 on smooth bed for Fr_1 = 2.84 at (x-x_1)/d_1 = 1.48 and 8.89, respectively. Overall, in both location, the difference between the experimental data and the Poisson distribution decreased to zero with the increasing $IAT_{\tau IA}$. Close to the jump toe i.e. (x-x_1)/d_1 = 1.48, the data suggested a higher deviation from Poisson law than that for (x-x_1)/d_1 = 8.89, suggesting a large clustering. Comparing to the rough bed with the same inflow Froude number Fr_1 = 2.84, close to the jump toe, rough bed showed larger deviations from theoretical distribution (Figure 7.21 A, D and Figure 7.23 A, B). At the characteristic elevations of Y_{Fmax} for all classes, on rough bed deviation from Poisson law was larger than on smooth bed. These findings were in agreement with the number of bubbles for each class; 3375, 2929, 1539, 868 for rough bed and 2078, 2723, 1414, 766 for smooth bed, for four classes, respectively (Table 7.4). Unlike the data of rough bed, the differences between the experimental data and the Poisson distribution for characteristic elevations of Y_{Fmax}, Y_{Cmax} and y* were small. Farther downstream of the jump toe, deviations from the Poisson distribution was pretty similar on both rough and smooth bed, suggesting the same rates of clustered bubbles. On both bed types, the data showed approximately the same deviations from the theoretical distribution (Figure 7.22 A, D and Figure 7.23 C, D).

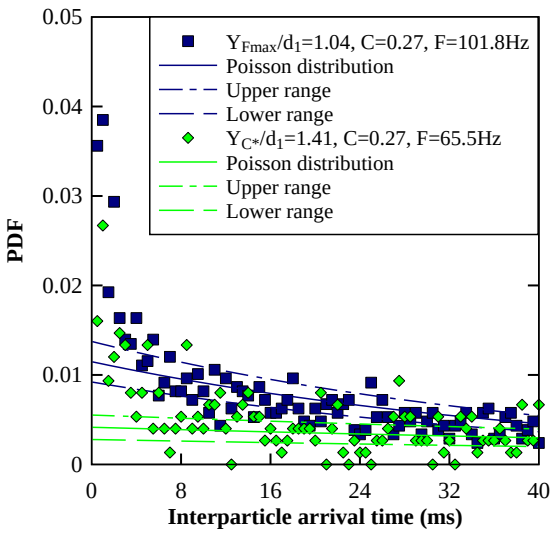

A: (x-x_1)/d_1 = 1.48, $t_{ch\text{-}ab}$: 0.0-0.5 ms

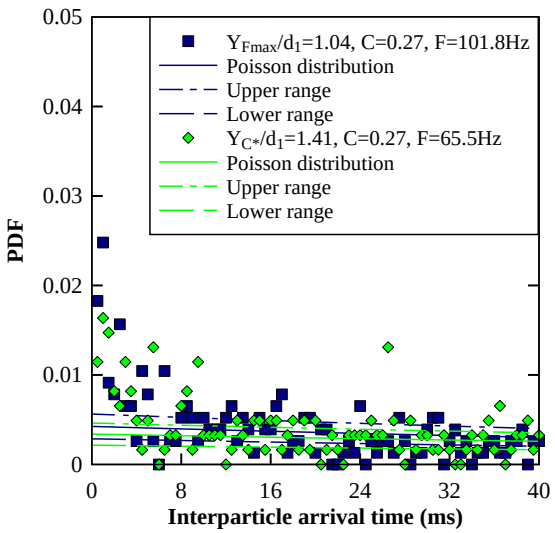

B: (x-x_1)/d_1 = 1.48, $t_{ch\text{-}ab}$: 3.0-5.0 ms

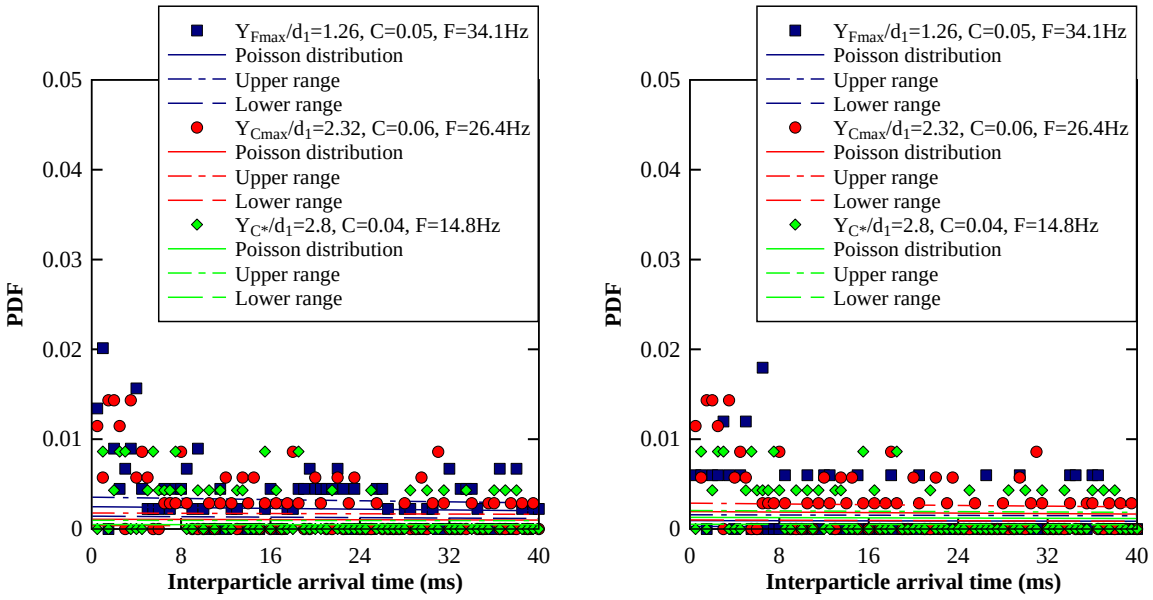

C: $(x\text{-}x_1)/d_1$ = 8.89, $t_{ch\text{-}ab}$: 0.0-0.5 ms D: $(x\text{-}x_1)/d_1$ = 8.89, $t_{ch\text{-}ab}$: 3.0-5.0 ms

Figure 7.23 Probability density function of interparticle arrival time for first and forth bubble chord classes at different characteristic elevations with the same longitudinal position. Smooth bed, flow conditions: Fr_1 = 2.84, Re_1 = 1.7E+5

To better highlight similarities or differences between the bubbly flows in hydraulic jump on rough and smooth bed configurations, the effects of the distance from the jump toe upon the clustering process were systematically investigated at the characteristic elevation of Y_{Fmax}. Figure 7.24 presents the distribution with the distance from the jump toe of the PDF for all the recorded bubbles with τ_{IA} from 0 to 0.5 ms (Figure 7.24A) and from 1.0 to 1.5 ms (Figure 7.24B). These ranges of τ_{IA} were here considered as they showed the largest deviation from Poisson law (Figure 7.21 to 7.22). Furthermore, these ranges were also considered by Gualtieri and Chanson (2013) in hydraulic jump and dropshaft flow allowing a comparative analysis. Note that d_i was the thickness of the nappe at the impingement point in the dropshaft (m) and z was the vertical distance from the pool free-surface, positive downward, in the dropshaft (m). A comparison between the present data and the data from Gualtieri and Chanson (2013) showed the same longitudinal trend of variation, that was for both ranges of τ_{IA}, the PDF value decreased with increasing dimensionless distance, i.e. $(x - x_1)/d_1$ for the hydraulic jump and z/d_i for the dropshaft. The highest magnitudes of PDF were observed in the dropshaft flow. Interestingly, close to the jump toe, i.e. $(x - x_1)/d_1 < 5$, the present data on rough bed with Fr_1 = 2.84 showed a magnitude similar to the data of Gualtieri and Chanson (2013) for hydraulic jump on smooth bed with Fr_1 = 14.3,. Independently from the distance, the frequency of bubbles with short τ_{IA} was on rough bed generally larger than on smooth bed. Overall, the decrease was more rapid for the hydraulic jump at low Fr_1.

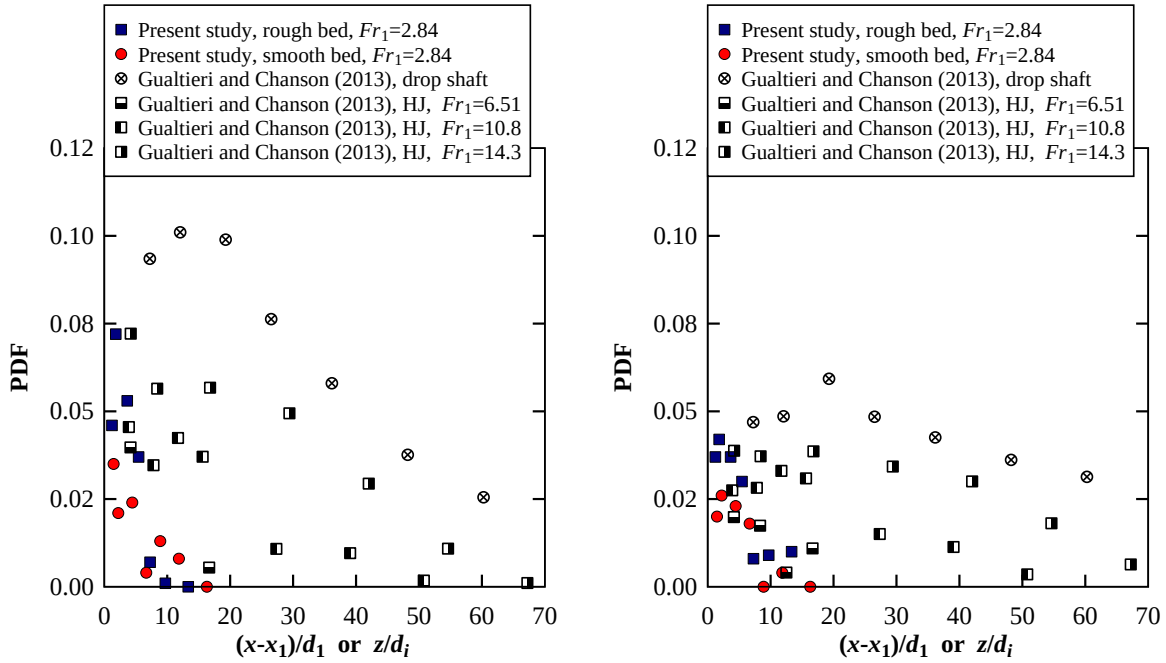

A: Bubbles with τ_{IA} from 0 to 0.5 ms B: Bubbles with τ_{IA} from 1.0 to 1.5 ms

Figure 7.24 Distribution with the distance of the PDF for bubbles in the hydraulic jump on rough and smooth bed configurations. Comparison with drop shaft and hydraulic jump on smooth bed by Gualtieri and Chanson (2013), HJ stands for hydraulic jump

The analysis of the effect of the distance from the jump toe suggested that the largest values of the PDF were observed, on both rough and smooth bed configurations, where turbulent shear stresses were very large, i.e. near the jump toe.

Figure 7.25 shows the distribution with Re_1 of the PDF for all the bubbles with τ_{IA} from 0 to 0.5 and 0.5 to 1.0 ms at the characteristic elevation of Y_{Fmax}. For τ_{IA} from 0 to 0.5, the data demonstrated that on rough bed, as the Reynolds number increased, the rate of increment in PDF magnitude was approximately the same for both ranges of τ_{IA}. That was the increment rate from 0.015 to 0.031 and from 0.021 to 0.037 for τ_{IA} from 0 to 0.5 and 0.5 to 1.0 ms. Regardless of τ_{IA} range, with the same inflow Froude number Fr_1 = 2.84 on rough and smooth beds, the data depicted the higher PDF magnitudes on rough bed. It demonstrated that for a similar Fr_1, the bubbly flow on rough bed had a structure where bubbles very close to each other were more frequent than on smooth bed. Comparing the present data with the data of Gualtieri and Chanson (2013) elucidated that although for the present study Re_1 was higher (Re_1 = 2.2E+5 and 1.7E+5 on rough and smooth bed, respectively), for both range of τ_{IA}, the PDF magnitude was lower that of Gualtieri and Chanson (2013) with 2.7E+3 < Re_1 <5.8E+4 for 6.51 < Fr_1 < 14.3. It highlighted the effect of inflow Froude number upon the value of PDF which resulted in larger density of bubbles per unit flux.

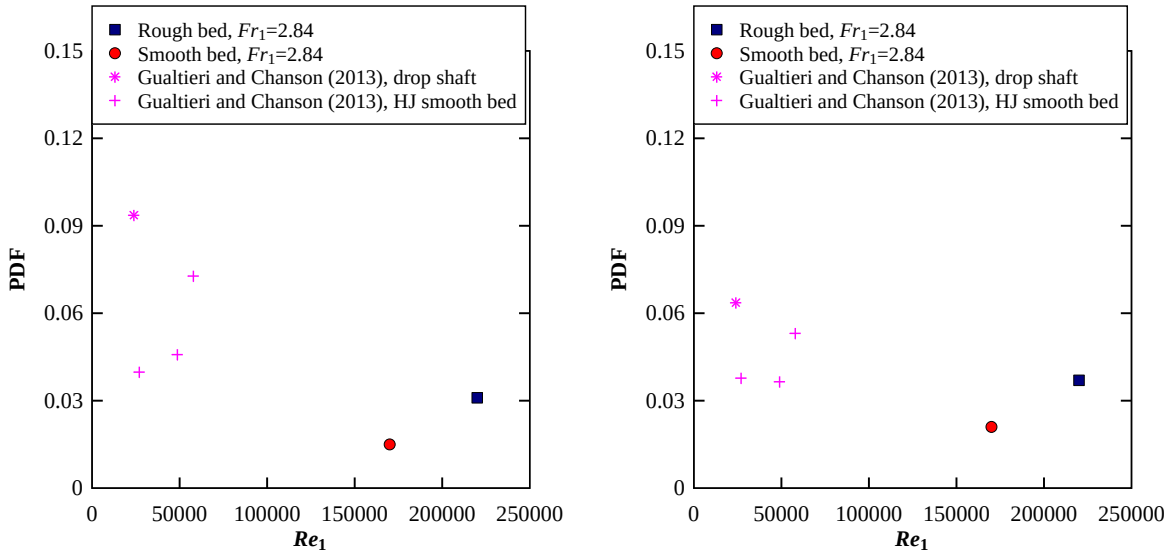

A: Bubbles with τ_{IA} from 0 to 0.5 ms B: Bubbles with τ_{IA} from 0.5 to 1.0 ms

Figure 7.25 Distribution with Re_1 of the PDF in the hydraulic jump on rough and smooth bed configurations. Comparison with dropshaft and hydraulic jump on smooth bed by Gualtieri and Chanson (2013), HJ stands for hydraulic jump

7.5 Summary

In this Chapter, the characteristic particle chord time and length as well as the basic features of particle grouping and clustering derived from the raw phase-detection probe signal, were presented. Properties including cluster count rate, cluster size and cluster proportion were studied based upon two Criteria: Criterion A, which was based on the comparison of the local instantaneous water chord time with a time-averaged characteristic water timescale, and Criterion B, which was based upon the analysis of the near-wake of the preceding bubble. Although the present analysis was 1D and conducted for a limited number of inflow conditions, the results demonstrated that the clustering index may provide a measure of the interaction between turbulence and bubbly flow, vorticity production rate and associated energy dissipation.

The analysis of air chord time indicated an increasing percentage of small bubbles in the downstream direction. The data showed that, on rough bed, the percentage of smaller air chord times far from the jump was higher than close to the jump toe.

For the hydraulic jump with a marked roller, i.e. Fr_1 = 2.8, independently from the bed type and clustering Criterion, the dimensionless magnitude of $(F_{clu})_{max}$ decreased as the distance from the jump tor increased. The reduced cluster count rate was associated with the diffusion of bubbles and buoyancy effect further downstream the roller. Regardless of bed type, in the

shear flow region, the longitudinal decay in cluster count rate was more rapid than that of the bubble count rate. According to Criterion A the average number of bubbles for each cluster was longitudinally constant and equal to 2.3, while, according to Criterion B, the number of bubbles per each cluster decreased with the distance from the jump toe and it was in average equal to 2.4.

The analysis of the interparticle arrival time (IAT) of the bubbles was carried out on both rough and smooth bed configurations. The distributions of τ_{IA} were compared with the Poisson distribution, which was characterizing a random process. The comparison showed that, for the same inflow Froude number, the deviation from the Poisson distribution for smaller τ_{IA} possessed the largest magnitude close to the jump toe and it decreased as the distance from the jump toe increased. Furthermore, the bubbly flow structure on the rough bed had a density of bubbles per unit flux larger than on smooth bed.

The existence of large amount of small interparticle arrival time confirmed the occurrence of small bubble clustering already observed in the analysis conducted with Criteria A and B.

8 Conclusion

8.1 Presentation of thesis work

The hydraulic jump is a complex phenomenon that remains incompletely understood, especially when it occurs on rough bed. The turbulent flow regions include a developing shear layer, the roller and the air-water interface. The intense turbulence and strong flow aeration in the hydraulic jump result in an important flow phenomenon in hydraulic, chemical and environmental engineering. It is believed that simultaneous measurements of the turbulent and air-water flow properties are challenging in such a complex flow and may require advanced data processing. In the present study, both the free surface fluctuations and the air-water properties were investigated experimentally in hydraulic jumps on pebbled rough bed. Two series of experiments were designed with the aims of (a) flow pattern observations and dynamic free-surface measurements and (b) air-water flow measurements. The involved instrumentation included Venturi meter, video camera, pointer gauge, and dual-tip phase-detection probes. The experiments were performed in a channel with partially-developed inflow conditions. The flume was 3.2 m long, 0.5 m wide and 0.41 m high and consisted of a horizontal high-density polyethylene (*HDPE*) bed and glass sidewalls. The gravel materials were mixed natural river pebbles sieved between 9.5 mm and 13.2 mm, with d_{50} = 0.011 m and ρ_s = 2530 kg/. The pebbles were installed on the bed for the whole length of the channel. The flow conditions for first group of experiments was 1.31 < Fr_1< 4.94, 4.2E+4 < Re_1 < 2.3E+5 and for second group of experiments was 1.7 < Fr_1< 2.84, 1.4E+5 < Re_1 < 2.2E+5 all with partially-developed inflow conditions on both rough and smooth bed configurations. Measurements were performed on the channel centreline at various longitudinal and vertical positions.

8.2 Review of key outcomes

The main outcomes are presented in Chapters 4 to 7. Herein, based on investigations which were done in each chapter, a summary of results are addressed:

Chapter 4: the flow patterns and free-surface dynamics in hydraulic jumps were studied based upon visual observations and non-intrusive free-surface measurements. The basic flow properties including the free-surface profile, conjugate depths and jump roller length were found to be function of the inflow Froude number. A larger Froude number Fr_1 resulted in a

larger conjugate depths ratio d_2/d_1 and in a longer roller L_r/d_1 and air flow L_{air}/d_1, with the same trends for both bed types. A smaller roller length was observed for rough bed due to the effect of the rough bed on the flow. Boundary friction force and shear stresses were investigated based upon the free-surface data and momentum considerations.

The macroscopic fluctuating nature of hydraulic jumps was analysed based upon high-speed videos. The dimensionless frequencies were decreasing with increasing Froude number on both rough and smooth beds. The findings suggested some correlations between the jump toe oscillation and large vortex formation. Comparable dimensionless velocities/celerities were observed for the vortex advection in the roller length. The velocities were constant independent of the Froude and Reynolds numbers on both bed types.

A survey of the fluctuations in impingement perimeter transverse profiles showed consistent statistical properties of longitudinally oscillating impingement positions across the central flow region on both bed types. Fluctuation of longitudinal water surface profile, extracted from side videos, showed the same trend on both bed types but a slightly higher standard deviation for smooth bed which was due to higher oscillation of water surface. Probability density functions of instantaneous jump toe position as well as instantaneous water surface profile with the best distribution fit was presented on both rough and smooth bed configurations with different inflow Froude numbers.

Chapter 5: The time-averaged void fraction, bubble count rate, air-water interfacial velocity, and characteristics flow depths were studied. A comprehensive comparative analysis of hydraulic jumps between the results of present study with those from literature showed that upstream of the jump toe, the time-averaged void fraction and bubble count rate as well as the interfacial velocity and turbulent intensity distributions were presented in terms of profile shapes in a vertical cross-section. Downstream of the jump toe, the distributions of two-phase flow properties observed in hydraulic jumps on both rough and smooth bed configurations were comparable. A shear layer region close to the channel bed and a recirculation region in the upper part of the hydraulic jump was observed. The roughness resulted in larger maximum and mean void fractions within a cross-section. In terms of local void fraction minimum values, between the shear layer and the recirculation regions, no significant difference was observed between rough and smooth bed. The effect of roughness led to increasing the momentum exchange between the boundary layer and the overlying shear layer, especially close to the jump toe. The bed roughness induced the bubble break-up processes into smaller bubbles and the formation of large-scale eddies which were transported downstream entrapping the air

bubbles. Comparing to smooth bed and rubber mat roughness (Felder and Chanson 2016, 2018), the pebbled roughness resulted in larger dimensionless maximum bubble count rate. Some characteristic air-water flow parameters were comparable on both rough and smooth bed configurations. This included several characteristic flow depths, the magnitude of maximum interfacial velocities in a cross-section and the mean void fraction in a cross- section. The increasing trend in characteristic elevations along the roller was a pseudo-linear process in the shear region and followed a self-similar depth increase trend above the roller.

Chapter 6: turbulent properties of the hydraulic jump roller were discussed in terms of turbulence intensity, characteristic turbulent length and time scales. High turbulence levels were detected in the roller free-surface region, which were related to the existence of self-sustained instabilities of the flow. Larger magnitudes of *Tu* were observed in both shear layer and recirculation regions. Close to the jump toe larger magnitudes of *Tu* were observed in the shear layer while further downstream larger magnitudes of *Tu* were seen near the surface. Larger magnitudes of *Tu* in the turbulent shear layer was possibly corresponded to maximum bubble count rate while in the recirculation region as well as near the surface was linked to the impact of large-scale fluctuating motions of the jump roller. Comparison showed the higher magnitude of turbulent intensity on rough bed. Furthermore, the turbulence dissipation process was affected by the Froude number. The relationship between turbulent intensity and dimensionless bubble count rate reflected an increase in turbulence associated with the number of entrained particles. The findings in terms of magnitude were in agreement with the data of skimming flow on stepped chutes and of hydraulic jump on rubber mat rough bed. The correlation time scales were deduced from the integration of the correlation functions from the maximum to the first zero-crossing point. The results showed that in the flow region immediately downstream of the jump toe, the maximum magnitude of $T_{xx} \times V_1/d_1$ was 0.82 and 0.73 on rough and smooth bed configurations, respectively, while the maximum magnitude of $T_{xx'} \times V_1/d_1$ was 0.7 and 0.63 on rough and smooth bed configurations, respectively. Results showed that, on both bed configurations, the increase in both velocity and auto-correlation time scale resulted in a rapid increase in the advective length scale with the increasing vertical elevation. The vertical increasing in length scale L_{xx} was related to the interaction between the turbulent air-water flow and the channel bed within the boundary layer. This kind of interaction on rough bed was higher than on smooth bed and associated with the formation of larger eddies. Further downstream, vortical structures tended to be dispersed, since the impact of large eddies in the upper shear region vanished.

Chapter 7: the characteristic particle chord time and length as well as the basic features of particle grouping and clustering derived from the raw phase-detection probe signal, were presented. Properties including cluster count rate, cluster size and cluster proportion were studied based upon two Criteria: Criterion A, which was based on the comparison of the local instantaneous water chord time with a time-averaged characteristic water timescale, and Criterion B, which was based upon the analysis of the near-wake of the preceding bubble. Although the present analysis was 1D and conducted for a limited number of inflow conditions, the results demonstrated that the clustering index may provide a measure of the interaction between turbulence and bubbly flow, vorticity production rate and associated energy dissipation.

The analysis of air chord time indicated an increasing percentage of small bubbles in the downstream direction. The data showed that, on rough bed, the percentage of smaller air chord times far from the jump was higher than close to the jump toe. For the hydraulic jump with a marked roller, i.e. Fr_1 = 2.8, independently from the bed type and clustering Criterion, the dimensionless magnitude of $(F_{clu})_{max}$ decreased as the distance from the jump tor increased. The reduced cluster count rate was associated with the diffusion of bubbles and buoyancy effect further downstream the roller. Regardless of bed type, in the shear flow region, the longitudinal decay in cluster count rate was more rapid than that of the bubble count rate. According to Criterion A the average number of bubbles for each cluster was longitudinally constant and equal to 2.3, while, according to Criterion B, the number of bubbles per each cluster decreased with the distance from the jump toe and it was in average equal to 2.4.

The analysis of the interparticle arrival time (IAT) of the bubbles was carried out on both rough and smooth bed configurations. The distributions of τ_{IA} were compared with the Poisson distribution, which was characterizing a random process. The comparison showed that, for the same inflow Froude number, the deviation from the Poisson distribution for smaller τ_{IA} possessed the largest magnitude close to the jump toe and it decreased as the distance from the jump toe increased. Furthermore, the bubbly flow structure on the rough bed had a density of bubbles per unit flux larger than on smooth bed. The existence of large amount of small interparticle arrival time confirmed the occurrence of small bubble clustering already observed in the analysis conducted with Criteria A and B.

8.3 Future work

After more than two centuries of successful research, the hydraulic jump still remains a fascinating turbulent flow in terms of turbulence, air bubble entrainment and interactions between entrained bubbles and coherent structures. The present data set adds some new information on the hydrodynamics of hydraulic jumps on pebbled rough bed with relatively low Froude numbers and large Reynolds numbers. However, the study has been confined to a few inflow conditions and one type rough bed. These limitations suggest a number of key aspects for which additional research is possible:

- Different type of roughness based upon d_{50} and K_s
- Different upstream gate opening and jump toe position, as well as different Fr_1 and Re_1
- Effect of vegetated channel on hydraulic jump properties

List of References:

ABBASPOUR, A., FARSADIZADEH, D., and GHORBANI, M. A. (2013). "Estimation of Hydraulic Jump on Corrugated Bed Using Artificial Neural Networks and Genetic Programming." Water Science and Engineering Volume 6, Issue 2, April 2013, pp. 189-198.

ABBASPOUR, A., HOSSEINZADEH DALIR, A., FARSADIZADEH, D., and SADRADDINI, A. A. (2009). "Effect of Sinusoidal Corrugated Bed on Hydraulic Jump Characteristics." Journal of Hydro-Environment Research, Vol. 3, No. 2, pp. 109–117, DOI: 10.1016/j.jher.2009.05.003.

AFZAL, N., BUSHRA, A., and SEENA, A. (2011)."Analysis of Turbulent Hydraulic Jump over a Transitional Rough Bed of a Rectangular Channel: Universal Relations." Civil Engineering Faculty Publications. 54. http://digitalcommons.unl.edu/civilengfacpub/54.

AGELINCHAAB, M., and TACHIE, M. F. (2008). "PIV Study of Separated and Reattached Open Channel Flow over Surface Mounted Blocks." ASME. Journal of Fluids Engineering. 130(6):061206-061206-9. doi:10.1115/1.2911677.

AHMED, H., GENDY, M., MIRDAN, A., ALI, A. and HALEEM, F. (2014). "Effect of Corrugated Beds on Characteristics of Submerged Hydraulic Jump." Ain Shams Engineering Journal, Volume 5, Issue 4, December 2014, Pages 1033–1042.

ALISEDA, A., and LASHERAS, J. C. (2011). "Preferential Concentration and Rise Velocity Reduction of Bubbles Immersed in a Homogeneous and Isotropic Turbulent flow." Physic of Fluids 23(9), 093301-11.

ANDERSON, T. W., and DARLING, D. A. (1952) "Asymptotic Theory of Certain 'Goodness of Fit' Criteria Based on Stochastic Processes." The Annals of Mathematical Statistics, Vol. 23, No. 2. (Jun., 1952), pp. 193-212.

BAYON, A., VALERO, D., GARCÍA-BARTUAL, R., VALLÉS-MORÁN, F. J. and LÓPEZ-JIMÉNEZ, P. A. (2016). "Performance Assessment of Open FOAM and FLOW-3D in the Numerical Modelling of a Low Reynolds Number Hydraulic Jump." Environmental Modelling & Software., nara 80 (pp. 322–335 ISSN 1364 8152 http://dx.doi.org/10.1016/j.envsoft.2016.02.018.

BELANGER, J. B. (1841). "Notes sur l'hydraulique." ("Notes on Hydraulic Engineering."). Ecole Royale des Ponts et Chaussées, Paris, France, session 1841-1842, 223 pages (in French).

BERTOLA, N., WANG, H. and CHANSON, H. (2018). "A Physical Study of Air-Water Flow in Planar Plunging Water Jet with Large Inflow Distance." International Journal of Multiphase Flow 100 155-171. https://doi.org/10.1016/j.ijmultiphaseflow.2017.12.015

BOES, R. M. (2000). "Scale Effects in Modelling Two-Phase Stepped Spillway Flow." International Workshop on Hydraulics of Stepped Spillways, Zürich, Switzerland, H.E. MINOR & W. H. HAGER Editors, Balkema Publisher, pp. 53-60.

BRATTBERG, T., CHANSON, H., and TOOMBES, L. (1998). "Experimental Investigations of Free-Surface Aeration in the Developing Flow of Two-Dimensional Water Jets." Journal

of Fluids Engineering, Transactions ASME, Vol. 120, No. 4, pp. 738-744. Brisbane, Australia.

BUNG, D. B. (2013). "Air-Water Surface Roughness in Self-Aerated Stepped Spillway Flows." Proceedings of 35th IAHR World Congress, Chengdu, China, Tsinghua University Press Publisher.

CAIN, P., and WOOD, I. R. (1981). "Measurements of Self-aerated Flow on Spillways." Journal of Hydraulic Division, ASCE, Vol. 107, No. HY11, pp. 1425-1444.

CAROLLO, F. G., FERRO, V., and PAMPALONE, V. (2007). "Hydraulic Jump on Rough Beds." Journal of Hydraulic Engineering, 133(9), pp. 989–999.

CAROLLO, F. G., FERRO, V., and PAMPALONE, V. (2009). "New Solutions of Classical Hydraulic Jump." Journal of Hydraulic Engineering, 135(6), pp. 527–531.

CAROLLO, F. G., FERRO, V., and PAMPALONE, V. (2013). "Sequent Depth Ratio of B-Jumps on Smooth and Rough Beds." Journal of Agricultural Engineering, 44(2), 82-86. doi.org/10.4081/jae.2013.e12.

CARTELLIER, A., and ACHARD, J. L. (1991). "Local Phase Detection Probes in Fluid/Fluid Two-Phase Flows." Review of Scientific Instruments, Vol. 62, No. 2, pp. 279-303.

CARVALHO, R., LEMOS, C. and RAMOS, C. (2008). "Numerical Computation of the Flow in Hydraulic Jump Stilling Basins." Journal of Hydraulic Research, 46, 739–752. C.

CASTRO-ORGAZ, O., and HAGER, W. H. (2009). "Classical Hydraulic Jump: Basic Flow Features." Journal of Hydraulic Research, Vol. 47, No. 6, pp. 744-754.

CHACHEREAU, Y., and CHANSON, H. (2010). "Free-Surface Turbulent Fluctuations and Air-Water Flow Measurements in Hydraulic Jumps with Small Inflow Froude Numbers." Hydraulic Model Report No. CH78/10, School of Civil Engineering, The University of Queensland, Brisbane, Australia, 133 pages.

CHACHEREAU, Y., and CHANSON, H. (2011a). "Bubbly Flow Measurements in Hydraulic Jumps with Small Inflow Froude Numbers." International Journal of Multiphase Flow, Vol. 37, No. 6, pp. 555-564.

CHACHEREAU, Y., and CHANSON, H. (2011b). "Free-Surface Fluctuations and Turbulence in Hydraulic Jumps." Experimental Thermal and Fluid Science, Vol. 35, No. 6, pp. 896-909 (DOI: 10.1016/j.expthermflusci.2011.01.009).

CHANSON, H. (1989). "Study of Air Entrainment and Aeration Devices." Journal of Hydraulic Research, Vol. 27, No. 3, pp. 301–319.

CHANSON, H. (1995). "Air Entrainment in Two-Dimensional Turbulent Shear Flows with Partially Developed Inflow Conditions." Journal of Multiphase Flow, Vol. 21, No. 6, pp. 1107-1121 (DOI: 10.1016/0301-9322(95)00048-3).

CHANSON, H. (1997a). "Air Bubble Entrainment in Free-Surface Turbulent Shear Flows." Academic Press, London, UK, 401 pages.

CHANSON, H. (1997b). "Air Bubble Entrainment in Open Channels: Flow Structure and Bubble Size Distributions." International Journal of Multiphase Flow, Vol. 23, No. 1, pp. 193-203.

CHANSON, H. (2002). "Air-Water Flow Measurements with Intrusive, Phase-Detection Probes: Can We Improve Their Interpretation?" Journal of Hydraulic Engineering, ASCE, Vol. 128, No. 3, pp. 252-255.

CHANSON, H. (2004a). "The Hydraulics of Open Channel Flow: An Introduction." Butterworth-Heinemann, Oxford, UK, 2nd edition, 630 pages.

CHANSON, H. (2004b). "Hydraulics of Rectangular Dropshafts." Journal of Irrigation and Drainage Engineering, ASCE, Vol. 130, No. 6, pp. 523-529.

CHANSON, H. (2005). "Air Bubble entrainment in Hydraulic Jumps. Similitude and Scale Effects." Hydraulic Model Report No. CH57/05, Department of Civil Engineering, The University of Queensland, Brisbane, Australia, 119 pages.

CHANSON, H. (2007a). "Bubbly Flow Structure in Hydraulic Jump." European Journal of Mechanics - B/Fluids, Vol. 26, No. 3, pp. 367-384.

CHANSON, H. (2007b). "Dynamic Similarity and Scale Effects Affecting Air Bubble Entrainment in Hydraulic Jumps." Proceedings of 6th International Conference on Multiphase Flow ICMF 2007, Leipzig, Germany, July 9-13, M. Sommerfield Editor. Session 7, 11 pages.

CHANSON, H. (2009a). "Advective Diffusion of Air Bubbles in Hydraulic Jumps with Large Froude Numbers: An Experimental Study." Hydraulic Model Report No. CH75/09, School of Civil Engineering, The University of Queensland, Brisbane, Australia, 76 pages.

CHANSON, H. (2009b). "Applied Hydrodynamics: An Introduction to Ideal and Real Fluid Flows." CRC Press, Taylor & Francis Group, Leiden, The Netherlands, 478 pages.

CHANSON, H. (2009c). "Current Knowledge in Hydraulic Jumps and Related Phenomena. A Survey of Experimental Results." European Journal of Mechanics - B/Fluids, Vol. 28, No. 2, pp. 191-210.

CHANSON, H. (2010). "Convective Transport of Air Bubbles in Strong Hydraulic Jumps." International Journal of Multiphase Flow, Vol. 36, No. 10, pp. 798-814 (DOI: 10.1016/j.ijmultiphaseflow.2010.05.006).

CHANSON, H. (2011). "Hydraulic Jumps: Turbulence and Air Bubble Entrainment." Journal La Houille Blanche, No. 3, pp. 5-16 (DOI: 10.1051/lhb/2011026) (ISSN 0018-6368).

CHANSON, H. (2012). "Momentum Considerations in Hydraulic Jumps and Bores." Journal of Irrigation and Drainage Engineering, ASCE, Vol. 138, No. 4, pp. 382-385.

CHANSON, H. (2013). "Hydraulics of Aerated Flows: qui pro quo?" Journal of Hydraulic Research, Vol. 51, No. 3, pp. 223-243.

CHANSON, H. (2015). "Energy dissipation in hydraulic structures". CRC Press.

CHANSON, H., and BRATTBERG, T. (1998). "Air Entrainment by Two-Dimensional Plunging Jets: the Impingement Region and the Very-Near Flow Field." Proceedings of 1998 ASME Fluids Engineering Conference, Washington DC, USA, June 21-25, 8 pages.

CHANSON, H., and BRATTBERG, T. (2000). "Experimental Study of the Air-Water Shear Flow in a Hydraulic Jump." International Journal of Multiphase Flow, Vol. 26, No. 4, pp. 583- 607.

CHANSON, H., AOKI, S., and HOQUE, A. (2006). "Bubble Entrainment and Dispersion in Plunging Jet Flows: Freshwater versus Seawater." Journal of Coastal Research, Vol. 22, No. 3, pp. 664-677.

CHANSON, H., and CAROSI, G. (2007a). "Advanced Post-Processing and Correlation Analyses in High-Velocity Air-Water Flows." Environmental Fluid Mechanics, Vol. 7, No. 6, pp. 495508.

CHANSON, H., and CAROSI, G. (2007b). "Turbulent Time and Length Scale Measurements in High-Velocity Open Channel Flows." Experiments in Fluids, Vol. 42, No. 3, pp. 385-401.

CHANSON, H., and CHACHEREAU, Y. (2013). "Scale Effects Affecting Two-Phase Flow Properties in Hydraulic Jump with Small Inflow Froude Number." Experimental Thermal and Fluid Science, Vol. 45, pp. 234-242.

CHANSON, H., and GUALTIERI, C. (2008). "Similitude and Scale Effects of Air Entrainment in Hydraulic Jumps." Journal of Hydraulic Research, Vol. 46, No. 1, pp. 35-44.

CHANSON, H., and TOOMBES, L. (2002a). "Air-Water Flows down Stepped Chutes: Turbulence and Flow Structure Observations." International Journal of Multiphase Flow, Vol. 28, No. 11, pp. 1737-1761.

CHANSON, H., and TOOMBES, L. (2002b). "Experimental Investigations of Air Entrainment in Transition and Skimming Flows down a Stepped Chute." Canadian Journal of Civil Engineering, Vol. 29, No. 1, pp. 145-156.

CHANSON, H., AOKI, S., and HOQUE, A. (2004). "Physical Modelling and Similitude of Air Bubble Entrainment at Vertical Circular Plunging Jets." Chemical Engineering Science, Vol. 59, No. 4, pp. 747-758.

CHIPPADA, S., RAMASWAMY, B. and WHEELER, M. (1994). "Numerical Simulation of Hydraulic Jump." International Journal of Numerical Methods in Engineering 37, 1381–1397.

CRANK, J. (1956). "The Mathematics of Diffusion." Oxford University Press, London, UK.

CROWE, C., SOMMERFIELD, M., and TSUJI, Y. (1998). "Multiphase Flows with Droplets and Particles." CRC Press, Boca Raton, USA, 471 pages.

CUMMINGS, P. D., and CHANSON, H. (1997). "Air Entrainment in the Developing Flow Region of Plunging Jets – Part 1: Theoretical Development." Journal of Fluids Engineering, Transactions ASME, Vol. 199, pp. 597-602.

DEFINA, A. and SUSIN, F. M. (2003). "Stability of a Stationary Hydraulic Jump in an Upward Sloping Channel," Physics of Fluids https://doi.org/PHFLE6 15, 3883.

DEFINA, A., SUSIN, F. M., and VIERO, D. P. (2008) "Bed Friction Effects on the Stability of a Stationary Hydraulic Jump in a Rectangular Upward Sloping Channel." Physics of fluids 20, 036601. DOI: 10.1063/1.2841622.

EAD, S.A., and RAJARATNAM, N. (2002). "Hydraulic Jumps on Corrugated Beds." Journal of Hydraulic Engineering, Vol. 128(7), pp. 656–663.

EBRAHIMI, S., SALMASI, F. and ABBASPOUR, A. (2013). "Numerical Study of Hydraulic Jump on Rough Beds Stilling Basins." Journal of Civil Engineering and Urbanism, 3(1): 19-24.

EDWARDS, C. F., and MARX, K. D. (1995). "Multipoint Statistical Structure of the Ideal Spray, Part I: Fundamental Concepts and the Realization Density." Atomization and Sprays, Vol. 5, pp. 435-455.

EDWARDS, C. F., and MARX, K. D. (1995). "Multipoint Statistical Structure of the Ideal Spray, Part II: Evaluating Steadiness Using the Interparticle Time Distribution." Atomization and Sprays, Vol. 5, pp. 435-455.

EHRENBERGER, I. (1926). "Wasserbewegung in Steilen Rinnen (Susstennen).mit Besonderer Berucksichtigung der Selbstbeliiftung." Zeitschrift des Osterreichischer Ingenieur und Architektenvereins, No. 15/16 and 17/18.

ELSEBAIE, I. H. and SHABAYEK SH. (2010). "Formation of Hydraulic Jumps on Corrugated Beds" International Journal of Civil & Environment al Engineering IJCEE-IJENS Vol:10 No:01. pp. 40-50.

FANG X., YANG Z., WANG B. C., TACHIE M. F. and BERGSTROM D. J. (2015). "Highly-Disturbed Turbulent Flow in a Square Channel with V-Shaped Ribs on One Wall." International Journal of Heat and Fluid Flow, 56 , pp. 182-197.

FARSADIZADEH, D., HOSSEINADEH DALIR, A., SADRADDINI, A. A., and ABBASPOUR, A. (2009). "Numerical Study of Hydraulic Jumps on Corrugated Beds Using Turbulence Models." Turkish Journal of Engineering & Environmental Sciences, Vol. 33, No. 1, pp. 61- 72.

FELDER, S. (2013). "Air-Water Flow Properties on Stepped Spillways for Embankment Dams: Aeration, Energy Dissipation and Turbulence on Uniform, Non-uniform and Pooled Stepped Chutes." PhD thesis, School of Civil Engineering, The University of Queensland, Brisbane, Australia. 454 pages.

FELDER, S., and CHANSON, H. (2009). "Turbulence, Dynamic Similarity and Scale Effects in High-Velocity Free-Surface Flows above a Stepped Chute." Experiments in Fluids, Vol. 47, No. 1, pp. 1-18.

FELDER, S., and CHANSON, H. (2011). "Air-Water Flow Properties in Step Cavity down a Stepped Chute." International Journal of Multiphase Flow, Vol. 37, No. 7, pp. 732-745.

FELDER, S., and CHANSON, H. (2012a). "Air-Water Flow Measurements in Instationary Free Surface Flows: a Triple Decomposition Technique." Hydraulic Model Report No. CH85/12, School of Civil Engineering, The University of Queensland, Brisbane, Australia, 161 pages.

FELDER, S., and CHANSON, H. (2012b). "Free-surface Profiles, Velocity and Pressure Distributions on a Broad-Crested Weir: a Physical Study." Journal of Irrigation and Drainage Engineering, ASCE, Vol. 138, No. 12, pp. 1068–1074.

FELDER, S., and CHANSON, H. (2015). "Phase-Detection Probe Measurements in High-Velocity Free-Surface Flows including a Discussion of Key Sampling Parameters." Experimental Thermal and Fluid Science, Vol. 61, pp. 66-78 (DOI:10.1016/j.expthermflusci.2014.10.009).

FELDER, S., and CHANSON, H. (2016). "An Experimental Study of Air-Water Flows in Hydraulic Jumps with Channel Bed Roughness." WRL Research Report WRL 259, University of New South Wales, Sydney, Australia, 166 pages (ISBN 9780733436574).

FELDER, S., and CHANSON, H. (2018). "Air–Water Flow Patterns of Hydraulic Jumps on Uniform Beds Macroroughness." Journal of Hydraulic Engineering, ASCE, Vol. 144, No. 3, Paper 04017068, 12 pages (DOI: 10.1061/(ASCE)HY.1943-7900.0001402) (ISSN 0733-9429).

FIGUEROA-ESPINOZA, B., and ZENIT, R. (2005). "Clustering in high Re monodispersed bubbly flows." Physics of Fluids 17(9), 091701-4.

GHARANGIK, A. M., and CHAUDHRY, M. H. (1991). "Numerical Simulation of Hydraulic Jump." Journal of Hydraulic Engineering, Vol. 117, No. 9, pp. 1195-1211.

GONZALEZ, A., and BOMBARDELLI, F. (2005). "Two-Phase Flow Theory and Numerical Models for Hydraulic Jumps, Including Air Entrainment." Proceedings of 31st IAHR Congress, Seoul, Korea, B. H. JUN, S. I. LEE, I. W. SEO and G. W. CHOI Editors.

GUALTIERI, C. and PULCI DORIA, G., (2012). "Gas Transfer at Unsheared Free Surfaces." In C. Gualtieri, C., and Mihailović, D. T., (Editors): Fluid Mechanics of Environmental Interfaces, 2nd Edition, pp.498, CRC Press/Balkema, Leiden, The Netherlands, pp.143–177.

GUALTIERI, C., and CHANSON, H. (2004). "Clustering Process and Interfacial Area Analysis in a Large-Size Dropshaft." Advances in Fluid Mechanics, Vol. 40, pp. 415-424.

GUALTIERI, C., and CHANSON, H. (2007a). "Experimental Analysis of Froude Number Effect on Air Entrainment in the Hydraulic Jump." Environmental Fluid Mechanics, Vol. 7, No. 3, pp. 217-238.

GUALTIERI, C., and CHANSON, H. (2007b). "Clustering process analysis in a large-size dropshaft and in a hydraulic jump." Proc. 32nd IAHR Biennial Congress, Venice, Italy, C1(b), 1–11, G. DiSilvio, S. Lanzoni, eds. (CD-ROM).

GUALTIERI, C., and CHANSON, H. (2010). "Effect of Froude Number on Bubble Clustering in a Hydraulic Jump." Journal of Hydraulic Research, Vol. 48, No. 4, pp. 504-508.

GUALTIERI, C., and CHANSON, H. (2013). "Interparticle Arrival Time Analysis of Bubble Distributions in a Dropshaft and Hydraulic Jump." Journal of Hydraulic Research, 51:3, 253-264.

HAGER, W. H. (1992). "Energy Dissipaters and Hydraulic Jump." Kluwer Academic Publishers, Water Science and Technology Library, Vol. 8, Dordrecht, the Netherlands, 288 pages.

HAGER, W. H., BREMEN, R., and KAWAGOSHI, N. (1990). "Classical Hydraulic Jump: Length of Roller." Journal of Hydraulic Research, IAHR, Vol. 28, No. 5, pp. 591-608.

HEINLEIN, J., and FRITSCHING, U. (2006). "Droplet Clustering in Sprays." Experiments in Fluids, Vol. 40, No. 3, pp. 464-472.

HOYT, J. W., and SELLIN, R. H. J. (1989). "Hydraulic Jump as 'Mixing Layer'." Journal of Hydraulic Engineering, Vol. 40, No. 3, pp. 1607-1614.

HUGHES, W. C., and FLACK, J. E. (1984). "Hydraulic Jump Properties over a Rough Bed." Journal of Hydraulic Engineering 110 (12), pp. 1755-1771.

JAVAN, M., and EGHBALZADEH, A. (2013). "2D Numerical Simulation of Submerged Hydraulic Jumps." Applied Mathematical Modelling, 37(10), 6661–6669.

KALINSKE, A. A., and ROBERTSON, J. M. (1943). "Closed Conduit Flow." Transactions, ASCE, Vol. 108, pp. 1435-1447.

KRAMER, M., and CHANSON, H. (2018). "Transition Flow Regime on Stepped Spillways: Air–Water Flow Characteristics and Step-Cavity Fluctuations." Environmental Fluid Mechanic, 18: 947. https://doi.org/10.1007/s10652-018-9575-y.

KUCUKALI, S., and CHANSON, H. (2007). "Turbulence in Hydraulic Jumps: Experimental Measurements." Hydraulic Model Report series CH, CH62/07. Civil Engineering, The University of Queensland.

KUCUKALI, S., and CHANSON, H. (2008). "Turbulence Measurements in Hydraulic Jumps with Partially-Developed Inflow Conditions." Experimental Thermal and Fluid Science, Vol. 33, No. 1, pp. 41-53.

LENG, X., and CHANSON, H. (2015). "Breaking Bore: Physical Observations of Roller Characteristics." Mechanics Research Communications, Vol. 65, pp. 24-29 (DOI: 10.1016/j.mechrescom.2015.02.008).

LEONARDI, S., ORLANDI, P., and ANTONIA, R. A. (2007). "Properties of D- and K-Type Roughness in a Turbulent Channel Flow." Physics of Fluids, 19(12), [125101]. DOI: 10.1063/1.2821908.

LEUTHEUSSER, H. J., SCHILLER, E. J. (1975). "Hydraulic Jump in a Rough Channel." International Water Power and Dam Construction, 27 (5), pp. 186-191.

LIGGETT, J. A. (1994). "Fluid Mechanics." McGraw-Hill, New York, USA.

LIGHTHILL, J. (1978). "Waves in Fluids." Cambridge University Press, Cambridge, UK.

LONG, D., STEFFLER, P. and RAJARATNAM, N. (1991). "A numerical Study of Submerged Hydraulic Jumps." Journal of Hydraulic Research, 29 (3), 293–308.

LUBIN, P., GLOCKNER, S., and CHANSON, H. (2009). "Numerical Simulation of Air Entrainment and Turbulence in a Hydraulic Jump." Proceedings of Colloque SHF Modèles Physiques Hydrauliques: Outils Indispensables du XXIe Siècle? Lyon, France, November 24-25, Société Hydrotechnique de France Publisher, pp. 109-114.

LUONG, J. T. K., and SOJKA, P. E. (1999). "Unsteadiness in Effervescent Sprays." Atomization and Sprays, Vol. 9, pp. 87-109.

MA, F., HOU, Y. and PRINOS, P. (2001). "Numerical Calculation of Submerged Hydraulic Jumps." Journal of Hydraulic Research 39, 493–503.

MA, J. S., OBERAI, A. A., LAHEY, R. T., and DREW, D.A. (2011). "Modelling Air Entrainment and Transport in a Hydraulic Jump Using Two-Fluid Rans and Des Turbulence Models." Heat and Mass Transfer, Vol. 47, No. 8, pp. 911-919.

MARSAGLIA, G., and MARSAGLIA, J. (2004). "Evaluating the Anderson-Darling Distribution." Journal of Statistical Software. DOI: 10.18637/jss.v009.i02.

MARTINEZ-BAZAN, C., MONTANES, J. L., and LASHERAS, J. C. (2002). "Statistical description of the bubble cloud resulting from the injection of air into a turbulent water jet." International Journal Multiphase Flow 28(4), 597–615.

MONTES, S. J. (1998). "Hydraulics of Open Channel Flow." ASCE Press, New York, USA, 697 pages.

MORTAZAVI, M., LE CHENADEC, V. and MANI, A. (2014). "Numerical Simulation of a Turbulent Hydraulic Jump: Characterization of the Free Interface and Large Bubble Structure." Centre for Turbulence Research Annual Research Briefs 2014.

MORTAZAVI, M., LE CHENADEC, V., MOIN, P., and MANI, A. (2016). "Direct Numerical Simulation of a Turbulent Hydraulic Jump: Turbulence Statistics and Air Entrainment." Journal of Fluid Mechanics, 797, 60-94.

MOSSA, M., and TOLVE, U. (1998). "Flow Visualization in Bubbly Two-Phase Hydraulic Jump." Journal of Fluids Engineering, ASME, Vol. 120, March, pp. 160-165.

MOUAZE, D., MURZYN, F., and CHAPLIN, J. R. (2005). "Free Surface Length Scale Estimation in Hydraulic Jumps." Journal of Fluids Engineering, Transactions ASME, Vol. 127, pp. 1191-1193.

MURZYN, F., and CHANSON, H. (2008). "Experimental Assessment of Scale Effects Affecting Two-Phase Flow Properties in Hydraulic Jumps." Experiments in Fluids, Vol. 45, No. 3, pp. 513-521.

MURZYN, F., and CHANSON, H. (2009). "Experimental Investigation of Bubbly Flow and Turbulence in Hydraulic Jumps." Environmental Fluid Mechanics, Vol. 9, No. 2, pp. 143159. (DOI: 10.1007/s10652-008-9077-4).

MURZYN, F., MOUAZE, D., and CHAPLIN, J. R. (2007). "Air-Water Interface Dynamic and Free Surface Features in Hydraulic Jumps." Journal of Hydraulic Research, IAHR, Vol. 45, No. 5, pp. 679-685.

NARAYANAN, R. (1975). "Wall Jet Analogy to Hydraulic Jump." Journal of Hydraulics Division, Vol. 101, No. HY3, pp. 347-359.

NELUWALA, N. G. P. B., KARUNANAYAKE, K. T. S., SANDARUWAN, K. B. G. M., and PATHIRANA, K. P. P. (2013). "Characteristics of Hydraulic Jumps over Rough Beds – an Experimental Study." Engineer: Journal of the Institution of Engineers, Sri Lanka. 46(3), pp.1–7. DOI: http://doi.org/10.4038/engineer.v46i3.6779.

NOYMER, P. D. (2000). "The Use of Single-Point Measurements to Characterise Dynamic Behaviours in Spray." Experiments in Fluids, Vol. 29, pp. 228-237.

PAGLIARA, S. and PALERMO, M. (2015). "Hydraulic Jumps on Rough and Smooth Beds: Aggregate Approach for Horizontal and Adverse-sloped Beds." Journal of Hydraulic Research, 53 (2), pp. 243–252.

PAGLIARA, S., CARNACINA, I., and ROSHNI, T. (2010). "Air-Water Flows in the Presence of Staggered and Row Boulders under Macro roughness Conditions." Water Resources Research, 46, W08535, doi:10.1029/2009WR008834.

PAGLIARA, S., LOTTI, I. and PALERMO, M. (2008). "Hydraulic Jumps on Rough Bed of Stream Rehabilitatiocummn Structures." Journal of Hydro-Environment Research, 2(1), pp. 29–38.

PAGLIARA, S., ROSHNI, T. and CARNACINA, I. (2011). "Turbulence, Aeration and Bubble Features of Air-Water Flows over Macro- And Intermediate Roughness." Water Science and Engineering 2011, 4(2).170-184 DOI: 10.3882/j.issn.16742370.2011.02.005.

PERRY, A. E., SCHOFIELD, W. H., and JOUBERT, P. N. (1969). "Rough wall Turbulent Boundary Layers." Journal of Fluid Mechanics, 37, pp. 383–413.

PROSPERETTI, A., and TRYGGVASON, G. (2009). "Computational Methods for Multiphase Flow." Cambridge University Press, London, UK, 488 pages.

RAIKAR, R. V. and KAMATAGI, P. B. (2015). "Use of Hydraulic Phenomena in Enhancement of Dissolved Oxygen Concentration." International Journal of Research in Engineering and Technology. Volume: 04 Issue: 02.

RAJARATNAM, N. (1962). "An Experimental Study of Air Entrainment Characteristics of the Hydraulic Jump." Journal of Instruction Engineering India, Vol. 42, No. 7, pp. 247-273.

RAJARATNAM, N. (1965). "The Hydraulic Jump as a Wall Jet." Journal of Hydraulics Division. ASCE, Vol. 91, No. HY5, pp. 107-132.

RAJARATNAM, N. (1967). "Hydraulic jumps." Advances in Hydroscience, Vol. 4, Ed. by V. T. Chow, Academic Press, N.Y., pp. 197-280.

RAO, N. S. L., and KOBUS, H.E. (1971). "Characteristics of Self-Aerated Free-Surface Flows." Water and Waste Water/Current Research and Practice, Vol. 10, Eric Schmidt Verlag, Berlin, Germany.

RESCH, F. J., and LEUTHEUSSER, H. J. (1972). "Reynolds Stress Measurements in Hydraulic Jumps." Journal of Hydraulic Research. Vol. 10, No. 4, pp. 409-429.

RICHARD, G. L., and GAVRILYUK, S. L. (2013). "The Classical Hydraulic Jump in a Model of Shear Shallow-Water Flows." Journal of Fluid Mechanics, Vol. 725, pp. 492-521.

ROACHE, P. J. (2009). "Fundamentals of Verification and Validation." Hermosa Publishers, Albuquerque, 476 pages.

ROUSE, H. (1970). "Work-Energy equation for the streamline." Journal of Hydraulics Division, Vol. 96, No. HY5, pp. 1179-1190.

SAMADI-BOROUJENI, H., GHAZALI, M., GORBANI, B. and FATTAHI NAFCHI R. (2013). "Effect of Triangular Corrugated Beds on the Hydraulic Jump Characteristic." Canadian Journal of Civil Engineering, 2013, 40(9): 841-847, 10.1139/cjce-2012-0019.

SARKER, M.A. and RHODES, D. G. (2002). "Physical Modelling and CFD Applied to Hydraulic Jumps." Proceedings of the Congress – International Association for Hydraulic Research, Vol. D, No. 1, pp. 525-530.

SHI, R., WANG, H., and CHANSON, H. (2018). "Bubble Convection and Bubbly Flow Turbulent Time and Length Scales in Two-Dimensional Plunging Jets." Experimental Thermal and Fluid Science, Volume 98, 2018, Pages 278-289, ISSN 0894-1777, https://doi.org/10.1016/j.expthermflusci.2018.06.008.

STEFANSKY, W. (1972). "Rejecting Outliers in Factorial Designs", Technometrics, 14, pp. 469-479.

STEPHENS, M. A. (1974). "EDF Statistics for Goodness of Fit and Some Comparisons." Journal of the American statistical Association, 69(347), 730-737.

STRAUB, L. G. and ANDERSON, A. G. (1958). "Experiments on Self-Aerated Flow in Open Channels." Jl of Hyd. Div., Proc. ASCE, 84(HY7), paper 1890, 35 pages.

SUN, S., and CHANSON, H. (2013). "Characteristics of Clustered Particles in Skimming Flows on a Stepped Spillway." Environmental Fluid Mechanics, Vol. 13, No. 1, pp. 73-87.

TACHIE, M. F., and ADANE, K. K. (2007). "PIV Study of Shallow Open Channel Flow over D-And K-Type Transverse Ribs." ASME. Journal of Fluids Engineering 129(8):1058-1072. doi:10.1115/1.2746910.

TACHIE, M. F., and SHAH, M. K. (2008). "Favourable Pressure Gradient Flow Over Straight and Inclined Ribs on Both Channel Walls.", Physics of Fluids, Vol. 20, pp. 1-22.

TAKAHASHI, M., GONZALEZ, C. A., CHANSON, H. (2006). "Self-Aeration and Turbulence in a Stepped Channel: Influence of Cavity Surface Roughness." International Journal of Multiphase Flow 32 (12) 1370–1385, http://dx.doi.org/10.1016/j.ijmultiphaseflow.2006.07.001.

THANDAVESWARA, B.S. (1974) "Self Aerated Flow Characteristics in Developing Zones and in Hydraulic Jumps." PhD thesis, Dept. of Civil Engineering, Indian Institute of Science, Bangalore, India, 399 pages.

TANI, I. (1987). "Equilibrium, or Nonequilibrium, of Turbulent Boundary Layer Flows." Proc. Jpn. Acad., Ser. B: Phys. Biol. Sci., 63, pp. 96–100.

TAŞTAN, K., YILDIRIM, N. (2014). "Effects of Froude, Reynolds and Weber Numbers on an Air-Entraining Vortex", Technical Note, IAHR, Journal of Hydraulic Research, 52(3), pp.421-425.

TOOMBES, L. (2002). "Experimental Study of Air-Water Flow Properties on Low-Gradient Stepped Cascades." PhD Thesis, Dept. of Civil Engineering, The University of Queensland.

TOOMBES, L., and CHANSON, H. (2007). "Surface Waves and Roughness in Self-Aerated Supercritical Flow." Environmental Fluid Mechanics, Vol. 7, No. 3, pp. 259-270.

TOOMBES, L., and CHANSON, H. (2008). "Interfacial Aeration and Bubble Count Rate Distributions in a Supercritical Flow past a Backward-Facing Step." International Journal of Multiphase Flow, Vol. 34, No. 5, pp. 427-436.

TSIKATA, J. M. (2012). "Experimental Study of Turbulent Flow over Inclined Ribs in Adverse Pressure Gradient." PhD thesis, The University of Manitoba.

VALIANI, A. (1997). "Linear and Angular Momentum Conservation in Hydraulic Jump." Journal of Hydraulic Research. Vol. 35, No. 3, pp. 323-354.

WANG L, HEJCIK J, and SUNDEN B. (2007). "PIV Measurement of Separated Flow in a Square Channel With Streamwise Periodic Ribs on One Wall." ASME. Journal of Fluids Engineering. 129(7):834-841. doi:10.1115/1.2742723.

WANG, H. (2014). "Turbulence and Air Entrainment in Hydraulic Jumps." Ph.D. thesis, School of Civil Engineering, The University of Queensland, Brisbane, Australia (DOI: 10.14264/uql.2014.542).

WANG, H., and CHANSON, H. (2015). "Air Entrainment and Turbulent Fluctuations in Hydraulic Jumps." Urban Water Journal, Vol. 12, No. 6, pp. 502-518 (DOI: 10.1080/1573062X.2013.847464).

WANG, H., and CHANSON, H. (2016). "Self-Similarity and Scale Effects in Physical Modelling of Hydraulic Jump Roller Dynamics, Air Entrainment and Turbulent Scales." Environmental Fluid Mechanic 16:1087–1110 (DOI: 10.1007/s10652-016-9466-z).

WANG, H., and CHANSON, H. (2018). "Estimate of Void Fraction and Air Entrainment Flux in Hydraulic Jump Using Froude Number." Canadian Journal of Civil Engineering, Vol. 45, No. 2, pp. 105-116 (DOI: 10.1139/cjce-2016-0279).

WANG, H., FELDER, S., and CHANSON, H. (2014a). "An Experimental Study of Turbulent Two-Phase Flow in Hydraulic Jumps and Application of a Triple Decomposition Technique." Experiments in Fluids, Vol. 55, No. 7, Paper 1775, 18 pages (DOI: 10.1007/s00348-014-1775-8).

WANG, H., MURZYN, F., and CHANSON, H. (2014b). "Pressure, Turbulence and Two-Phase Flow Measurements in Hydraulic Jumps." Hydraulic Model Report No. CH95/14, School of Civil Engineering, The University of Queensland, Brisbane, Australia, 154 pages.

WANG, H., MURZYN, F., and CHANSON, H. (2015). "Interaction between Free-Surface, Two-Phase Flow and Total Pressure in Hydraulic Jump." Experimental Thermal and Fluid Science, Vol. 64, pp. 30-41 (DOI: 10.1016/j. Experimental Thermal and Fluid Science.2015.02.003).

WANG, H., LENG, X., and CHANSON, H. (2017). "Hydraulic jumps and breaking bores: modelling and analysis." Proceedings of the Institution of Civil Engineers–Engineering and Computational Mechanics, 170(1), 25-42.

WEI, W. R., XU, W. L., DENG, J., TIAN, Z., and ZHANG, F. X., (2018). "Analysis on Link between the Macroscopic and Microscopic Air-Water Properties in Self-Aerated Flows." China Ocean Engineering., 32(5): 1–10, doi: https://doi.org/10.1007/s13344-017-0000-00.

WEI, W. R., XU, W. L., DENG, J., TIAN, Z., and ZHANG, F. X., (2018). "Experimental Study on Air-Water Interface Properties in Self-Aerated Flows." Journal of Hydrodynamic, https://doi.org/10.1007/s42241-018-0162-y.

WITT, A., GULLIVER, J. and SHEN, L. (2015). "Simulating Air Entrainment and Vortex Dynamics in a Hydraulic Jump." International Journal Multiphase Flow 72, 165e180. ISSN 0301- 9322. http://dx.doi.org/10.1016/j. International Journal Multiphase Flow. 2015.02.012.

WOOD, I. R. (1991). "Air Entrainment in Free-Surface Flows." IAHR Hydraulic Structures Design Manual No. 4, Hydraulic Design Considerations, Balkema Publisher, Rotterdam, the Netherlands, 149 pages.

WU, S., and RAJARATNAM, N. (1996). "Transition from Hydraulic Jump to Open Channel Flow." Journal of Hydraulic Engineering, ASCE, Vol. 122, No. 9, pp. 526-528.

XIANG, M., CHEUNG, S. C. P., TU, J. Y. and ZHANG W. H. (2014), "A Multi-Fluid Modelling Approach for the Air Entrainment and Internal Bubbly Flow Region in Hydraulic Jumps." Ocean Engineering, 91 (2014), pp. 51–63

ZHANG, G., WANG, H., CHANSON, H. (2013). "Turbulence and Aeration in Hydraulic Jumps: Free-Surface Fluctuation and Integral Turbulent Scale Measurements." Environmental Fluid Mechanics, Vol. 13, No. 2, pp. 189–204 (DOI: 10.1007/s10652-012-9254-3).

ZHAO, Q., MISRA, S. K., SVENDSEN, I. A., and KIRBY, J. T. (2004). "Numerical Study of a Turbulent Hydraulic Jump." Proceedings of 17th ASCE Engineering Mechanics Conference, June 13-16, 2004, Newark, USA, pp. 1-7.

ZHOU, J. and STANSBY, P. (1999). "2D Shallow Water Flow Model for the Hydraulic Jump." International Journal for Numerical Method in Fluids 29, 375–387.

Appendix A: Photographs of Hydraulic Jumps

Comprehensive photographs of the hydraulic jump flow patterns were recorded for both smooth and rough bed configurations using high speed camera. The flow patterns were described in detail in Chapter 4 based on some key inflow Froude numbers. This Appendix complements the flow patterns observations with a systematic documentation of the flow patterns of hydraulic jumps with and without bed roughness. The figures herein are sorted in terms of inflow Froude number for smooth and rough bed respectively. They encompass the full range of flow rates investigated in the present study. Different types of hydraulic jump as defined by Chanson (2004) including free surface fluctuations and air entrainment properties are presented here based on inflow Froude and Reynolds numbers as listed in Tables 3.3 and 3.4 in Chapter 3. Note that for all runs the upstream gate opening was h = 0.06 m.

a. Small undular hydraulic jump, run *AS*9, Q = 0.044 m^3/s, d_1 = 0.06 m, Fr_1 =1.92, Re_1 = 9.5E+4

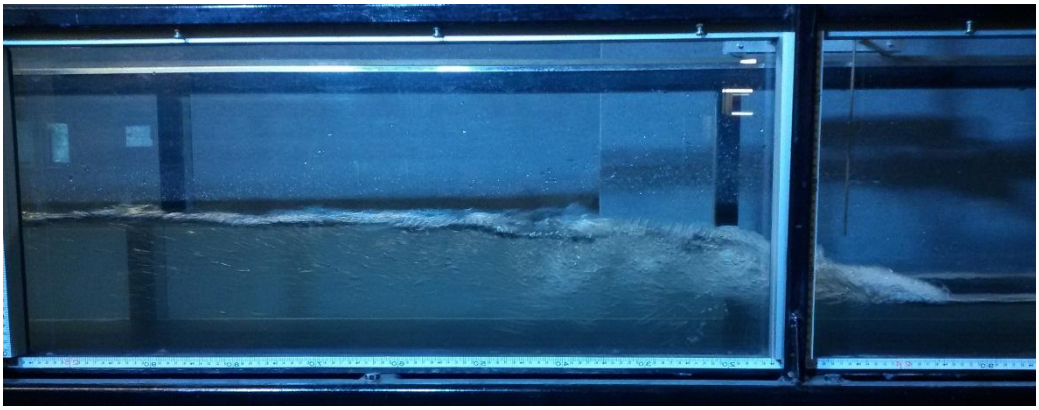

b. Small undular hydraulic jump with air entrainment, run *AS*10, Q = 0.048 m^3/s, d_1 =0.06 m, Fr_1 = 2.18, Re_1 = 1.0E+5

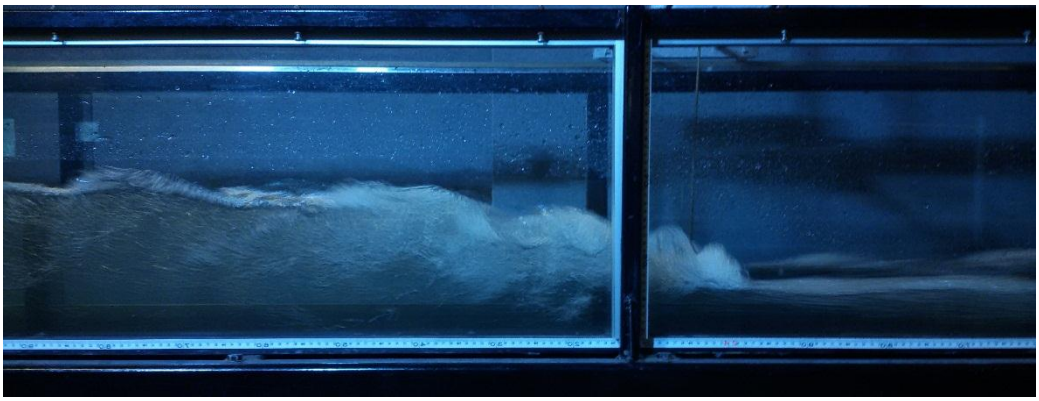

c. Undular hydraulic jump with air entrainment, run *AS*11, Q = 0.054 m^3/s, d_1 = 0.06 m, Fr_1 = 2.47, Re_1 = 1.2E+5

d. Hydraulic jump with roller and fluctuations of jump toe, run *AS*12, Q = 0.073 m^3/s, d_1 = 0.061 m, Fr_1 = 3.12, Re_1 = 1.6E+5

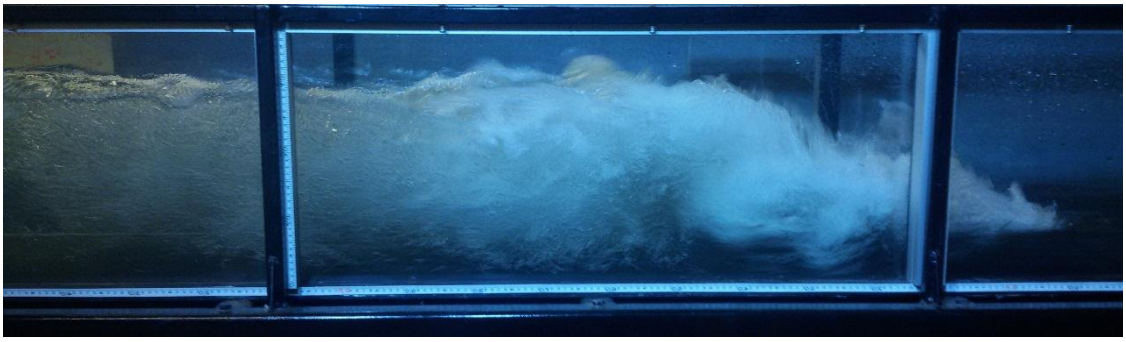

e. Hydraulic jump floating on top of clear water flow region, run *AS*13, Q = 0.078 m^3/s, d_1 = 0.062 m, Fr_1 = 3.25, Re_1 = 1.7E+5

f. Hydraulic jump with strong vortex shedding and free-surface fluctuations, run *AS*14, Q = 0.089 m^3/s, d_1 = 0.063 m, Fr_1 = 3.62, Re_1 = 1.9E+5

Figure A.1: Hydraulic jump patterns for smooth bed configuration, h = 0.06 m. Flow direction from right to left

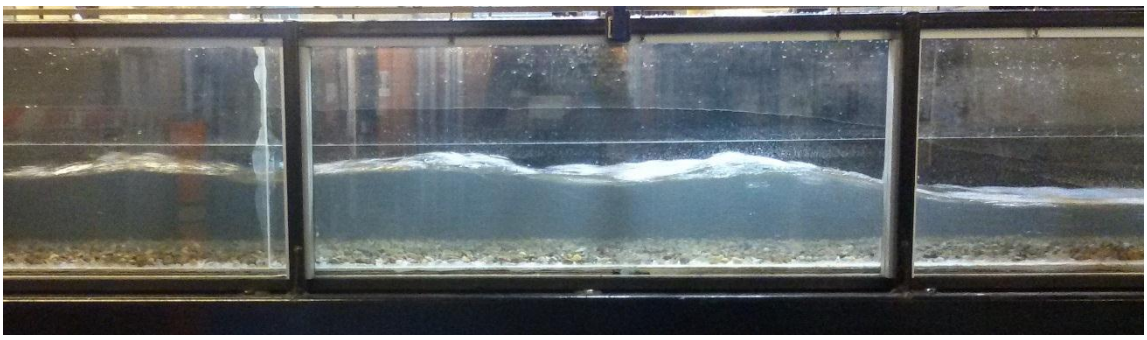

a. Small undular hydraulic jump, run *AR*1, Q = 0.043 m^3/s, d_1 = 0.078 m, Fr_1 = 1.31, Re_1 = 9.6E+4

b. Undular hydraulic jump, run *AR*2, Q = 0.051m^3/s, d_1 = 0.0785 m, Fr_1 = 1.57, Re_1 = 1.1E+5

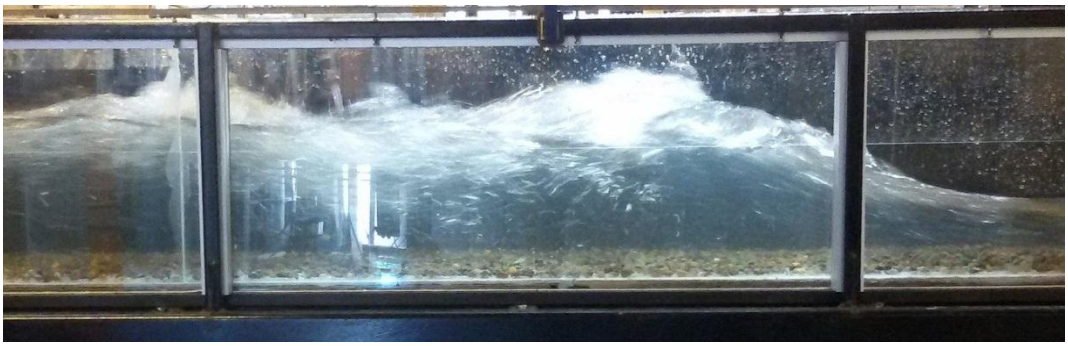

c. Undular hydraulic jump with air entrainment, run *AR*4, Q = 0.07m^3/s, d_1 = 0.084m, Fr_1 = 1.93, Re_1 = 1.6E+5

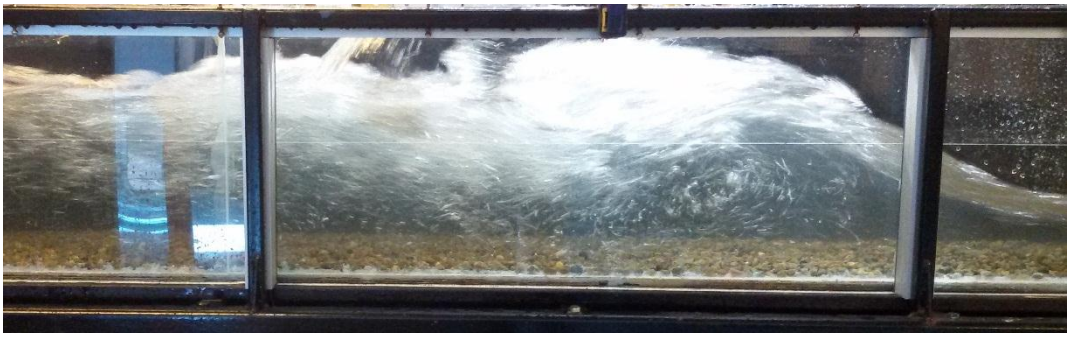

d. Hydraulic jump with roller and vortex street on clear water, run *AR*5, Q = 0.076 m^3/s, d_1 = 0.085 m, Fr_1 = 2.07, Re_1 = 1.7E+5

e. Hydraulic jump with vortex shedding, run *AR*6, Q = 0.085 m^3/s, d_1 = 0.083 m, Fr_1 = 2.4, Re_1 = 1.9E+5

f. Hydraulic jump with strong vortex shedding, run *AR*7, Q = 0.092 m^3/s, d_1 = 0.084 m, Fr_1 = 2.56, Re_1 = 2.1E+5

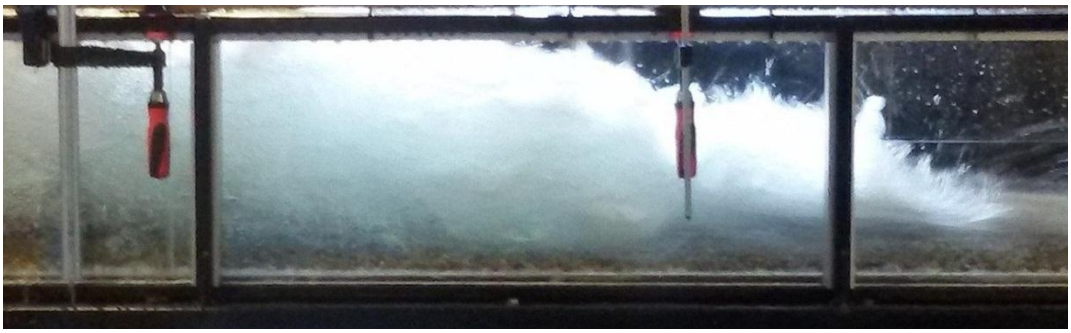

f. Hydraulic jump with strong vortex shedding and splashing, run *AR*8, Q = 0.1 m^3/s, d_1 = 0.085 m, Fr_1 = 2.87, Re_1 = 2.3E+5

Figure A.2: Hydraulic jump patterns for rough bed configuration, h = 0.06 m. Flow direction from right to left

Appendix B: Two-phase Flow Data of Hydraulic Jumps

Appendix B presents the two-phase flow experimental data of the present study on both smooth and rough bed configurations in tabular form. Parameters including the time-averaged void fraction C and bubble count rate F were measured on the leading tip of dual-tip phase-detection probe, while the interfacial velocity V, auto-/cross-correlation time scales T_{xx} and $T_{xx'}$ and turbulence intensity Tu were extracted from the auto-/cross-correlation functions between the leading and trailing sensor signals. Since the phase-detection probe mounted reversely pointing the downstream direction, the negative velocity V_{rec} was recorded in the recirculation region with minimised interference of the probe itself (V_{rec} > 0 in the downstream direction). The correlation analysis failed to provide meaningful results at some locations as denoted "--". For all experiments, the leading tip was positioned in channel centre line. The hydraulic jump toe was located at x_1 = 1 m downstream of the sluice gate and the provided longitudinal locations are relative to the jump toe. Herein, the data are presented first for rough bed condition regarding three inflow Froude number for different cross-sections and then for smooth bed condition.

B.1: Experimental data on rough bed

Fr_1 = 1.7, Q = 0.061 m^3/s, Re_1=1.4×10^5, h = 0.06 m; d_1=0.083 m: x-x_1 = -0.3 m

Y (mm)	*C* [-]	*F* [Hz]	*V* [m/s]	T_{xx} [s]	T_{xx} ' [s]	*Tu* [-]	R_{xx}'(max)
15	0.00003		-	0.000333	-	-	0.348797
30	0.00003	0.033333	-	0.000235	1.38E-05	-	0.373955
45	6.53E-05	0.088889	2.20339	0.000899	0.00082	0.291345	0.529017
55	7.5E-05	0.111111	2.241379	0.000454	-	0.137639	0.284239
65	3.89E-05	0.072222	2.131148	0.000333	-	0.078918	0.35085
70	0.000133	0.138889	2.166667	0.001186	0.00097	0.488862	0.387466
72	0.000543	0.266667	2.20339	0.005227	0.00507	0.997117	0.790714
74	0.002906	0.872222	2.241379	0.003762	0.004077	0.728319	0.814369
76	0.018157	3.744444	2.20339	0.008998	0.009154	1.072121	0.886288
77	0.039215	7.361111	2.280702	0.011054	0.011374	1.298122	0.896683
78	0.103218	15.56667	2.280702	0.012762	0.012934	1.407131	0.909634
79	0.189347	22.57778	2.280702	0.016411	0.016483	1.660435	0.92005
80	0.305753	29.33889	2.280702	0.01554	0.015444	1.68383	0.924626
81	0.481744	33.47222	2.280702	0.016342	0.016006	1.647498	0.92556
82	0.659628	29.50556	2.280702	0.01678	0.016302	1.554997	0.927168
83	0.800027	22.36111	2.321429	0.015242	0.014631	1.402689	0.922183
84	0.900162	14.2	2.280702	0.013519	0.012501	1.166343	0.911503
85	0.94962	7.955556	2.241379	0.014066	0.012561	1.103947	0.901561
86	0.978416	3.833333	2.241379	0.012857	0.011069	0.925177	0.895769
87	0.991759	1.772222	2.20339	0.010858	0.009173	0.811327	0.867223

Appendix B: Two-phase flow data of hydraulic jumps

Fr_1 = 1.7, Q = 0.061 m^3/s, Re_1=1.4×10^5, h = 0.06 m; d_1=0.083 m: x-x_1 = 0.1 m

Y (mm)	*C* [-]	*F* [Hz]	*V* [m/s]	T_{xx} [s]	T_{xx} ' [s]	*Tu* [-]	R_{xx}'(max)
10	0	0	-	0.041451	0.036844	-	0.510813
35	1.03E-05	0.022222	-	0.000129	3.38E-06	-	0.071869
60	2.5E-05	0.038889	-	0.000594	0	-	0.039562
70	1.61E-05	0.027778	2.03125	0.000609	0	-	0.063521
80	0.000738	0.155556	2.20339	0.003359	0.00287	1.6979	0.364757
83	0.000399	0.161111	2.166667	0.003117	0.00298	1.176875	0.633451
86	0.004267	0.638889	2.03125	0.011253	0.008253	1.599443	0.709826
89	0.014376	1.788889	2.166667	0.020217	0.017208	1.762104	0.720021
90	0.025244	2.655556	2.166667	0.026296	0.02335	2.686609	0.738261
92	0.075171	6.061111	2.280702	0.021166	0.017395	2.615874	0.668609
93	0.089866	7.266667	2.241379	0.022023	0.018236	2.768969	0.671432
94	0.115531	7.661111	2.166667	0.030387	0.027023	3.181401	0.758991
96	0.179733	12.31111	2.166667	0.031583	0.027673	3.83013	0.750349
98	0.299828	12.9	2.20339	0.03564	0.032153	4.482625	0.759794
100	0.44151	14.33333	2.20339	0.046083	0.042792	-	0.796614
102	0.480791	14.67222	2.241379	0.043389	0.040404	-	0.783617
105	0.669511	12.66667	2.280702	0.042599	0.040752	-	0.78316
107	0.665459	11.14444	2.20339	0.04469	0.042431	-	0.788074
109	0.848222	7.277778	2.241379	0.044537	0.044587	-	0.783385
111	0.882911	6.172222	2.166667	0.039805	0.040667	-	0.770291
113	0.920256	5.027778	2.241379	0.027618	0.028383	-	0.702952
115	0.944356	2.988889	2.6	0.025144	0.026169	-	0.695752
118	0.950473	2.938889	2.166667	0.031328	0.031266	-	0.731901
122	0.977969	1.383333	2.131148	0.040246	0.042341	-	0.740306
126	0.991968	0.588889	2.096774	0.031655	0.03187	-	0.732837

Appendix B: Two-phase flow data of hydraulic jumps

Fr_1 = 1.7, Q = 0.061 m^3/s, Re_1=1.4×10^5, h = 0.06 m; d_1=0.083 m: x-x_1 = 0.15 m

Y (mm)	*C* [-]	*F* [Hz]	*V* [m/s]	T_{xx} [s]	T_{xx} ' [s]	*Tu* [-]	R_{xx}'(max)
10	1.25E-05	0.011111	-	0.001122	1.45E-05	-	0.083838
25	1.25E-05	-	-	9.11E-05	0.011729	-	0.304559
40	7.87E-06	0.016667	-	4.92E-05	1.92E-05	-	0.275592
50	6.39E-06	0.011111	-	0.000262	1.19E-05	-	0.275145
60	5.56E-06	-	-	2.94E-05	9.52E-06	-	0.700101
70	5.56E-06	-	-	0.000154	2.79E-05	-	0.358186
77	5.56E-06	0.011111	-	0.000241	8.02E-07	-	0.070505
84	9.72E-06	0.011111	-	0.000392	0	-	0.312937
90	1.92E-05	0.033333	-	0.000317	2.86E-05	-	0.111851
95	0.015255	1.677778	2.407407	0.027456	0.021794	2.343941	0.668197
98	0.060147	-	2.063492	0.016929	0.012679	2.226803	0.560934
102	0.119149	7.161111	2.321429	0.031269	0.025561	4.665007	0.655234
103	0.131825	6.527778	2.321429	0.037187	0.03107	4.890205	0.682837
104	0.145238	7.244444	2.131148	0.029772	0.024453	4.429248	0.598654
105	0.15346	8.244444	2.708333	0.030771	0.025423	4.556258	0.676335
106	0.229641	9.627778	2.407407	0.034172	0.029243	-	0.684319
107	0.2849	11.32778	2.321429	0.037244	0.031902	-	0.698441
108	0.341648	9.95	2.6	0.036613	0.032567	-	0.687471
110	0.369834	-	-	0.045481	0.042049	-	0.737197
113	0.495072	10.65	2.45283	0.047933	0.043926	-	0.77272
115	0.554808	11.3	2.407407	0.04838	0.045207	-	0.777407
118	0.68405	9.294444	2.280702	0.039887	0.03858	-	0.747477
120	0.683128	7.927778	2.321429	0.046074	0.044445	-	0.760334
123	0.759353	8.127778	2.321429	0.041449	0.041111	-	0.747257
126	0.803389	6.405556	2.5	0.037579	0.036895	-	0.716419
130	0.839128	-	2.363636	0.043011	0.035111	-	0.667134
135	0.936974	3.133333	2.063492	0.043614	0.043232	-	0.716264
140	0.987903	0.938889	1.940299	0.027806	0.028509	-	0.67361

Appendix B: Two-phase flow data of hydraulic jumps

Fr_1 = 1.7, Q = 0.061 m^3/s, Re_1=1.4×10^5, h = 0.06 m; d_1=0.083 m: x-x_1 = 0.3 m

Y (mm)	*C* [-]	*F* [Hz]	*V* [m/s]	T_{xx} [s]	T_{xx} ' [s]	*Tu* [-]	R_{xx}'(max)
10	0.000008	-	-	-	-	-	-
25	0.00001	-	-	-	-	-	-
40	0.00002	-	-	-	-	-	-
55	0.00003	-	-	-	-	-	-
70	0.00004	-	-	-	-	-	-
80	0.00005	-	-	-	-	-	-
90	0.00006	-	-	-	-	-	-
100	0.00007	-	-	-	-	-	-
110	0.00008	-	-	-	-	-	-
120	0.00009	-	-	-	-	-	-
125	0.000402	0.054444	-	0.008712	0.005935	-	0.3463
130	0.001053	0.15	-	0.011499	0.010955	-	0.306663
135	0.00085	0.177778	0.992366	0.007768	0.004425	0.900067	0.412804
138	0.001001	0.294444	1.048387	0.006782	0.005447	1.32873	0.458213
141	0.001103	0.255556	1.226415	0.005769	0.004005	1.844152	0.345014
145	0.002745	0.405556	1.048387	0.013841	0.012571	1.630543	0.573191
148	0.006091	0.961111	1.397849	0.01464	0.011266	2.345199	0.540411
151	0.023696	1.85	-	0.037735	0.031062	4.755948	0.692427
155	0.039211	3.538889	-	0.029598	0.024362	2.802028	0.684864
158	0.038859	3.494444	1.25	0.014814	0.012551	1.613568	0.633394
161	0.059809	5.394444	1.287129	0.019301	0.016286	1.827435	0.633566
165	0.10249	6.683333	1.192661	0.021801	0.018115	1.721425	0.672771
168	0.118987	6.894444	1.340206	0.028235	0.024796	2.428528	0.700427
175	0.123943	8.7	1.340206	0.025719	0.022849	2.240036	0.734238
176	0.222797	10.80556	1.604938	0.036084	0.033327	2.240036	0.791507
178	0.23529	12.57778	1.64557	0.031348	0.028625	2.240036	0.782091
180	0.337135	14.88333	1.413043	0.03343	0.030976	-	0.749921
190	0.540567	14.60556	1.460674	0.037955	0.036268	-	0.77865
200	0.764242	10.88333	1.511628	0.033652	0.034301	-	0.774423
210	0.825955	9.55	1.444444	0.032675	0.033714	-	0.783196
220	0.908377	6.038889	1.444444	0.025309	0.028269	-	0.756204
230	0.969275	2.544444	1.444444	0.021596	0.02546	-	0.727937
240	0.988006	1.005556	1.382979	0.021755	0.017823	-	0.686127
250	0.998	0.705556	1.181818	0.021363	0.017831	-	0.717207

Appendix B: Two-phase flow data of hydraulic jumps

Fr_1 = 1.7, Q = 0.061 m^3/s, Re_1=1.4×10^5, h = 0.06 m; d_1=0.083 m: x-x_1 = 0.45 m

Y (mm)	*C* [-]	*F* [Hz]	*V* [m/s]	T_{xx} [s]	T_{xx} ' [s]	*Tu* [-]	R_{xx}'(max)
10	5.69E-05	0.016667	-	0	0	0	0.194074
25	5.69E-05	-	-	0.013842	0	0	0.352074
40	8.75E-05	0.011111	-	0	1.54E-06	0	0.036257
55	1.25E-05	0.016667	-	0.00291	0	0	0.154098
70	1.67E-05	0.016667	-	0.002728	0	0	0.17617
80	1.77E-05	-	-	0.005016	1.99E-05	0	0.297136
90	4.22E-05	0.016667	-	0.001417	1.82E-06	0	0.027705
100	0.000981	-	-	0.004793	6.16E-05	0	0.313666
110	2.25E-05	0.016667	0.890411	0.001123	0	0	0.106889
120	7.31E-05	0.05	-	0.007207	0	0	0.028063
130	0.000235	0.077778	1.150442	0.0106	0	0.321194	0.261437
140	0.006413	2.783333	1.477273	0.002959	0.001975	0.56949	0.41006
145	0.008032	3.216667	1.477273	0.004531	0.004118	0.552487	0.440277
150	0.001139	0.272222	0.955882	0.004459	0.003966	0.640821	0.283755
155	0.002208	0.416667	1.354167	0.006882	0.005343	1.576974	0.340426
160	0.00263	0.444444	1.101695	0.005887	0.004618	0.864191	0.37398
165	0.006157	0.95	1.056911	0.010206	0.007703	1.008328	0.474782
170	0.008126	1.372222	1.07438	0.010882	0.009892	1.2181	0.6122
175	0.018627	2.338889	1.262136	0.016617	0.015107	1.559444	0.735228
180	0.026347	3.161111	1.25	0.017516	0.016857	1.780295	0.718207
185	0.034286	4.55	1.326531	0.017805	0.017546	1.58669	0.75724
190	0.050874	5.783333	1.3	0.021491	0.021712	2.059121	0.778951
195	0.084335	8.222222	1.368421	0.024844	0.024703	2.098519	0.81512
200	0.104618	9.761111	1.413043	0.025394	0.025192	2.067949	0.826303
205	0.163094	11.98333	1.397849	0.036848	0.036947	3.734944	0.865073
210	0.20918	14.13889	1.413043	0.030863	0.031359	2.742621	0.867319
215	0.253186	15.31111	1.397849	0.034555	0.034482	3.020967	0.877951
220	0.3599	16.82222	1.413043	0.036539	0.036615	3.594134	0.887945
225	0.430482	18.52222	1.382979	0.037163	0.037427	3.399953	0.880378
230	0.501806	17.01667	1.397849	0.039147	0.03939	3.599687	0.900331
240	0.671587	15.83889	1.368421	0.037236	0.037035	3.278149	0.886384
250	0.826297	10.35	1.313131	0.03584	0.035336	2.706008	0.888219
260	0.923926	5.533333	1.262136	0.031785	0.031202	2.045358	0.881163
270	0.971548	2.522222	1.203704	0.024904	0.024079	1.781441	0.855514
280	0.995736	0.527778	1.262136	0.021953	0.020078	0.888324	0.742102

Appendix B: Two-phase flow data of hydraulic jumps

Fr_1 = 1.7, Q = 0.061 m^3/s, Re_1=1.4×10^5, h = 0.06 m; d_1=0.083 m: x-x_1 = 0.65 m

Y (mm)	*C* [-]	*F* [Hz]	*V* [m/s]	T_{xx} [s]	T_{xx} ' [s]	*Tu* [-]	R_{xx}'(max)
10	0	0	-	0.006201	0	0	0.458548
30	1.22E-05	0.011111	-	1.79E-05	0	-	0.41229
50	5.75E-05	0.011111	-	0.002759	1.2E-06	0	0.019531
70	7.11E-05	0.038889	-	0.001225	2.55E-06	0	0.01644
90	0.000136	0.061111	-	0.001482	0.000688	-	0.120748
110	0.000552	0.222222	1.130435	0.001852	0	0.518264	0.181456
130	0.001314	0.455556	1.056911	0.002547	0.001705	0.552804	0.272921
145	0.0033	1.233333	1.27451	0.003246	0.002459	0.548367	0.320313
160	0.009996	2.805556	1.340206	0.00891	0.007875	0.787831	0.458937
167	0.02284	5.75	1.529412	0.010996	0.010402	0.964201	0.61339
171	0.035476	6.516667	1.625	0.017623	0.016772	2.11226	0.681732
176	0.054599	8.855556	1.547619	0.022294	0.021192	2.178131	0.744361
181	0.104128	11.78333	1.585366	0.034796	0.032956	4.266514	0.803927
184	0.146141	15.16667	1.585366	0.034446	0.03347	4.403865	0.804674
188	0.200179	17.14444	1.625	0.039242	0.037761	-	0.82732
194	0.357806	18.37778	1.666667	0.047859	0.045708	-	0.870611
198	0.375316	17.66111	1.666667	0.050215	0.048043	-	0.877161
203	0.456697	17.11111	1.625	0.051221	0.048475	-	0.884552
207	0.564511	15.83333	1.666667	0.05417	0.05146	-	0.88792
212	0.659719	13.98333	1.64557	0.053869	0.051399	-	0.894115
218	0.787292	11.13889	1.733333	0.050679	0.04737	-	0.88869
225	0.846586	8.655556	1.64557	0.052958	0.048902	-	0.890973
235	0.942447	4.905556	1.547619	0.041381	0.036955	-	0.853723
245	0.977143	2.361111	1.666667	0.043287	0.037764	-	0.872534
255	0.994527	0.661111	1.494253	0.028452	0.024575	-	0.828296

Appendix B: Two-phase flow data of hydraulic jumps

Fr_1 = 1.7, Q = 0.061 m^3/s, Re_1=1.4×10^5, h = 0.06 m; d_1=0.083 m: x-x_1 = 1.0 m

Y (mm)	*C* [-]	*F* [Hz]	*V* [m/s]	T_{xx} [s]	T_{xx} ' [s]	*Tu* [-]	R_{xx}'(max)
10	8.94E-05	0	65	0.012304	0	0	0.248342
30	8.94E-05	0.044444	0.802469	0.001482	0	-	0.283836
50	0.00016	0.055556	0.860927	0.001785	0	0	0.031655
70	0.000421	0.188889	0.553191	0.002128	0.000492	-	0.14803
90	0.009807	0.286667	1.031746	0.002292	0.00073	0.547863	0.121048
110	0.000862	0.405556	1.203704	0.001718	0	0.47904	0.137182
120	0.001019	0.633333	1.287129	0.001248	0.000414	0.25221	0.203499
130	0.003494	1.083333	1.428571	0.006	0.004927	0.907495	0.322008
137	0.008512	1.838889	1.326531	0.011146	0.009028	1.334011	0.434281
144	0.012087	2.516667	1.477273	0.018522	0.015693	2.621478	0.530615
151	0.059249	6.188889	1.428571	0.039421	0.034952	-	0.695875
153	0.036702	4.644444	1.354167	0.032123	0.028087	-	0.612825
155	0.054798	4.827778	1.397849	0.036675	0.032902	-	0.648244
157	0.085763	7.544444	1.585366	0.043046	0.039089	-	0.75834
159	0.093285	8.472222	1.625	0.042264	0.038481	-	0.733571
162	0.108054	9.594444	1.511628	0.045483	0.040418	-	0.7277
164	0.098396	9.35	1.494253	0.044032	0.038578	-	0.733261
166	0.129183	11.24444	1.547619	0.047816	0.043954	-	0.759937
169	0.132934	10.38889	1.477273	0.040022	0.034668	-	0.659976
172	0.157959	12.32222	1.368421	0.047252	0.042255	-	0.734651
176	0.177877	13.54444	1.547619	0.044992	0.040267	-	0.720196
181	0.337682	16.14444	1.604938	0.052568	0.049014	-	0.76808
185	0.410194	17.48333	1.444444	0.055419	0.050981	-	0.798747
190	0.513379	18.34444	1.585366	0.053862	0.050655	-	0.792869
195	0.616094	17.21667	1.444444	0.052764	0.049515	-	0.795345
200	0.624998	16.71667	1.460674	0.054646	0.051799	-	0.802449
205	0.749489	13.23333	1.477273	0.047137	0.04507	-	0.767755
210	0.770475	13.05556	1.477273	0.0493	0.047033	-	0.762885
220	0.873415	8.172222	1.428571	0.042449	0.040946	-	0.733621
230	0.938995	4.55	1.460674	0.038384	0.036316	-	0.656239
240	0.975102	2.283333	1.262136	0.027186	0.026285	-	0.621323
250	0.984638	1.266667	1.326531	0.021552	0.01987	-	0.45853

Appendix B: Two-phase flow data of hydraulic jumps

Fr_1 = 1.7, Q = 0.061 m^3/s, Re_1=1.4×10^5, h = 0.06 m; d_1=0.083 m: x-x_1 = 1.15 m

Y (mm)	*C* [-]	*F* [Hz]	*V* [m/s]	T_{xx} [s]	T_{xx} ' [s]	*Tu* [-]	R_{xx}'(max)
10	0.000123	0	-	0.000113	0	0	0.468196
30	0.000123	0.061111	-	0.002321	0	0.053921	0.109776
50	0.022567	0.08	0.890411	0.003161	0	0.171627	0.144676
65	0.000135	0.1	0.955882	0.001036	0	0.099332	0.155432
80	0.000313	0.133333	0.915493	0.001581	0.0002	0.097558	0.128577
95	0.000301	0.172222	0.962963	0.001353	0	0.063037	0.165711
110	0.00047	0.211111	1.023622	0.00172	0.000899	0.396197	0.26619
125	0.025081	-	1.031746	0.001273	0	0.358151	0.197144
140	0.000917	0.472222	0.909091	0.001318	0	0.103075	0.142211
155	0.001142	0.6	-	0.001666	0	0.871831	0.167526
170	0.002039	0.983333	1.160714	0.002228	0.001379	0.633164	0.270941
180	0.00336	1.511111	1.04	0.002465	0.001611	0.656575	0.192759
187	0.005094	1.894444	0.955882	0.004569	0.002897	0.488715	0.286667
194	0.009715	3.188889	1.023622	0.006328	0.004836	0.793555	0.365208
200	0.012608	3.438889	0.935252	0.008371	0.006694	0.887459	0.397497
202	0.018898	3.988889	0.992366	0.014715	0.014007	1.892107	0.485601
204	0.024383	4.172222	1.015625	0.018008	0.016039	1.735128	0.582415
206	0.02554	5.116667	0.970149	0.016607	0.014343	1.835629	0.534317
208	0.040062	5.994444	0.992366	0.023028	0.020878	2.092003	0.634197
211	0.041483	7.055556	0.984848	0.019726	0.01761	1.874206	0.584143
214	0.071798	7.694444	0.992366	0.03371	0.031269	3.717196	0.712597
217	0.086202	8.4	0.970149	0.036027	0.033863	3.754962	0.720665
220	0.124133	9.838889	0.984848	0.042711	0.039886	-	0.778513
225	0.175471	12.18333	0.948905	0.044197	0.041219	-	0.80627
230	0.257428	14.08889	-	0.013077	0.012566	-	0.832837
236	0.359164	14.36667	0.977444	0.051347	0.047779	-	0.844744
242	0.502513	13.43333	1.015625	0.052676	0.049681	-	0.878141
246	0.548044	13.11111	0.948905	0.052518	0.049434	-	0.871194
255	0.718583	10.66111	0.992366	0.049768	0.046937	-	0.870324
265	0.871171	6.344444	0.962963	0.046237	0.042874	-	0.85865
275	0.949368	3.577778	0.928571	0.036819	0.032841	-	0.803774
285	0.96846	1.5	0.984848	0.029061	0.02571	-	0.732326
290	0.992076	0.577778	-	0.020876	0.016117	-	0.681014

Fr_1 = 1.96, Q = 0.07 m^3/s, Re_1=1.6×10^5, h = 0.06 m; d_1=0.083 m: x-x_1 = -0.3 m

Y (mm)	*C* [-]	*F* [Hz]	*V* [m/s]	T_{xx} [s]	T_{xx} ' [s]	*Tu* [-]	R_{xx}'(max)
10	0.001576	-	-	-	-	-	-
20	0.001576	-	-	-	-	-	-
30	0.001576	-	-	-	-	-	-
40	0.002576	-	-	0.000342	0	0.465973	0.177202
50	6.78E-05	0.133333	2.765957	0.000655	0.000402	0.326417	0.20409
60	7.11E-05	0.194444	2.6	0.000249	0	0.127366	0.155273
65	0.000114	0.188889	2.6	0.000627	0.000469	0.215288	0.219656
70	0.000209	0.205556	2.708333	0.00136	0.000805	0.198218	0.506178
73	0.001672	0.644444	2.708333	0.003982	0.003224	0.859819	0.567817
75	0.010863	2.505556	2.765957	0.012114	0.012047	1.941693	0.834617
76	0.029155	5.45	2.653061	0.016095	0.016032	1.878887	0.857045
77	0.050022	8.244444	2.653061	0.020501	0.02037	2.474466	0.875657
78	0.104829	15.53889	2.6	0.020649	0.01998	2.267751	0.878797
79	0.194338	24.31667	2.653061	0.023305	0.02297	2.825545	0.890065
80	0.271279	29.31111	2.653061	0.023811	0.023322	2.753971	0.890999
81	0.391338	32.66111	2.653061	0.026788	0.025892	2.87486	0.898686
82	0.507852	34.85556	2.653061	0.025836	0.024932	2.905023	0.891121
83	0.660597	31.32222	2.653061	0.025377	0.024359	2.94242	0.887133
84	0.775077	25.23333	2.653061	0.027639	0.026587	3.264876	0.885428
85	0.853949	20.21667	2.653061	0.021777	0.02101	2.738154	0.871451
86	0.924023	12.54444	2.653061	0.018371	0.017071	2.251601	0.845607
87	0.956028	7.688889	2.708333	0.017878	0.017018	2.167894	0.833337
88	0.980949	4.227778	2.653061	0.01177	0.011069	1.458857	0.812252
89	0.989395	2.477778	2.653061	0.011122	0.010684	1.545596	0.803401

Appendix B: Two-phase flow data of hydraulic jumps

Fr_1 = 1.96, Q = 0.07 m^3/s, Re_1=1.6×10^5, h = 0.06 m; d_1=0.083 m: x-x_1 = 0.1 m

Y (mm)	*C* [-]	*F* [Hz]	*V* [m/s]	T_{xx} [s]	T_{xx} ' [s]	*Tu* [-]	R_{xx}'(max)
10	4.31E-05	-	-	-	-	-	-
20	4.31E-05	-	-	-	-	-	-
30	4.31E-05	-	-	-	-	-	-
40	4.31E-05	-	-	-	-	-	-
50	4.31E-05	-	-	-	-	-	-
60	4.31E-05	-	-	-	-	-	-
70	4.31E-05	0.05	1.969697	0.001184	0.000592	0.218817	0.481772
73	3.22E-05	0.05	0.872483	0.001404	0	0.051084	0.342823
76	0.000355	0.316667	2.20339	0.00335	0.00271	0.9585	0.474003
78	0.000191	0.2	1.181818	0.001196	0.000372	0.102342	0.165434
80	0.00024	0.277778	1.688312	0.002422	0.001486	0.303878	0.357179
83	0.001128	0.488889	1.969697	0.007643	0.006431	1.622845	0.630493
86	0.002723	1.005556	2.363636	0.010406	0.009107	1.840669	0.647795
89	0.022086	4.583333	2.241379	0.01695	0.012839	1.846627	0.617153
92	0.044523	6.088889	1.805556	0.019415	0.015972	2.037063	0.616958
95	0.059061	7.25	2.03125	0.022148	0.01726	2.282458	0.618551
98	0.099956	12.35	2.166667	0.031803	0.025692	3.852727	0.673506
101	0.193204	14.43333	2.096774	0.039429	0.033863	-	0.710519
104	0.37283	21.51667	2.131148	0.046869	0.042582	-	0.737609
107	0.580235	20.32222	2.20339	0.043916	0.04109	-	0.729488
125	0.822396	14.30556	-	0.042114	0.040172	-	0.647633
130	0.864937	13.35556	-	0.039261	0.037346	-	0.626598
135	0.950164	4.883333	-	0.034495	0.034099	-	0.561943
140	0.974452	3.672222	-1.64557	0.028971	0.030038	-	0.510015

Appendix B: Two-phase flow data of hydraulic jumps

Fr_1 = 1.96, Q = 0.07 m^3/s, Re_1=1.6×10^5, h = 0.06 m; d_1=0.083 m: x-x_1 = 0.15 m

Y (mm)	*C* [-]	*F* [Hz]	*V* [m/s]	T_{xx} [s]	T_{xx} ' [s]	*Tu* [-]	R_{xx}'(max)
10	3.89E-06	-	-	7.18E-05	0	0	0.554297
20	3.89E-06	0.011111	-	0.007616	0	0	0.17553
30	2.67E-05	0.016667	-	0.002427	1.95E-05	0	0.146229
40	3.06E-06	0.011111	-	0	2.67E-05	0	0.547374
50	2.5E-05	-	-	0.000152	0	0	0.273224
60	2.5E-05	0.022222	-	0.001195	0	0	0.024484
67	0.090636	-	-	0.000162	2.63E-05	0	0.087763
74	1.47E-05	0.016667	-	0.000464	0.001115	0	0.209197
81	8.28E-05	0.072222	1.181818	0.001603	0.000546	0.093798	0.423177
88	0.000199	0.216667	1.666667	0.002777	0.003171	0.559197	0.455579
92	0.000802	0.622222	1.733333	0.004727	0.004373	1.092054	0.555912
95	0.000487	0.388889	1.511628	0.004872	0.004874	0.539818	0.575444
102	0.002436	1.188889	2.280702	0.007595	0.006477	2.051045	0.639117
105	0.011067	4.361111	1.911765	0.012577	0.009711	2.219729	0.578664
109	0.005626	2.172222	2.063492	0.012509	0.009913	1.924774	0.595275
112	0.036158	7.394444	2.131148	0.016711	0.01309	2.205068	0.599969
114	0.051129	3.194444	2.6	0.013878	0.01058	2.942639	0.496897
116	0.113078	12.77778	2	0.034561	0.027177	-	0.642153
123	0.139361	10.8	1.911765	0.037415	0.031011	-	0.640077
127	0.275109	17.28333	2.241379	0.046278	0.039891	-	0.696799
130	0.379165	22.72222	1.857143	0.04395	0.03922	-	0.698825
134	0.507649	22.75556	2.45283	0.045742	0.040968	-	0.694932
144	0.668545	19.45556	2.653061	0.043577	0.040045	-	0.672924
148	0.711241	20.67778	3.023256	0.041922	0.039227	-	0.653909
152	0.678334	18.85	3.095238	0.047115	0.044109	-	0.688791
160	0.880451	9.533333	3.611111	0.037979	0.036857	-	0.633993
170	0.883833	8.705556	3.513514	0.036739	0.035071	-	0.615616
180	0.925074	6.777778	4.0625	0.032858	0.030016	-	0.613253
190	0.96017	4.355556	4.814815	0.02724	0.025586	-	0.599472
200	0.962422	3.683333	2.888889	0.025882	0.023811	-	0.55899
210	0.97137	3.255556	3.023256	0.023051	0.021204	-	0.525216
220	0.98171	2.405556	3.421053	0.019023	0.017043	-	0.489997

Appendix B: Two-phase flow data of hydraulic jumps

Fr_1 = 1.96, Q = 0.07 m^3/s, Re_1=1.6×10^5, h = 0.06 m; d_1=0.083 m: x-x_1 = 0.3 m

Y (mm)	*C* [-]	*F* [Hz]	*V* [m/s]	T_{xx} [s]	T_{xx} ' [s]	*Tu* [-]	R_{xx}'(max)
10	2.06E-05	0.016667	-	0	0	0	0.356462
20	9.17E-06	0.011111	-	8.63E-05	4.28E-05	0	0.398101
30	8.61E-06	0.03	-	0.0004	1.79E-05	0	0.214605
40	0.000148	0.05	-	0.004235	3.89E-05	0	0.128303
50	3.94E-05	0.016667	-	0.000275	0.000189	0	0.480265
60	9.89E-05	0.038889	-	0.005456	0.000169	0	0.29762
70	0.00013	0.061111	1.397849	0.005591	0.00554	2.19E-08	0.129635
90	0.000185	0.111111	1.083333	0.004872	0	0.427721	0.096813
100	0.088339	-	1.3	0.00404	0.003294	1.883673	0.164613
110	0.063021	-	1.428571	0.003311	0.001666	0.394103	0.180167
120	0.022888	-	1.413043	0.0042	0.002637	1.214078	0.283869
125	0.032269	-	1.666667	0.006602	0.006051	2.02649	0.338318
130	0.003292	1.038889	1.585366	0.009204	0.004354	1.364861	0.41911
135	0.007229	1.933333	1.604938	0.008886	0.007197	1.704948	0.444481
140	0.008015	2.194444	1.566265	0.008678	0.007921	2.109107	0.460401
145	0.014318	3.444444	1.494253	0.012387	0.01144	2.826056	0.504127
150	0.015562	3.822222	1.566265	0.010286	0.009005	2.122151	0.54143
155	0.020801	3.816667	1.494253	0.01498	0.014399	2.774962	0.596982
160	0.028581	6.105556	1.547619	0.01239	0.012415	2.480594	0.580548
165	0.036561	7.216667	1.547619	0.014032	0.013879	2.67718	0.618871
170	0.045558	9.105556	1.64557	0.014404	0.013763	2.895846	0.604072
175	0.075078	12.17778	1.625	0.016155	0.016411	3.02397	0.65918
180	0.078096	13.15556	1.625	0.018489	0.018471	3.151861	0.678869
185	0.159067	16.66667	1.666667	0.025968	0.024664	3.848461	0.699541
190	0.110583	16.55	1.625	0.020712	0.020404	3.341733	0.683312
195	0.162407	21.01111	1.585366	0.021412	0.021217	3.251097	0.695261
200	0.151394	22.42222	1.547619	0.019629	0.019722	2.701376	0.689678
205	0.199808	26.12222	1.604938	0.020261	0.020443	3.063049	0.712978
210	0.246505	28.30556	1.666667	0.021855	0.022027	3.186916	0.720536
214	0.379924	34.21111	1.666667	0.022603	0.022057	3.165197	0.724873
217	0.377304	31.80556	1.666667	0.024451	0.024494	-	0.730674
235	0.513117	35.14444	1.688312	0.023703	0.022949	-	0.717313
245	0.669359	29.57222	1.688312	0.024271	0.022887	-	0.702006
255	0.722845	25.36667	1.710526	0.024437	0.023479	-	0.695993
265	0.832082	17.26111	1.733333	0.023154	0.021688	-	0.678611
275	0.850431	16.82222	1.604938	0.021256	0.020587	-	0.673532
285	0.932103	8.227778	1.64557	0.019401	0.01762	-	0.648835
295	0.945776	5.794444	1.566265	0.020235	0.018773	-	0.677658
305	0.971485	3.461111	1.604938	0.016426	0.015881	-	0.611355

Appendix B: Two-phase flow data of hydraulic jumps

Fr_1 = 1.96, Q = 0.07 m^3/s, Re_1=1.6×10^5, h = 0.06 m; d_1=0.083 m: x-x_1 = 0.45 m

Y (mm)	*C* [-]	*F* [Hz]	*V* [m/s]	T_{xx} [s]	T_{xx} ' [s]	*Tu* [-]	R_{xx}'(max)
10	9.06E-05	0.011111	-	0.004312	0	0	0.016935
25	3.28E-05	0.011111	-	0.001658	1.51E-07	0	0.005518
40	0.000135	0.05	-	0.003014	0	0	0.035562
55	4.08E-05	-	-	0.000489	1.03E-06	0	0.032683
70	8.47E-05	0.066667	-	0.000994	0.000748	0	0.046084
85	8.5E-05	0.061111	-	0.001069	0.000435	0.12765	0.147306
100	0.00145	0.644444	0.347594	0.002288	0.000459	0.14971	0.071816
110	0.001733	0.816667	0.860927	0.002789	0.001081	0.282913	0.162778
120	0.001903	1	1.3	0.002072	0.001018	0.469595	0.165667
130	0.002981	1.477778	0.849673	0.002467	0.001861	0.650337	0.180243
140	0.004675	2.094444	0.928571	0.003394	0.003058	0.794156	0.254246
150	0.006721	2.805556	1.065574	0.004178	0.002641	0.816004	0.216476
160	0.009399	3.661111	1.287129	0.005132	0.00405	1.113729	0.303234
168	0.017526	5.7	1.287129	0.007704	0.0067	1.352115	0.436748
176	0.023269	8.4	1.262136	0.006491	0.005862	1.130162	0.45999
184	0.034568	9.516667	1.340206	0.010921	0.010614	1.6682	0.542523
192	0.061592	14.94444	1.460674	0.016133	0.015661	2.141501	0.651842
200	0.078826	17.98889	1.444444	0.01764	0.017628	2.182657	0.674606
208	0.120238	21.72222	1.511628	0.021309	0.02154	2.71762	0.725645
216	0.153328	25.80556	1.529412	0.02171	0.021463	2.611613	0.747993
224	0.240132	31.31111	1.529412	0.028986	0.028608	-	0.789214
232	0.28275	31.83333	1.511628	0.032184	0.031633	-	0.8068
240	0.403217	33.14444	1.547619	0.035212	0.034584	-	0.821052
250	0.44834	31.2	1.511628	0.038953	0.037814	-	0.828626
260	0.552189	29.6	1.494253	0.038877	0.037124	-	0.826098
270	0.697502	22.68333	1.511628	0.040019	0.038014	-	0.834226
280	0.731019	21.16111	1.460674	0.03891	0.037034	-	0.829067
290	0.761139	19.01667	1.368421	0.037633	0.035674	-	0.823639
300	0.872499	11.78889	1.382979	0.037514	0.033397	-	0.817044
310	0.941477	6.144444	1.368421	0.02827	0.025753	-	0.810492
315	0.968001	3.777778	1.428571	0.02619	0.022394	-	0.808244

Appendix B: Two-phase flow data of hydraulic jumps

Fr_1 = 1.96, Q = 0.07 m^3/s, Re_1=1.6×10^5, h = 0.06 m; d_1=0.083 m: x-x_1 = 0.6 m

Y (mm)	*C* [-]	*F* [Hz]	*V* [m/s]	T_{xx} [s]	T_{xx} ' [s]	*Tu* [-]	R_{xx}'(max)
10	0.0001	-	-	0.005578	1.46E-05	0	0.255883
20	0.0001	-	-	0.004114	1.78E-05	0	0.075551
30	0.0002	-	-	0.003634	2.92E-06	0	0.027755
40	0.0003	597.8722	0.747126	0.00294	0	0.086803	0.06867
50	0.000419	0.177778	0.764706	0.001753	0	0.171447	0.069417
60	0.000646	0.227778	-	0.002194	8.27E-05	0	0.018697
70	0.000611	0.244444	-	0.002026	0.000547	1.07784	0.092124
78	0.000755	0.338889	0.677083	0.001654	0.000645	0.585113	0.090862
86	0.000921	0.422222	0.860927	0.001469	0.000389	0.691363	0.057659
94	0.002408	0.888889	0.695187	0.002719	0.001418	0.497933	0.202028
102	0.001767	0.727778	0.822785	0.001954	0.000431	0.693592	0.07309
110	0.002147	0.911111	0.849673	0.002094	0.000635	0.342103	0.148586
118	0.002339	1.038889	0.935252	0.0019	0.000673	0.624205	0.119331
126	0.003332	1.577778	0.992366	0.002162	0.001424	0.544324	0.195546
134	0.004737	1.988889	1.27451	0.002985	0.001679	0.731537	0.268691
142	0.006244	3.094444	1.171171	0.003154	0.002594	0.861093	0.244991
150	0.007037	3.483333	1.238095	0.003104	0.002047	0.434947	0.288764
158	0.008781	4.205556	1.287129	0.003195	0.00262	0.664246	0.321137
166	0.013219	6.1	1.287129	0.003443	0.002709	0.630525	0.368093
174	0.012484	6.15	1.368421	0.0039	0.003139	0.501002	0.396846
182	0.024516	11.07222	1.477273	0.005658	0.005273	0.683462	0.496564
190	0.035161	14.5	1.529412	0.007937	0.007575	0.932761	0.562879
198	0.051176	17.96667	1.566265	0.010299	0.010187	0.990517	0.619424
206	0.088183	22.1	1.585366	0.019614	0.019195	1.874955	0.701186
214	0.115133	25.67778	1.585366	0.021745	0.021181	2.207965	0.73065
222	0.240081	35.28889	1.625	0.032287	0.031841	-	0.805743
230	0.242444	34.51667	1.585366	0.030233	0.02995	-	0.786132
240	0.418061	35.63889	1.625	0.036698	0.035937	-	0.840476
250	0.520244	30.88889	1.604938	0.038942	0.037687	-	0.847912
260	0.668359	27.83889	1.625	0.035109	0.033515	-	0.839708
270	0.769927	20.59444	1.64557	0.035367	0.033692	-	0.844924
280	0.811841	18.10556	1.64557	0.034155	0.031599	-	0.843495
290	0.93728	6.344444	1.64557	0.029538	0.027041	-	0.815318
300	0.954084	4.788889	1.710526	0.027101	0.024515	-	0.794466
310	0.970683	21.93889	1.566265	0.024675	0.022651	-	0.783627

Appendix B: Two-phase flow data of hydraulic jumps

Fr_1 = 1.96, Q = 0.07 m^3/s, Re_1=1.6×10^5, h = 0.06 m; d_1=0.083 m: x-x_1 = 0.8 m

Y (mm)	*C* [-]	*F* [Hz]	*V* [m/s]	T_{xx} [s]	T_{xx} ' [s]	*Tu* [-]	R_{xx}'(max)
10	0.0001	-	5.909091	2.43E-05	0	0	0.582859
20	0.0003	-	-7.22222	0.002185	4.97E-05	0	0.174421
30	0.0004	-	-10.8333	0.004661	2.36E-05	0	0.139903
40	0.000597	0.183333	0.8125	0.002647	0	1.04003	0.079751
50	0.000932	0.338889	0.698925	0.00214	0.000779	0.410756	0.13559
60	0.001018	0.35	0.844156	0.001986	0	0.421715	0.046739
70	0.001601	0.638889	1.140351	0.00195	0.000639	0.953641	0.07302
80	0.029498	-	0.902778	0.001429	0	0.411989	0.07293
90	0.036318	-	0.915493	0.001611	0.000741	0.308623	0.085163
100	0.000949	0.494444	1.083333	0.001551	0.000669	0.574906	0.138016
110	0.001163	0.766667	1.031746	0.001266	0.000501	0.503975	0.109974
120	0.001686	1.127778	1.111111	0.001278	0.000402	0.309359	0.147667
130	0.002271	1.444444	1.25	0.001463	0.000716	0.45706	0.192566
140	0.003331	2.35	1.340206	0.001392	0.000779	0.298804	0.263143
150	0.004541	3.011111	1.397849	0.001711	0.001166	0.332833	0.309529
160	0.005777	4.244444	1.529412	0.001632	0.001206	0.340988	0.307219
170	0.008509	5.961111	1.64557	0.002642	0.002105	0.41005	0.371896
180	0.018513	10.15	1.688312	0.00859	0.008241	0.961202	0.537767
190	0.134383	26.82222	1.780822	0.038394	0.037259	-	0.808668
200	0.289152	35.15	1.756757	0.044107	0.04275	-	0.839612
210	0.480346	38.06667	1.710526	0.04425	0.042869	-	0.837181
220	0.698452	31.47778	1.688312	0.044956	0.043939	-	0.829541
230	0.861907	17.70556	1.688312	0.037976	0.037295	-	0.807846
240	0.920638	12.8	1.585366	0.032891	0.032769	-	0.764346
250	0.97617	5.122222	1.444444	0.023536	0.022153	-	0.67564
260	0.991598	2.227778	1.511628	0.017637	0.016307	-	0.619101

Appendix B: Two-phase flow data of hydraulic jumps

Fr_1 = 1.96, Q = 0.07 m^3/s, Re_1=1.6×10^5, h = 0.06 m; d_1=0.083 m: x-x_1 = 1.1 m

Y (mm)	*C* [-]	*F* [Hz]	*V* [m/s]	T_{xx} [s]	T_{xx} ' [s]	*Tu* [-]	R_{xx}'(max)
10	0.00001	-	-	0.004577	1.13E-05	0	0.185837
20	0.0001	-	-	0.004058	0.006388	0	0.356546
30	0.0002	-	-	0.00044	0	0	0.341723
40	0.0003	-	-	9.98E-05	0	0	0.274584
50	0.000379	0.133333	0.948905	0.001574	0.000291	0.302273	0.097003
60	0.000386	0.133333	0.604651	0.001705	0	0.097357	0.066199
70	0.000521	0.244444	1.111111	0.001942	0.000262	0.498858	0.079331
80	0.000422	0.25	0.970149	0.001266	0.000527	0.109998	0.097265
90	0.00026	0.15	0.833333	0.001002	0	0	0.051405
100	0.000506	0.338889	0.915493	0.001109	0.000395	0.140803	0.141838
107	0.000667	0.5	1.313131	0.00108	0.000269	0.333807	0.070045
114	0.001062	0.55	0.849673	0.001581	0.000647	0.385353	0.121033
121	0.000824	0.5	1.25	0.00117	0.000131	0.240521	0.059795
128	0.00096	0.711111	1.203704	0.001208	0.000515	0.614207	0.125044
135	0.000999	0.838889	1.340206	0.001009	0.000311	0.563878	0.06021
142	0.001352	0.972222	1.397849	0.001889	0.000798	0.43027	0.144516
149	0.00195	1.611111	1.566265	0.001148	0.000593	0.371238	0.21609
156	0.001776	1.438889	1.444444	0.001427	0.001227	0.504523	0.194688
163	0.003229	2.222222	1.460674	0.003297	0.002299	0.608359	0.269226
170	0.003708	2.222222	1.444444	0.003225	0.002125	0.558038	0.232144
177	0.04947	8.361111	1.547619	0.020413	0.019014	2.754147	0.590863
184	0.008085	3.844444	1.368421	0.007249	0.005742	1.44999	0.370994
191	0.010058	4.805556	1.287129	0.006031	0.004906	0.91558	0.374734
198	0.021921	6.7	1.382979	0.012211	0.010079	2.28779	0.443267
205	0.022291	7.183333	1.340206	0.013897	0.012313	2.25285	0.476296
212	0.081185	12.58333	1.262136	0.024465	0.021328	2.866664	0.611359
219	0.106829	14.63889	1.3	0.031112	0.027335	-	0.667234
226	0.155385	18.15	1.368421	0.036183	0.033845	-	0.731463
233	0.313734	20.40556	1.287129	0.048789	0.046073	-	0.793205
240	0.245951	19.41667	1.262136	0.046183	0.043127	-	0.774084
250	0.459935	20.02778	1.238095	0.054731	0.051687	-	0.824023
260	0.559942	20.67778	1.192661	0.053524	0.050178	-	0.807876
270	0.733332	16.43333	1.238095	0.04702	0.044588	-	0.776704
280	0.808477	13.44444	1.065574	0.047751	0.044906	-	0.793371
290	0.8679	12.08889	1.065574	0.036621	0.033811	-	0.730195
300	0.956137	4.355556	1.192661	0.0316	0.029475	-	0.685376
310	0.980884	2.383333	0.902778	0.022369	0.019166	-	0.578113

Appendix B: Two-phase flow data of hydraulic jumps

Fr_1 = 2.84, Q = 0.1 m^3/s, Re_1=2.2×10^5, h = 0.06 m; d_1=0.082 m: x-x_1 = -0.3 m

Y (mm)	*C* [-]	*F* [Hz]	*V* [m/s]	T_{xx} [s]	T_{xx} ' [s]	*Tu* [-]	R_{xx}'(max)
5	0.000583	1.366667	2.407407	0.00061	0.000241	0.288872	0.160306
10	0.000493		2.6	0.001602	0.000452	0.690307	0.140997
15	0.000927	1.777778	2.407407	0.00078	0.000601	0.533027	0.227022
20	0.001936	3.644444	3.095238	0.001418	0.001043	0.515784	0.287263
25	0.002358	4.188889	3.25	0.001002	0.000904	0.586511	0.324994
30	0.004013	5.544444	3.333333	0.001916	0.001817	0.599965	0.469164
35	0.007029	9.166667	3.421053	0.003286	0.003127	0.529956	0.547228
40	0.01194	12.05556	3.513514	0.004277	0.004454	0.556296	0.588554
45	0.014221	12.36667	3.421053	0.003967	0.004508	0.615753	0.587953
50	0.030498	18.38889	3.513514	0.010858	0.012505	1.104	0.623014
55	0.070334	28.12222	3.611111	0.018461	0.018861	2.332357	0.70027
60	0.147868	39.58889	3.611111	0.023318	0.022471	3.526317	0.766804
61	0.165736	43.54444	3.611111	0.025677	0.024241	3.395371	0.759747
62	0.184721	47.05556	3.611111	0.028035	0.027215	3.658075	0.795077
63	0.212791	47.54444	3.611111	0.027621	0.026157	3.864073	0.789846
64	0.25476	51.44444	3.611111	0.028208	0.026694	-	0.811957
65	0.253607	53.14444	3.611111	0.029382	0.028538	-	0.804331
66	0.293117	51.15556	3.714286	0.030434	0.029449	-	0.837575
67	0.330835	49.62222	3.714286	0.03662	0.034946	-	0.841837
68	0.381496	54.14444	3.714286	0.036168	0.035199	-	0.853676
69	0.39838	55.87778	3.714286	0.033313	0.03198	-	0.852239
70	0.453006	55.03333	3.714286	0.034697	0.033632	-	0.861453
71	0.479434	51.44444	3.714286	0.036208	0.035107	-	0.87255
72	0.534335	52.6	3.714286	0.035539	0.033911	-	0.870996
73	0.577674	53.08889	3.714286	0.036204	0.034303	-	0.878707
74	0.638156	49.77778	3.714286	0.035293	0.033632	-	0.878565
75	0.655515	53.07778	3.714286	0.033664	0.031983	-	0.878297
76	0.659151	44.98889	3.714286	0.03489	0.033656	-	0.892939
77	0.707541	43	3.714286	0.033595	0.032423	-	0.885157
78	0.70669	44.03333	3.611111	0.032085	0.03095	-	0.890896
79	0.784863	39.26667	3.611111	0.031747	0.030809	-	0.888894
80	0.81645	42.33333	3.714286	0.026695	0.0257	-	0.878307
81	0.817759	36.11111	3.611111	0.02673	0.025509	-	0.894265
82	0.802512	37.45556	3.611111	0.025125	0.024688	-	0.903413
83	0.811057	39.46667	3.513514	0.019813	0.019399	-	0.905219
84	0.894087	29.86667	3.513514	0.01734	0.016921	-	0.885437
85	0.874727	37.36667	3.513514	0.013682	0.013377	-	0.881122
86	0.876792	30.43333	3.421053	0.016382	0.015822	-	0.89897
87	0.905588	28.45556	3.421053	0.014075	0.013871	-	0.88348
88	0.919787	24.72222	3.421053	0.010712	0.010609	-	0.887806
89	0.95858	15.33333	3.611111	0.013155	0.013131	-	0.869682
90	0.960757	11.93333	3.714286	0.017875	0.01762	-	0.878503
91	0.977943	8.255556	3.714286	0.014427	0.01445	-	0.853668

92	0.979179	8.588889	3.714286	0.011956	0.011863	-	0.844652
93	0.977991	7.588889	3.714286	0.014447	0.014124	-	0.876267

Appendix B: Two-phase flow data of hydraulic jumps

Fr_1 = 2.84, Q = 0.1 m^3/s, Re_1=2.2×10^5, h = 0.06 m; d_1=0.082 m: x-x_1 = 0.1 m

Y (mm)	*C* [-]	*F* [Hz]	*V* [m/s]	T_{xx} [s]	T_{xx} ' [s]	*Tu* [-]	R_{xx}'(max)
10	0.000199	0.3		0.000645	0	5.02E-09	0.05228
15	0.00027	0.611111	2.241379	0.000385	0	0.117379	0.12696
20	0.000269	0.9	3.023256	0.000277	0.000121	0.4443	0.087532
25	0.000601	1.544444	2.888889	0.000598	0.000335	0.938723	0.105648
30	0.001011	2.188889	2.6	0.000617	0.000442	0.263673	0.279517
35	0.002323	3.977778	2.954545	0.001862	0.001778	1.033608	0.407358
40	0.003499	5.444444	2.708333	0.002705	0.002613	0.851	0.439993
45	0.006318	10.44444	2.888889	0.00259	0.002317	1.131036	0.388356
50	0.007864	10.88889	3.023256	0.002956	0.003287	1.167987	0.544654
55	0.01689	20.23333	3.095238	0.004405	0.004107	1.540038	0.554531
60	0.024498	28.32222	3.170732	0.003453	0.00333	1.415834	0.570452
63	0.034678	33.97778	3.095238	0.005053	0.004953	1.826608	0.594992
66	0.047014	46.32222	3.023256	0.0044	0.004433	1.720767	0.58769
69	0.062865	53.96667	3.023256	0.004788	0.004716	1.744727	0.617524
72	0.079049	64.18889	3.023256	0.005163	0.004824	1.826758	0.605384
75	0.098624	72.4	3.095238	0.005469	0.005245	2.064826	0.618401
78	0.141029	90.41111	3.095238	0.00543	0.005311	1.982874	0.633157
81	0.176528	106.4333	3.023256	0.005568	0.005394	2.162264	0.62939
84	0.193473	111.4333	2.954545	0.00678	0.006565	2.223195	0.612593
87	0.247287	124.0333	3.023256	0.006702	0.006103	2.374801	0.601924
90	0.300115	130.8667	2.954545	0.006486	0.006078	2.382075	0.605277
93	0.307293	130.5667	2.888889	0.007351	0.006878	2.483987	0.601405
96	0.366468	124.6667	2.826087	0.008325	0.00781	2.645241	0.578991
99	0.338785	103.8222	2.765957	0.010409	0.009042	3.200069	0.570921
102	0.335604	92.12222	2.888889	0.011777	0.01045	3.832942	0.562896
105	0.332708	83.15556	2.765957	0.012131	0.010247	-	0.540484
108	0.341177	79.93333	2.765957	0.014259	0.012053	-	0.544048
111	0.311441	82.48889	2.45283	0.012845	0.011226	-	0.530005
114	0.326846	74	2.5	0.016871	0.014219	-	0.533231
117	0.336679	55.93333	2.6	0.021804	0.018287	-	0.547772
120	0.313765	51.23333	2.653061	0.022633	0.019062	-	0.526902
123	0.252812	46.65556	2.765957	0.020742	0.017975	-	0.512263
130	0.262966	36.57778	-	0.026596	0.022903	-	0.496933
140	0.245427	34.36667	-2.20339	0.022759	0.020124	-	0.486975
150	0.319693	31.52222	-1.52941	0.029043	0.026969	-	0.5576
160	0.30908	23.2	-1.41304	0.029091	0.02541	-	0.598724
170	0.474712	22.53333	-1.44444	0.032136	0.030539	-	0.628367
180	0.616179	19.35556	-1.26214	0.033	0.03193	-	0.639897
190	0.815611	12.55556	-2.13115	0.031082	0.030227	-	0.636584
200	0.888491	7.8	-1.73333	0.035472	0.033127	-	0.625323
210	0.912486	7.355556	-2.09677	0.030853	0.027534	-	0.573712
220	0.934188	5.522222	-1.41304	0.032625	0.029772	-	0.593724
230	0.934293	4.722222	-1.25	0.033378	0.029029	-	0.641569

240	0.963671	3.333333	-1.31313	0.029694	0.027583	-	0.554845
250	0.982083	2.177778	-1.54762	0.027927	0.023144	-	0.523387

Appendix B: Two-phase flow data of hydraulic jumps

Fr_1 = 2.84, Q = 0.1 m^3/s, Re_1=2.2×10^5, h = 0.06 m; d_1=0.082 m: x-x_1 = 0.15 m

Y (mm)	*C* [-]	*F* [Hz]	*V* [m/s]	T_{xx} [s]	T_{xx} ' [s]	*Tu* [-]	R_{xx}'(max)
10	0.000638	1.322222	1.3	0.000484	0.00014	0.131836	0.055855
15	0.000912	1.922222	2.5	0.000731	0.000478	0.708075	0.127546
20	0.001002	2.166667	2.407407	0.000767	0.000442	0.859711	0.146239
25	0.001871	4.122222	2.653061	0.000932	0.000643	0.556026	0.167116
30	0.002382	4.7	2.888889	0.001247	0.001401	0.68316	0.311535
35	0.004036	7.288889	2.826087	0.001868	0.001808	0.697379	0.38497
40	0.004366	8.1	2.954545	0.001876	0.001875	0.808857	0.383073
45	0.010399	16.3	2.888889	0.002877	0.002987	1.389677	0.479969
50	0.020184	26.93333	2.888889	0.004365	0.004308	1.55267	0.541582
55	0.034206	35.84444	3.023256	0.004802	0.004929	1.784129	0.609194
60	0.049896	49.61111	3.023256	0.004736	0.004877	1.840109	0.605025
63	0.04097	44.83333	2.954545	0.005349	0.004844	1.838811	0.590487
66	0.054924	53.68889	3.095238	0.004924	0.005017	1.925947	0.610436
69	0.070853	65.46667	3.023256	0.005438	0.005318	1.950664	0.615723
72	0.08532	80.32222	2.888889	0.004907	0.004917	1.852034	0.588153
75	0.106558	90.36667	2.954545	0.004972	0.00519	2.023322	0.616549
78	0.133862	102.0778	3.023256	0.005443	0.005695	2.230737	0.624114
81	0.158374	111.5667	2.888889	0.005938	0.005759	2.203124	0.626657
84	0.176703	121.0111	2.826087	0.005515	0.005308	2.222465	0.592378
87	0.208798	132.3444	2.888889	0.005419	0.005417	2.231191	0.594266
90	0.261661	137.9556	2.954545	0.006183	0.006132	2.477222	0.61091
93	0.291507	140.7333	2.765957	0.005944	0.005889	2.299439	0.58359
96	0.326279	136.3333	2.765957	0.006705	0.006308	2.524331	0.572614
99	0.352573	134.0778	2.708333	0.007554	0.006988	2.823283	0.561102
102	0.357796	122.6444	2.5	0.009132	0.008864	2.94345	0.552004
105	0.335568	127.7444	2.54902	0.008742	0.00817	2.931898	0.538876
108	0.364098	112.3333	2.54902	0.011022	0.010302	3.852145	0.528196
111	0.362865	105.0333	2.6	0.01134	0.010469	3.881269	0.52075
114	0.362479	98.42222	2.407407	0.01309	0.011707	3.782715	0.514221
117	0.337626	86.33333	2.407407	0.014176	0.011756	-	0.488452
120	0.329691	83.36667	2.20339	0.014806	0.013186	-	0.485658
125	0.317367	71.54444	2.54902	0.016647	0.014381	-	0.480505
130	0.307817	57.84444	-	0.02206	0.019737	-	0.480846
135	0.297893	50.76667	-	0.022845	0.019951	-	0.477625
140	0.288311	50.14444	-	0.022269	0.019652	-	0.464554
145	0.299377	46.88889	-	0.022402	0.020978	-	0.486737
150	0.243176	44.91111	-	0.0196	0.018156	-	0.440093
155	0.270978	43.68889	-1.54762	0.023271	0.023491	-	0.496697
160	0.345447	43.77778	-1.66667	0.024693	0.02343	-	0.530791
165	0.334318	43.2	-1.2381	0.025688	0.023846	-	0.544491
170	0.341071	39.42222	-1.36842	0.025987	0.026656	-	0.572408
180	0.528447	43.18889	-1.18182	0.031877	0.031513	-	0.626437
190	0.664827	29.85556	-1.39785	0.031581	0.031409	-	0.657975

200	0.734936	28.58889	-1.18182	0.034293	0.034471	-	0.644218
210	0.765676	25.02222	-1.26214	0.032089	0.032518	-	0.637976
220	0.910448	12.43333	-1.68831	0.028499	0.028964	-	0.603446
230	0.920294	10.58889	-1.34021	0.032842	0.030914	-	0.623415
240	0.937427	7.877778	-1.47727	0.032902	0.031104	-	0.62031
250	0.951877	5.588889	-	0.029794	0.026438	-	0.595742
260.02	0.98438	2.333333	-0.78313	0.019676	0.017502	-	0.418462

Appendix B: Two-phase flow data of hydraulic jumps

Fr_1 = 2.84, Q = 0.1 m^3/s, Re_1=2.2×10^5, h = 0.06 m; d_1=0.082 m: x-x_1 = 0.3 m

Y (mm)	*C* [-]	*F* [Hz]	*V* [m/s]	T_{xx} [s]	T_{xx} ' [s]	*Tu* [-]	R_{xx}'(max)
10	0.001772	2.688889	-	0.001216	0.000271	0.474961	0.063068
17	0.002233	4.111111	-	0.00078	0.000551	1.047366	0.081162
24	0.002966	5.844444	2.131148	0.001564	0.001312	0.815497	0.196299
31	0.004693	8.466667	2.280702	0.00221	0.002074	0.76186	0.27802
38	0.006833	11.96667	2.5	0.002642	0.00226	1.19993	0.285284
45	0.01168	19.34444	2.45283	0.002467	0.002585	1.174988	0.333026
52	0.016599	24.6	2.6	0.003117	0.002801	1.302781	0.399546
59	0.030796	39.84444	2.54902	0.003756	0.003537	1.484985	0.452962
65	0.049738	57.55556	2.653061	0.004311	0.004286	1.640732	0.474143
70	0.061116	65.77778	2.45283	0.005046	0.004752	1.785896	0.452345
75	0.075737	78.01111	2.5	0.004405	0.004233	1.773588	0.455017
80	0.092277	88.27778	2.45283	0.004514	0.004458	1.761842	0.483955
85	0.153461	115.7333	2.5	0.005317	0.005116	2.129325	0.511608
90	0.176671	119.5889	2.45283	0.00554	0.005265	2.246835	0.493012
95	0.199307	122.5667	2.321429	0.005924	0.005284	2.259929	0.475316
100	0.221213	115.4	2.280702	0.006577	0.006346	2.625061	0.489045
105	0.15173	99.78889	2.241379	0.005891	0.005329	2.238685	0.449119
110	0.167929	99.85556	2.166667	0.006923	0.00628	2.288752	0.441534
115	0.162756	104.1778	2.03125	0.005935	0.00512	2.103219	0.402848
120	0.245821	106.5889	2.03125	0.009631	0.008741	3.072557	0.447756
125	0.212509	104.5667	1.940299	0.007691	0.006851	2.709291	0.399368
130	0.252474	89.55556	2.03125	0.012895	0.011136	4.183764	0.446673
135	0.211964	85.22222	2.20339	0.00973	0.008437	3.729615	0.384632
140	0.212366	75.2	2	0.013029	0.010529	3.846198	0.389869
145	0.211078	65.46667	2.166667	0.014858	0.012896	-	0.417133
150	0.187883	57.77778	2.063492	0.013705	0.011601	-	0.390137
155	0.165196	48.01111	2.131148	0.014898	0.012142	-	0.389369
160	0.156053	46.07778	-	0.016798	0.013725	-	0.380597
165	0.152673	43.65556	-	0.016915	0.013644	-	0.37078
170	0.146949	36.28889	-	0.018987	0.01663	-	0.409316
175	0.119057	30.01111	-	0.01827	0.015458	-	0.411143
180	0.132361	29.64444	-2.16667	0.019603	0.018437	-	0.416191
185	0.139128	28.86667	-2.45283	0.022682	0.020453	-	0.433219
190	0.125627	25.75556	-1.54762	0.021092	0.018985	-	0.444766
200	0.154683	25.47778	-1.46067	0.026534	0.026409	-	0.524778
210	0.199359	26.9	-2.45283	0.028908	0.027179	-	0.559586
220	0.290969	29.35556	-1.46067	0.036527	0.036784	-	0.641878
230	0.531151	28.74444	-1.88406	0.040369	0.040394	-	0.677281
240	0.65002	24.88889	-1.66667	0.040795	0.041722	-	0.707679
250	0.764585	17.57778	-2.03125	0.043207	0.044386	-	0.726738
260	0.836516	14.21111	-	0.04138	0.042013	-	0.701554
270	0.878936	10.88889	-2.24138	0.038318	0.038823	-	0.674081
280	0.926063	7.533333	-1.58537	0.036507	0.038003	-	0.678742

290	0.95683	5.255556	-1.85714	0.031139	0.030187	-	0.605558
300	0.968797	3.822222	-	0.027689	0.026016	-	0.586354

Appendix B: Two-phase flow data of hydraulic jumps

Fr_1 = 2.84, Q = 0.1 m^3/s, Re_1=2.2×10^5, h = 0.06 m; d_1=0.082 m: x-x_1 = 0.45 m

Y (mm)	*C* [-]	*F* [Hz]	*V* [m/s]	T_{xx} [s]	T_{xx} ' [s]	*Tu* [-]	R_{xx}'(max)
8	0.001749	2.466667	0.955882	0.000892	0.00012	0.234129	0.051712
15	0.002837	3.8	1.529412	0.000999	0.00049	0.621052	0.093211
22	0.003212	4.911111	1.529412	0.000935	0.000823	0.855171	0.10523
29	0.004649	7.344444	2	0.001469	0.001208	0.893832	0.170504
36	0.006394	11.01111	2.241379	0.001301	0.001118	0.766344	0.191229
43	0.008094	14.15556	2.096774	0.001614	0.001291	0.714402	0.219752
50	0.011782	18.83333	2.20339	0.002497	0.002159	0.836079	0.280003
57	0.015214	24.62222	2.20339	0.002544	0.002504	1.113807	0.291384
63	0.031323	42.92222	2.321429	0.003017	0.00292	1.26112	0.35519
68	0.034868	46.96667	2.321429	0.003402	0.003239	1.35103	0.346395
73	0.040318	51.43333	2.241379	0.00318	0.003063	1.289587	0.33942
78	0.043874	54.86667	2.241379	0.003404	0.003056	1.319294	0.34096
83	0.054376	63.48889	2.131148	0.003755	0.003651	1.504168	0.360108
88	0.059434	67.67778	2.131148	0.003676	0.003446	1.502031	0.344916
93	0.060966	66.1	2.20339	0.004074	0.003816	1.698819	0.323948
98	0.072815	76	2.096774	0.003311	0.002923	1.447731	0.324691
103	0.077969	76.71111	2.063492	0.003772	0.003191	1.516021	0.3195
108	0.080581	75.87778	2.063492	0.004263	0.003717	1.639365	0.315881
113	0.113497	90.98889	2	0.005283	0.004298	1.936378	0.357097
118	0.106532	81.91111	1.857143	0.005055	0.004216	1.82272	0.31844
123	0.111012	83.82222	1.756757	0.004928	0.004501	1.898859	0.32308
128	0.100516	73.97778	1.805556	0.004646	0.004129	1.784071	0.294954
133	0.113108	73.64444	1.830986	0.005474	0.00435	2.467003	0.295369
138	0.108489	70.08889	1.688312	0.005252	0.004361	1.972734	0.314331
143	0.116679	67.7	1.911765	0.006058	0.004999	2.593414	0.297934
148	0.119993	66.47778	1.64557	0.006984	0.005108	2.381596	0.294303
153	0.12679	57.54444	1.733333	0.009213	0.007706	3.346786	0.338937
158	0.115788	57.21111	1.625	0.007214	0.00605	2.806527	0.300138
165	0.112384	53.6	2	0.008663	0.006927	3.807746	0.270431
172	0.108478	47.63333	1.547619	0.008054	0.006196	2.950456	0.253198
179	0.115294	44.11111	1.780822	0.01117	0.009038	-	0.287307
186	0.104094	37.71111		0.012219	0.009641	-	0.292367
193	0.093845	33.26667	1.529412	0.012346	0.009785	-	0.276788
200	0.095315	28.74444	2.5	0.015573	0.011287	-	0.288874
208	0.082322	26.52222	2.321429	0.013666	0.010293	-	0.278692
218	0.064856	20.74444	-2.16667	0.013029	0.011603	-	0.256459
228	0.094195	22.28889	-2.03125	0.020891	0.018074	-	0.372671
238	0.084418	19.48889	-2	0.02185	0.01926	-	0.389673
248	0.12336	22	-2.13115	0.027422	0.024992	-	0.48466
258	0.156895	22.64444	-	0.032967	0.031417	-	0.544649
268	0.369175	23.95556	-	0.045408	0.044293	-	0.685015
278	0.565074	20.6	-	0.047212	0.046518	-	0.730497
288	0.823623	12.44444	-	0.044786	0.044789	-	0.718173

298	0.921791	7.077778	-	0.040347	0.040858	-	0.687505
308	0.926649	6.988889	-	0.04428	0.041883	-	0.694608
313	0.955606	4.466667	-	0.036253	0.033886	-	0.668688

Appendix B: Two-phase flow data of hydraulic jumps

Fr_1 = 2.84, Q = 0.1 m^3/s, Re_1=2.2×10^5, h = 0.06 m; d_1=0.082 m: x-x_1 = 0.6 m

Y (mm)	*C* [-]	*F* [Hz]	*V* [m/s]	T_{xx} [s]	T_{xx} ' [s]	*Tu* [-]	R_{xx}'(max)
10	0.002618	1.988889	0.488722	0.001468	0	2.79E-09	0.039938
20	0.004819	4.5	1.354167	0.001552	0.000813	1.286434	0.068669
30	0.005358	5.488889	2.363636	0.001279	0.00054	1.532034	0.059017
40	0.007374	8.4	1.604938	0.001481	0.001163	0.839968	0.117784
50	0.008506	10.63333	1.884058	0.001274	0.000792	1.012911	0.130355
60	0.01312	15.78889	1.884058	0.002117	0.001851	1.036	0.165919
70	0.013899	18.81111	1.733333	0.002001	0.001417	0.784399	0.150226
80	0.018313	24.28889	1.884058	0.001961	0.001588	0.888086	0.194587
90	0.025361	31.03333	1.940299	0.002199	0.00173	1.079776	0.197262
100	0.032519	36.86667	1.911765	0.002504	0.002436	1.327562	0.211569
110	0.034451	37.32222	1.710526	0.002818	0.001925	1.025828	0.202953
120	0.044641	43.98889	1.780822	0.00386	0.003276	1.537734	0.245139
130	0.041574	42.16667	1.566265	0.003521	0.0028	1.207594	0.218481
140	0.051213	44.68889	1.666667	0.003973	0.003306	1.590355	0.224903
150	0.056217	43.7	1.940299	0.003822	0.00299	2.166712	0.195397
160	0.061207	44.3	1.529412	0.004192	0.002505	1.696455	0.166836
170	0.066717	42.9	1.604938	0.004149	0.003448	2.400931	0.179883
180	0.067609	41.16667	1.111111	0.003955	0.002114	1.272344	0.147273
190	0.067525	38.78889	1.733333	0.005701	0.003568	2.806093	0.157731
200	0.062427	32.97778	1.07438	0.005751	0.003564	1.773042	0.15579
210	0.06747	30.92222	1.25	0.007353	0.005217	2.832299	0.176803
220	0.061022	26.72222	0.935252	0.006381	0.003644	2.197216	0.138251
230	0.057885	23.44444	1.111111	0.006914	0.004413	2.799005	0.143321
240	0.055611	22.12222	2.096774	0.007949	0.005173	-	0.163172
250	0.048257	17.74444	1.477273	0.008882	0.006034	-	0.166744
260	0.041616	14.2	1.101695	0.009992	0.005081	-	0.14719
270	0.064861	17.25556	2.131148	0.019663	0.015275	-	0.293187
280	0.145088	17.86667	-	0.04183	0.039976	-	0.614041
290	0.162717	16.51111	-	0.047788	0.045505	-	0.646987
300	0.426006	19.07778	-	0.055483	0.054242	-	0.777738
310	0.512904	16.91111	2.407407	0.057604	0.05732	-	0.79735
320	0.705399	13.06667	1.413043	0.055985	0.054166	-	0.798196
330	0.789157	10.01111	1.710526	0.055133	0.054279	-	0.809258
340	0.865841	6.933333	1.477273	0.054058	0.051513	-	0.791509
350	0.938738	3.677778	1.181818	0.04609	0.04206	-	0.758805
360	0.964582	2.411111	1.604938	0.041628	0.035439	-	0.704022
365	0.972554	2.166667	1.171171	0.040303	0.036579	-	0.66645

Appendix B: Two-phase flow data of hydraulic jumps

Fr_1 = 2.84, Q = 0.1 m^3/s, Re_1=2.2×10^5, h = 0.06 m; d_1=0.082 m: x-x_1 = 0.8 m

Y (mm)	*C* [-]	*F* [Hz]	*V* [m/s]	T_{xx} [s]	T_{xx} ' [s]	*Tu* [-]	R_{xx}'(max)
8	0.001862	1.6	-	0.001099	3.86E-05	0	0.025819
18	0.003048	2.811111	1.056911	0.001051	0	0.39479	0.043145
28	0.003498	4.244444	1.413043	0.000976	0.000236	0.926479	0.043936
38	0.004209	5.3	1.313131	0.001378	0.000662	0.505337	0.089162
48	0.005018	6.655556	1.25	0.000964	0.000384	0.380297	0.079091
58	0.006417	9.222222	1.666667	0.001073	0.000595	0.687865	0.096805
68	0.006763	9.633333	1.688312	0.001255	0.000816	1.010755	0.083127
78	0.009167	13.35556	1.710526	0.001284	0.000776	0.614836	0.12937
88	0.011057	16.24444	1.911765	0.001302	0.000832	0.712679	0.13471
98	0.014803	19.34444	1.604938	0.001405	0.001316	0.745864	0.138073
108	0.015234	20.08889	1.756757	0.00156	0.000769	0.816419	0.125291
118	0.018531	22.96667	1.780822	0.001925	0.001344	1.144103	0.165254
128	0.020285	24.41111	1.585366	0.002008	0.00122	0.870087	0.140704
138	0.024848	28.01111	1.625	0.002055	0.00129	1.289202	0.130078
148	0.030143	31.88889	1.382979	0.002015	0.001273	0.803391	0.130462
158	0.035286	32.16667	1.460674	0.002384	0.001537	1.540459	0.119337
168	0.034788	29.78889	1.428571	0.00246	0.001231	1.524405	0.11252
178	0.034348	26.18889	-	0.002866	0.001729	0.662862	0.087713
188	0.035083	25.77778	1.382979	0.003854	0.00251	2.599701	0.107366
198	0.038863	25.25556	2.20339	0.004197	0.002025	3.109108	0.104539
208	0.036804	23.48889	1.428571	0.003313	0.002141	1.87451	0.107677
218	0.039268	23.26667	1.733333	0.004151	0.002965	3.001445	0.116798
228	0.037383	19.75556	0.992366	0.004211	0.001914	1.893378	0.08869
238	0.034733	18.56667	1.203704	0.004116	0.002583	2.375797	0.102597
248	0.031156	15.18889		0.005107	0.00249	1.713442	0.077976
258	0.030425	13.64444	1.444444	0.006193	0.003025	1.937074	0.114634
268	0.031439	13.68889	-	0.005451	0.003089	-	0.077744
278	0.03006	11.86667	-	0.006997	0.004749	-	0.130948
288	0.029305	9.577778	1.171171	0.011934	0.005395	-	0.134015
298	0.042371	9.377778	-	0.022649	0.017	-	0.321284
308	0.110223	11.26667	1.494253	0.040841	0.036844	-	0.587044
318	0.25528	11.13333	-	0.054202	0.052412	-	0.747881
328	0.401	11.84444	1.382979	0.057331	0.053373	-	0.75632
338	0.575855	10.22222	1.326531	0.058686	0.055746	-	0.812065
348	0.68825	8.844444	1.428571	0.060469	0.058021	-	0.823045
358	0.875509	4.522222	1.07438	0.053033	0.050691	-	0.805114
362	0.892507	4.766667	1.031746	0.051391	0.047454	-	0.796262

Appendix B: Two-phase flow data of hydraulic jumps

Fr_1 = 2.84, Q = 0.1 m^3/s, Re_1=2.2×10^5, h = 0.06 m; d_1=0.082 m: x-x_1 = 1.1 m

Y (mm)	*C* [-]	*F* [Hz]	*V* [m/s]	T_{xx} [s]	T_{xx} ' [s]	*Tu* [-]	R_{xx}'(max)
10	0.001227	0.733333	-	0.001463	0.000284	-0.00929	0.061641
20	0.002301	1.566667	0.77381	0.001436	0.000142	0.166469	0.059299
30	0.003149	2.1	-	0.001605	0.000316	0.191528	0.05696
40	0.003356	2.5	-	0.001582	0.000267	0.366623	0.050952
50	0.00455	3.455556	1.111111	0.001602	0.000441	0.490031	0.064034
60	0.005215	3.977778	0.643564	0.001501	0.000347	0.247235	0.076483
70	0.007054	5.9	1.065574	0.001276	0.000354	0.630687	0.05247
80	0.007748	6.733333	1.688312	0.001579	0.000602	1.077891	0.064783
90	0.006569	6.488889	1.262136	0.00112	0.000442	0.775057	0.071843
100	0.009877	9.866667	1.150442	0.001177	0.000527	0.493437	0.090675
110	0.010177	9.777778	1.354167	0.001124	0.000498	0.732657	0.077603
120	0.016512	13.74444	1.171171	0.001371	0.000467	0.63221	0.092744
130	0.019423	15.97778	1.428571	0.001951	0.001229	0.683119	0.117178
140	0.018882	16.66667	1.477273	0.001483	0.000631	0.531787	0.105326
150	0.018667	16.06667	1.101695	0.001472	0.000858	0.660703	0.083493
160	0.020167	16.88889	1.354167	0.001537	0.000589	0.747311	0.095752
170	0.023224	17.15556	1.25	0.001723	0.000775	0.686323	0.085537
180	0.02401	18.85556	1.27451	0.001753	0.000753	1.091007	0.077071
190	0.025127	18.72222	1.326531	0.001872	0.000778	1.03769	0.088027
200	0.027655	19.92222	0.948905	0.001818	0.000721	0.437824	0.097916
210	0.025265	18.35556	1.238095	0.001917	0.000617	1.205922	0.076367
220	0.028102	19.31111	1.511628	0.00231	0.001051	1.689267	0.080235
230	0.026102	18.34444	1.444444	0.002246	0.001023	1.377042	0.096788
240	0.025573	16.05556	0.962963	0.002093	0.000857	0.908849	0.087783
250	0.028454	15.84444	1.023622	0.002659	0.001407	1.308508	0.083095
260	0.030313	17.51111	1.460674	0.002467	0.001368	1.945538	0.0833
270	0.028662	15.6	0.807453	0.00259	0.001223	1.13276	0.073386
280	0.031874	14.33333	1.111111	0.0039	0.001211	0.99708	0.07275
290	0.031258	14.17778	0.833333	0.003929	0.002142	1.055747	0.075693
300	0.031528	13.62222	0.607477	0.003654	0.001073	0.671274	0.068941
310	0.033467	13.4	0.921986	0.004338	0.001763	1.92447	0.067809
320	0.035795	13.98889	1	0.003868	0.001158	1.159834	0.083804
330	0.039094	10.83333	1.092437	0.011018	0.005868	-	0.164768
340	0.08442	12.42222	0.833333	0.02971	0.024935	-	0.4852
350	0.192191	15.45556	1.007752	0.043212	0.041629	-	0.716281
360	0.406518	14.15556	0.935252	0.054081	0.050477	-	0.796137
365	0.559702	13.1	0.878378	0.054144	0.050651	-	0.814133

B.2: Experimental data on smooth bed

Fr_1 = 2.84, Q = 0.078 m^3/s, Re_1=1.7×10^5, h = 0.06 m; d_1=0.067 m: x-x_1 = -0.3 m

Y (mm)	*C* [-]	*F* [Hz]	*V* [m/s]	T_{xx} [s]	T_{xx} ' [s]	*Tu* [-]	R_{xx}'(max)
10	0.000129	-	-	7.89E-05	1.05E-05	-	0.270729
15	0.000129	-	-	7.38E-05	9.24E-06	-	0.169628
25	0.000129	-	2.708333	0.000263	0	-	0.234085
35	0.000129	0.366667	2.653061	0.000387	0.000241	-	0.258107
45	0.000166	0.4	2.6	0.000594	0.000129	-	0.17224
50	0.000138	0.277778	2.826087	0.001812	0.000298	0.440518	0.229264
51	0.000138	0.4	2.708333	0.00145	0	0.142937	0.107458
52	0.000157	0.377778	2.765957	0.001856	0.000307	0.339706	0.308574
53	0.000172	0.344444	2.6	0.001079	0.000862	0.316132	0.285227
54	0.000177	0.344444	2.708333	0.000531	0.000319	0.200583	0.217575
55	0.000424	0.444444	3.25	0.001699	0.001629	0.758477	0.370377
56	0.000421	0.544444	2.6	0.001296	0.001269	0.7247	0.378161
57	0.001517	0.566667	2.765957	0.004335	0.003447	0.888505	0.535746
58	0.001776	0.755556	2.708333	0.005787	0.005383	0.660278	0.628957
59	0.003259	0.966667	2.826087	0.006578	0.006399	1.013793	0.834452
60	0.00445	1.333333	3.023256	0.009047	0.008854	1.157375	0.714148
61	0.010995	2.711111	2.888889	0.01408	0.012905	2.001811	0.852695
62	0.019003	4.633333	2.888889	0.011954	0.011498	1.025568	0.864325
63	0.047109	10.82222	2.954545	0.015533	0.014754	1.399512	0.8962
64	0.088051	17.76667	2.954545	0.02479	0.024541	2.100515	0.923499
65	0.189145	31.92222	2.954545	0.02631	0.025499	2.004375	0.925404
66	0.373302	42.08889	2.888889	0.033173	0.032283	2.579894	0.936027
67	0.536156	45.15556	2.954545	0.032392	0.031821	-	0.932312
68	0.744169	36.27778	2.954545	0.030415	0.030094	2.367583	0.922257
69	0.818546	27.67778	2.888889	0.031364	0.030835	2.641064	0.915633
70	0.921057	14.22222	2.954545	0.028387	0.027115	2.516772	0.898938
71	0.968503	7.544444	2.888889	0.017731	0.016742	1.190199	0.847989
72	0.969541	6.222222	2.954545	0.02528	0.021431	1.257605	0.794966
73	0.97311	2.422222	2.826087	0.017538	0.012169	1.004977	0.727295
74	0.991617	1.822222	2.826087	0.028141	0.011059	-	0.567366

Appendix B: Two-phase flow data of hydraulic jumps

Fr_1 = 2.84, Q = 0.078 m^3/s, Re_1=1.7×10^5, h = 0.06 m; d_1=0.067 m: x-x_1 = 0.1 m

Y (mm)	*C* [-]	*F* [Hz]	*V* [m/s]	T_{xx} [s]	T_{xx} ' [s]	*Tu* [-]	R_{xx}'(max)
20	0.047503	-	1.911765	0.002645	0.001713	0.416384	0.276633
25	0.001566	1.977778	2.363636	0.003324	0.002907	0.854929	0.429847
30	0.001117	1.688889	2.45283	0.001806	0.001858	0.746244	0.451699
35	0.003833	3.644444	2.45283	0.003918	0.00378	1.183079	0.453386
40	0.001555	2.1	2.280702	0.002599	0.002583	1.307106	0.471639
45	0.010627	10.24444	2.096774	0.004432	0.004158	1.231657	0.556371
50	0.017393	15.01111	2.363636	0.00441	0.004708	1.455095	0.602662
55	0.030082	23.1	2.280702	0.005631	0.005823	1.472538	0.620342
60	0.066779	45.82222	2.321429	0.005157	0.005342	1.654737	0.634375
65	0.125559	73.44444	2.280702	0.006004	0.005933	1.726704	0.607024
70	0.266563	101.7889	2.20339	0.009635	0.008956	1.894676	0.60676
75	0.273438	96.82222	2	0.006865	0.006529	2.07607	0.563307
80	0.301422	89.1	1.911765	0.008779	0.008463	2.569602	0.549117
85	0.362538	68.75556	1.733333	0.013236	0.011685	-	0.533467
90	0.333946	51.02222	1.884058	0.020979	0.017962	-	0.540889
95	0.266349	65.54444	1.688312	0.012019	0.010744	-	0.509997
100	0.312938	47.98889	2	0.021571	0.018751	-	0.512918
105	0.338316	40.97778	-	0.024491	0.021364	-	0.515498
110	0.424188	34.81111	-	0.02656	0.024919	-	0.523466
115	0.453081	35.17778	-1.78082	0.029754	0.02905	-	0.565589
120	0.525237	31.24444	-1.83099	0.031684	0.030526	-	0.600008
125	0.612968	26.27778	-1.2381	0.030037	0.029757	-	0.581364
130	0.73866	22.47778	-1.625	0.029481	0.028103	-	0.603914
135	0.897689	11.54444	-1.08333	0.027617	0.025604	-	0.533754
140	0.935321	7.266667	-0.90909	0.027923	0.026026	-	0.524308
145	0.927205	8.666667	-1.11111	0.025574	0.024129	-	0.53825
150	0.933865	8.144444	-1.46067	0.026929	0.024906	-	0.557804
155	0.987485	1.511111	-	0.026079	0.016394	-	0.495495

Appendix B: Two-phase flow data of hydraulic jumps

Fr_1 = 2.84, Q = 0.078 m^3/s, Re_1=1.7×10^5, h = 0.06 m; d_1=0.067 m: x-x_1 = 0.15 m

Y (mm)	*C* [-]	*F* [Hz]	*V* [m/s]	T_{xx} [s]	T_{xx} ' [s]	*Tu* [-]	R_{xx}'(max)
20	0.088735	0.12	-	0.00106	0.000829	-	-
25	0.023753	0.16	-	0.001098	0.001475	-	-
30	0.001186	1.322222	-	0.002398	0.002406	-	-
35	0.078751	-	-	0.002368	0.001743	-	-
40	0.005939	6.488889	2.363636	0.003553	0.003397	1.389447	0.470482
45	0.008532	8.188889	2.280702	0.004204	0.004083	1.314503	0.508972
50	0.026659	26.28889	2.20339	0.00414	0.003971	1.444751	0.461232
55	0.041218	32.92222	2.131148	0.005164	0.005076	1.597963	0.532058
60	0.066557	48.46667	2.063492	0.005227	0.00492	1.494749	0.546474
65	0.08872	58.88889	2	0.005365	0.005055	1.707279	0.524155
70	0.138953	77.91111	1.969697	0.005559	0.005251	1.858517	0.517503
75	0.17934	79.87778	1.911765	0.006929	0.006756	2.251152	0.531419
80	0.197175	76.42222	1.756757	0.008363	0.007522	2.380917	0.495282
85	0.277226	67.25556	1.733333	0.012699	0.011242	3.276634	0.50371
90	0.199433	63.86667	1.666667	0.010579	0.009631	3.060769	0.497566
95	0.256085	47.17778	1.511628	0.018394	0.015682	-	0.489084
100	0.281032	41.4	1.830986	0.020242	0.01674	-	0.492847
105	0.229173	33.5	-	0.020425	0.017238	-	0.47419
110	0.188375	37.23333	1.529412	0.017755	0.014602	-	0.452731
115	0.203071	30.33333	1.733333	0.021143	0.017934	-	0.498736
120	0.295607	26.34444	-	0.024521	0.022938	-	0.52527
125	0.344469	26.57778	-1.75676	0.028265	0.026585	-	0.574578
130	0.339055	26.52222	-1.60494	0.02608	0.024737	-	0.565806
135	0.650824	20.18889	-1.78082	0.029188	0.026772	-	0.582612
140	0.495457	23.23333	-1.41304	0.030538	0.030242	-	0.60845
145	0.551845	22.81111	-	0.031478	0.029097	-	0.608214
150	0.630482	20.91111	-1.41304	0.029967	0.029735	-	0.605087
155	0.813979	13.95556	-1.34021	0.03137	0.03054	-	0.604595
160	0.882653	8.922222	-1.47727	0.028818	0.025641	-	0.582616
165	0.89227	8.555556	-1.9403	0.030607	0.027989	-	0.58938
170	0.917023	6.666667	-1.51163	0.031089	0.028793	-	0.588766
180	0.93226	5.855556	-	0.02979	0.025558	-	0.566472
185	0.960774	3.266667	-	0.025193	0.022903	-	0.522365

Appendix B: Two-phase flow data of hydraulic jumps

Fr_1 = 2.84, Q = 0.078 m^3/s, Re_1=1.7×10^5, h = 0.06 m; d_1=0.067 m: x-x_1 = 0.3 m

Y (mm)	*C* [-]	*F* [Hz]	*V* [m/s]	T_{xx} [s]	T_{xx} ' [s]	*Tu* [-]	R_{xx}'(max)
5	0.001	246.2333	1.780822	-	0.000696	0.222412	-
11	0.001	423.3667	2.20339	-	0.000727	0.213938	-
17	0.002	191.6222	1.940299	-	0.002164	0.852326	-
23	0.003833	5.466667	2.20339	0.002328	0.001837	0.700108	0.359082
29	0.007604	9.211111	2.20339	0.003262	0.003157	1.211593	0.35931
35	0.014159	15.18889	2.03125	0.004266	0.003823	1.42717	0.392772
41	0.022122	21.83333	2	0.004433	0.004032	1.220256	0.435802
47	0.03725	33.17778	1.969697	0.00546	0.004927	1.520829	0.44575
53	0.047642	38.75556	2	0.005088	0.004756	1.615667	0.461229
59	0.060018	47.42222	1.969697	0.004848	0.004336	1.584014	0.428045
65	0.072139	50.75556	1.884058	0.005513	0.004912	1.706284	0.447766
71	0.096867	59.28889	1.805556	0.006454	0.006046	2.134874	0.461778
77	0.118634	65.44444	1.780822	0.006478	0.00605	2.058735	0.463877
83	0.102078	57.8	1.733333	0.006227	0.004926	2.04035	0.395444
89	0.183964	63.52222	1.604938	0.010082	0.009028	2.598064	0.487119
95	0.17868	62.53333	1.494253	0.009923	0.008949	2.512846	0.459731
101	0.166115	53.01111	1.666667	0.010576	0.009401	3.379363	0.432037
107	0.153991	47.66667	1.368421	0.012303	0.010097	3.20849	0.404712
113	0.188398	39.92222	1.444444	0.020137	0.017399	-	0.481409
119	0.154179	36.61111	1.354167	0.015909	0.012602	-	0.408672
125	0.205192	38.8	2.708333	0.019955	0.016853	-	0.445407
131	0.180243	30.71111	1.857143	0.021153	0.017665	-	0.451656
137	0.162938	29.68889	-	0.021236	0.018389	-	0.439074
143	0.227084	30.21111	-1.91176	0.026681	0.024595	-	0.481897
149	0.259746	29.4	-2.70833	0.02571	0.022481	-	0.481818
155	0.299017	29.08889	-2.20339	0.025584	0.022275	-	0.499208
161	0.337244	30	-2.45283	0.028481	0.02694	-	0.576073
167	0.330462	25.98889	-	0.03312	0.030932	-	0.605656
173	0.464671	26.85556	-	0.03561	0.034662	-	0.628354
179	0.642973	22.92222	-	0.032598	0.031162	-	0.614955
185	0.630369	24.47778	-2.76596	0.034748	0.034588	-	0.63585
191	0.687807	21.78889	-	0.035839	0.035699	-	0.655126
197	0.703576	19.12222	-	0.038279	0.036235	-	0.660288
203	0.831176	12.84444	-	0.036303	0.035215	-	0.662928
209	0.872843	10.42222	-	0.035289	0.033095	-	0.651662
215	0.920533	7.444444	-	0.02918	0.027935	-	0.585592
221	0.961193	4.222222	-	0.026587	0.023552	-	0.566171
227	0.929661	6.155556	-	0.035846	0.033674	-	0.64547
233	0.946948	5.066667	2.954545	0.033759	0.029845	-	0.600224
239	0.967249	3.677778	1.911765	0.027744	0.023504	-	0.566107
245	0.985132	1.555556	0.884354	0.026495	0.021677	-	0.521833

Appendix B: Two-phase flow data of hydraulic jumps

Fr_1 = 2.84, Q = 0.078 m^3/s, Re_1=1.7×10^5, h = 0.06 m; d_1=0.067 m: x-x_1 = 0.45 m

Y (mm)	*C* [-]	*F* [Hz]	*V* [m/s]	T_{xx} [s]	T_{xx} ' [s]	*Tu* [-]	R_{xx}'(max)
5	0.003133	3.955556	-	0.002155	0.002236	1.013725	0.233878
12	0.000827	1.288889	-	0.000695	0.000527	0.242446	0.107326
19	0.005423	7.011111	-	0.002375	0.002499	1.226187	0.284733
26	0.009715	11.47778	-	0.003385	0.003186	1.150709	0.327661
33	0.015164	16.2	1.830986	0.003774	0.003766	1.217618	0.352358
40	0.019835	20.94444	1.830986	0.003494	0.003312	1.156812	0.314018
47	0.02922	27.73333	1.830986	0.004003	0.00381	1.091179	0.355989
54	0.03386	31.44444	1.780822	0.003611	0.003495	1.296504	0.348829
61	0.037457	32.3	1.733333	0.003836	0.003518	1.46719	0.346097
68	0.049709	38.57778	1.756757	0.004226	0.00361	1.659829	0.346367
75	0.067372	44.91111	1.625	0.005272	0.004654	1.751315	0.367839
82	0.070264	43.8	1.585366	0.005752	0.004886	1.780524	0.345958
89	0.063074	40.32222	1.585366	0.00445	0.003763	1.720848	0.305006
96	0.105827	47.55556	1.477273	0.008281	0.00756	2.358461	0.383663
103	0.08031	39.43333	1.413043	0.006588	0.005415	2.127902	0.338955
110	0.087898	38.88889	1.368421	0.006703	0.005171	2.012299	0.296098
117	0.109923	35.44444	1.494253	0.0118	0.009234	3.088805	0.360925
124	0.110368	33.14444	1.382979	0.012062	0.009102	3.124899	0.34085
131	0.0946	28.37778	1.238095	0.011651	0.008641	2.850239	0.316624
138	0.095474	25.42222	1.397849	0.013663	0.01069	3.804104	0.375876
145	0.083489	22.83333	1.494253	0.013923	0.011062	-	0.309459
152	0.097751	21.34444	-	0.020041	0.016014	-	0.398099
159	0.086706	18.82222	-	0.016326	0.010419	-	0.322123
166	0.104099	18.58889	-	0.022584	0.016495	-	0.404701
173	0.148316	20.36667	-	0.020942	0.017972	-	0.428152
180	0.168919	23.32222	-	0.025367	0.021758	-	0.461201
187	0.248297	23.11111	-	0.033366	0.032844	-	0.591545
194	0.250717	24.48889	-	0.035293	0.033498	-	0.614305
201	0.2473	21.51111	-	0.036835	0.032164	-	0.630872
208	0.415946	22.32222	-	0.038095	0.037092	-	0.671113
215	0.510743	21.33333	-	0.044213	0.043184	-	0.718519
222	0.718623	15.48889	-	0.040951	0.039439	-	0.695416
229	0.760177	13.96667	2.363636	0.045729	0.042997	-	0.737531
236	0.857148	10.57778	-	0.040608	0.03677	-	0.677166
243	0.884405	8.166667	3.170732	0.041095	0.038258	-	0.689381
250	0.936361	4.866667	2.407407	0.037298	0.035491	-	0.679237
257	0.929701	5.533333	1.64557	0.038844	0.034781	-	0.655806
264	0.963219	3.333333	2.20339	0.030252	0.027047	-	0.584402
271	0.979954	2.344444	0.977444	0.024913	0.017437	-	0.495422
278	0.986751	32.92222	-	0.025246	0.017334	-	0.497329

Appendix B: Two-phase flow data of hydraulic jumps

Fr_1 = 2.84, Q = 0.078 m^3/s, Re_1=1.7×10^5, h = 0.06 m; d_1=0.067 m: x-x_1 = 0.6 m

Y (mm)	*C* [-]	*F* [Hz]	*V* [m/s]	T_{xx} [s]	T_{xx} ' [s]	*Tu* [-]	R_{xx}'(max)
5	0.002068	2.288889	1.884058	0.001247	0.001288	-	-
13	0.00449	5.444444	1.780822	0.002005	0.001986	0.649587	0.247825
21	0.008127	9.111111	1.688312	0.002676	0.002315	0.803074	0.268048
29	0.011637	12.45556	1.625	0.00345	0.003184	0.933194	0.263347
37	0.013915	14.42222	1.64557	0.002509	0.002189	0.879367	0.237735
45	0.017183	17.03333	1.64557	0.002513	0.002203	1.019663	0.239114
53	0.027435	25.04444	1.688312	0.003256	0.002906	1.06667	0.284705
61	0.033694	27.33333	1.604938	0.004254	0.003562	1.20926	0.310453
69	0.038194	29.91111	1.511628	0.003839	0.003538	1.421111	0.257786
77	0.042438	30.62222	1.444444	0.003919	0.003299	1.307331	0.249594
85	0.050439	34.06667	1.547619	0.00421	0.003164	1.387053	0.271418
93	0.047065	32.1	1.547619	0.003238	0.002604	1.399062	0.227871
101	0.04997	31.13333	1.529412	0.003954	0.003283	1.702236	0.244531
109	0.053278	30.53333	1.340206	0.003973	0.002795	1.428065	0.223058
117	0.046906	27.78889	1.444444	0.003079	0.002402	1.617232	0.180513
125	0.053405	28.27778	1.111111	0.004001	0.002879	1.37936	0.195343
133	0.058629	27.36667	1.192661	0.005859	0.004147	2.056563	0.194284
141	0.058743	26.13333	1.140351	0.004789	0.002776	1.671874	0.174105
149	0.057611	25.27778	1.171171	0.004827	0.00321	1.622383	0.174642
157	0.065291	26.36667	1.192661	0.006247	0.003983	2.042795	0.182507
165	0.062675	22.86667	1.413043	0.007915	0.005357	-	0.196283
173	0.055725	20.16667	1.262136	0.006644	0.004275	2.371348	0.179088
181	0.047862	16.86667	1.023622	0.006361	0.00348	1.510043	0.150405
189	0.043067	14.84444	0.822785	0.006488	0.003955	1.781806	0.169531
197	0.044733	14.18889	1.326531	0.009692	0.006035	-	0.189139
205	0.043859	13.16667	1.494253	0.009635	0.006593	-	0.200641
213	0.070141	12.87778	1.547619	0.020119	0.016077	-	0.381774
221	0.095081	13.15556	2.241379	0.031729	0.028768	-	-
229	0.122206	12.86667	1.413043	0.03758	0.035447	-	0.630485
237	0.250087	13.91111	1.203704	0.047473	0.044534	-	0.746448
245	0.381588	14.1	1.566265	0.050082	0.048955	-	0.787551
253	0.479535	14.17778	1.444444	0.053042	0.051302	-	0.81305
261	0.715915	10.16667	1.340206	0.051377	0.048506	-	0.805586
269	0.821665	8.022222	1.547619	0.046769	0.046994	-	0.772053
277	0.880871	5.955556	1.04	0.045293	0.042174	-	0.785598
285	0.91343	4.444444	0.977444	0.044548	0.040114	-	0.780687
293	0.976497	1.977778	0.687831	0.0332	0.028687	-	-
301	0.982469	1.322222	1.092437	0.029188	0.025839	-	0.693167

Appendix B: Two-phase flow data of hydraulic jumps

Fr_1 = 2.84, Q = 0.078 m^3/s, Re_1=1.7×10^5, h = 0.06 m; d_1=0.067 m: x-x_1 = 0.8 m

Y (mm)	*C* [-]	*F* [Hz]	*V* [m/s]	T_{xx} [s]	T_{xx} ' [s]	*Tu* [-]	R_{xx}'(max)
5	0.002006	1.811111	1.354167	0.001199	0.00053	-	-
15	0.005098	4.988889	1.585366	0.001851	0.000908	0.667027	0.177899
25	0.008061	8.044444	1.413043	0.001974	0.001341	0.556463	0.169768
35	0.012487	11.1	1.511628	0.002894	0.002365	0.92663	0.204512
45	0.014149	12.64444	1.397849	0.002836	0.001883	0.595348	0.207046
55	0.015165	12.93333	1.444444	0.002133	0.001902	0.866255	0.186796
65	0.018855	14.43333	1.368421	0.002475	0.001571	0.879472	0.155889
75	0.024174	18.92222	1.382979	0.002489	0.001887	0.805683	0.191858
85	0.028884	21.24444	1.238095	0.002602	0.001653	0.942525	0.169412
95	0.028503	19.62222	1.25	0.002399	0.001583	0.825114	0.171234
105	0.037998	23	1.25	0.003553	0.00213	1.284865	0.16567
115	0.036329	21.21111	1.27451	0.00312	0.001796	1.081362	0.15441
125	0.029957	18.08889	1.048387	0.003013	0.001543	0.932648	0.151199
135	0.041325	20.78889	1.25	0.003717	0.001921	1.34428	0.152307
145	0.04306	20.23333	1.226415	0.004547	0.002807	2.021905	0.14229
155	0.035689	17	1.130435	0.004082	0.002826	1.654475	0.14102
165	0.035473	16.2	1.092437	0.004464	0.002543	2.102762	0.111037
175	0.032459	13.31111	0.928571	0.004765	0.003246	2.250016	0.115367
185	0.034366	14.51111	1.130435	0.003968	0.002031	1.562277	0.093013
195	0.031405	11.42222	1.150442	0.004502	0.001765	2.031479	0.091716
205	0.027237	9.622222	0.878378	0.00506	0.002114	1.641481	0.102912
215	0.032509	9.377778	1.140351	0.00987	0.005776	-	0.181167
225	0.036789	9.588889	-	0.012775	0.010678	-	0.22737
235	0.142996	12.6	1.25	0.037193	0.032643	-	0.607844
245	0.174645	12.71111	1.007752	0.045444	0.041254	-	0.696968
255	0.331582	13.63333	1.160714	0.050883	0.048334	-	0.782715
265	0.450209	11.28889	1.382979	0.057104	0.055245	-	0.82637
275	0.605871	10.24444	1.262136	0.05742	0.055657	-	0.84559
285	0.751833	8.277778	1.101695	0.052903	0.050378	-	0.834861
295	0.886058	5.255556	1.092437	0.048344	0.046826	-	0.809023
300	0.948436	2.811111	1.181818	0.043977	0.042116	-	0.821888

Appendix B: Two-phase flow data of hydraulic jumps

Fr_1 = 2.84, Q = 0.078 m^3/s, Re_1=1.7×10^5, h = 0.06 m; d_1=0.067 m: x-x_1 = 1.1 m

Y (mm)	*C* [-]	*F* [Hz]	*V* [m/s]	T_{xx} [s]	T_{xx} ' [s]	*Tu* [-]	R_{xx}'(max)
5	-	-	1.056911	0.001078	0	0.123765	-
15	0.002291	1.922222	1.015625	0.001295	0.000374	0.184247	0.081952
25	0.002891	2.466667	1.065574	0.001285	0.00056	0.34279	0.096331
35	0.003374	2.844444	1.27451	0.001354	0.00042	0.626569	0.092386
45	0.004021	3.244444	1.3	0.001578	0.000443	0.551511	0.102635
55	0.004761	4.066667	1.101695	0.001286	0.000368	0.371953	0.080011
65	0.006265	4.822222	1.494253	0.001775	0.000864	1.236668	0.086237
75	0.006724	5.222222	1.25	0.001453	0.000715	0.67138	0.105772
85	0.008431	6.3	1.238095	0.001952	0.000968	0.49532	0.090145
95	0.009734	7.422222	1.056911	0.001572	0.000794	0.855824	0.077244
105	0.010154	7.477778	1.092437	0.001527	0.000569	0.737135	0.077592
115	0.011739	8.077778	1.477273	0.001797	0.000615	1.103237	0.074832
125	0.011921	8.311111	1.226415	0.002253	0.000948	0.956683	0.082457
135	0.011871	8.344444	0.935252	0.001939	0.00075	1.015066	0.08532
145	0.012176	7.355556	1.065574	0.002015	0.000629	1.032832	0.059127
155	0.015138	9.388889	0.962963	0.001939	0.000761	0.838558	0.068438
165	0.013386	7.966667	1.083333	0.002153	0.000671	0.832327	0.06283
175	0.01251	6.888889	-	0.002121	-	-	-
185	0.013465	6.977778	0.935252	0.002479	0.000818	1.022351	0.060199
195	0.013668	7.077778	0.687831	0.002066	0.000447	0.298672	0.046276
205	0.011549	5.677778	0.442177	0.002246	0.000404	0.396449	0.054866
215	0.01301	6.188889	0.702703	0.002318	0.000312	0.822577	0.04344
225	0.011905	5.355556	0.828025	0.002495	0.000837	1.459281	0.05119
235	0.014049	5.688889	0.486891	0.003132	0.00099	0.63409	0.066564
245	0.015786	6.066667	0.935252	0.003499	0.001012	0.971885	0.061793
255	0.025753	6	0.909091	0.016457	0.012898	-	0.323012
265	0.042562	6.322222	1.111111	0.024959	0.02129	-	-
275	0.146792	7.266667	0.792683	0.04413	0.04006	-	0.734169
285	0.352775	9.966667	0.866667	0.053412	0.049624	-	0.82619
295	0.646778	10.6	0.909091	0.050634	0.04702	-	0.822877
303	0.788691	7.566667	0.948905	0.053648	0.051011	-	0.84395